FORMATION AND SELECTION OF HIGHLY NONLINEAR MICROSTRUCTURE DURING DIRECTIONAL SOLIDIFICATION

by

NARAYANAN RAMPRASAD

B. Tech., Indian Institute of Technology, Madras, India

(1985)

M.S.C.E.P., Massachusetts Institute of Technology

(1987)

Submitted to the Department of Chemical Engineering
in partial fulfillment of the requirements
for the degree of
DOCTOR OF PHILOSOPHY
at the
MASSACHUSETTS INSTITUTE OF TECHNOLOGY
September, 1991

Signature of Author ______________________________.

Department of Chemical Engineering
August, 1991

Certified by ______________________________.

Robert A. Brown
Professor, Department of Chemical Engineering
Thesis Supervisor

Accepted by ______________________________.

William M. Deen
Professor, Department of Chemical Engineering
Chemical Engineering Graduate Officer

FORMATION AND SELECTION OF HIGHLY NONLINEAR MICROSTRUCTURE DURING DIRECTIONAL SOLIDIFICATION

by

NARAYANAN RAMPRASAD

Submitted to the Department of Chemical Engineering
on August 30, 1991, in partial fulfillment of the
requirements for the Degree of Doctor of Philosophy in
Chemical Engineering

Abstract

Interfacial microstructure that forms during the solidification of an alloy is important in determining the end properties of the material. This thesis studies the formation of two-dimensional morphologies during the directional solidification of a thin-film sample of a dilute binary alloy where the sample is translated through a unidirectional temperature field. The heat and mass transfer near the melt-solid interface and the thermodynamics of the interface are examined for this system.

Above a critical solidification rate, a variety of interfacial patterns are observed in thin-film solidification experiments. The planar interface undergoes a transition to nonuniform small amplitude cells. Uniform deep cells, with nearly constant wavelengths and three-dimensional dendrites are seen as the growth rate V is increased.

Transitions near the onset of cellular solidification are well characterized. Linear stability analysis of the directional solidification system predicts a marginal stability curve of neutrally stable wavelengths as a function of the growth rate, $V = V_c(\lambda_c)$. The dependence of V_c on λ_c is extremely weak due to the small surface energy typical of these experimental systems. Consequently, a band of wavelengths becomes unstable for growth rates that are only slightly above V_c; this leads to nonlinear transitions between families of cells of different wavelengths and causes the complex cellular patterns that are observed. The work of this thesis emphasizes structures that are seen far from this transition.

Finite element calculations are performed to predict the transition from shallow cells to deep cells as V is increased. Reduction of the primary spacing of cellular families by repeated tip-splitting and wavelength halving, which has been previously reported for shallow cells, are shown to be a generic characteristic of deep cells, with only minor changes in the connectivity of solution families. During wavelength halving, a family of solutions of wavelength λ that bifurcates off the planar state, terminates at a secondary bifurcation on the $\lambda/2$ family; in deep cells, this transition occurs after the family goes through a turning point in the dimensionless growth rate or Peclet number P. As the secondary bifurcation is approached, cells with wavelength λ undergo tip-splitting, whereby an indentation forms at the tip and grows until the cell has half the primary spacing.

This thesis is the first study to conclusively show that no mechanism exists for the selection of deep cells based on the existence or stability of steady-states. Cells exist for a range of wavelengths at each growth rate. The range is bounded on the left by the marginal stability curve and on the right by a curve of limit points that correspond to the turning points with increasing growth rate.

The results of the numerical simulation compare well with the experimental data of de Cheveigné *et al.* (1986) for the CBr_4-Br_2 alloy system, where wavelength reduction with increasing growth rate and no selection mechanism are observed. The range of wavelengths predicted at a given growth rate brackets the experimentally observed values. The computed and experimental cell shapes at a given growth rate and wavelength compare favorably. The curve of limit points is shown to scale as $\lambda \sim V^{-0.5}$. This scaling is reported in experimental studies. However, the experimental data gives cells of a smaller wavelength at any growth rate. It is likely that the experimentally observed wavelength is a function of the time history of the experiment; any wavelength that is specified has to be a quantity that is statistically averaged over time and across the interface.

An asymptotic analysis of deep cells is reported, based on the slenderness of the sidewall. The perturbation analysis is used to determine the sidewall shape and position it in the domain by applying an overall solute balance at an arbitrary cross-section of the cell. The cell tip and bottom regions are decoupled and may be analyzed separately, although no closed form expressions were found for these portions of the interface. A numerical procedure is developed to calculate only the cell tip and sidewall regions; this technique is used to calculate cells to high growth rates, with the introduction of an anisotropic surface energy. No transition is predicted between deep cells and two-dimensional protodendritic shapes with parabolic tips. Using an anisotropic surface energy deep cells are calculated up to higher growth rates, but these cells still undergo tip-splitting and wavelength halving, so that no transition to protodendrites is indicated. It is possible that time-dependent calculations and/or a three-dimensional model are necessary to simulate needle-shaped structures.

Thesis Supervisor: Dr. Robert A. Brown
Title : Professor of Chemical Engineering

Acknowledgments

I wish to express my appreciation to my advisor Professor Robert A. Brown for his support and guidance and for his limitless energy, which has been a constant source of encouragement. I also wish to thank Prof. Armstrong, Prof. Hatton and Prof. Ungar for their input as members of my thesis committee.

I wish to thank the members of my research group, both past and present, for the numerous illuminating discussions that we've had, both academic and extracurricular. In particular I'd like to acknowledge Lyle Ungar, Phil Sackinger, Paul Thomas, Do Kim, Sanjay Patnaik, Raghu Menon, Howard Covert, Kostas Tsiveriotis, Tom Kinney, Angelos Kyrlidis, Dimitri Maroudas, Aparna Bhave, Suresh Ramalingam, and Reza Mehrabi. I wish to specially thank Mark Bennett and John Lee; working with them was very enjoyable.

I also wish to thank my other friends at MIT and elsewhere - Jeffrey, Ganesh, GK, Mani & Shampa, Murali, Padmaraj, Preeti & Ben, Rama, RamaRao, Ramnath, Ratna, Sanjay, Ski & Anu, Suresh, Varada & Chinni and Vats - for their help and support over the years and for their immense contribution to my happiness and good health.

Finally and foremost, I wish to acknowledge my family. Amma, Anna, Mambuli, Ravi & Mala, Suji & Ramesh and Chandru - to you, I dedicate this thesis.

Contents

List of Tables

List of Figures

Chapter 1

Microstructure In Solidified Materials

Summary

Solidification is a common process for making a variety of man-made materials, including metals, semiconductors, glasses and polymers, and also is important in the formation of most naturally occurring solid matter from snow flakes to rocks. The most widely-used materials produced by solidification are metallic alloys which constitute materials ranging from those produced in the tons by continuous casting, like cast iron, to the relatively small quantities of high-purity crystals, like Gallium Arsenide. In many applications, solidification results in the formation of microscopic patterns along the melt-solid interface that are incorporated into the material as microstructure, which affects the mechanical and electrical properties of the material. Once created, these micron-scale structural variations are difficult to eliminate and persist through further processing of the material. Solidification theory thus plays a vital role in determining the end properties of these materials. This thesis has an overall aim of contributing to the understanding of selected aspects of the theory of microscale solidification.

Directional solidification is the method of solidification of an alloy caused by translating the melt sample through an imposed unidirectional temperature field. The range of imposed

temperatures bounds the melting point of the alloy so that, at steady-state, the material is solidified at a rate equal to the translation rate. Zone-refining, Czochralski and Bridgman growth of crystals and electroslag remelting are some processes which employ directional solidification (Winegard 1964, Kurz & Fisher 1986, Brown 1988).

The interface patterns that form during directional solidification are either periodic finger-like smooth structures called cells or highly-branched protrusions called dendrites. The interest in microstructure formation in this thesis and in other recent studies, both theoretical (Kessler *et al.* 1988) and experimental (Eshelman *et al.* 1988, de Cheveigné *et al.* 1988) stems from a need to understand the concepts governing the connection between processing conditions and the length and time scales associated with these microstructures.

Experimental study of the solidification process in metals has been hampered by their high melting points and opacity and most recent experimental studies use the popular thin-film solidification configuration shown schematically in Fig. 1.1 and pioneered by Jackson & Hunt (1965) who showed that certain transparent organic materials solidify like metals and can be used effectively to study directional solidification.

The results from these experiments show that the planar interface is unstable for translation rates greater than a critical value at fixed temperature gradient. Interface shape from a thin-film experiment by Trivedi (1984) using a succinonitrile-acetone alloy are shown in Fig. 1.2. For growth rates just above the critical value, a cellular pattern results as shown in Fig. 1.2a. This pattern becomes deeper and its spatial wavelength decreases as the velocity is further increased as shown in Fig. 1.2b. At relatively higher velocities dendritic patterns are seen as shown in Fig. 1.2c are seen. The experiments also indicate that while cells near the planar-cellular transition are non-uniform in both amplitude and spatial wavelength, the deeper cells at higher velocities are more uniform (Venugopalan & Kirkaldi 1984).

Theoretical studies that combine transport phenomena with concepts of thermodynamics and material science have since been developed with three specific goals in trying to predict the features seen in experiments:

(i) the onset of cellular interfaces,

(ii) the change in amplitude and spatial wavelength as the growth rate is increased, and

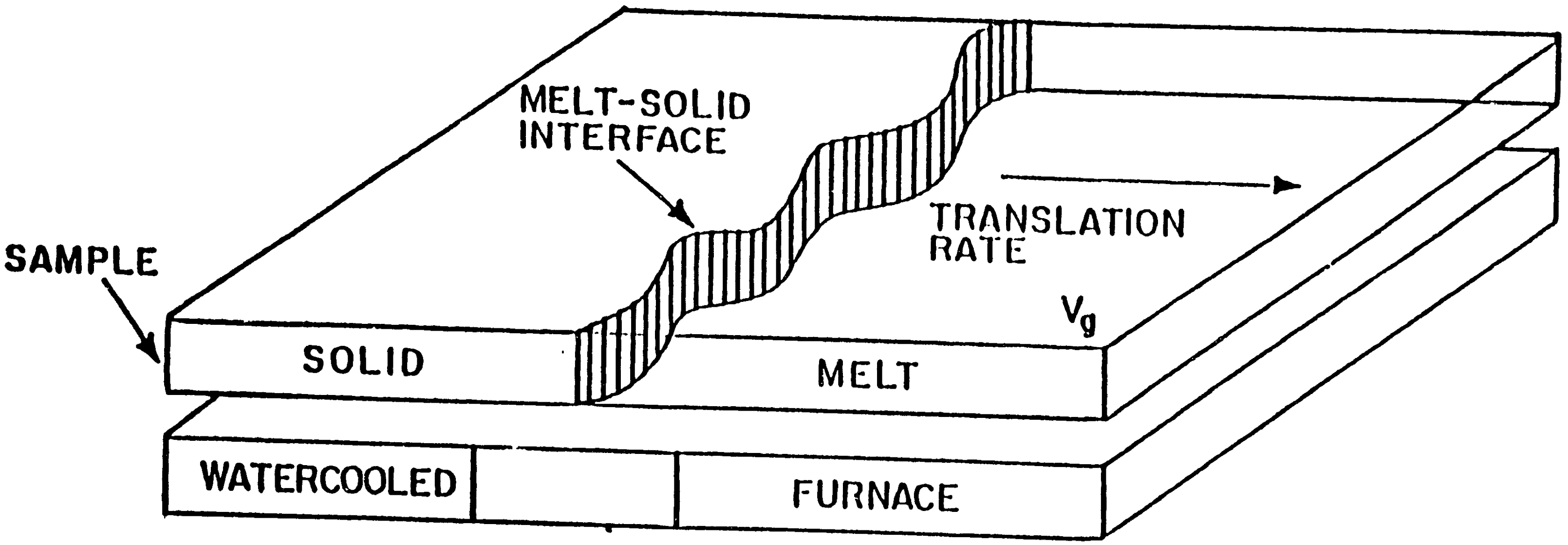

Figure 1: Schematic representation of the thin-film directional solidification experiment.

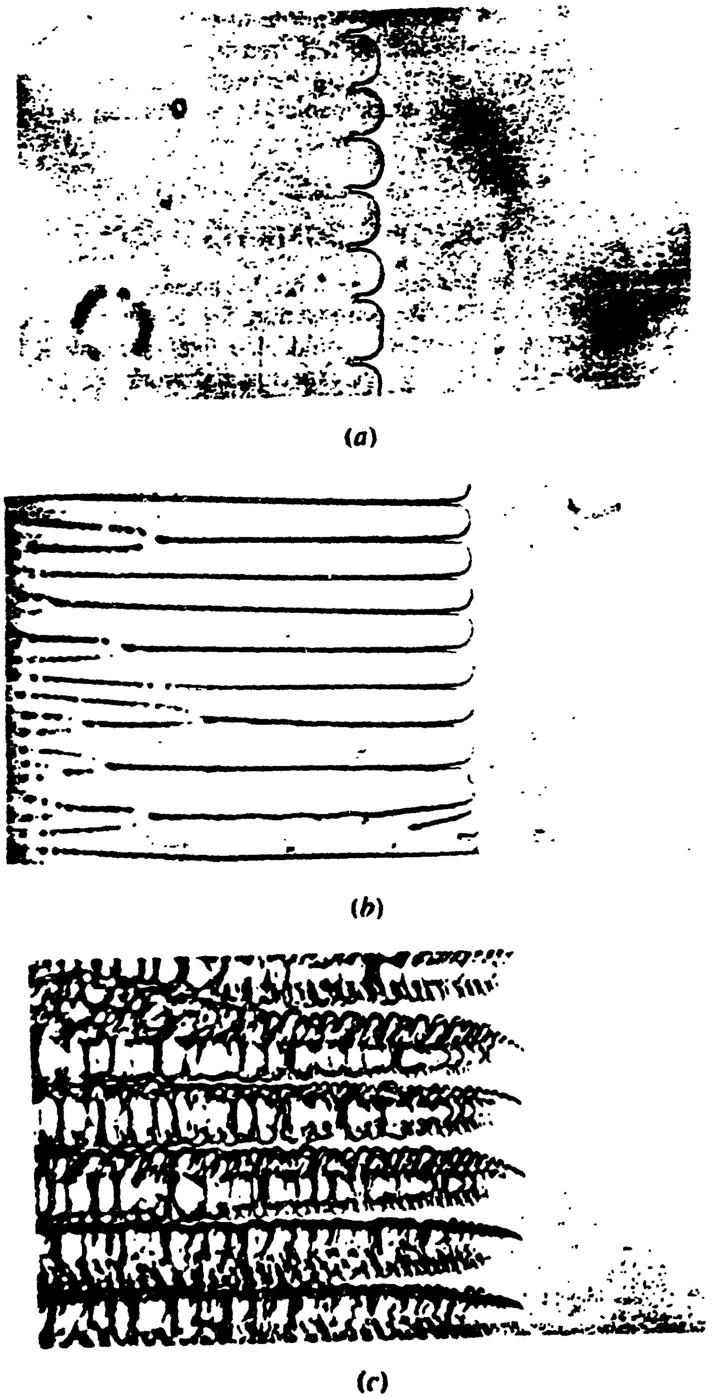

Figure 1.2: Interface shapes from a thin-film experiment with a succinonitrile-acetone alloy (from Trivedi 1984): (a) shallow cells: $V = 0.4\mu\text{m/sec}$, (b) deep cells: $V = 0.58\mu\text{m/sec}$, (c) dendrites: $V = 10\mu\text{m/sec}$.

(iii) the transition to dendritic patterns.

The onset of the morphological instability and characteristics of the small amplitude cells that are found near onset have both been extensively studied (Coriell *et al.* 1984, 1985, 1987, Langer 1980, Ungar 1984, Bennett 1990).

Simple thermodynamic scaling arguments about the melt directly ahead of the interface by Tiller *et al.* (1953) resulted in the constitutional supercooling criterion which predicts the critical pulling rate at the onset of instability of the planar interface for a given imposed temperature gradient. This relationship between processing conditions is reasonably accurate but it does not predict the spatial length scale of these instabilities or the time scale for their growth. Two-dimensional thermosolutal models which combine heat and mass transfer in the two phases with the thermodynamics of the phase transition have since been employed to predict these characteristics. Mullins & Sekerka (1964) first performed linear stability analysis of the planar interface solution using a simple thermal-solutal model to predict more precisely the onset of instability. The analysis shows that for any velocity less than a critical growth rate $V > V_c$ modes with a range of wavelengths are linearly unstable to small perturbations. Extensions of this analysis have since been conducted to include other physical effects such as anisotropy of the surface energy (Coriell & Sekerka 1976).

Nonlinear analyses of these solidification models by Wollkind & Segal (1970) and McFadden *et al.* (1987) among others and numerical solutions by Ungar (1984) and Bennett (1990) have been successful in predicting the kind of interface forms seen right near the the onset of morphological instability. But the deep cells that are formed at conditions relatively far from critical are less well-characterized. Ungar & Brown (1985) have shown that deep cells with reentrant grooves can be simulated using two-dimensional thermal-solutal models of solidification but the transition from shallow cells to deep cells is not well-characterized. Another feature of cellular morphologies that is of particular interest is pattern selection; both steady-state and time-dependent analyses (Karma 1986, Dombre & Hakim 1987, Ben-Amar & Moussallam 1988) have been used to determine whether a steady-state pattern with a particular spatial wavelength is selected by the theory or whether the selected pattern is a function of the history of the evolving interface; the results of these studies are inconclusive.

The third main objective of theoretical studies has been to predict the transition from cells to dendrites. While dendritic patterns have been simulated in theory (Langer 1980), the transition from cells to dendrites has not been predicted. While both steadily-growing and dynamically changing cellular morphologies have been predicted, it is expected that dendrites are dynamically changing three-dimensional structures (Trivedi 1984).

This thesis attempts to clarify some of the issues presented above; specifically
(i) predict steadily-growing and time-dependent morphologies far beyond onset, and
(ii) determine whether cellular morphology of a unique wavelength is selected.

1.1 Interfacial Morphologies During Solidification

The primary reason for the study of microstructure formation in solidified materials is the influence of this structure on the properties of the material. For some applications the presence of microstructure is advantageous; the additional mechanism for plastic slip associated with polycrystalline materials (Flemings 1974) increases the strength of the material. For more delicate uses like electronic devices the presence of these spatial variations in properties is often a hindrance to the performance of the material.

Besides the specific importance of solidification microstructure in the processing of metals and semiconductors, the formation of these interfaces is of much current interest in theoretical physics because the formation of these patterns is a classical example of pattern formation in transport processes. Other systems which exhibit qualitatively similar behavior include flow transitions in fluid mechanical systems, like the Rayleigh-Bénard natural convection experiments (Busse 1982), the Taylor problem of flow between concentric rotating cylinders (Wesfreid & Zaleski 1984) and Saffman-Taylor fingering (Park & Homsy 1984) during fluid flow in porous media. It is hoped that the study of any one of these systems will give some insight into pattern formation in the others. This Section describes the kinds of microstructures that are formed during solidification from the melt and gives an introduction to the types of interfaces studied in this work.

The particular case of directional solidification is introduced in Section 1.2 and experimental work in this area is summarized in Section 1.3. Previous research on nonlinear analysis of theoretical models of directional solidification is described in Section 1.4. One of the most important characteristics of pattern formation during solidification - *pattern selection* is introduced in Section 1.5. The experimental system apparently selects a particular pattern from among many possible spatial structures which are all linearly unstable. This section summarizes the experimental evidence in this area and reviews the theoretical studies to date. The remainder of this thesis is outlined in Section 1.6.

1.1.1 Solidification from the Melt

Many of the most commonly-used techniques used in manufacturing like casting, welding, soldering and directional solidification involve solidification from the melt. In each case solidification starts with nucleation which is defined as the formation of a single solid particle surrounded by melt. Once nucleation has begun, a solid-liquid interface has been established. The growth of this interface depends on the kinetics of atomic attachment to this interface, on heat and mass-transfer at the interface and on the thermodynamics of the interface. It is usually assumed that in the growth of non-faceted solids, atoms attach themselves so rapidly to the interface that the kinetics does not limit the growth of the interface (Kurz & Fisher 1986). The type of interface that develops depends on whether the melt is a pure material or a mixture and whether growth is into a positive temperature gradient or a negative one. The two cases of a pure material and a mixture are considered below.

1.1.1.1 Solidification of a Pure Material

When the surface of a crystal of a pure substance is in contact with its melt there is a temperature below which further solidification occurs. This temperature is the equilibrium melting temperature. When there is no growth the normal temperature gradients at the interface in the two phases are such that the heat flow in the melt equals that in the solid.

These temperature gradients follow the interfacial energy balance

$$\kappa_s \tilde{G}_s = \kappa_m \tilde{G}_m \quad , \tag{1.1}$$

where κ_s and κ_m are the thermal conductivities in the solid and melt, respectively, and $\tilde{G}_s$ and $\tilde{G}_m$ are the temperature gradients in the solid and melt, respectively.

When the crystal is growing, latent heat is generated at the interface and the rate of growth depends on the rapidity with which this heat can be conducted away. The local rate of growth at any point on the surface therefore depends on the thermal conditions and on the orientation of the surface. The normal temperature gradients are now related by

$$\kappa_s \tilde{G}_s = \kappa_m \tilde{G}_m + L_v V A \quad , \tag{1.2}$$

where L_v is the latent heat per unit volume, V is the rate of growth in the normal direction and A is the cross-sectional area. Another important effect is the dependence of the equilibrium temperature on the curvature of the interface. The interaction between the the local growth rate and the effect of the geometry of the interface on local heat flow and on the melting temperature is responsible for the complex morphologies seen in solidification. Early experiments with metallic alloys, in which liquid was rapidly removed (decanted) from the growing solid, confirmed this dependence of the structure of the solid-liquid interface on the conditions of solidification (Winegard 1964).

When the temperature gradient in the liquid is positive the melt-solid interface is planar and structureless, at least on a size scale greater than 10^{-3}cm. The solid has no microscale variations but has a macroscopic structure which is an array of rods of hexagonal or square cross-section about 1 sq. mm in area, separated by low angle grain boundaries; see Fig. 1.3. This macromosaic of ripples or striations were first shown to exist in the solidification of lead by Weinberg & Chalmers (1951). Solidification into a positive temperature gradient is often referred to as columnar or constrained growth.

The stability of the planar interface during columnar growth can be easily explained. Consider a perturbation of amplitude ϵ which grows on the interface as shown in Fig. 1.4. If the temperature field were allowed to deform during columnar growth, the temperature would increase in the z-direction. The interface is located where the temperature T_q imposed

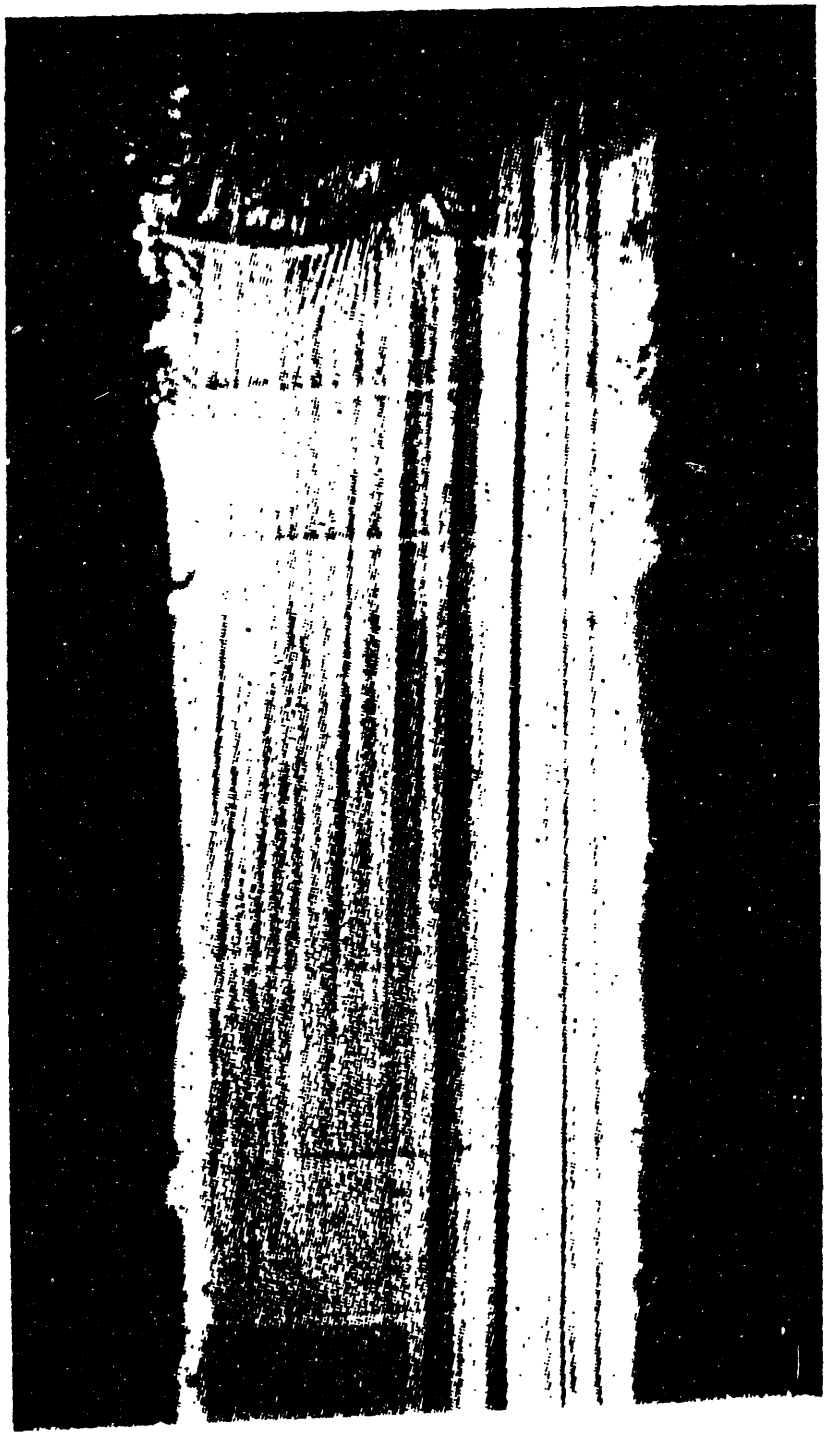

Figure 1.3: Columnar solidification of a pure substance (Chalmers 1964).

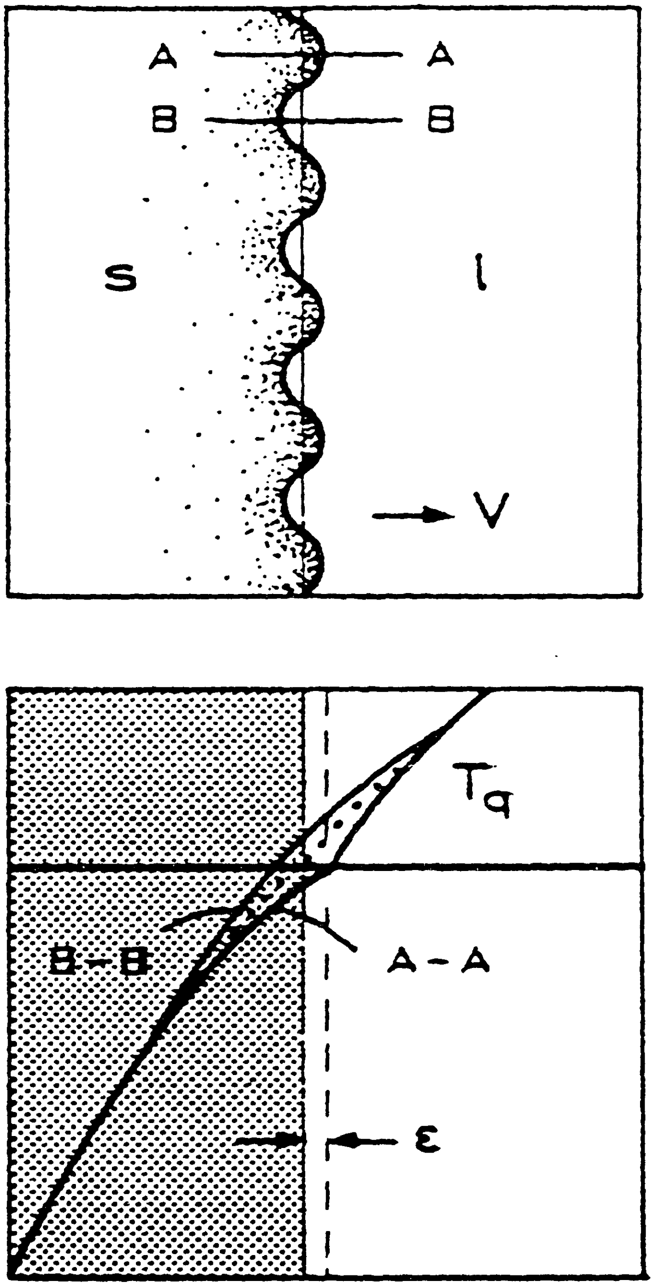

Figure 1.4: Columnar solidification of a pure substance (Kurz & Fisher 1986). The temperature here always increases with distance ahead of the interface and the direction of heat flow is opposite to the direction of growth. The planar interface is stable.

by the temperature flux equals the equilibrium melting temperature T_f. The temperature field around a perturbed interface must be deformed so that the temperature gradient in the liquid at the tip (A-A) increases while that in the solid decreases to keep the entire interface at the melting point T_f. Thus the heat flux towards the tip in the liquid increases and that in the solid away from the tip decreases. The effect at the bottom (trough) of the perturbation is exactly the opposite. The solid lines in Fig. 1.4 show the temperature gradients along A-A and B-B and the dotted line indicates the temperature profile for a planar interface. The perturbation will thus tend to damp out. If the temperature field is fixed, the temperature at the tip of the perturbation is higher the than the temperature over the rest of the interface which is the equilibrium melting temperature T_f . The interface perturbation cannot persist because it cannot remain at the melting point over its entirety.

When the temperature gradient ahead of the interface is negative, the structure that forms is quite different. Fig. 1.5 is a schematic description of growth under these conditions. Here the melt ahead of the interface is thermally undercooled since it is below the equilibrium melting temperature. When a projection forms on the interface, the tip of the projection is in a region of greater undercooling and experiences a greater flux of heat away from it than the rest of the interface. As before, the solid and dotted lines in Fig. 1.5 indicate the temperature profiles ahead of the tip of the perturbed interface and the planar interface, respectively. This increased thermal diffusion aids the growth of the projection and the planar interface is hence always unstable. Growth into a negative temperature gradient is therefore often referred to as free, equiaxed or unconstrained.

The latent heat generated by the solidification process at the tip is conducted towards the rest of the interface and has the effect of decreasing the thermal undercooling ahead of the rest of the interface thus retarding its growth and resulting in the formation of a spike. In a similar fashion branches develop on the spike and these branches serve as stalks for further branches. This branched structure is called a dendrite. The branches of the dendrite coincide with the crystallographic planes where preferred growth occurs. For example, in face-centered and body-centered cubic structures, dendritic growth is observed to take place in the cube directions. Fig. 1.6 (Chalmers 1964) shows a photograph by Weinberg of dendritic growth in lead. The primary growth direction and secondary branching are both

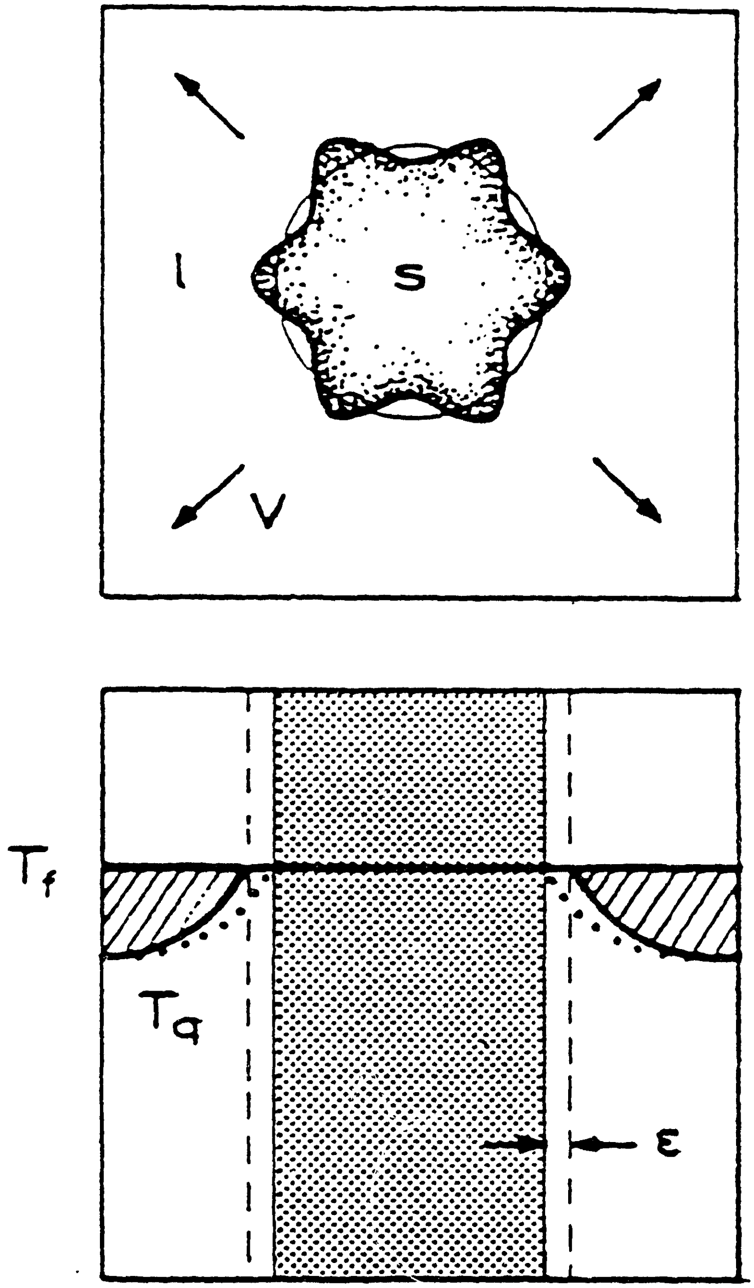

Figure 1.5: Equiaxed growth of a pure material (Kurz & Fisher 1986). The direction of heat flow here is in the direction of growth and the planar interface is unstable.

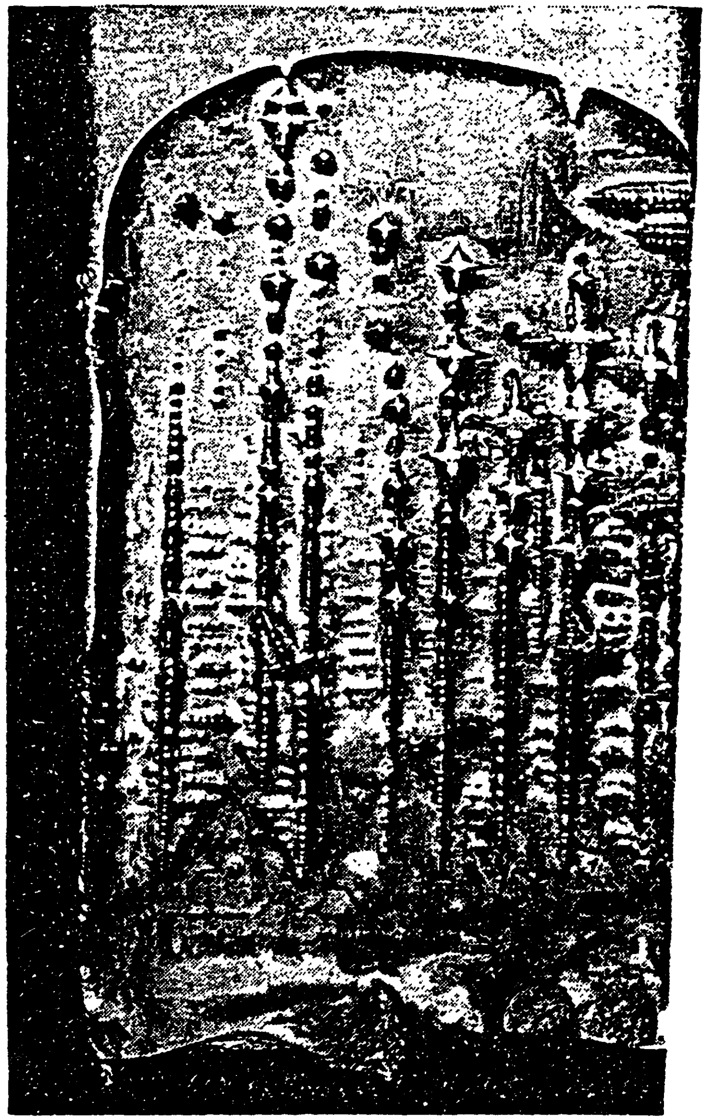

Figure 1.6: Photograph of dendritic growth in lead by Weinberg (Chalmers 1964) showing both primary and secondary branching.

observed here.

1.1.1.2 Solidification of an Alloy

The criterion for stability of the planar interface during the solidification of alloys is complicated by of the effect of solute segregation at the interface. During the solidification of a binary alloy, typically, the solid retains less solute than the melt at equilibrium with it. Thus solute piles up in the melt ahead of the interface and diffusion of solute away from the interface plays an important role in determining the rate of growth of the solid. In addition, freezing-point depression usually occurs so that the equilibrium melting temperature of an alloy is lower than that of the pure metal. Detailed analysis of each of these effects is presented in Section 1.2. A simple explanation of their effect on solidification into both positive and negative temperature gradients in given in this Section.

Growth of an alloy into a negative temperature gradient is very similar to the equiaxed growth of a pure metal. The instability of the planar interface is caused by thermal undercooling and dendritic morphology is always seen as in the case of a pure material.

During the growth of an alloy into a positive temperature gradient, the planar interface is stable only under certain processing conditions unlike in the case of a pure material; segregation and freezing point depression contribute another source of instability in addition to thermal undercooling. The mechanism termed as *constitutional supercooling* can be explained as follows: the melt ahead of the interface is again undercooled and aids the growth of a perturbation but with one difference - the undercooling is caused not because of the imposed temperature field, but because of segregation and freezing-point depression. This instablity results in the growth of three kinds of morphologies. In addition to dendritic patterns similar to those seen in equiaxed growth, cellular interfaces are also seen.

Cells are unbranched finger-like structures seen at the onset of the instability of the planar interface. These cells are sinusoidal in shape and small in amplitude for processing conditions that are close to the onset but become deeper and more complex at the conditions beyond the planar-cellular transition. Three-dimensional cells are packed in a hexagonal pattern parallel to the direction of growth; see Fig. 1.7 (Rutter 1958). The top free-surface of a crystal containing this microstructure is corrugated (Rutter & Chalmers 1958) as in Fig. 1.8. These variations along the top-surface can be explained by microsegregation. The solute rejected by the interface piles up in the grooves of the cell resulting in a higher concentration of the dilute component along slender paths running the length of the solid. This nonuniform incorporation of the solute can often result in dislocations (Tiller 1958). If the concentration in the grooves reaches a eutectic composition, a second solid phase can form (McLean 1983) and cross-section of the resulting crystal can be alternatively composed of the two phases (see Fig. 1.9). These non-uniformities in microstructure affect the properties of the resulting material.

At conditions further away from those at the transition point, dendrites are observed. The microstructure is very similar to that seen in pure metals except that the rejection of solute by a growing dendrite results in formation of a substructure similar to that in cellular growth due to the subsequent constitutional supercooling (Winegard 1964). The direction of growth of dendrites is influenced by the crystallography of the material. As in equiaxed growth, dendrites grow mostly along preferred crystallographic orientations. The effects of microsegregation seen in cellular growth are also seen in dendritic solidification; see Fig. 1.10 taken from McLean (1983).

This thesis considers a model problem for the growth of a dilute binary alloy into a positive temperature gradient. This problem exhibits all three kinds of interface morphologies described above. The model system belongs to the class of solidification methods called directional solidification. The analysis of such systems involves the solution of both the thermal and the solute concentration fields, as illustrated in the next section.

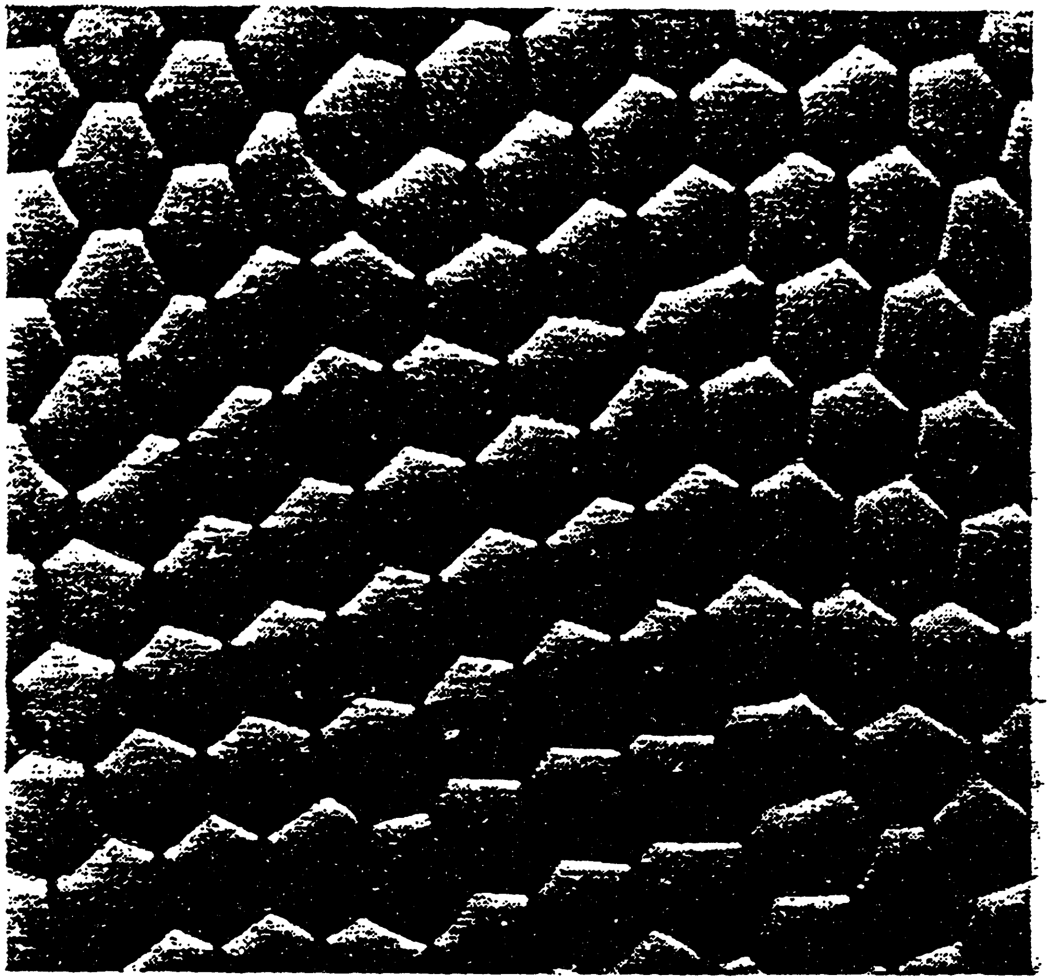

Figure 1.7: Decanted solid-liquid interface showing that the cellular substructure which runs parallel to the direction of growth is hexagonal in cross-section (Rutter 1958).

Figure 1.8: The top free-surface of the cellular microstructure in alloys showing corrugations (Rutter and Chalmers 1953).

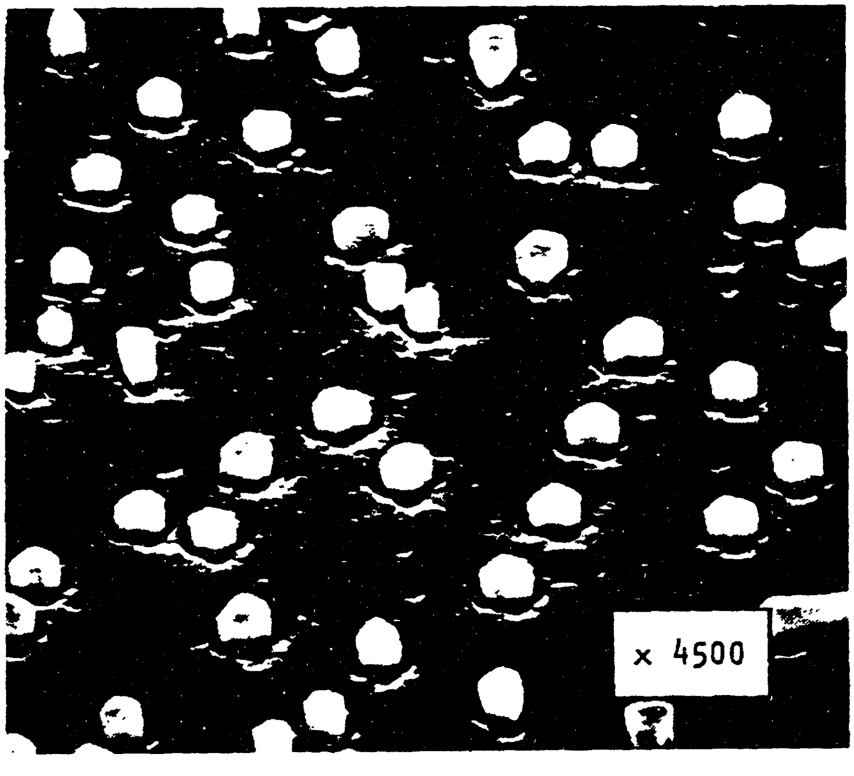

Figure 1.9: Solidification of an eutectic alloy in two phases (from Mclean (1983)).

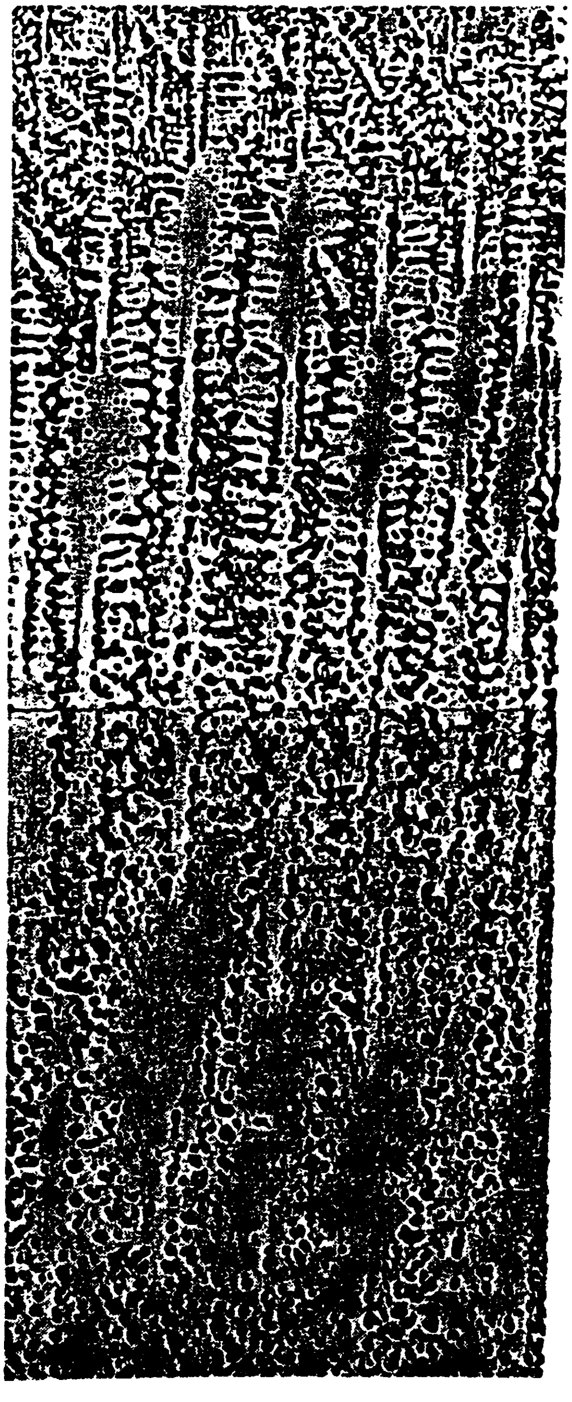

Figure 1.10: Longitudinal sections of an metallic alloy quenched from steady-state solidification in order to freeze-in the shape of the interface (McLean 1983) showing microsegregation during dendritic solidification.

1.2 Directional Solidification

Directional solidification is the solidification of a material into a unidirectional positive temperature gradient. This thermal field is typically established by an external source which adds heat to the melt and an external sink which removes heat from the solid. This process is extensively employed to produce single crystal semiconductor materials used in electronic applications. The Bridgman, Czochralski and floating-zone techniques used to produce these crystals and the directional casting process used in the manufacture of some products like turbine blades all involve directional solidification (McLean 1983, Brice 1965, 1986). Most experimental observations of directional solidification have involved organic materials called plastic crystals which have a low entropy of melting like metals and grow in a non-faceted manner (Kurz & Fisher 1986). These materials are useful for the *in situ* observation of solidification of microstructure formation in solidification and the results can be used to deduce the likely behavior of metals without the problems posed by the high reactivity, opacity and high melting point of metals.

The most commonly used configuration for observing microstructure formation is the thin-film experiment first used by Jackson & Hunt (1965); a schematic of a typical system is shown in Fig. 1.1. During the experiment, a thin sample of a dilute binary alloy of the organic crystals sandwiched between two transparent solid plates is translated through a temperature field. This field is established by having a furnace at one end at a constant temperature which is higher than the equilibrium melting temperature $\tilde{T}_f$ and a heat reservoir at a temperature that is lower than $\tilde{T}_f$ at the other end.These zones are separated by a nearly adiabatic zone in the middle permits viewing of the solidification interface.

When the sample is stationary a constant temperature gradient is established in each phase in the sample; if the thermal conductivities in the two phases are equal, these gradients are identical. Most of the heat flows through the solid plates (generally made of glass) because they are usually an order-of-magnitude thicker than the gap between them and also because the conductivity of glass is typically higher than that of the alloy. The temperature of the hot and cold reservoirs are chosen so that a stationary interface which is planar is in the middle of the viewing area. The temperature field is usually not perfectly linear for a translating sample. The heat of fusion generated by the solidifying sample and the convection of this heat due to sample translation cause the temperature field to deviate slightly from linearity even at moderate pulling rates.

As the sample is pulled, the interface may not remain planar. For pulling rates that are very small the interface remains planar, but as the pull rate is increased beyond a critical value, the planar interface becomes unstable and shallow cells are formed as shown in Fig. 1.2a. Deep cells are formed at higher pulling rates as shown in Fig. 1.2b. At even higher growth rates, dendritic interfaces,such as those shown in Fig. 1.2c are the norm. This general sequence of transitions is well-established. In addition, the onset of instability of the planar interface is well-characterized as described in the following section, but the other details of cellular and dendritic solidification are not well-understood. In particular the following questions need to be answered:

(i) What are the details of the development of deep cellular interfaces, including the dependence of the cell shape on operating conditions and apparent selection of the wavelength of the steady cellular front?

(ii) When does the transition from cells to dendrites occur?

(iii) What are the dynamics of cellular and dendritic solidification?

Before an attempt is made to answer these questions, a clear understanding is required of some of the concepts that are specific to directional solidification of an alloy. Specifically, the presence of the solute has two implications that are obvious when the phase diagram is analyzed: segregation of solute and freezing-point depression. In addition, the curvature of the interface has an effect on the equilibrium melting point. Each of these effects is described below.

1.2.1 Redistribution of Solute and Freezing-point Depression

Equilibrium between a binary solid and its melt is represented conveniently by a binary phase diagram with a liquidus curve, above which the liquid is the only stable phase and a solidus curve, below which the solid is the stable phase. A typical phase diagram for an alloy that forms a eutectic phase is shown in Fig. 1.11. For a range of temperatures two

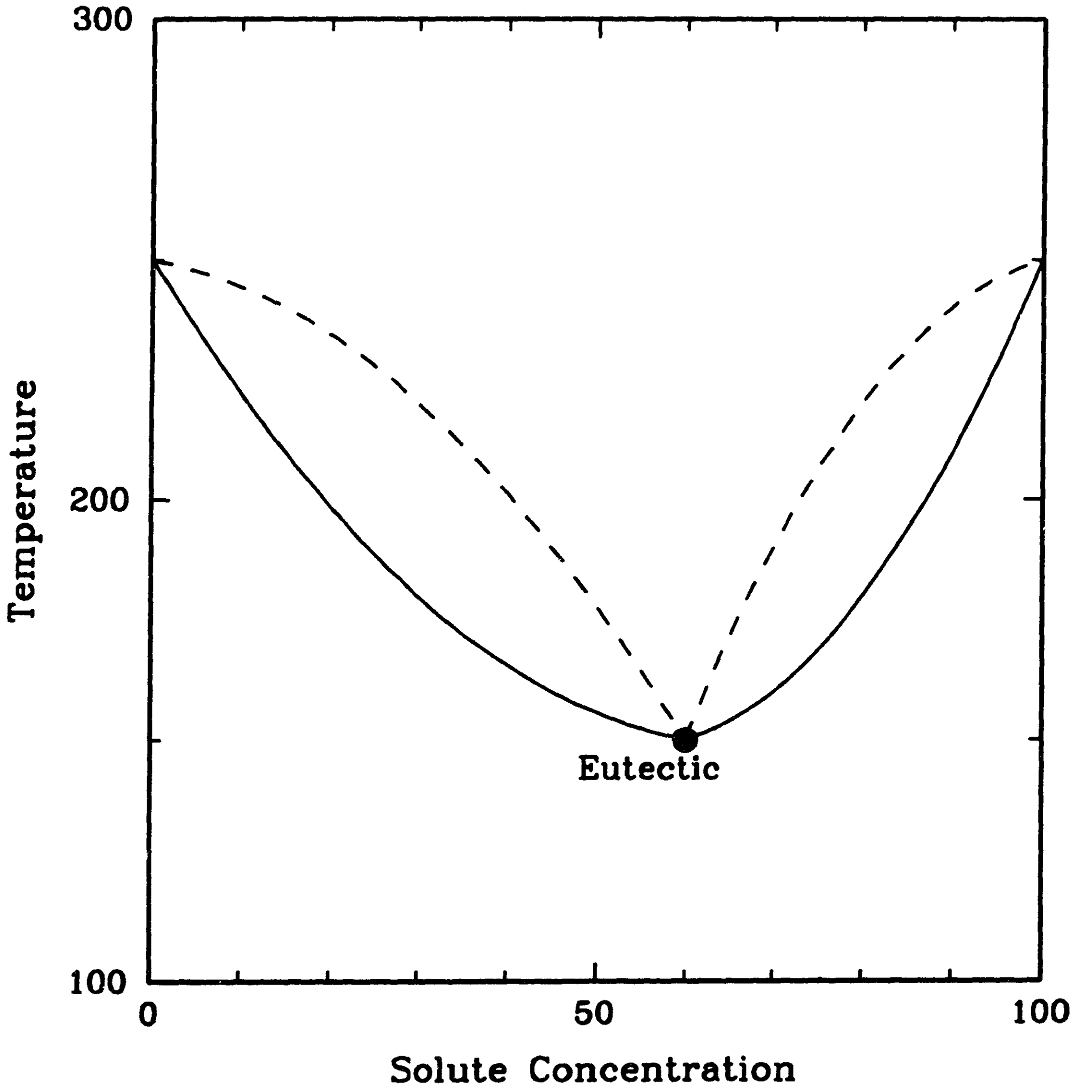

Figure 1.11: Typical phase diagram for a binary alloy. The solid line is the solidus curve and the dashed line is the liquidus curve.

phases exist and the composition of the solid and liquid are generally different except for the pure material. Though the liquidus and solidus curves generally are not straight lines, it is convenient to assume that they are straight lines for dilute binary alloys, as shown in Fig. 1.12. This makes the theoretical analysis simpler and does not seriously affect the conclusions in the case of a dilute binary alloy, as long as the range of compositions under consideration is not too large.

The equilibrium segregation coefficient k is defined as the ratio of the concentration of the solute in the solid c_s to that in the the melt c_m in equilibrium with the solid. Hence, at the interface

$$k = \frac{c_s}{c_m} \quad . \tag{1.3}$$

Another important characteristic of the system is the slope of the liquidus line m. Together, k and m define the simple phase diagram completely. Though both k and m could have a range of values, the discussion presented here and the results of this work assume $k < 1$ and $m < 0$. The first assumption is valid for solids that retain less solute than the melt. During solidification, excess solute is rejected and accumulates in front of the interface. This causes undercooling which results in the instability of the planar interface. This effect is discussed in the Section 1.2.4. The second assumption, that of a liquidus line which slopes downward is usually referred to as *freezing point depression*, an effect commonly applied in the salting of highways to melt snow. This assumption, true for a majority of mixtures, states that the equlibrium melting temperature of a dilute alloy is less than that of the corresponding pure material.

1.2.2 Thermal Equilibrium at Curved Interfaces

Any solid/liquid interface has an excess free-energy required for its creation. For a curved interface the increase in energy per unit surface in comparison with a planar interface is given by

$$\Delta G = \gamma(2\tilde{\mathcal{H}}) \quad , \tag{1.4}$$

where γ is the surface energy and $2\tilde{\mathcal{H}}$ is the mean interface curvature (Chalmers 1964).

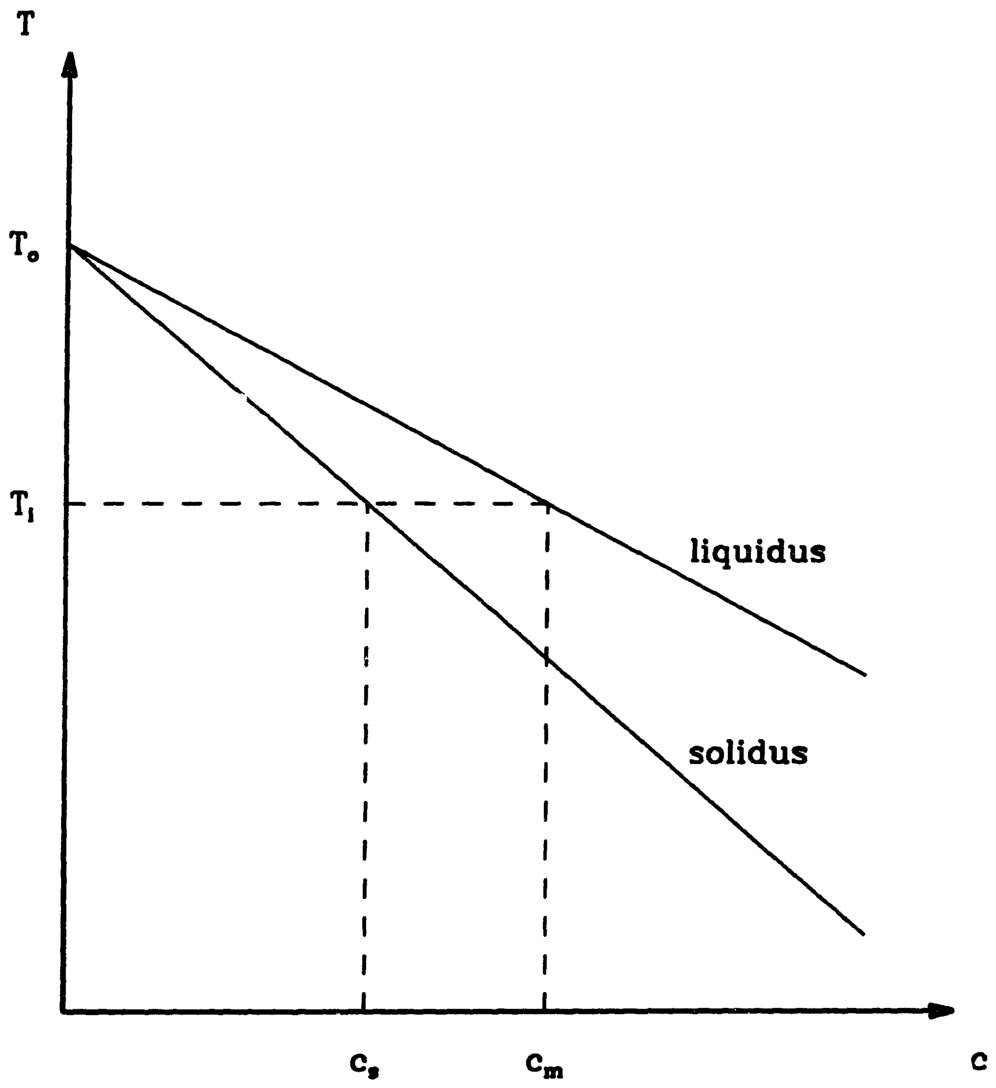

Figure 1.12: Simple phase diagram for a dilute binary alloy with linearized liquidus and solidus lines.

Since at equilibrium the two phases have identical free-energies, the above excess free-energy is exactly compensated by a corresponding decrease due to the lowering of the equilibrium melting point from $\tilde{T}_f$ to say, T. The value of ΔG is hence also given by the free-energy difference that would exist between the two phases at T but at the same pressure. At constant pressure, ΔG is calculated as follows:

$$\Delta G = \Delta H - T\Delta S \quad , \tag{1.5}$$

where H is the enthalpy and S is the entropy of the system. ΔH is also called the latent heat of fusion L.

But at $T = \tilde{T}_f$, $\Delta G = 0$; therefore, assuming ΔH and ΔS are independent of temperature,

$$\Delta S = \frac{\Delta H}{\tilde{T}_f} \quad . \tag{1.6}$$

Substituting Eq. (1.6) in Eq. (1.5) gives

$$\Delta G = \Delta H(1 - \frac{T}{\tilde{T}_f}) \quad . \tag{1.7}$$

It follows from Eqns. 1.4 and 1.7 that

$$T = \tilde{T}_f + \tilde{\Gamma}(2\tilde{\mathcal{H}}) \quad . \tag{1.8}$$

The above equation is referred to as the *Gibbs-Thomson equation* and $\tilde{\Gamma}$ called the Gibbs-Thomson coefficient (or the capillary length) is given by

$$\tilde{\Gamma} = \frac{\gamma \tilde{T}_f}{L} \quad . \tag{1.9}$$

Thus a curved interface melts at a different temperature than the planar interface. The curvature $2\tilde{\mathcal{H}}$, and the Gibbs-Thomson coefficient $\tilde{\Gamma}$, are defined so that a positive undercooling (freezing point decrease) is associated with an interface that is convex with respect to the melt phase.

1.2.3 Effect of Anisotropy

Most simple models of solidification assume that material properties are isotropic, i.e. they are independent of the orientation in relation to the direction of growth. Anisotropic effects are generally considered likely to affect the surface energy and the interface attachment kinetics (kinetic terms only arise if the interface is not in equilibrium).

To account for the anisotropic in the kinetic terms, the Gibbs-Thomson condition Eq. (1.8) is first rewritten for non-equilibrium interfaces as

$$T = T_f + \tilde{\Gamma}(2\tilde{\mathcal{H}}) - f(V) \quad , \tag{1.10}$$

where the function $f(V)$ accounts for any deviation from equilibrium as a function of the growth rate (Boettinger 1982). For anisotropic attachment kinetics, the function $f(V)$ is also assumed to be a function of the orientation. In general, anisotropy is introduced through both the surface energy $\tilde{\gamma}$ and the function $f(V)$. The effect of anisotropic interface attachment kinetics has been examined in a linear stability analysis by Coriell & Sekerka (1976) and using a nonlinear evolution equation by Young *et al.* (1987). These studies show that anisotropic attachment kinetics causes the cells to grow at an angle to the normal of the planar front and travel along the interface in time. In this thesis, it is assumed that the interface is near equilibrium so that any kinetic effects are neglected. Experimental studies do not mention any effect of attachment kinetics in thin-film solidification and thus support this assumption; see Section 1.3.

More commonly, studies of anisotropic solidification assume that only the surface energy is dependent on orientation. The capillary length $\tilde{\Gamma}$ in a more rigorous definition is dependent on the surface tension γ as (Mullins 1962)

$$\tilde{\Gamma} = (\gamma + \gamma_{\theta\theta})\frac{\tilde{T}_f}{\Delta H} \quad , \tag{1.11}$$

where θ is the angle made by the unit vector normal to the interface with the plane perpendicular to the growth direction and the subscript θ denotes differentiation. Typically, a crystal with a four-fold symmetry is assumed; this assumption is appropriate for crystals that are formed in cubic lattices, i.e., face-centered and body-centered cubic crystals. For this specific choice the surface energy is written as

$$\gamma = \gamma_o[1 + \epsilon_\gamma \cos(4\theta)] \quad , \tag{1.12}$$

where γ_o is the anisotropic surface tension and $0 \leq \epsilon_\gamma \leq 1$ is a constant which determines the degree of anisotropy. This expression is substituted into Eq. (1.11) to yield

$$\tilde{\Gamma} = \tilde{\Gamma}_o[1 - 15\epsilon_\gamma \cos(4\theta)] \quad , \tag{1.13}$$

where $\tilde{\Gamma}_o$ the isotropic capillary length is defined as

$$\tilde{\Gamma}_o \equiv \frac{\gamma_o \tilde{T}_f}{\Delta H} \quad . \tag{1.14}$$

The Gibbs-Thomson equation Eq. (1.8) can be rewritten as[1]

$$T = T_f + \tilde{\Gamma}_o[1 - 15\epsilon_\gamma \cos(4\theta)](2\tilde{\mathcal{H}}) \quad . \tag{1.15}$$

Mullins (1962) has shown that the equlibrium interface shape excludes certain high energy areas that result when the degree of anisotropy ϵ_γ is large. It is clear from Eq. (1.15) that when ϵ_γ attains a value 1/15 the effective capillary length goes to zero; at any value greater than this certain cusp-shaped high energy areas are formed on the interface. These regions are not allowed at equlibrium. Certain orientations are thus excluded; see Voorhees *et al.* (1984) for a discussion of this effect.

For shallow cells where θ varies little from zero, it is expected that the effect of anisotropy will be negligible (Bennett 1990), but the effect for deep cells may be considerable depending on the degree of anisotropy. The degree of anisotropy of plastic crystals is generally small. Estimates of ϵ_γ range from 0.005 for SCN to 0.05 for pivalic acid (Huang & Glicksman 1981a, 1981b).

1.2.4 Constitutional Supercooling

The instability of the planar interface during directional solidification of an alloy is not caused by thermal undercooling (unlike during equiaxed growth of materials as described in Section 1.1). The undercooling is caused by solute redistribution and is termed constitutional supercooling. The mechanism was first described by Rutter & Chalmers (1953) and later quantified by Tiller *et al.* (1953). They described the one-dimensional solute field in

---

[1] The value $\epsilon_a = 15\epsilon_\gamma$ indicates the effect of anisotropy on the capillary length and will henceforth be referred to simply as anisotropy.

the melt during steady-state solidification at a planar interface with a growth rate V by the transport equation

$$\mathcal{D}_m \nabla^2 \tilde{c}_m + V \frac{\partial \tilde{c}}{\partial \tilde{y}} = 0 \quad , \tag{1.16}$$

written in a coordinate y fixed to the interface and orthogonal to it. Assuming conservation of solute at the interface, a constant segregation coefficient k and solving equation Eq. (1.16) yields

$$\tilde{c}_m(\tilde{y}) = c_\infty \left[1 + \frac{1-k}{k} \exp\left(-\frac{V\,\tilde{y}}{\mathcal{D}_m}\right)\right] \quad , \tag{1.17}$$

where c_∞ is the bulk concentration of solute in the melt. Eq. (1.17) describes an exponential diffusion layer that forms ahead of the interface, as shown in Fig. 1.13. Combining this profile with the dependence of the equilibrium melting temperature $\tilde{T}_f$ on the concentration of solute, as given by the liquidus line, yields the expression for $\tilde{T}_f$ as a function of distance from the interface:

$$T_f(\tilde{y}) = \tilde{T}_o + \tilde{m}\, c_\infty \left[1 + \frac{1-k}{k} exp\left(-\frac{V\tilde{y}}{D_m}\right)\right] \quad . \tag{1.18}$$

The elevated concentration in the diffusion layer is shown in Fig. 1.13 and corresponds to a melt that solidifies at a lower temperature. The actual temperature field near the interface can be approximated by a linear profile

$$\tilde{T}_m(\tilde{y}) = \tilde{T}_o + \tilde{G}_m \tilde{y} \quad , \tag{1.19}$$

as and also is shown in the figure. Comparing the two profiles it is evident that if the gradient of the actual temperature field $\tilde{G}_m$ is less than that of the melting point given by Eq. (1.18), i.e when

$$\begin{aligned} \tilde{G}_m &< \left.\frac{d\tilde{T}_f}{d\tilde{y}}\right|_{\tilde{y}=0} , \\ &< \frac{\tilde{m} c_\infty V}{\mathcal{D}_m}\left(\frac{k-1}{k}\right) \quad , \end{aligned} \tag{1.20}$$

there will be a small region of melt in front of the interface where the temperature is actually lower than the equilibrium melting temperature T_f for a melt of that concentration. Thus a small perturbation of the interface into the melt is likely to grow. When this undercooling does not exist any small projection into the melt would be surrounded by hot liquid, and would thus melt until the interface was planar again. The cause of this

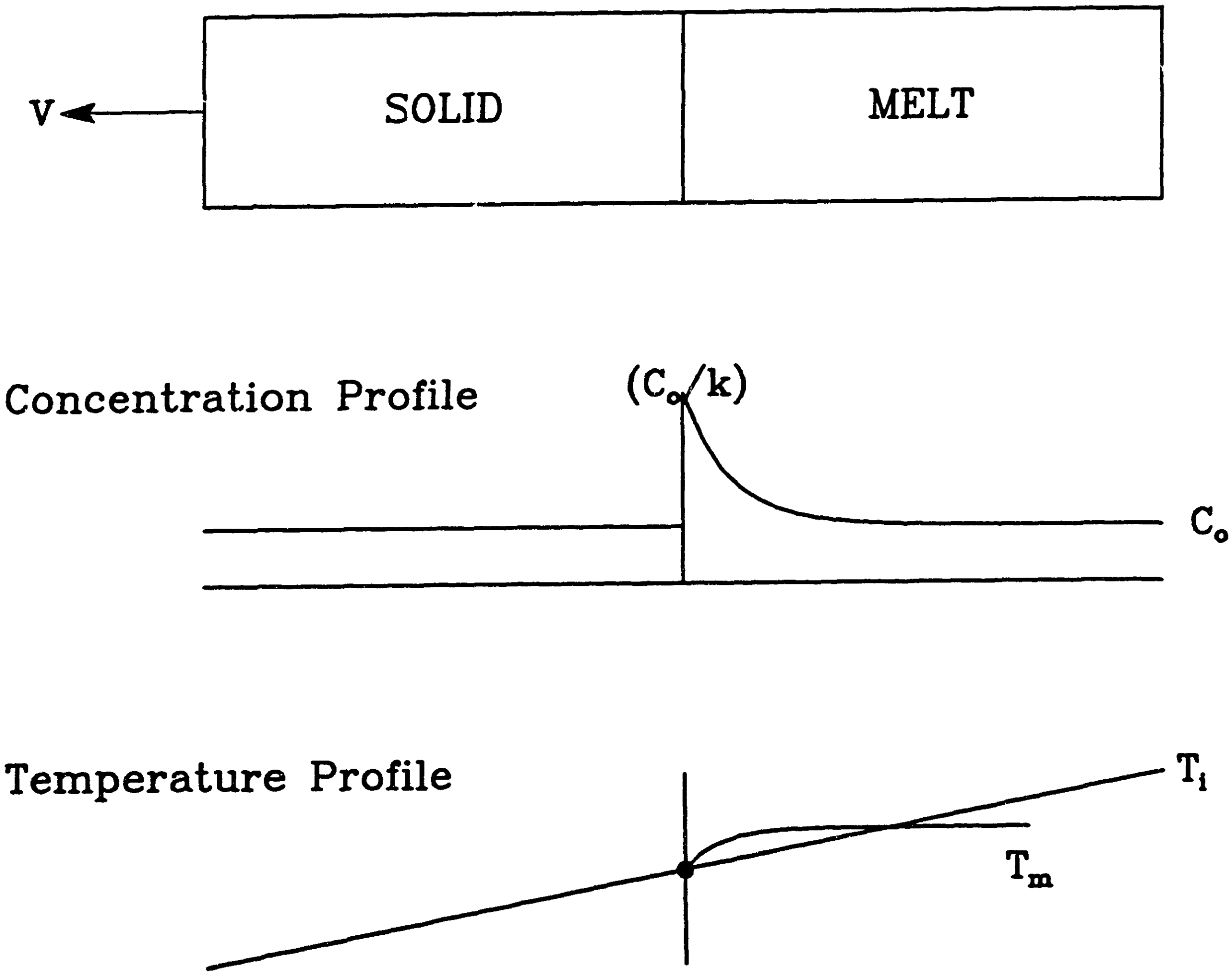

Figure 1.13: Solute concentration $\tilde{c}_m(\tilde{y})$ and temperature $T(\tilde{y})$ plotted as a function of distance from the interface in the one-dimensional solidification problem. The liquidus temperature $\tilde{T}_m$ is plotted for comparison.

instability of the planar interface is termed constitutional supercooling and Eq. (1.20) is called the *constitutional supercooling criterion.*

The criterion Eq. (1.20) is often written in terms of the concentration gradient $\tilde{G}_c$ ahead of the planar interface as

$$\tilde{G}_m < \tilde{m}\tilde{G}_c \quad , \tag{1.21}$$

for stability of the planar interface where

$$\tilde{G}_c \equiv \frac{\tilde{m}c_\infty V}{\mathcal{D}_m}\left(\frac{k-1}{k}\right) \quad . \tag{1.22}$$

Experimental studies show a qualitative agreement with the theory. Many such studies are reviewed by Flemings (1974). The criterion Eq. (1.20) predicts the value of the growth parameters at which the transition from planar interfaces to cellular patterns occurs. However, the theory only compares length scales of the temperature and concentration profiles in the direction of growth and hence is unable to indicate the spatial length scale of the microstructure in the transverse direction or predict the dynamic behavior of these morphologies.

1.2.5 Linear Stability Analysis

The deficiency of the constitutional supercooling criterion Eq. (1.20) arises because the analysis does not take into account the effects of the rates of material and energy transport on the evolution of the interface perturbation. In addition, the effect of the surface energy given by the Gibbs-Thomson equation Eq. (1.20) is neglected. The increase in melting point due to capillarity for small-wavelength (high curvature) disturbances compensates somewhat for the constitutional supercooling.

Mullins & Sekerka (1964) analyzed the stability of the planar interface solution to small disturbances by a rigorous solution of an extended version of the solute and heat transport model used by Tiller *et al.* (1953). They assumed heat transfer in both phases and solute transport in the melt and developed the corresponding diffusion equations with respect to a coordinate system fixed to the steadily solidifying interface:

$$\frac{\partial \tilde{c}_m}{\partial \tilde{t}} = \mathcal{D}_m \tilde{\nabla}^2 \tilde{c}_m + V\frac{\partial \tilde{c}_m}{\partial \tilde{y}} \quad , \tag{1.23}$$

$$\frac{\partial \tilde{T}_m}{\partial \tilde{t}} = \alpha_m \tilde{\nabla}^2 \tilde{T}_m + V\frac{\partial \tilde{T}_m}{\partial \tilde{y}} \quad , \tag{1.24}$$

$$\frac{\partial \tilde{T}_s}{\partial \tilde{t}} = \alpha_s \tilde{\nabla}^2 \tilde{T}_s + V\frac{\partial \tilde{T}_s}{\partial \tilde{y}} \quad . \tag{1.25}$$

It was further assumed that local equilibrium applies at the interface $\tilde{y} = \tilde{h}(\tilde{x}, \tilde{t})$ and that the temperature there is described by the Gibbs-Thomson equation,

$$\tilde{T} = \tilde{T}_o + \tilde{m}\tilde{c} + \tilde{\Gamma}(2\tilde{\mathcal{H}}) \quad , \tag{1.26}$$

The linear stability theory asks the question of whether a disturbance to the planar interface ($\tilde{h}(\tilde{x}, \tilde{t}) = 0$) will grow with time or disappear. A sinusoidal perturbation of small time-dependent amplitude is considered since any disturbance can be described by a Fourier series of sinusoidal forms.

A linear stability analysis of a simpler version of the physics considered by Mullins & Sekerka is presented here. It is assumed that the thermal field is represented by a linear temperature profile with a constant temperature gradient in the two phases $G_m = G_s = G$. The conditions where this assumption is valid are discussed in Section 2.1. The system of equations describing the system now reduces to the solute field equation Eq. (1.24) in the melt. The steady-state solution to the field equations in the base case of a planar interface with this simplification is

$$\tilde{c}_m^{ss}(\tilde{x}, \tilde{y}) = c_\infty \left[1 + \left(\frac{1-k}{k}\right) \exp(-\frac{V\tilde{y}}{\mathcal{D}_m})\right] \quad . \tag{1.27}$$

Following Mullins & Sekerka (1964) the solution to Eq. (1.24) with the perturbed interface

$$\tilde{h}(\tilde{x}, \tilde{t}) = \epsilon \sin(\omega \tilde{x}) \exp(\sigma \tilde{t}) \tag{1.28}$$

is postulated as

$$\tilde{c}_m^{per}(\tilde{x}, \tilde{y}, \tilde{t}) = \tilde{c}_m^{ss}(\tilde{x}, \tilde{y}) + \epsilon \; \hat{c}_m \sin \omega \tilde{x} \; \exp(\omega^* \tilde{y}) \quad , \tag{1.29}$$

with

$$\omega^2 = \hat{\mathsf{k}} \cdot \hat{\mathsf{k}} \quad , \tag{1.30}$$

and

$$\omega^* = (V/2\mathcal{D}_m) + \sqrt{(V/2\mathcal{D}_m)^2 + \omega^2} \quad , \tag{1.31}$$

where the amplitude of the perturbation satisfies $\epsilon \ll 1$. The new expressions are substituted back into the governing equations and boundary conditions. The resulting system of equations is then linearized by neglecting all terms with powers of ϵ greater than or equal to two. From the linearized equations a relation is derived for σ as a function of the system parameters and ω. If for specified values of parameters and ω the real part of σ is positive, then perturbations of the interface with wavenumber ω will grow exponentially. On the other hand, if the real part of σ is negative, then perturbations of wavenumber ω will decay at a rate $\exp(\sigma t)$. Thus for $Re(\sigma) > 0$ the interface is unstable with respect to perturbation of wavenumber ω, and for $Re(\sigma) < 0$ the interface is stable with respect to these perturbations. When $Re(\sigma) = 0$ perturbations of wavenumber ω will neither grow nor decay, and the interface is said to be neutrally stable. The linear stability of the planar interface is given by

$$\mathcal{S}(\omega) \equiv -\tilde{T}_o\tilde{\Gamma}\omega^2 - \tilde{G} + \frac{\tilde{m}\, c_\infty(k-1)V\left[\omega^* - (V/\mathcal{D}_m)\right]}{\mathcal{D}_m k\left[\omega^* - (V/\mathcal{D}_m)(1-k)\right]} \quad . \tag{1.32}$$

The stability of the planar interface depends on the value of the parameter $\mathcal{S}$:

$$\mathcal{S}(\omega) < 0, \qquad \text{stable} \quad , \tag{1.33}$$

$$\mathcal{S}(\omega) > 0, \qquad \text{unstable} \quad , \tag{1.34}$$

$$\mathcal{S}(\omega) = 0, \qquad \text{neutrally stable} \quad . \tag{1.35}$$

The stability can also be analyzed in terms of another control parameter M,

$$M \equiv \frac{(V/\mathcal{D}_m)}{\tilde{G}/(-\tilde{m}c_\infty)}\left(\frac{1-k}{k}\right) \quad , \qquad \text{or} \tag{1.36}$$

$$M \equiv \frac{m\tilde{G}_c}{\tilde{G}} \quad , \tag{1.37}$$

in terms of the growth conditions that can most easily be controlled in thin-film experiments, the velocity, the bulk concentration of the solute and the temperature gradient. The control parameter is defined so that the constitutional supercooling criterion Eq. (1.20) can be rewritten as

$$M < 1.0 \quad , \tag{1.38}$$

for stability of the planar interface. In the stability analysis presented above, as in the constitutional supercooling theory, for small values of the control parameter the planar interface is stable with respect to perturbations of all possible wavenumbers and $Re(\sigma) < 0$ for all ω. This case applies to small pull rates, large temperature gradients, and small concentrations. Now if all system parameters are held constant while the pull rate is gradually increased, for example, eventually there will be a value of pull rate where the planar interface is neutrally stable with respect to one wavenumber and stable to perturbations of all other wavenumbers. The pull rate, or equivalently the solidification velocity, at which this occurs is called the critical velocity V_c, and the corresponding wavenumber is called the critical wavenumber ω_c. Unlike the constitutional supercooling criterion, linear stability analysis predicts the value of the critical wavelength $\tilde{\lambda}_{ms} \equiv 2\pi/\omega_c$ at the onset of instability. The result of the linear stability analysis is plotted with the growth rate V as a function of the critical wavelength $\tilde{\lambda}_c$ at that velocity as shown in Fig. 1.14. The curve in Fig. 1.14 separates the region in $V - \tilde{\lambda}$ space where the planar state is stable from the region where the planar state is not a stable solution and is referred to as the *neutral stability curve* or the *marginal stability curve.*

The stabilizing effect of the surface energy has an important consequences. The critical value of the control parameter M in the Mullins and Sekerka analysis is greater than 1.0 and the melt ahead of the planar interface can be constitutionally supercooled and yet be stable. Kurz & Fisher (1986) show that the conditions at onset of instability may be rewritten as

$$\tilde{G} = \tilde{m}\tilde{G}_c - \frac{\tilde{\Gamma}\tilde{T}_o k V^2}{\mathcal{D}_m{}^2} \quad . \tag{1.39}$$

Thus in terms of the control parameter the conditions for stability is respecified as

$$M \leq 1 + \frac{\tilde{\Gamma}\tilde{T}_o k}{\tilde{G}} \left(\frac{V}{\mathcal{D}_m}\right)^2 \quad . \tag{1.40}$$

Since the surface energy is usually small and $\tilde{\Gamma} \ll 1$, the critical value of M predicted by linear stability theory will be very close to 1.0 (Woodruff 1973). Experimentally measured values of the critical velocities are relatively close to that predicted by linear theory. Eshelman & Trivedi (1987) reported a critical growth velocity that was within 10% of that predicted by linear theory in experiments with a succinonitrile-acetone alloy; see Section 1.3.

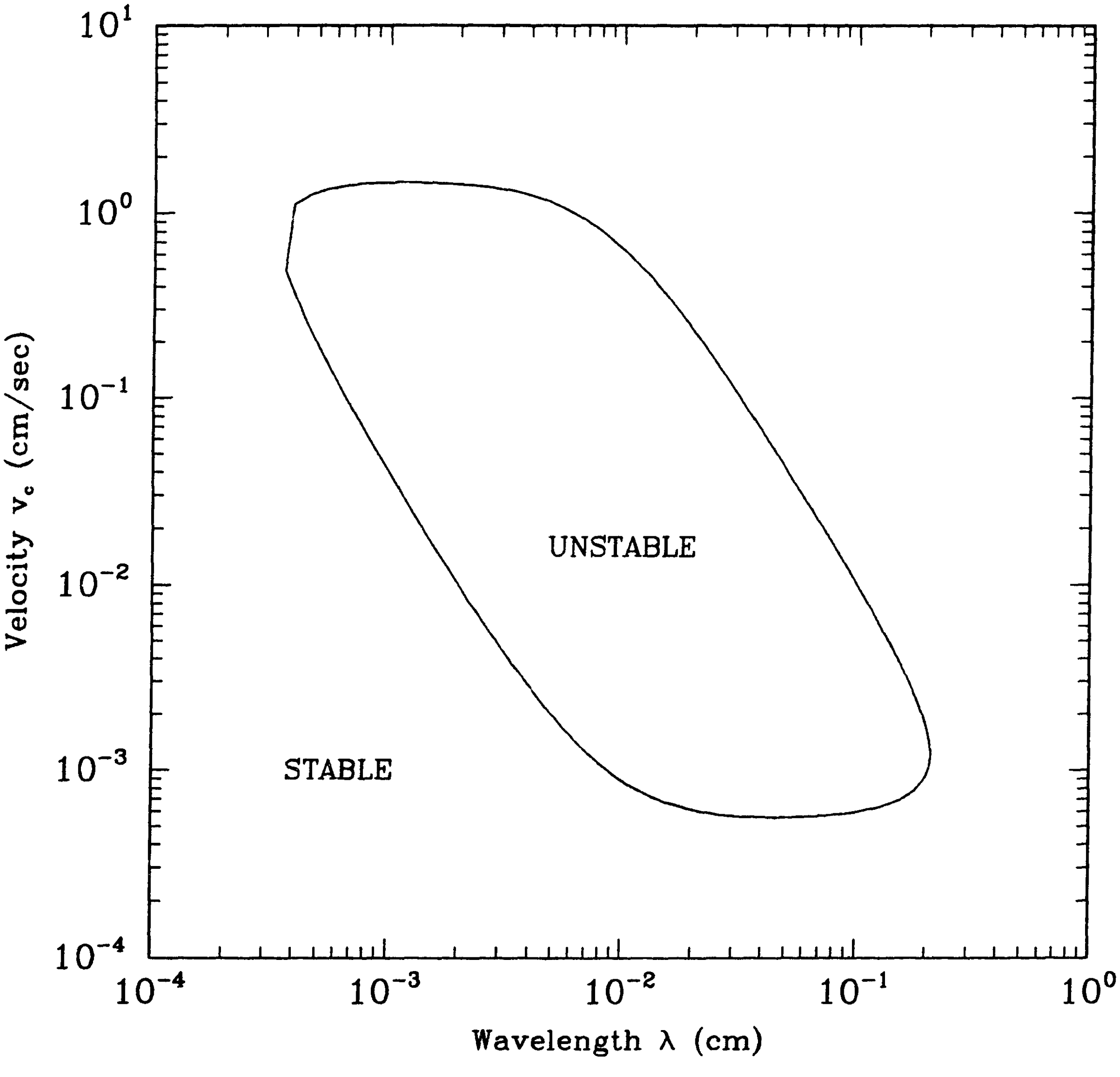

Figure 1.14: A typical neutral stability curve.

However, the critical wavelength predicted by the theory is generally higher than the wavelength of cells at the onset of stability in experiments. The deviation is discussed in Section 1.3 where directional solidification experiments are reviewed.

An important result of the linear analysis is the prediction of closed neutral stability curves irrespective of the specific material constants used. This closure of the stability curve for high growth rates is termed absolute stability (Kurz & Fisher 1986). This is caused by the stabilization of the planar interface due to tightening of the diffusion boundary layer ahead of the interface. Examination of Eq. (1.40) reveals that as the growth rate is increased the control parameter M first increases to violate the inequality and the planar interface becomes unstable but at high growth rates the right hand side of the equation grows faster than M resulting in restabilization. The condition is written as

$$\begin{aligned} M &= \frac{\tilde{\Gamma}\tilde{T}_o k}{\tilde{G}}\left(\frac{V}{\mathcal{D}_m}\right)^2 \quad , \quad \text{or} && (1.41) \\ V &= \frac{\tilde{m}\mathcal{D}_m(1-k)c_\infty}{k^2\tilde{T}_o\tilde{\Gamma}} \quad , && (1.42) \end{aligned}$$

(Kurz & Fisher 1986, Boettinger *et al.* 1984). Unfortunately the velocities predicted by the Eq. (1.42) are usually very high and some of the assumptions of the stability analysis may not be valid under these growth conditions. In particular the interface may not be at equilibrium; this possibility is discussed in Chapter 2.

For values of the control parameter M between onset on cellular growth and absolute stability a range of wavelengths is unstable, as shown in Fig. 1.14. The lower limit of this range is a consequence of the stabilizing effect of surface energy on small-wavelength, and hence high-curvature features.

Considerable work has been done to improve the simple model of solidification that was first considered by Mullins & Sekerka. In particular, additional physical effects such as anisotropy of surface properties (Coriell & Sekerka 1976), non-equilibrium segregation (Coriell & Sekerka 1983), Soret diffusion (Hurle 1983) and bouyancy (Coriell & McFadden 1989) have been considered and an extension to multicomponent systems has been developed (Coriell *et al.* 1987). The effect of the lateral thickness of the thin-film sample on morphological has also been investigated (Caroli *et al.* 1986).

It is important to note that while linear theory is sufficient for determining the stability of a planar interface, nonlinear interactions become important for deformed interfaces and the approximations made in deriving the linear equations set are not valid. Nonlinear analysis of models akin to the one presented in this Section have been performed to understand these interactions. A summary of these studies is presented in section 1.4.

1.3 Experiments in Directional Solidification

The existence of dendritic morphologies in metals has been known since the 18th century (Mehl & Cahn 1983) but cellular structures were not recorded until the first half of this century (Sekerka 1968). Spurred on by the work of Rutter & Chalmers (1953) and Mullins & Sekerka (1964), experimental investigation of these periodic microstructures has been extremely popular over the last 20 years. Before reviewing the theoretical studies of directional solidification after Mullins & Sekerka (1964) it is useful to look at the large volume of experimental work in this field.

Most early experimental investigations of cellular and dendritic morphologies in directional solidification were done on bulk samples of metals and alloys which allow hundreds of cells and dendrites to exist in both directions perpendicular to that of growth. These experiments on bulk samples have the disadvantage that convection in the melt usually occurs and the melt-solid interface is macroscopically nonplanar (Pamplin 1975, Brown 1988). Besides, morphological stability has been shown to be influenced by convection (Glicksman *et al.* 1986, Coriell *et al.* 1980, Caroli *et al.* 1985 and McFadden *et al.* 1988). In addition, the high melting points and opacity make direct observation of the interface during solidification impossible in experiments with metals and alloys (Chalmers 1964, Glicksman 1971).

Most recent experiments therefore have used some transparent organic materials called plastic crystals which have an entropy of fusion that is comparable to metals and alloys. These materials exhibit similar interfacial microstructures as metals and alloys. Following the pioneering work of Hunt & Jackson (1966, 1967) and Jackson *et al.* (1967), other researchers have carried out thin-film solidification experiments in a system similar to that used by Jackson & Hunt (1965). Most experiments have used succinonitrile (SCN) as the solvent because the thermophysical properties are the best known of the organic solvents. Glicksman and coworkers (Glicksman *et al.* 1976, Huang & Glicksman 1981a, Huang & Glicksman 1981b) determined most of these properties while examining the dendritic growth of pure SCN. A review of some of the more relevant work in cellular solidification is presented below. The experimental data on the evolution of cells and dendrites is reviewed here; the evidence regarding selection of these patterns based on wavelength is considered in

Section 1.5.

1.3.1 Trivedi and Coworkers

Trivedi and coworkers (Somboonsuk *et al.* 1984, Trivedi 1984, Trivedi & Somboonsuk 1984a, Trivedi & Somboonsuk 1984b, Trivedi & Somboonsuk 1985, Eshelman & Trivedi 1987, Eshelman & Trivedi 1988, Eshelman *et al.* 1988, and Seetharaman *et al.* 1988) examined both cellular and dendritic microstructures using a thin-film experimental system with succinonitrile as the solvent and acetone as the solute. The early papers deal mostly with dendritic solidification and report two-dimensional cells, protodendrites and three-dimensional dendrites with widths $\mathcal{O}(10^2 - 10^3)\mu$m; see Figs 1.2 and 1.15.

The more recent work of Trivedi and coworkers focuses on cellular solidification. Eshelman & Trivedi (1987) look at the planar-to-cellular transition. The observed growth rate V_c at the onset of instability was found to be within 10% of that predicted by both the constitutional supercooling criterion and the linear stability analysis. The wavelength at onset was observed to be less than that predicted by linear stability theory.

When the growth rate was increased to a value above V_c, long transients $\mathcal{O}(10^4)$ seconds were observed. In addition, they report a deviation of the dynamics of cell growth from that predicted by the linear stability analysis even when the aspect ratio of the cell was only 10%; this indicates that complex nonlinear behavior is seen begins very close to onset of the instability. They also report that wavelength selection in this regime was not sharp as discussed in Section 1.5.

Another important result was the hysteresis in growth rate during the transition; the growth rate at which the planar interface first loses stability as the velocity is increased is higher than the growth rate at which the interface undergoes the cellular-to-planar transition as the velocity is stepped down. A similar result was reported by de Cheveigné *et al.* (1985, 1986). One possible reason for this effect is that finite amplitude cells exist for growth rates that are sub-critical. It should be noted that while linear stability theory predicts the lowest growth rate at which an infinitesimal perturbation on the interface is stabilized,

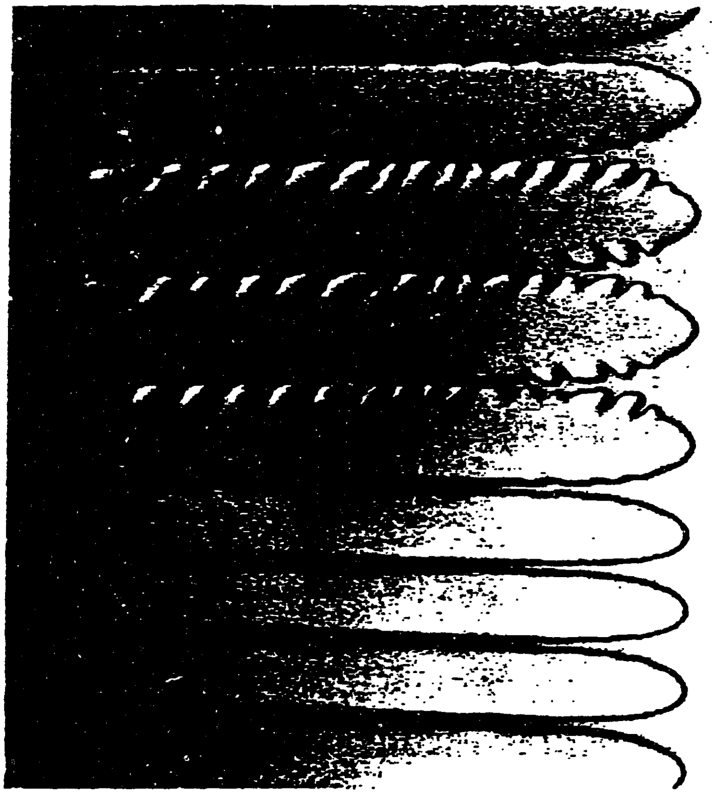

Figure 1.15: Protodendritic microstructure from thin sample directional solidification experiments with a succinonitrile - acetone alloy. Solid is on the left, melt on the right (from Trivedi 1984, p. 981).

the theory does not rule out that possibility that finite amplitude perturbations can exist at lower growth rates. The growth of cellular families towards lower values of growth rate is termed a *subcritical bifurcation*; see Section 1.4 for a discussion. The hysteresis effect could be the result of a subcritical bifurcation, but numerical computations corresponding to the CBr_4-Br_2 alloy of de Cheveigné *et al.* (1985, 1986) system by us (Ramprasad *et al.* 1991) predicted a subcritical bifurcation over a much smaller range of growth rates than the hysteresis effect.

It is therefore our hypothesis that fluctuations in the pull rate (reported steady to 0.1μm/sec; Eshelman *et al.* 1988) or inadequate accounting for the transient time necessary to achieve steady-state are possible causes of the hysteresis. This may also be the reason why Eshelman *et al.* (1988) observe a small variation in cell spacing at a given velocity even after a long duration of the experiment; true steady-state has probably not been achieved. Another possibility is that reported by Lee (1991); the onset velocity in his experiments with the succinonitrile-acetone system decreased with time and was attributed to an increase in the impurity level due to thermal degradation of the material. Lee reports that any real hysteresis effect is small when the thermal degradation is controlled and any subcritical bifurcation could indeed be small.

Eshelman *et al.* (1988) conducted experiments over a range of growth rates. They divide the range of experimental velocities in their experiments into three parts:

(i) A range of growth rates between V_c and V_t where the cell spacing decreased with growth rate and the aspect ratio of the cell was $\mathcal{O}(1)$. For the alloys studied V_t was found to be about $9V_c$.

(ii) A range of velocities between V_t and V_m over which the cell-dendrite transition occurred; either only stable cells, or only dendrites, or coexisting cells and dendrites were observed in this range in different experiments. The cell aspect ratios were $\mathcal{O}(10)$ and the tip became very sharp and parabolic (protodendritic). The cell spacing was found to sharply increase with growth rate.

(iii) Velocities above V_t where only dendrites were observed. The cell spacing decreased with growth rate. A hysteresis was observed in the cell-dendrite transition.

Seetharaman *et al.* (1988) continued the work of Eshelman *et al.* (1988) concentrating on the dynamics of cellular evolution. They performed experiments with both the SCN-acetone alloy and a pivalic acid-ethanol alloy where the velocity was stepped-up from $V < V_c$ to $V > V_c$ in a single step. They record that in SCN any increase in cell spacing was achieved by *cell elimination* in which a cell is squeezed out of existence by adjacent cells. Typically, once the tip of a cell falls below that of adjacent cells, its growth is further retarded by the excess solute rejected by the neighboring cells until the cell is eliminated. Any decrease in cell spacing was achieved by a localized perturbation called *tip-splitting*, a process where the tip of the cell gets progressively rounder and flatter, then an indentation starts in the middle of the tip and becomes increasingly deeper until the cell divides. Alternating periods of cell elimination and tip-splitting were observed as long as the experiment was in progress. During this process, the amplitude steadily increased in the beginning and leveled off a a constant value. They also note that cell interfaces do not respond quickly to small changes in the growth rate and a significantly large change in growth rate is required to alter the spacing. For the pivalic acid-ethanol alloy the wavelength and amplitude were both increased with time.

1.3.2 de Cheveigné and Coworkers

Another group which has contributed significantly to the experimental study of cellular solidification is de Cheveigné and coworkers (de Cheveigné *et al.* 1985, de Cheveigné *et al.* 1986, de Cheveigné *et al.* 1988, and Kurowski *et al.* 1990). Unlike most other researchers in this field de Cheveigné and coworkers use carbontetrabromide as the solvent. Using CBr_4 has both advantages and disadvantages. The obvious disadvantage is that its properties have not been as well characterized as has SCN. Besides, spontaneous decomposition of CBr_4 into bromine in the presence of sunlight makes any accurate estimate of the amount of Br_2 (the solute) in the system impossible. One possible advantage, which de Cheveigné and colleagues have pointed out, comes from the higher critical velocity CBr_4 ($V_c \sim \mathcal{O}(10^1)\mu\text{m}/s$), compared to succinonitrile ($V_c \sim \mathcal{O}(10^0)\mu\text{m}/s$). They employ the result of Tiller *et al.* (1953) for initial transients to estimate that the transient time for a step change in the pull rate from a lower speed to a higher velocity V_h is given by $\mathcal{D}_m/kV_h$ (de Cheveigné *et al.* 1986); this indicates that steady-states should be achieved in less time for the CBr_4 system for growth rates close to the critical velocity than for the SCN system.

The experiments of de Cheveigné *et al.* (1985, 1986) also show the hysteresis behavior seen by Eshelman *et al.* (1987) and believe it is caused by a subcritical bifurcation at onset. Numerical computations using a two-dimensional model which accounts for solute diffusion in the two phases (Ramprasad *et al.* 1991) show only a small subcritical bifurcation, $(V_{\max} - V_{\min}) < 0.001 \mu\text{m/sec}$, at onset that cannot be detected by the experiment (pull rate steady to $\pm 0.1 \mu\text{m/sec}$; de Cheveigné *et al.* 1985). As with the experiments of Eshelman *et al.* (1987) it is believed that the sample may not have been held at at each growth rate for long enough to achieve steady-state (Seetharaman *et al.* 1987). As reported by Lee (1991), thermal degradation of CBr_4 is also a significant problem.

As the pull rate was increased past the onset of the transition the cell spacing was seen to decrease; the decrease occurred through the process of tip-splitting as shown in Fig. 1.16. The cells do not undergo tip-splitting simultaneously; the decrease in the average wavelength of the interface occurs by tip-splitting of a few cells at any point in time. The evidence of selection in the experiments of de Cheveigné and coworkers is reviewed in Section 1.5.

de Cheveigné *et al.* (1986) measure the impurity level c_∞, the liquidus slope $\tilde{m}$ and the segregation coefficient k for the CBr_4-Br_2 alloy and use the constitutional supercooling criterion Eq. (1.20) to estimate the diffusivity $\mathcal{D}_m$ of the alloy. They then apply the Mullins & Sekerka criterion to estimate the predicted wavelength at the onset of the instability λ_{ms}. They report based on experiments at two different imposed temperature gradients $G = 70°K/\text{cm}$ and $G = 120°K/\text{cm}$ that while the experimentally selected wavelength λ_{exp} is constant to within a few percent, it is smaller than the predicted value λ_{ms} by a factor of two or three. Again, numerical computations done by us (Ramprasad *et al.* 1991) show that this is probably because families of cells with wavelengths close to λ_{ms} exist for too narrow a range of velocities (less than $0.02 \mu\text{m/sec}$) to be detected by the experiment. This result is discussed further in Chapter 3.

A significant result in de Cheveigné *et al.* (1986) is that the experimentally observed velocity V_{exp} at which the planar interface loses stability to a cellular morphology is affected by the distance ϵ between the confining glass plates. They report that when the sample

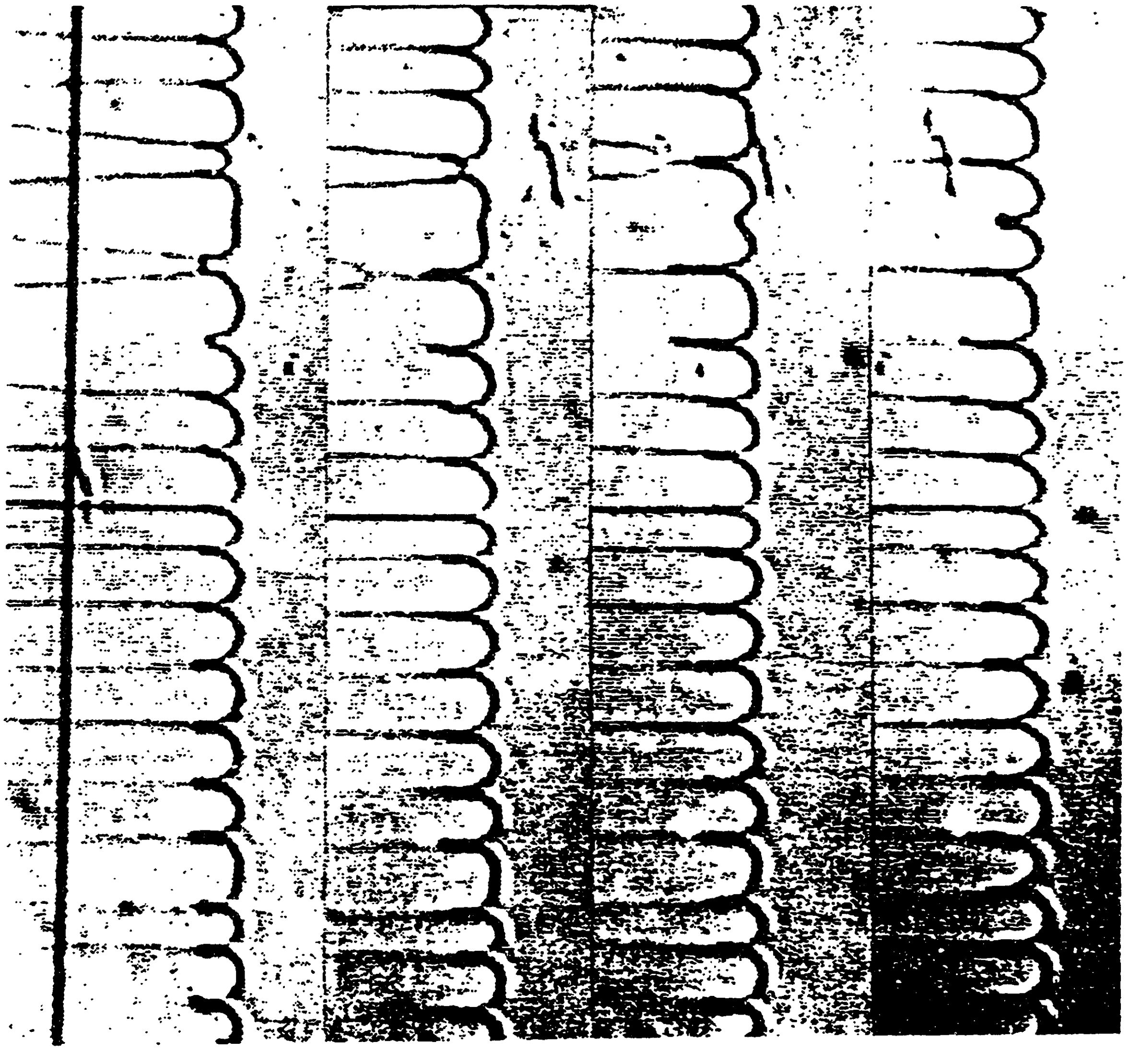

Figure 1.16: Sequence of four cellular interfaces during growth of CBr_4-Br_2 alloy. Wide cell near the top of the picture undergoes tip-splitting (from de Cheveigné *et al.* 1986, p. 2100).

thickness ϵ was small V_{exp} was found to decrease with ϵ. This is in agreement with the results of an asymptotic analysis by Caroli *et al.* (1986) where the effects of the lateral dimension (perpendicular to the plane of growth) were modeled in terms of the wetting angle between the crystal and the glass plates; see Fig. 1.17. However the experimental cell spacing was unaffected by ϵ in disagreement with the results of the analysis.

Kurowski *et al.* (1990) find that cell shape are self-similar with respect to a relative velocity $V_r = (V - V_c)/V_c$ for velocities within a range from V_c to about $(8 - 9)V_c$. They report a sharp increase in the cell width at higher velocities with cells that change shape, the widest ones becoming dendrites. These results compare well with the results of Eshelman *et al.* (1987). Kurowski *et al.* (1990) found the dendritic transition to be *local.* The entire interface does not become dendritic simultaneously; only selected wide cells undergo this conversion. The dimensionless growth rate P scaled in terms of the diffusion rate ($P = V\lambda/\mathcal{D}_m$) corresponding to these cell widths exceeded $2 - 3$. Kurowski *et al.* (1990) also attempt to compare the cell shapes at small growth rates with the Saffman-Taylor finger. Contrary to theoretical predictions discussed in Section 1.5.2, this comparison was not found to be satisfactory.

Kurowski *et al.* (1989) report another feature sometimes seen during experiments. Deep cellular interface were shown to exhibit *drop shedding*; the cells undergo a dynamic process where the bulbous bottoms of the grooves of the deep cell containing high concentration of the solute are periodically pinched off from the groove; see Fig. 1.18. This was achieved by imposing a sinusoidal modulation on the voltage to the motor that ensures the translation of the sample. They believe that the mechanism is not related to changes at the tip resulting from the modulation and that the transition from the two-dimensional cellular structure to a three-dimensional spherical droplet plays an important role. Brattkus (1989) uses a linear stability analysis of thin three-dimensional axisymmetric roots between the cells to show that the roots are always unstable due to surface energy and the resulting oscillatory instability causes drop-shedding. Corresponding two-dimensional calculations reveal no such instability. This agree with the time-dependent calculations presented in Chapter 3 of this thesis.

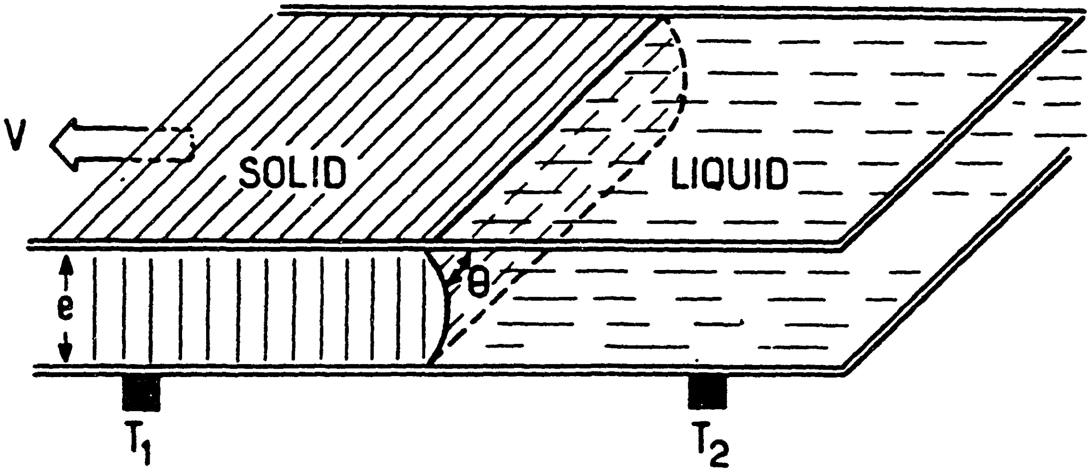

Figure 1.17: Schematic diagram showing the contact angle θ between the solid plastic crystal and the glass plate in the thin-film experiment (from Caroli *et al.* 1986).

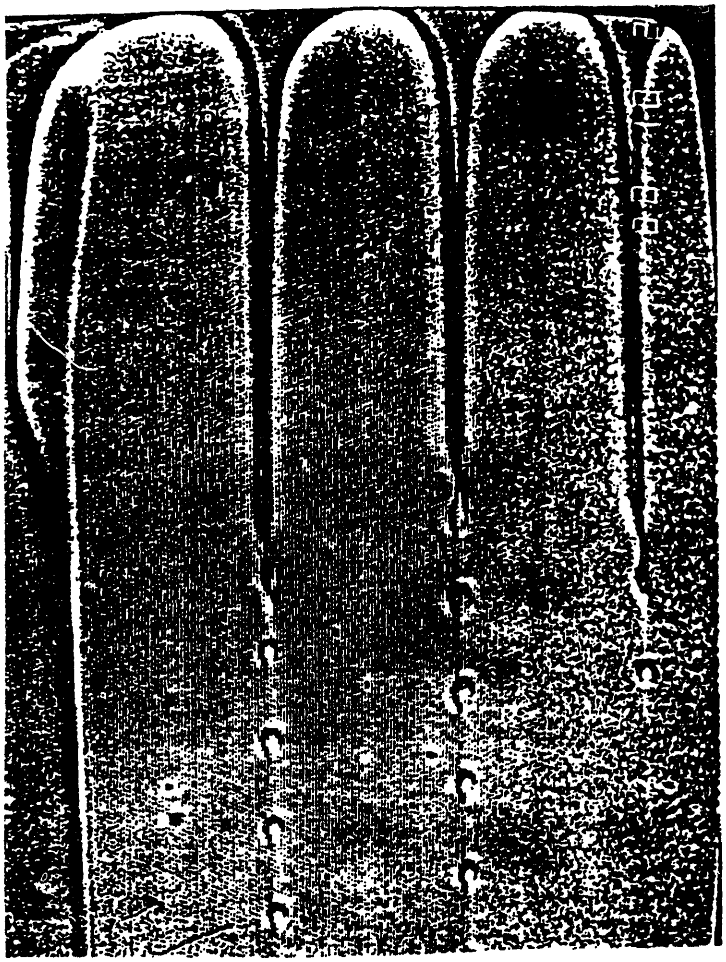

Figure 1.18: Drop-shedding in experiments with CBr_4-Br_2 alloy (from Kurowski *et al.* 1989).

1.3.3 Lee

Lee (1991) used a carefully designed experimental system which allows for long time-scale experiments to be performed, to study the interface morphology of the well-characterized succinonitrile-acetone system. Most of the experiments were conducted near the planar-to-cellular transition.

Lee reports that with careful control of the growth rate near onset, long wavelength low amplitude undulations can be observed. These undulations had a wavelength which correspond to the critical wavelength predicted by linear stability theory. Thus, these results were the first to overcome the problems caused by poor control over the pull rate in the other studies which resulted in the observation of a much smaller wavelength for cells at onset than that predicted by linear stability analysis.

Another important observation of Lee (1991) is that thermal decomposition of the sample due to exposure to the heating unit caused an increase in the overall impurity content along the length of the sample during solidification. This resulted in lower critical solidification rates at the end of the experiment relative to those at the beginning of the experimental run. Lee concluded that this was the cause of the hysteresis in the critical solidification rates that was reported by Trivedi & coworkers and de Cheveigné & coworkers.

For experiments a constant growth rate, Lee observed that when cellular patterns have been established everywhere along the interface, the amplitude remained relatively constant. However, the wavelength distribution was disperse with a mean value that was three to four times smaller than the critical wavelength. This agrees with the results of the previous two groups of researchers. Tip-splitting and cell elimination constantly occurred and the pattern was chaotic in both space and time even after long solidification rates. Lee concludes that wavelength selection for these structures is weak.

Lee also performed some experiments where deep cells were observed. He found that for low concentration sample shallow cells were observed only for a small range of growth rates and the broad dispersion which was observed for small-amplitude cells quickly gave way to a deep cells with sharply selected wavelengths. As the growth rate was increased, no variation in the wavelength was seen in contrast to the results of the previous two sets of researchers who reported a wavelength that depended on the growth rate as $V^{-0.5}$.

It is not clear why there is a discrepancy in these results. The results of this thesis predict that at any growth rate, deep cells exist for a range of wavelengths. This range is predicted to move towards lower wavelengths at higher growth rates. As discussed in Chapter 3, it is possible that the experimental system selects from this range of wavelengths so that the discrepancy in the results of the three studies discussed above arises from the fact that different experimental systems were used.

1.3.4 Other Experimental Studies

Other researchers who have used the thin-film experimental set-up for directional solidification of organic alloys include Venugopalan & Kirkaldy (Venugopalan & Kirkaldy 1982, Venugopalan & Kirkaldy 1984) and Libchaber and coworkers (Heslot & Libchaber 1985, Bechhoefer & Libchaber 1987).

Venugopalan & Kirkaldy use succinonitrile as the solvent with salol as the solute. For parameter values well above the critical values predicted by the Mullins & Sekerka analysis they find regularly spaced cells and two-dimensional protodendrites. However, near the transition values of the growth rate irregular morphologies were observed, whose spacing, length and shape changed across the interface. Eshelman *et al.* (1988) and de Cheveigné *et al.* (1988) conclude that this is because the system was still exhibiting transient behavior. Bennett (1990) notes that the concentrations of salol used in their experiments are almost certainly too high for the assumption of a dilute solution in the Mullins & Sekerka analysis to be applicable.

Libchaber and coworkers used SCN (Heslot & Libchaber 1985) and pivalic acid (Bechhoefer & Libchaber 1987). The results were all in the cellular-dendritic transition region. They also recorded deep cells which often exhibited drop-shedding. The wavelength of the cells was seen to increase with growth velocity in agreement with the results of Eshelman *et al.* (1988) in the cellular-dendritic transition regime. The cells in the SCN experiments had rounded tips and the cell-dendrite transition took place by an oscillatory instability of the cell tip which results in asymmetric tip-splitting and protodendritic shapes (see Fig. 1.19). Heslot & Libchaber believe that protodendrites are a result of crystalline anisotropy, a theory that has been questioned by Bennett (1990) who shows very similar cells with an isotropic model. The experiments with pivalic acid yielded deep cells which had parabolic tips similar to those seen in dendrites (Huang & Glicksman 1981a, 1981b). Tip-splitting of cells was not observed. Bechhoefer and Libchaber believe that this is due to the large anisotropy of pivalic acid in relation to that of SCN (10-fold). This is in agreement with the results of this thesis described in Chapter 3.

Billia *et al.* (1990) have analyzed a large volume of the experimental results for the succinonitrile-acetone system to examine the conditions at the transition from cells (finite cells or FC in their terminology) to protodendritic forms (deep cells or DC according to Billia *et al.*) and the subsequent transition to dendritic patterns (termed D). A schematic representation of the regimes that are expected is shown in Fig. 1.20. As the velocity is increased the interface changes from being planar to cellular to dendritic, and then back to cellular and planar interfaces at the absolute stability limit. Billia *et al.* relate the growth parameters at these transitions to the critical velocity at onset V_c and the velocity at absolute stability V_a. They conclude that the transition to protodendritic forms occurs near $2V_c$ and that the transition to dendrites occurs at a velocity that is proportional to ${V_a}^{1/5}{V_c}^{4/5}$. The velocity at the transition to protodendritic forms is in disagreement with the estimate of de Cheveigné and coworkers and Trivedi and coworkers; both report a velocity of about $8V_c$.

1.3.5 Summary of Experimental Studies

The experimental studies are generally in qualitative agreement about a variety of the features seen in directional solidification. However, there are some important unresolved differences. A brief summary of these features is given below.

All researchers report the planar-cellular transition at pull rates that agree with the Mullins & Sekerka analysis. The wavelength at the onset of instability is however generally lower than that predicted by the analysis. Possible causes are the poor control over the pull

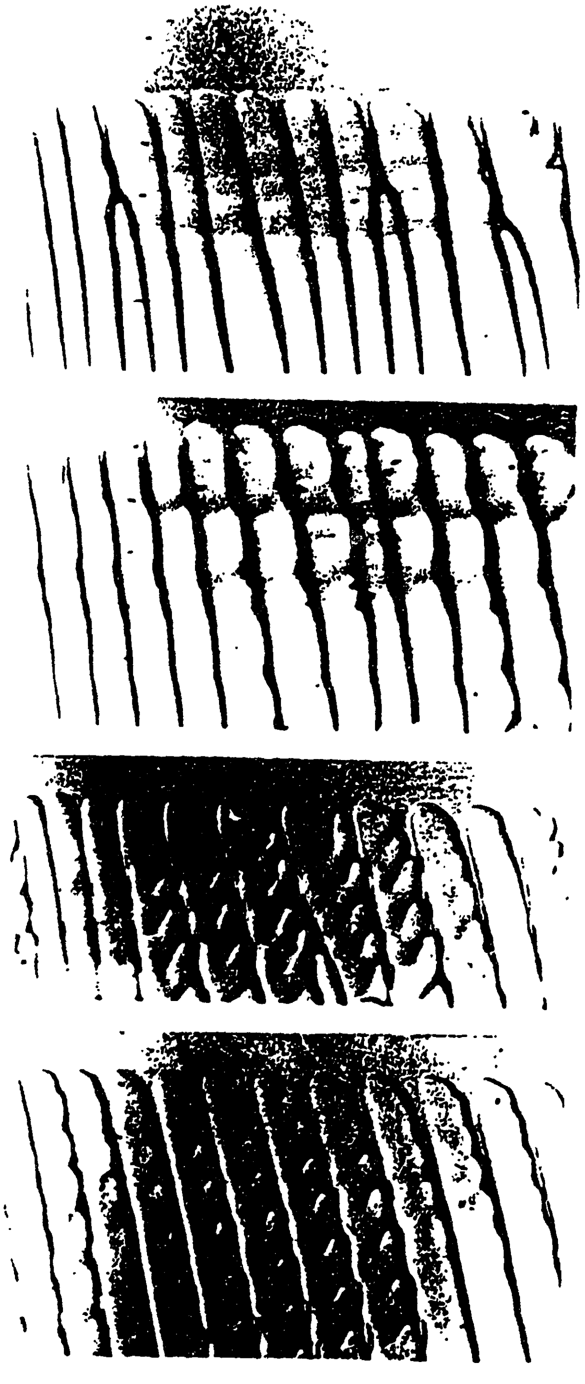

Figure 1.19: Cells exhibiting oscillatory instability which resembles tip-splitting and shoulder rolling (from Heslot & Libchaber 1985, p. 128).

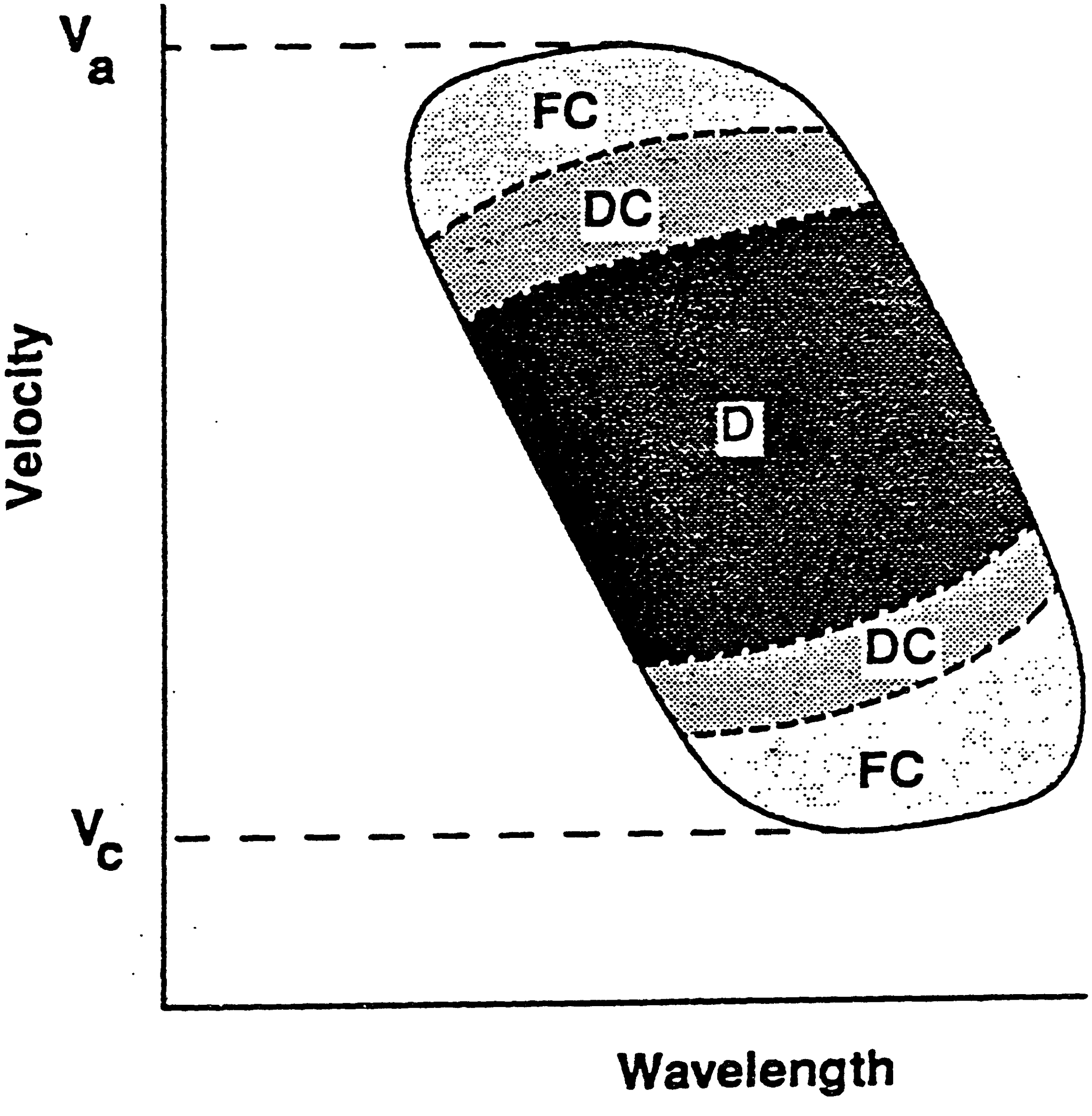

Figure 1.20: A schematic representation of the regimes of interface morpholologies in directional solidification along with the marginal stability curve: FC - cells, DC - protodendrites, D - dendrites. (from Billia *et al.* 1990, p. 411).

rate (a feature of most of the experimental systems) and inadequate accounting for transient times before steady-state is achieved. The results of Chapter 3 will show that the decrease in wavelength of steady-state solutions with pull rate is indeed appreciable. Poor control over the pull rate, long transients and thermal degradation of the alloy are probably the reasons for the ever-changing shapes seen at pull rates near the planar-cellular transition; no clear evidence of spatial wavelength selection thus exists in shallow cells.

As the pull rate is increased further, the evidence is conclusive that the cells get deeper. While Trivedi & coworkers and de Cheveigné & coworkers report that the wavelength decreased as the growth rate is increased, Lee reports that the wavelength remained a constant. However, all studies believe that this spacing is sharply selected.

The primary spacing of the pattern in all the experiments increased sharply near the cell-dendrite transition. At higher pull rates, the microstructure was exclusively dendritic and the primary spacing of the morphology was seen to decrease with pull rate. The theory and experimental evidence of pattern selection are reviewed in detail in Section 1.5.

While qualitative comparison of experimental results with numerical computations like those in this thesis is relatively simple, quantitative comparison is difficult, particularly in the area of selection. This is partly because the amount of data is inadequate and the data has generally not been proven to be reproducible. In addition, the individual experimental systems have some problems. In particular, the high concentrations in the experiments of Venugopalan & Kirkaldy and the poor characterization of the impurities in the experiments of Libchaber and coworkers make accurate quantitative comparison impossible. The spontaneous photo-decomposition of CBr_4 to Br_2 in the experiments of de Cheveigné *et al.* implies that the concentration of solute cannot be measured accurately and could change during the course of the experiment. In general, poor characterization of the material properties of the organic alloy is a problem. In particular, the solute and thermal diffusivities in the solid are not well-known. While the diffusion in the solid may well be negligible for metals and alloys (the ratio of solutal diffusivities is typically $R_m\,[=\mathcal{D}_s/\mathcal{D}_m] \sim \mathcal{O}(10^{-4} - 10^{-6})$), for plastic crystal alloys it is generally estimated to be higher; estimates of R_m range from $\sim \mathcal{O}(10^{-3} - 10^{-4})$ (Caroli *et al.* 1982) to $\sim \mathcal{O}(10^{-1} - 10^{-2})$ (Voorhees 1984) for plastic crystals near their melting points.

Finally, the nonidealities in the experimental system can often not be modeled easily. The experiment may not be truly two-dimensional. The set-up may not be really adiabatic - heat loss could render the model invalid. These concerns are addressed in detail by Lee (1991).

Notwithstanding these difficulties, this thesis attempts to make a quantitative comparison of the experimental data of de Cheveigné and coworkers with numerical results using a two-dimensional solute diffusion model. The results of this comparison are presented in Section 3.6.

1.4 Nonlinear Analysis

While linear stability analyses of continuum models like that presented in Section 1.2.5 predict the parameters at the onset of morphological instability, nonlinear analysis is necessary to follow the growth of the resulting microstructure. Analytical methods have been successful in predicting the characteristics of almost planar interfaces but numerical analysis is necessary to model the highly deformed interfaces that are observed for parameter values that are far from those at the breakdown of the planar interface.

There is some important differences between small-amplitude and large-amplitude interfaces. Deep cells are characterized by their long, slender sidewall which is reentrant; this feature is not seen in shallow cells. A schematic of a cell with a sidewall that folds over is shown in Fig. 1.21. Here, solid that forms at some point on the interface, say point A, is convected down to a point B where the solid *melts* again before it *resolidifies* at the bottom of the cell. The bottoms of deep cells are highly curved in comparison to shallow cells. The effect of surface energy is therefore more important in this region for deep cells. Hence, the analysis of shallow cells cannot be automatically extended to highly-deformed interfaces.

The previous analytical and numerical work in this area is reviewed in this section. Before the theoretical results of previous studies are looked at, it is necessary to review the models of solidification that have been used in these studies. These models are discussed in detail in Chapter 2 but an outline is presented here.

As Mullins & Sekerka (1964) first demonstrated, thermal-solutal models which include diffusion of heat and solute in the melt and solid, solute segregation at the interface between the two phases, freezing-point depression caused by the solute, and the dependence of the melting point on the surface energy through the curvature of the melt-solid interface capture the essence of morphological instability of the interface. These models also simulate many of the other features of directional solidification, as the review in this section and the results of the later chapters of this thesis will show. Generally, simplified versions of the general thermal-solutal model have been used in previous studies; these versions are summarized in Table 1.1 The main difference in these versions is whether solute and energy transport

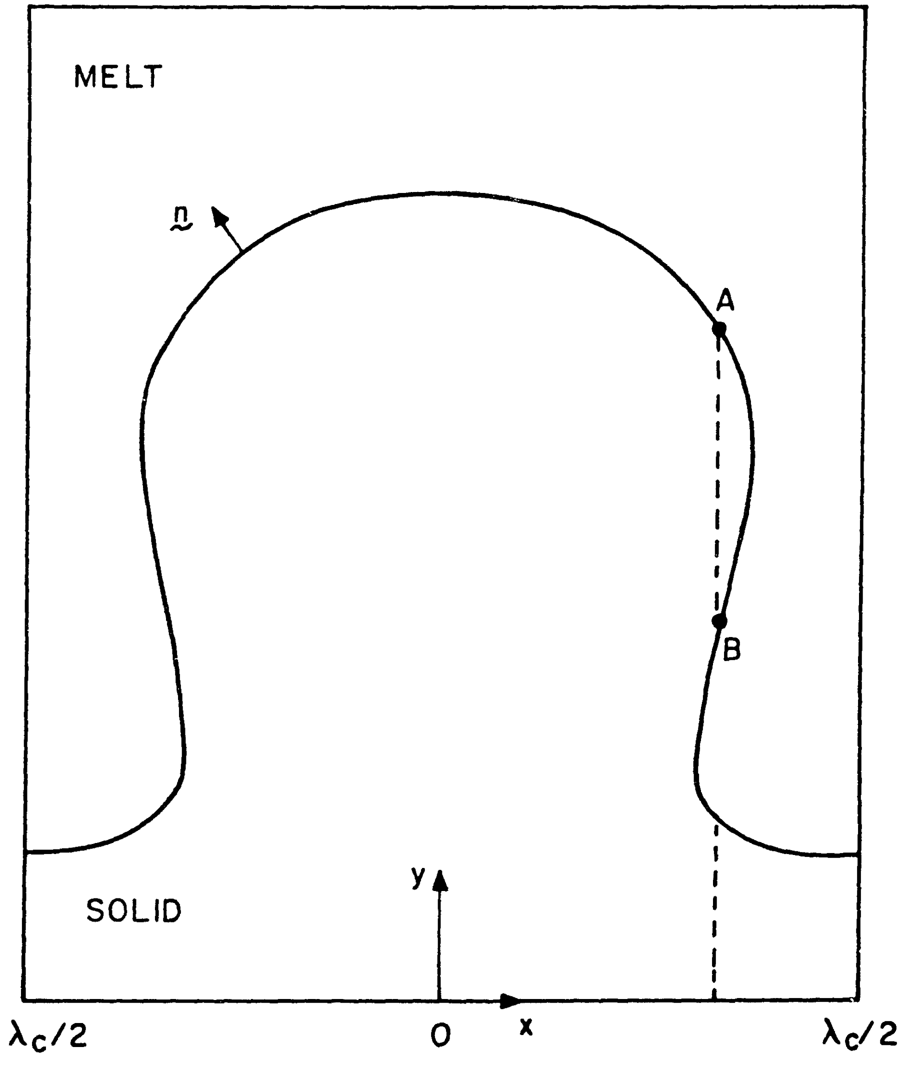

Figure 1.21: Schematic of a cell showing a sidewall that folds over. From Ungar *et al.* (1988).

Model	Energy Transport	Solute Transport in Melt	Solute Transport in Solid
Thermal-Solutal Model (TSM) (Two-sided TSM)	yes	yes yes	yes
Symmetric TSM	yes	yes	yes
		Equal diffusivities in two phases	
One-Sided TSM	yes	yes	no
Thermal Model (TM)	yes	no	no
Solutal Model (SM) (Two-sided SM)	no	yes	yes
Symmetric SM	no	yes	yes
		Equal diffusivities in two phases	
One-Sided SM	no	yes	no

Table 1.1: Summary of models used by previous studies of directional solidification. A "yes" in the second column indicates that the diffusion of heat in the two phases is included. The third and fourth columns indicate whether solute diffusion in the melt and solid are considered.

are considered in both phases. Models which account only for solute diffusion and termed solutal models, while models that are based purely on the diffusion of heat are termed thermal models. Some models account for diffusion only in the melt and are called *one-sided* models, while others that account for transport in both phases are referred to as *two-sided* models. Some two-sided models assume equal thermophysical properties in the two-phases; these are called symmetric models. The analyses presented in this section typically use one of these versions. The equations that describe the most general thermal-solutal model are discussed in Chapter 2.

The reentrant nature of deep cells is important in determining which of the models listed in Table 1.1 is applicable for such interfaces. When the grooves of the cells start folding over, as shown in Fig. 1.21, the one-sided models are invalid. In these models, the value of the concentrations at points A and B on Fig. 1.21 are independently determined. However, the concentrations of solute in the melt at these two points ought to be the same since the solid is convected down from point A to point B before melting. Thus a two-sided model, with a small diffusion coefficient in the solid that is typical of solid phases of the organic materials, is essential for the simulation of reentrant cells. This feature is discussed again in Section 2.3 in connection with its application to numerical methods.

1.4.1 Analytical Methods

Analytical methods have been applied to study the thermal solutal models listed in Table 1.1 and have been successful in explaining the transitions that are observed for families of cells that have small amplitudes. These analyses, which are discussed below, are not applicable for the highly deformed interfaces of deep cells.

Weakly-nonlinear analysis of a thermal-solutal model of solidification was first conducted by Wollkind & Segal (1970) who performed an amplitude expansion around the conditions at the onset of the morphological instability using a two-dimensional one-sided model of solidification . Using a multiple time scale analysis, they recover the result of Mullins & Sekerka (1964) at leading order. They write down a Landau equation for the amplitude for the third order solution,

$$\frac{d\mathcal{A}}{d\tau} = a_0\mathcal{A} - a_1\mathcal{A}^3 \quad , \tag{1.43}$$

where $A(\tau)$ is the amplitude describing the evolution of sinusoidal interface perturbations. The constant a_0 represents the growth rate of such perturbations and a_1 is called the Landau coefficient. Equation (1.43) describes the dynamics of the interaction of the planar solution with a spatial mode of a given wavelength. Steady-state analysis of Eq. (1.43) predicts two types of behavior depending on the physical parameters as shown in Fig. 1.22. In the first case (Fig. 1.22a), the system undergoes a *supercritical* bifurcation as the control parameter is increased and the planar interface goes unstable to a family of solutions with sinusoidal shapes. In the other case (Fig. 1.22b) the system undergoes a *subcritical* transition where there are no stable solutions predicted past the critical value of control parameter and the

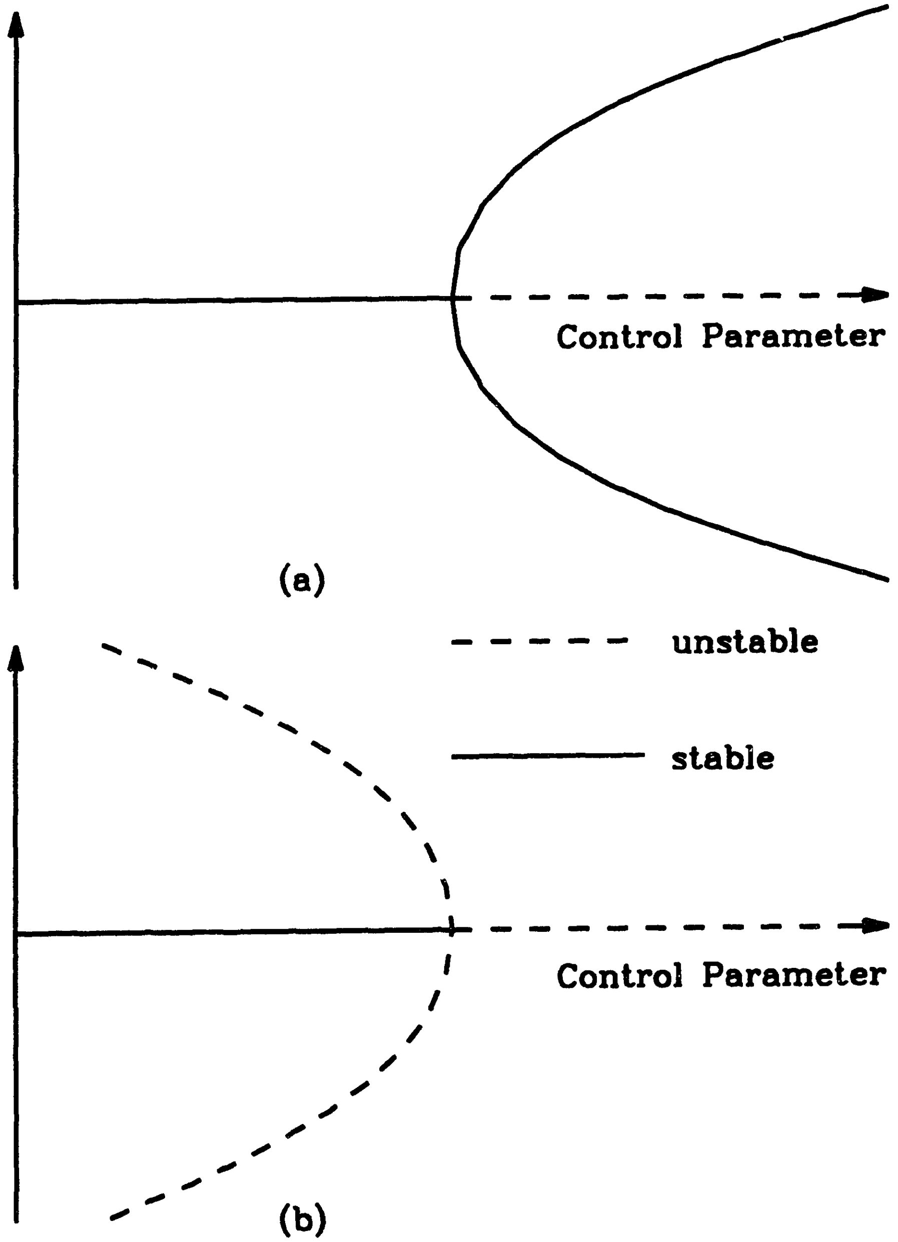

Figure 1.22: (a) Supercritical and (b) Subcritical bifurcations.

system shows hysteresis; the planar interface is unstable for values of the control parameter even lower than the critical value for large enough perturbations. This behavior leads to a hysteresis in experimental observations of the value of the control parameter at the bifurcation.

Wollkind and coworkers (Sriranganathan *et al.* 1983, Wollkind *et al.* 1984) have extended the analysis to three-dimensional solidification. They predict that when the interfacial surface energy is permitted to vary with solute concentration, steady-state microstructures of nodes, elongated cells and hexagonally-arranged cells are obtained in sequence as the growth rate is increased. This sequence is in qualitative agreement with experiments of Morris & Winegard (1969). Caroli *et al.* (1982) extended the analysis of Wollkind & Segal (1970) to the two-sided model and Alexander *et al.* (1986) incorporated the effects of latent heat in the nonlinear analysis and McFadden *et al.* (1988a) conducted a weakly-nonlinear analysis for a three-dimensional model with anisotropic surface energy; both analyses predict transitions that are similar to the results of Wollkind & Segal (1970).

Langer and coworkers (Langer & Turski 1977, Langer 1977, Langer 1980) and Dee & Mathur (1983) use a Green's function formulation to reduce the system of equations for the one-sided (Dee & Mathur 1983) or two-sided symmetric model (Langer & coworkers) to a single integro-differential equation for the interface shape. An approximate solution is derived using a truncated Fourier representation of the interface shape. The interaction of solution branches with a fundamental wavelength with respect to a continuous band of wavelengths was studied. The results were very similar to those of Wollkind & Segal (1970). The neutral stability curve of Fig. 1.14 shows that families of two wavelengths λ_1 and λ_2 go unstable simultaneously for any velocity V above critical. Hence near onset it is expected that at leading order interactions between families of cells of two wavelengths would have to be considered. Dee & Mathur (1983) consider this interaction and predict both pure (one-wavelength) and mixed (two-wavelength) solutions.

Kerzberg (1983a, 1983b, 1984) also used a Fourier expansion method for a one-sided model of solute diffusion. Third-, fourth- and fifth-order expansions of the amplitude equations revealed periodic arrays of sinusoidal cells in two-dimensions and triangular and hexagonal patterns of cells in three-dimensions similar to those seen by Sriranganathan *et al.*

(1983).

Haug (1987) also studied the bifurcation of the one-sided and symmetric models using the method of normal forms in which the symmetries of the solidification problem are used to derive an algebraic amplitude equation valid around the bifurcation point. Haug found that any two primary branches with wavelengths $n\omega$ and $(n+1)\omega$ were connected through a common mixed secondary branch except when $n = 1$ where the two branches were directly connected to each other through a secondary bifurcation; this feature was first reported by Ungar (1984) for small-amplitude cells. The results of Chapter 3 for families of large amplitude solutions reproduce this feature.

Clearly, the nonlinear analyses reviewed above have been able to qualitatively predict the nonlinear transitions that are seen right near the onset of the instability of the planar interface; however, the transition to deep cells with reentrant sidewalls and pendant bottoms cannot be predicted with weakly nonlinear analyses. Hence, recent analytical studies of thermal-solutal models (Dombre & Hakim 1987, Kessler & Levine 1988) have mostly focused on asymptotic analysis of one-sided and symmetric models of solidification to find pattern selection mechanisms for deep cells in directional solidification that are similar to those that have been derived for dendritic solidification and viscous fingering in multiphase fluid flow; the analyses that predict pattern selection mechanisms for these systems and the subsequent attempt to apply the results to cellular solidification are described in Section 1.5.2.

1.4.2 Numerical Methods

Numerical analysis of the free- and moving-boundary problems that describe directional solidification provide the only effective method of determining the structure of deep cells and dendrites that evolve from the planar front. Numerical methods have been developed by many researchers for this purpose and are discussed below.

An important characteristic of the deep cell that has to be simulated by the numerical method is the reentrant nature of the sidewall; simple representations of the interface have generally proved inadequate for this purpose as described later in Chapter 2. In addition, the narrow grooves make accurate computation of these cells difficult. Typically, a compromise has been made in the numerical methods between the simplicity of the numerical algorithm and its efficiency, accuracy and robustness. The techniques used range from boundary-integral methods to finite-difference and finite-element methods. These methods differ in the interface representation, the approximations used to satisfy the field equations, and in the iteration schemes involved in solution of the resulting nonlinear algebraic equations. Studies that employ each of these techniques are discussed below.

1.4.2.1 Boundary-Integral Methods

Boundary-integral methods (or potential methods) are useful when the equations governing solute and thermal diffusion can be reduced to one-dimensional integro-differential equations defined only along the melt/solid interface. Here interface shapes which cannot be easily represented by single-valued functions in any simple coordinate system can be accomodated. However, these methods are only useful for some solidification systems where the time scales for diffusion of solute and heat are much smaller than that for the motion of the solidification front. This pseudo-steady-state assumption leads to field equations which only depend parametrically on time. Unfortunately, full time-dependence cannot be incorporated without adding volume integrals which destroy the one-dimensional nature of the equation set. Simple closed-form and numerical solutions of these integro-differential equations have been derived for limiting values of certain parameters as described below (Karma 1986, Ben-Amar & Moussallam 1988, Weeks & van Saarloos 1989, Mashaal *et al.* 1990) but a complete numerical solution has been reported only recently (Kessler & Levine 1989a, 1989b). The main goal of most of these methods has been to look for wavelength selection mechanisms for deep cells in directional solidification; each of these studies is discussed below.

Karma (1986) and Ben-Amar & Moussallam (1988) employed a Green's function formulation of the one-sided model of solidification and approximate the Green's function by logarithmic functions for small Peclet numbers. An infinitely long groove is assumed to exist far from the tip of the cell. This result due to Scheil and Hunt (Hunt 1979) is used as a boundary condition and the integro-differential equation is solved to check for the existence of a mechanism for wavelength selection. The assumption of an asymptotic sidewall simplifies the analysis but an an important characteristic of the deep cell shape, i.e. the reentrant sidewall, is lost. This assumption is discussed in detail in Section 1.5.

A constant miscibility gap was also assumed - here the difference between the concentrations of the solute in the melt and crystal at equilibrium is assumed constant:

$$[\tilde{c}_{\mathrm{m}} - \tilde{c}_{\mathrm{s}}]_{\mathrm{interface}} = \text{constant} \quad . \tag{1.44}$$

The more commonly-used assumption is that of linear liquidus and solidus slopes which yields the equlibrium relationship for a constant segregation coefficient; see Eq. (1.3).

While Karma (1986) predicts the existence of a selection mechanism, the results of Ben-Amar & Moussallam (1988) indicate no such mechanism as described in Section 1.5; the results of Ben-Amar & Moussalam are in agreement with the results of this thesis. Recently, Mashaal *et al.* (1990) have extended the results of Ben-Amar & Moussallam for the more realistic segregation relationship given by Eq. (1.3) to produce similar results.

Weeks & van Saarloos (1989) use a similar procedure valid at finite Peclet numbers but small segregation coefficients to develop expressions for the spacing of the rounded bottoms that are an essential characteristic of deep cells. However, as the analysis of Section 2.3 will show, the one-sided model is invalid when the sidewall of the cell becomes reentrant. Thus, the results of Weeks & van Saarloos is invalid for deep cells.

The results of Kessler & Levine (1989a, 1989b) are described in Section 3.6 where the results of the numerical procedure used in this thesis are compared with their work and with experimental data.

1.4.2.2 Finite-Difference Methods

Finite-difference methods (McFadden & Coriell 1984, McFadden *et al.* 1987, McCartney & Hunt 1984, Hunt & McCartney 1987, Wheeler 1986) and finite element methods (Ungar 1984, Sullivan & Lynch 1987, Bennett 1990) have both been successfully developed to solve the free- and moving-boundary problems that arise in solidification. The finite element method is the technique of choice in this work and is described in Chapter 2.

McCartney & Hunt (1984) used the finite-difference method for the numerical solution of the full three-dimensional equation set that accounts for the diffusion of heat in the two phases; diffusion of the solute in the solid was neglected. They examined cells with large amplitudes that were far from the planar-to-cellular transition. No systematic attempt was made to follow the evolution of these cells from the planar state. They found steady-state solutions for a range of imposed cell half-widths. They hypothesize that the selected cell spacing is bounded by the maximum wavelength for which solution could be calculated with their scheme. Using this hypothesis, they show that the selected cell width would decrease as the pull rate is increased. The discretization used in their calculations employed only 11 mesh points along the interface leading to questions about the accuracy of their results; the results of Chapter 3 will show that accurate approximation of the complex structure of deep cells requires a finer discretization. Hunt & McCartney (1987) extended this work to include the effect of solute diffusion in the solid. In both works, no mechanism for the selection of steadily growing cells was detected. This is in agreement with the results of this thesis (see Section 3.5).

An important error in the calculation of McCartney and Hunt is the use of the one-sided model to compute deep cells. The analysis of Section 2.3 will show that only a model which accounts for solute diffusion in both phases can accurately model deep cell with interfaces that are reentrant. Hence, the results of Hunt and McCartney can be applied only for small-amplitude interfaces.

McFadden & Coriell (1984) also developed a finite-difference method to solve a two-dimensional model that accounts for thermal diffusion in both phases and solute diffusion only in the melt. Using the physical properties for an Al-Ag system, they again found that solutions exist for a range of wavelengths at any pull rate. McFadden *et al.* (1987) extended the analysis for a three-dimensional system. Using a solutal model they show that the depth of the cells is bounded for segregation coefficients greater than 1.0. Using the bulk concentration c_∞ as the control parameter for the Al-Ag system ($k = 1.8$) they find that families of hexagonally-arranged cells (nodes) and families with a rectangular waveform (rolls or bands) bifurcate from the planar family. These interface morphologies in three-dimensional systems are well known in experiment; see Fig. 1.23. In both studies only small-amplitude cells were considered.

Wheeler (1986) devised a boundary-fixing technique where the unknown interface is transformed to a fixed position and solved the resulting nonlinear equation set using a finite-difference scheme. He reports that the solution was in qualitative agreement with linear theory and other weakly-nonlinear analyses near the onset of cellular interfaces; no deep cellular interfaces were simulated.

All the finite-difference analyses reviewed here have one common feature: the results are applicable only for small amplitude interfaces that are non-reentrant.

1.4.2.3 Finite Element Methods

The numerical method used in this thesis is based on the technique used by Ungar and Brown in a series of four papers: Ungar & Brown (1984a, 1984b, 1985) and Ungar *et al.* (1985). The numerical method is described in detail in Chapter 2 and only a brief review of their results is presented here. The thermal-solutal model presented in Section 2.1 is used. In essence, the unknown interface shape in the free- or moving-boundary problem is mapped to a fixed domain using a non-orthogonal transformation. The transformed equations are discretized using Galerkin finite element methods and the resulting set of nonlinear algebraic equations is solved by a modification of the isotherm-Newton method of Ettouney & Brown (1983) to determine the field variables of temperature and concentration and the interface shape simultaneously. Solution families are calculated using computer-aided solution tracking techniques.

Ungar and Brown calculate steady-state interfaces for several different models. The calculations were done for the thermophysical properties of a Pb-Sb alloy with a *half-wavelength* method; the size of the computational domain is fixed at half the wavelength of the desired solution as shown in Fig. 1.24. This is achieved by reflective symmetry (no-flux) boundary conditions imposed at the sides of the domain. This method only permits the appearance of solutions for which the width of the computational domain is an integer

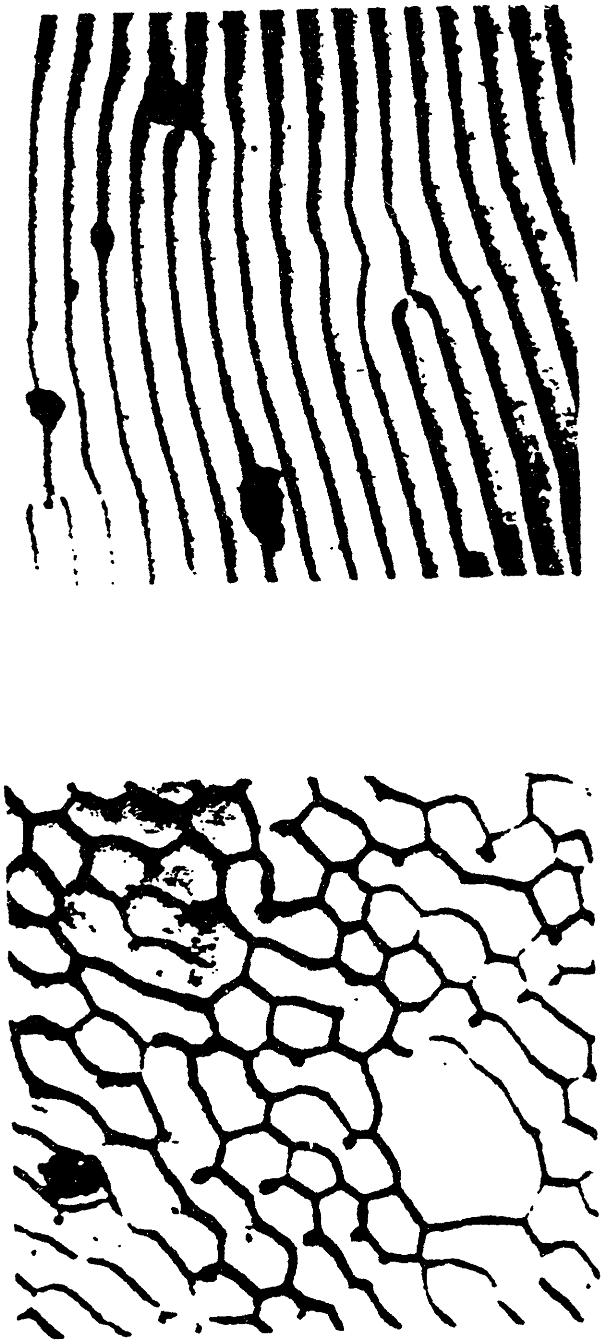

Figure 1.23: Cellular microstructure revealed by decanting of the melt during a solidification experiment (as viewed from above): (a) rolls or bands with less supercooling, (b) hexagonally-arranged cells with more supercooling (from Chadwick 1967, p. 123).

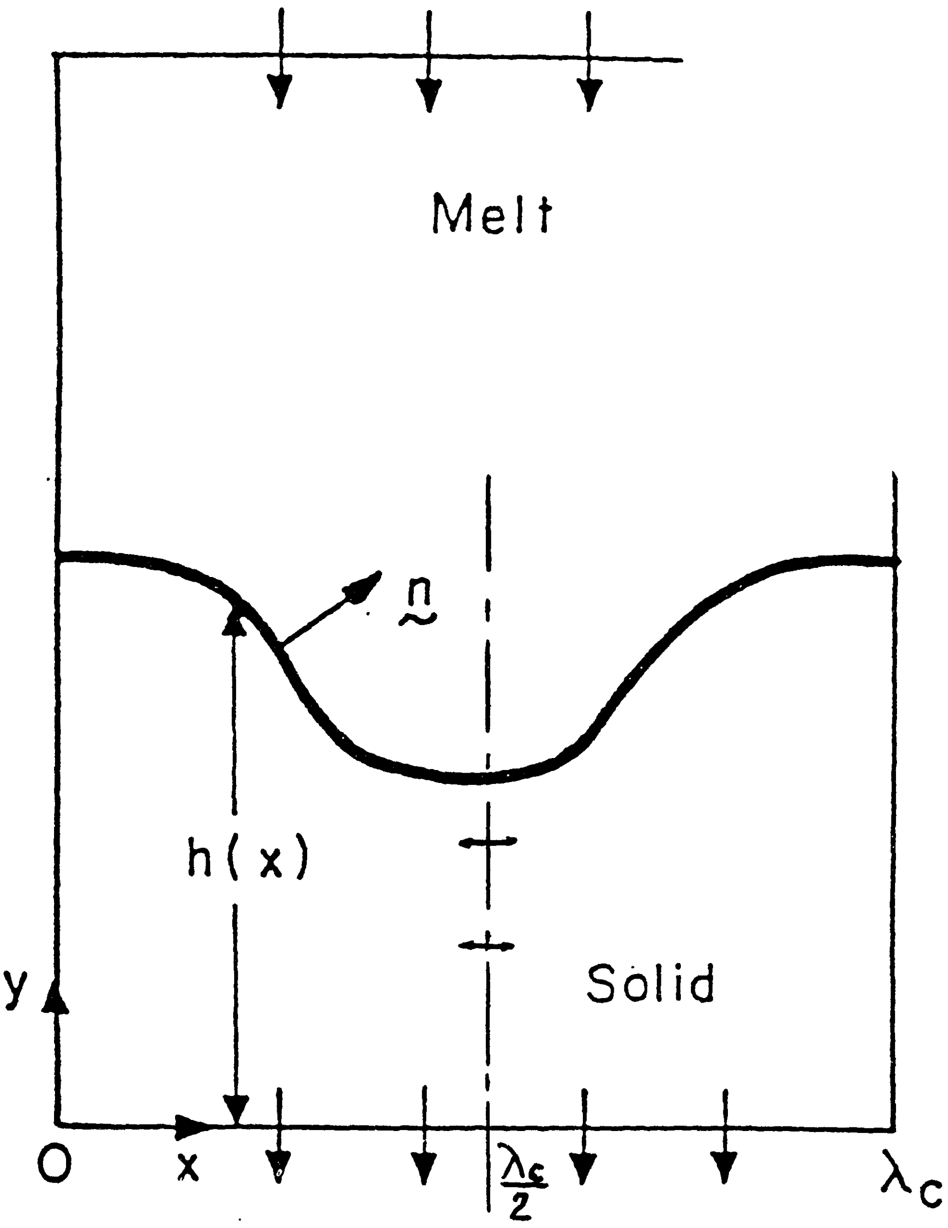

Figure 1.24: Schematic representation of half-wavelength method used by Ungar (1984) for the computation of cellular morphologies.

multiple of the half-wavelength of solution. Most of the calculations performed by Ungar employed the Mongé representation of the interface, $y = h(x)$ which is valid only for shallow cells, as discussed in Chapter 2; the representation results in a multivalued function $h(y)$ for deep cells with reentrant sidewalls, like that shown in Fig. 1.21.

The procedure was used to locate the growth parameters at the onset of the morphological instability in agreement with linear stability analysis. Solution tracking techniques were used to follow the family of solutions that bifurcated from the planar solution at the critical point, using the temperature gradient as the control parameter. Typically, a family of cellular solutions with the critical wavelength λ_c (referred to henceforth as the $1\lambda_c$ family) bifurcated either subcritically or supercritically (depending on the model used) but always turned towards lower (supercritical) values of the temperature gradient. The cells were tracked towards increasing deformation and were seen to become "molar" in shape and this $1\lambda_c$ family eventually terminated at a secondary bifurcation point on a family of solutions with half the wavelength of the original family (the $\frac{1}{2}\lambda_c$ family). Typical results from Ungar (1984) are shown in Fig. 1.25 with the interface deflection (aspect ratio) of the cell plotted as a function of the temperature gradient along with sample shapes from the two families, also taken from Ungar (1984). The $\frac{1}{2}\lambda_c$ family which originated as a bifurcation from the planar solution was calculated to higher levels of deformation until the sidewalls of the cells started to become very steep and the Mongé representation failed. The transition from the $1\lambda_c$ family to the $\frac{1}{2}\lambda_c$ family took place within a 1% change from the critical value and is likely to be undetected by the experiment (see discussion in Section 1.3).

Ungar & Brown (1984b) also examined the effect of grain boundaries on cellular morphology. Using a singular perturbation analysis valid for small grain boundary slopes they showed that grain boundaries introduce an imperfection into the symmetry of the growing interface; using two-dimensional computations they also showed qualitatively the initial formation of bands near the grain boundary as seen in experiments by Glicksman *et al.* (1972).

Bennett (1990) extended the work of Ungar and Brown and showed that wavelength halving by tip-splitting was a generic phenomenon in steady-state simulations. Performing extensive dynamic calculations with domain sizes that were larger than the wavelength of

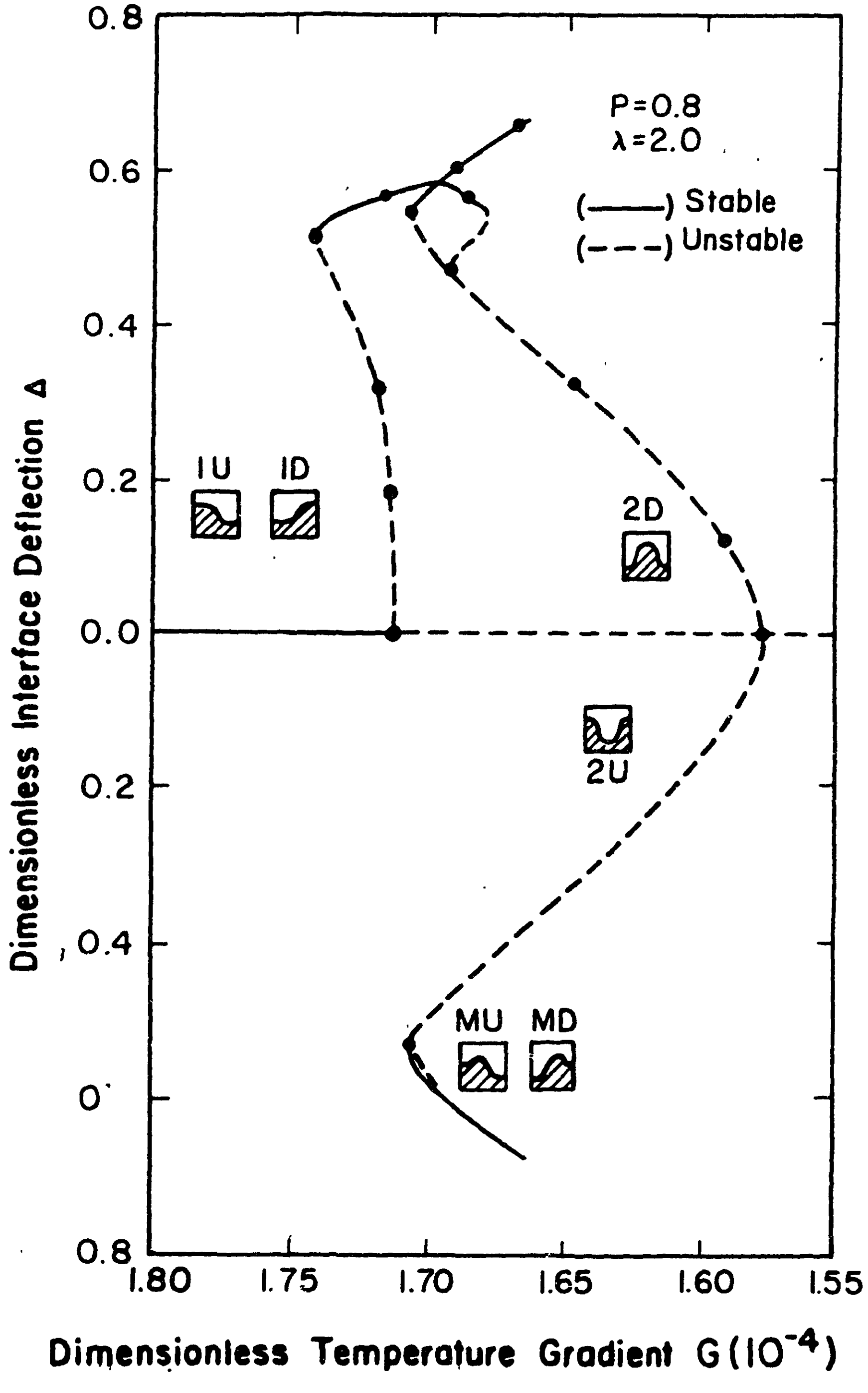

Figure 1.25: Families of shallow cellular interfaces that bifurcate from the planar state plotted with interface deflection as a function the temperature gradient. From Ungar (1984).

the family of interest, he showed that changes in the microstructure occurred through three fundamental types of behavior: the addition of cells by tip-splitting, removal of cells by cell elimination and the oscillation of the amplitude of the cells. Bennett performed calculations with a fully-implicit time-dependent scheme with both reflective symmetry and periodic boundary conditions at the sides of the domain and showed that within a 2% increase in the growth rate from critical, multiple stable steady-states and time-periodic solutions occur for both types of boundary conditions; in addition, traveling wave solutions were seen with the periodic boundaries. The wavelength was seen to decrease on the average as the velocity was increased in the time-dependent runs. Bennett concluded, however, that a statistical description of the system's wavelength was needed, due to the variety and complex nature of the dynamics in his simulations; the possibilities for wavelength selection is directional solidification are discussed in the following section.

In their final paper, Ungar & Brown (1985) use a mixed-coordinate mapping to track the $\frac{1}{2}\lambda_c$ family of cells to much higher deformations (deep cells). This procedure which allows for the calculation of cells with sidewalls that fold over, forms a basis for the work in this thesis.

1.5 Pattern Selection

One of the most important characteristics of microstructure formation in directional solidification is pattern selection; the concept of pattern selection is introduced in this section and previous studies of pattern selection are described. It is generally accepted that cellular interfaces that are seen right near onset of the morphological instability of the planar interface are not selected in experiment but that the deep cellular interfaces seen at higher growth rates are selected based on their spatial wavelength, i.e., the experimentally observed interface is believed to be spatially periodic with a unique wavelength at given growth conditions; this observation is discussed in Section 1.5.1 where the experimental evidence of wavelength selection of cellular and dendritic morphologies is summarized.

Another reason for the interest in pattern selection in cellular solidification arises from theories that predict selection mechanisms for other systems which exhibit fingered growth phenomena; in particular selection mechanisms have been derived for dendritic solidification and viscous fingering in porous media. Several studies of pattern formation in fluid mechanical and solidification systems over the last few years have focused on determining a quintessential mechanism for pattern selection in these systems. The main thrust of these studies has been to establish a unique relationship between the wavelength of the periodic pattern and the growth parameters; Langer (1980) has presented a comprehensive review of the work on pattern selection published until that date. These theories are discussed in Section 1.5.2. Mechanisms of wavelength selection that have been derived for dendritic solidification are reviewed in Section 1.5.2.1 and previous studies of pattern selection for fluid flow in porous media are described in Section 1.5.2.2. Studies which have attempted to find similar selection mechanisms for the cellular solidification system are discussed in Section 1.5.2.3. Finally, the possible scenarios by which patterns could be selected in the experimental system are surveyed in Section 1.5.3.

1.5.1 Cellular and Dendritic Spacings in Experiment

As mentioned in Section 1.3, the experimental evidence of selection of steady-state shapes in cellular and dendritic solidification is inconclusive. It is generally believed that the shallow cell seen right near onset are continuously changing. The transient time is generally believed to be too large to achieve true steady-states ($\mathcal{O}(10^4$ secs as reported by Eshelman & Trivedi 1987). A Fourier analysis of the evolving interface in experiments by Eshelman & Trivedi (1988) showed that initially, during a linear growth phase one Fourier mode is dominant; however, this component was rapidly overtaken by other modes and a broad peak of smaller wavenumber was finally seen, indicating that wavelength selection was not sharp. This decrease in wavelength was also seen in experiments by de Cheveigné and coworkers as described in see Section 1.3. As reported earlier, according to Lee (1991), thermal degradation of the sample with time leads to an increased impurity content and a consequent decrease in the observed critical wavelength at onset. This could also be the cause of the apparent decrease in the wavelength of the interface in the experiments of Trivedi & coworkers and de Cheveigné & coworkers. In summary, the wavelength selection of shallow cells in experiments has not been conclusively shown.

At higher pull rates, deep cellular interfaces are seen. These patterns have a more uniform spacing and the cell widths in this regime are better characterized. The scaling $\tilde{\lambda} \propto V^{-0.5}$ has been reported by Eshelman *et al.* (1988). At higher velocities a transition from cells to protodendritic shapes is accompanied by a sharp increase in wavelength. Dendritic shapes that follow at even higher velocities have a spacing that again decreases with pull rate. This generic behavior is plotted in Fig. 1.26 as taken from Eshelman & Trivedi (1988). de Cheveigné *et al.* (1986) also report a similar scaling expression $\tilde{\lambda} \propto V^{-0.4\pm0.1}$. The power (-0.5) is also the classical power-law relation between tip curvature and velocity in dendritic solidification and has led researchers to look for unified selection theories for the dendritic and cellular solidification systems (Kessler & Levine 1988).

The results of de Cheveigné *et al.* (1986) indicating the above scaling are shown in Fig. 1.27. The experimentally observed wavelengths are plotted along with the marginal stability curves for two temperature gradients ($G = 120°K/\text{cm}$ and $G = 70°K/\text{cm}$) deduced

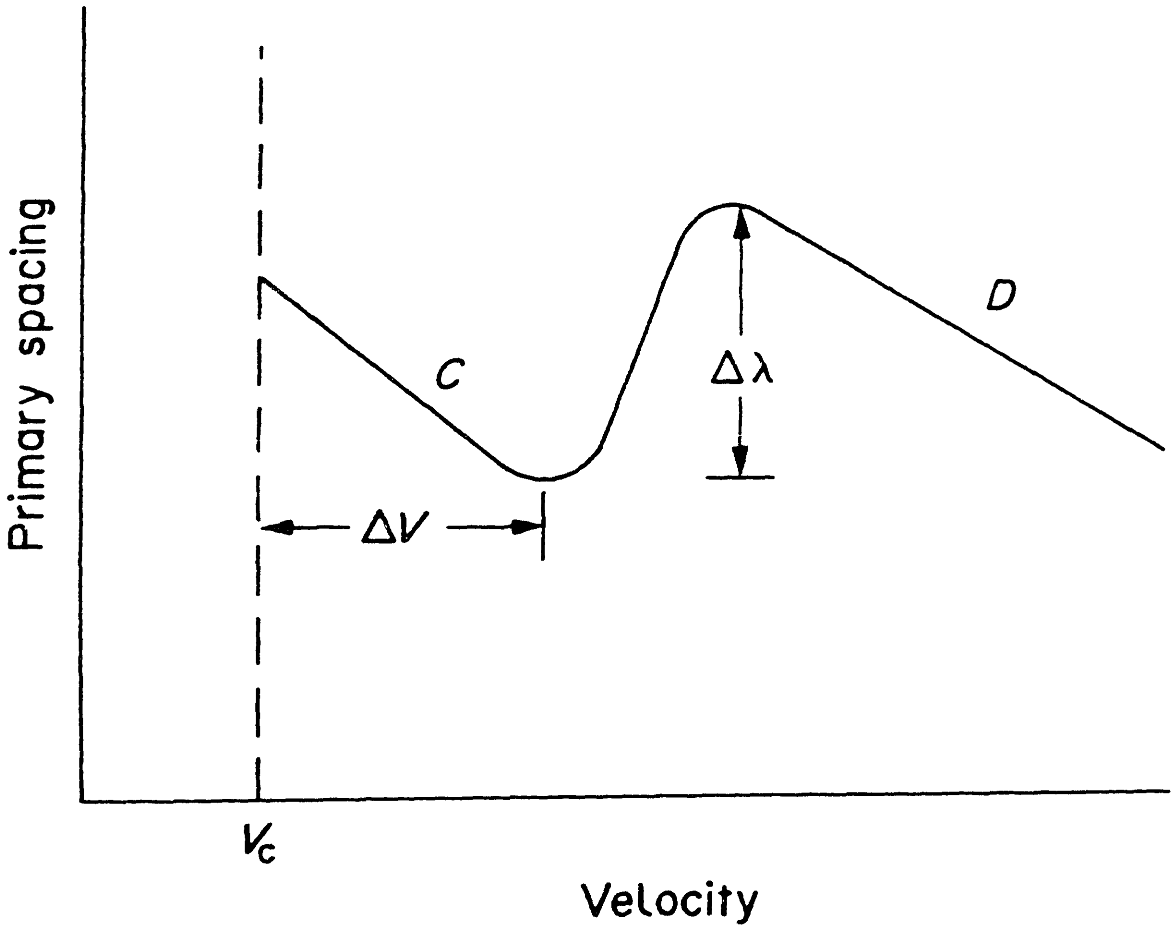

Figure 1.26: Experimentally observed generic relationship between primary spacing of interface and pull rate (from Eshelman *et al.* 1988).

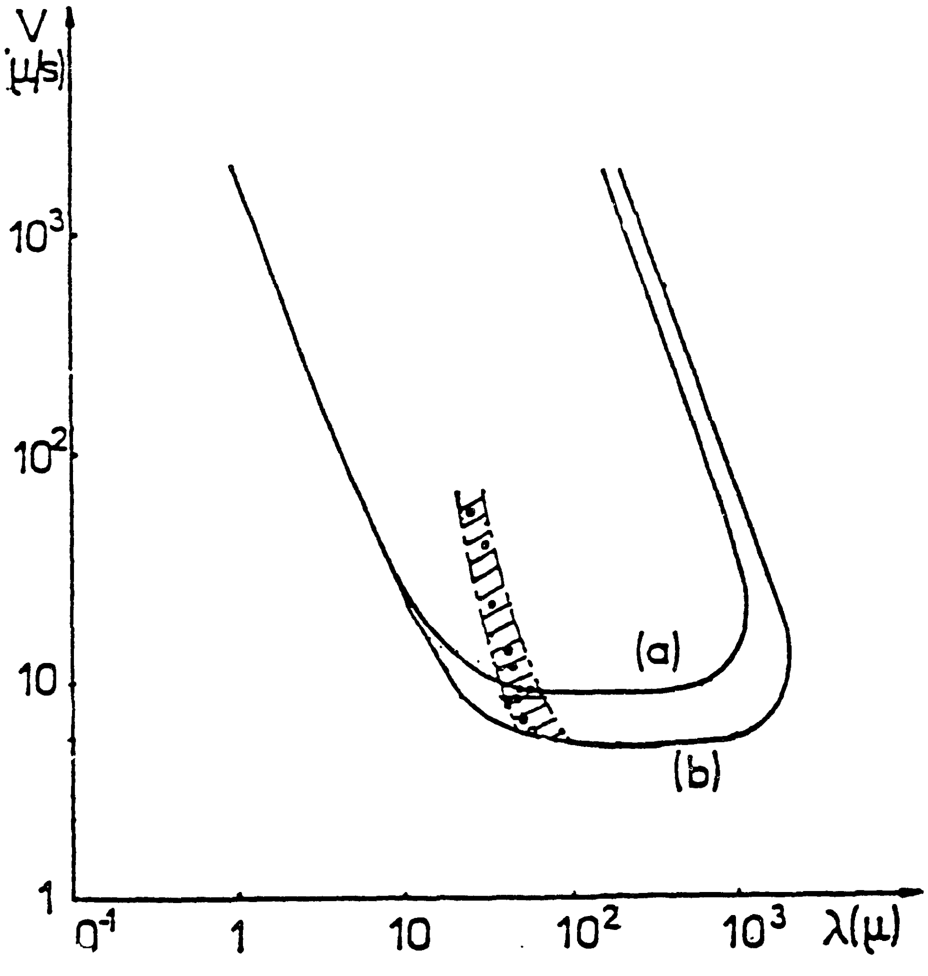

Figure 1.27: Experimentally observed wavelength as a function of in experiments with a CBr_4-Br_2 alloy. The full curves are the marginal stability curves for two temperature gradients. (a) and full circles: $G = 120°K/cm$, (b) and empty circles: $G = 70°K/cm$ (from de Cheveigné *et al.* 1986).

from linear stability analysis. They assert that experimentally a wavelength is selected to within a few tenths of 1 percent. Another feature of the data in Fig. 1.27 is the lack of any significant dependence of the selected wavelength on the temperature gradient. The data for both temperature gradients fall within the same range of wavelengths at a given velocity. As discussed in Chapter 3 this result is in contrast with the results of this thesis and leads to the question of whether these cellular interfaces are selected by the particular experimental system being used.

It is not clear whether the selection that is seen in these experiments is an artifact the experimental system; adequate reproducible data does not yet exist for the deep cellular regime to check this possibility. It is also not clear that the cells in these experiments are truly steadily-growing; the long time-scale transients that have been reported for shallow cells in experiments (Eshelman & Trivedi 1987) leads to the question of whether these interfaces are indeed steady. The possibilities for selection in the experimental system are discussed further in Section 1.5.3.

1.5.2 Theoretical Prediction of Selection

Early theoretical studies which have tried to explain wavelength selection in cellular and dendritic patterns (Billia *et al.* 1987, Trivedi 1980) based on phenomenological models which include assumptions about the concentration or temperature somewhere along the interface. Recent analytical studies of pattern selection have mostly attempted to find a unified theory for selection for many fingered growth phenomena. Finger-like patterns have been observed in dendritic and cellular solidification, in fluid mechanical systems like immiscible displacement in porous media, Taylor-Couette flow and Rayleigh-Bénard convection and in electrochemical deposition. Researchers have attempted to find a unified theory that predicts selection mechanisms in these systems. Kessler *et al.* 1988 has presented a comprehensive review of these studies.

Most of the recent theoretical work in pattern selection in fingered growth phenomena was spurred on by the results obtained in the model problem of steady-state solidification of a pure material into an undercooled melt. As described below, in the absence of surface tension, the problem has a family of *needle crystal* solutions due to Ivantsov (1947) in which the interface is exactly a parabola (Langer 1980, Glicksman 1985, Horvay & Cahn 1961). The family of Ivantsov parabolas is degenerate at constant undercooling and does predict a unique relationship between the tip-radius of the needle crystal and the growth velocity; the theory predicts that the product of the growth velocity and the radius of the tip is a constant. Many studies over the last few years have attempted to solve this problem by introducing the surface tension as a new length scale; this provides a solvability condition for the existence of stable steady interfaces. This approach was then extended to other problems of patterns formation in fluid mechanical and solidification systems as described in the following section.

1.5.2.1 Selection in Dendritic Solidification

Most analyses of pattern selection in dendritic growth have been attempts to determine from first principles the growth velocity and the tip radius of the growing dendrite (Caroli *et al.* 1986). The problem of steady-state dendritic solidification has a family of needle crystal solutions in the absence of surface tension. This result is a consequence of the fact that the diffusion equation in a frame of reference moving at the growth rate is separable in parabolic coordinates (Horvay & Cahn 1961). The two-dimensional versions of the energy equations in the two phases are

$$\alpha_m \tilde{\nabla}^2 \tilde{T}_m + V\frac{\partial \tilde{T}_m}{\partial \tilde{y}} = 0 \quad , \tag{1.45}$$

$$\alpha_s \tilde{\nabla}^2 \tilde{T}_s + V\frac{\partial \tilde{T}_s}{\partial \tilde{y}} = 0 \quad , \tag{1.46}$$

where $\tilde{T}_m$ and $\tilde{T}_s$ are the temperature in the melt and solid and α_m and α_s are the thermal diffusivities in the melt and solid respectively. The boundary conditions at the interface are (i) conservation of heat at the interface

$$\left[\hat{\mathbf{n}} \cdot \kappa_m \tilde{\nabla} \tilde{T}_m - \hat{\mathbf{n}} \cdot \kappa_s \tilde{\nabla} \tilde{T}_s = \left\{\hat{\mathbf{n}} \cdot \hat{\mathbf{e}}_{(y)}\right\} LV\right]_{\text{interface}} \quad , \tag{1.47}$$

where the interface is defined by $\tilde{y} = \tilde{h}(\tilde{x})$. L is the latent heat of solidification, κ_m and κ_s are the thermal conductivities in the melt and solid respectively, and $\hat{\mathbf{n}}$ and $\hat{\mathbf{e}}_{(y)}$ are the unit outward normal and the unit vector in the direction of growth respectively, and (ii) the Gibbs-Thomson equation

$$\left[\tilde{T}_m = \tilde{T}_s = \tilde{T}_o\{1 + \tilde{\Gamma}(2\tilde{\mathcal{H}})\}\right]_{\text{interface}} \quad . \tag{1.48}$$

The temperature is forced to approach a bulk value in the melt far from the tip in *all* directions. This is unlike the cellular solidification system where lateral symmetry boundary conditions are imposed to simulate an array of growing cells. The model here thus defines the problem for the growth of an *isolated* dendrite growing into an infinite undercooled melt.

The details of the solution of this equation set by separation of variables in parabolic coordinates are given in Horvay & Cahn (1961). The interface shape is determined to be a isothermal parabola; see Fig. 1.28. The length scale of the shape is related to the temperature field by the oft-quoted result

$$\Delta = \exp(P_r)\ \sqrt{\pi P_r}\ \operatorname{erfc}(\sqrt{P_r}) \quad , \tag{1.49}$$

where P_r is the thermal Peclet number based on the radius r of the tip of the dendrite; $P_r \equiv Vr/2\alpha_m$ is a dimensionless measure of the growth rate. The dimensionless thermal undercooling at the interface Δ is defined as

$$\Delta = \frac{T_{\text{interface}} - T_{\text{bulk}}}{L/\rho c_p} \quad , \tag{1.50}$$

where $T_{\text{interface}}$ and T_{bulk} are the temperature at the interface and that very far from the growing solid, c_p is the specific heat, and ρ is the specific gravity of the material. Experimental evidence is in rough agreement with Eq. (1.49); Kessler *et al.* 1988. An analogous derivation for the three-dimensional equation set gives an interface which is an elliptic paraboloid.

The solution can also be derived by the method of similarity. The parameter P_r can be viewed as a similarity variable which combines the two unknowns r and V; the solution is determined only as a function of this combined variable. The variation of the cell shape or the temperature field in terms of r or V alone, cannot be explicitly determined.

Eq. (1.49) shows that the Peclet number P_r is specified for a given undercooling Δ; the growth rate and tip radius are thus not independent. This is not surprising since the only

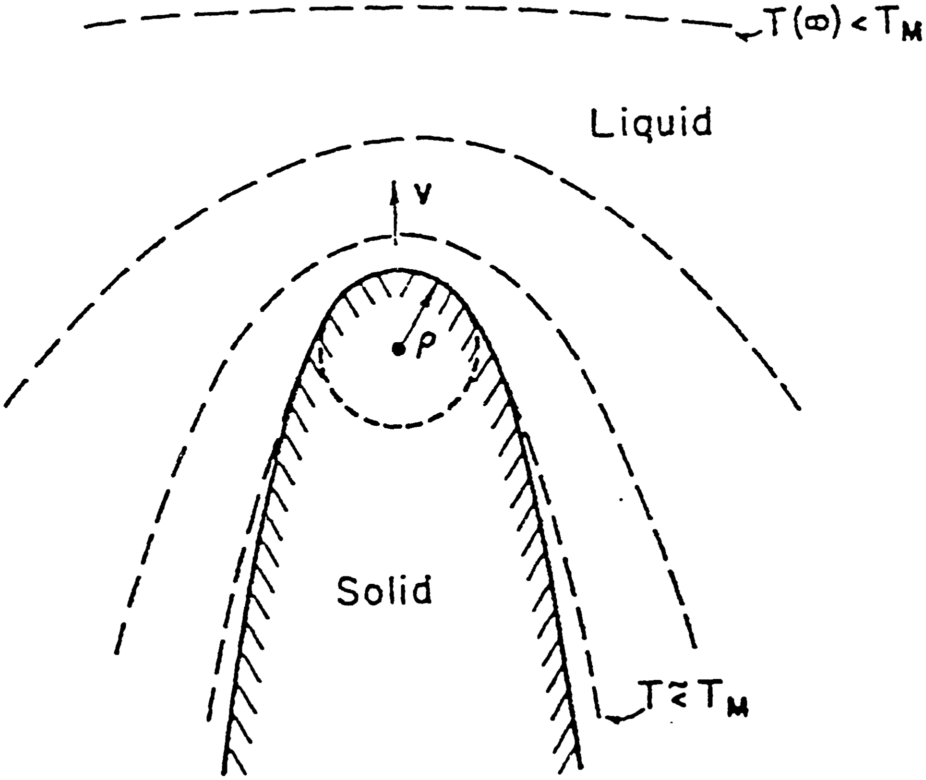

Figure 1.28: The parabolic interface solution to steady-state dendritic solidification in the absence of surface tension (Ivantsov 1947).

length scales in the problem are the diffusive length scale $2\alpha/V$ and the tip radius r and one dimensionless relation is all that can be expected between these scales. Experimentally, however, the growth rate and tip radius are found to be unique and reproducible and sharply selected (Langer 1980, Huang & Glicksman 1981). In addition, the Ivantsov solution has been shown to be unstable, where as experimentally, quasi-stable propagating dendrites are observed (Kessler *et al.* 1988). Attempts have therefore been made to incorporate the surface tension in a variety of approximate and perturbation methods. Nash & Glicksman (1971) solved the steady-state equations with surface tension approximately and found a continuum of solutions; they hypothesized that the dendrite with the maximum velocity would be selected from among these solutions. As we shall see later, the existence of a continuum of solutions in the presence of surface tension has been widely disputed since. Another hypothesis proposed is that the marginal stability controls the selected tip radius (Langer & Müller-Krumbhaar 1978, Langer 1980). Linear stability analysis was conducted under the assumption that the tip was spherical and the surface tension was added perturbatively. The select tip radius was assumed to be that of the marginally stable shape from the analysis. Although the procedure yields results that explain experimental data, no rigorous dynamical basis has been discovered for the marginal stability hypothesis.

Most recent analyses focus on the singular nature of the surface tension as a perturbation to the Ivantsov problem. In most capillary problems the surface tension is a singular perturbation only in that it is necessary only to satisfy the boundary conditions, because the surface tension multiplies the highest derivative terms of the interface shape variable in the Gibbs-Thomson equation. The Ivantsov solution is unique in that it already satisfies the condition of reflective symmetry at the cell tip. Based on the belief that solutions can therefore be obtained if the surface tension is introduced at the onset itself, researchers have employed non-perturbative methods to introduce the surface tension into simple *local* models of solidification that are valid at the interface. Here the fully non-local (two- or three-dimensional) continuum equations describing the transport of heat and solute are replaced by phenomenological laws describing the motion of the interface. These models are chosen so that they continue to have Ivantsov-like needle crystal solutions in the absence of surface tension. This general procedure has been shown to yield a solvability condition called the *microscopic solvability*[2] criterion because of the profound effect of the microscopically small value of the surface tension on the pattern of the dendrite.

Kessler and coworkers (Brower *et al.* 1984 and Kessler *et al.* 1984) used so-called *geometric* models where the evolution equation describing the interface is assumed to be impervious to temperature variations along the interface. An isotropic surface tension yielded no solutions but the equation could be solved with the introduction of a small but finite anisotropy. In general, the interface has a needle-like shape whose side approaches a straight line far from the tip.

Langer and coworkers (Ben-Jacob *et al.* 1983 and Langer 1986) devised local *boundary layer* models where the evolution equation is derived based on a heat balance within a boundary layer near the interface. This assumption, valid in the case of large undercoolings, yields a parabolic interface which allows tip-splitting in the absence of anisotropy and branching instabilities akin to the dendritic system with the addition of anisotropy.

Non-local models have been employed more recently by Caroli *et al.* (1986), who begin with the exact integro-differential equation that describes steady-state solutions to the two-dimensional one-sided model (thermal conduction in the solid is neglected). The equation is then expanded in powers of ${P_r}^{-1}$ for large Peclet numbers $P_r \gg 1$, which corresponds to large undercooling, and the equation for the interface is linearized around the Ivantsov result for non-zero surface tension. Pelcé & Pomeau (1986) and Ben-Amar & Moussalam (1987) consider the symmetric model (equal diffusivities in the two phases) in the limit of small undercooling. Kessler & Levine (1986a), Bensimon *et al.* (1987) and Saito *et al.* (1988) consider the quasi-steady approximation (valid only for small undercooling) to the one-sided model, which was also used by Mullins & Sekerka (1964).

The analysis of these models has been carried out using a variety of methods. Shraiman (1986), Langer (1986) and Caroli *et al.* (1986) used the WKB approximation to solve the resulting equations. Kessler *et al.* (1986a,1986b), Ben-Amar & Moussalam (1987), Tan-

---

[2] The term microscopic solvability was originally coined by Kessler & Levine for the solvability condition derived for the selection of steady-state fingers in viscous fingering but the name is more generally used now in connection with other fingered growth systems as well.

veer (1987) and Saito *et al.* (1988) among others have used numerical methods. Other methods employed include the power series method of Dashen *et al.* (1986) and the method of Kruskal & Segur (1987) originally devised for the geometric model where the integro-differential shape equation is replaced by a differential equation near the relevant singularity in the complex plane.

The solvability condition is obtained using either of two methods:
(i) Shraiman (1986) and Caroli *et al.* (1986) argue that the inhomogenous linear equation that results can only have solutions if the inhomogenous term is orthogonal to the null space of the homogeneous operator.
(ii) Langer (1986) and Karma (1986) (among others) invoke the symmetry condition at the tip. The equation resulting from the modeling is integrated from an asymptotic side-wall region towards the tip. This *shooting* method produces a solution only when the slope of the interface is zero at the cell tip.

Both types of local models give a solvability condition that the tip radius r and the growth rate V must satisfy for the existence of solutions. No solutions are found (or the solutions are unstable) in the absence of surface tension anisotropy. With a small but finite anisotropy a discrete tip velocity is selected. In general, these steady-state shapes remain close to the Ivantsov parabola.

The problem of selection of one of these steady-states has also been recently addressed from a stability standpoint. Based on the belief that the selection was connected to the dynamics of the steady-state, Bensimon *et al.* (1987), Kessler & Levine (1986a, 1986b) and Tanveer (1987) have looked at the stability of the discrete solutions. The all concur that the n-th solution possessed n unstable modes; the lowest order solution ($n = 0$) was the only linearly stable solution and was selected. This solution was the fastest moving and had the sharpest tip. The needle crystal was weakly stable against both tip-splitting and side-branch formation. Noise was assumed to trigger an oscillatory instability about the steady-state solution which causes side-branching (Kessler *et al.* 1988).

However, the findings are not unanimous; van Saarloos & Weeks (1985) believe that a continuous family of steady-state solutions could still exist. Using a simple modification of the boundary layer model of Ben-Jacob *et al.* (1983) they argue the existence of a continuous family of dendrites at large undercoolings. They believe that the simple truncations used in the local models cannot correctly describe the nature of the singularity in surface tension and argue for a more rigorous solution of the steady-state equations.

The procedures that have been applied to solve the selection puzzle in dendritic systems have been subsequently employed to solve the problems of viscous fingering and cellular solidification. A review of these works is presented below for each problem.

1.5.2.2 Selection of Patterns During Viscous Fingering

Immiscible displacement during flooding in porous media is usually simulated by experiments of multiphase fluid flow in a thin-film apparatus called the Hele-Shaw cell (Hele-Shaw 1898). A nonviscous fluid such as air displaces a more viscous fluid such as water in the narrow gap between two glass plates (Saffman & Taylor 1958). The viscous fluid is not displaced uniformly (in plug flow) under some conditions and the less viscous fluid grows into the more viscous fluid in the form of a finger (see Fig. 1.29). This problem is considered the hydrodynamic equivalent of dendritic solidification.

The flow in the Hele-Shaw cell is described by Darcy's law. For an incompressible fluid the pressure field in the viscous fluid satisfies the equation

$$\nabla^2\phi = 0 \quad , \tag{1.51}$$

where ϕ is a modified pressure field. The pressure field in the less viscous fluid is considered uniform (non-viscous fluid). Eq. (1.51) is solved along with the interfacial boundary condition of conservation of mass

$$[-\hat{\mathbf{n}} \cdot \nabla\phi = v_n]_{\text{interface}} \quad , \tag{1.52}$$

where v_n is the normal velocity of the interface. In addition, the pressure difference across the interface is related to the interfacial curvature $2\mathcal{H}$ through the surface tension $\tilde{\gamma}$ as

$$\phi = \tilde{\gamma}(2\mathcal{H}) \quad . \tag{1.53}$$

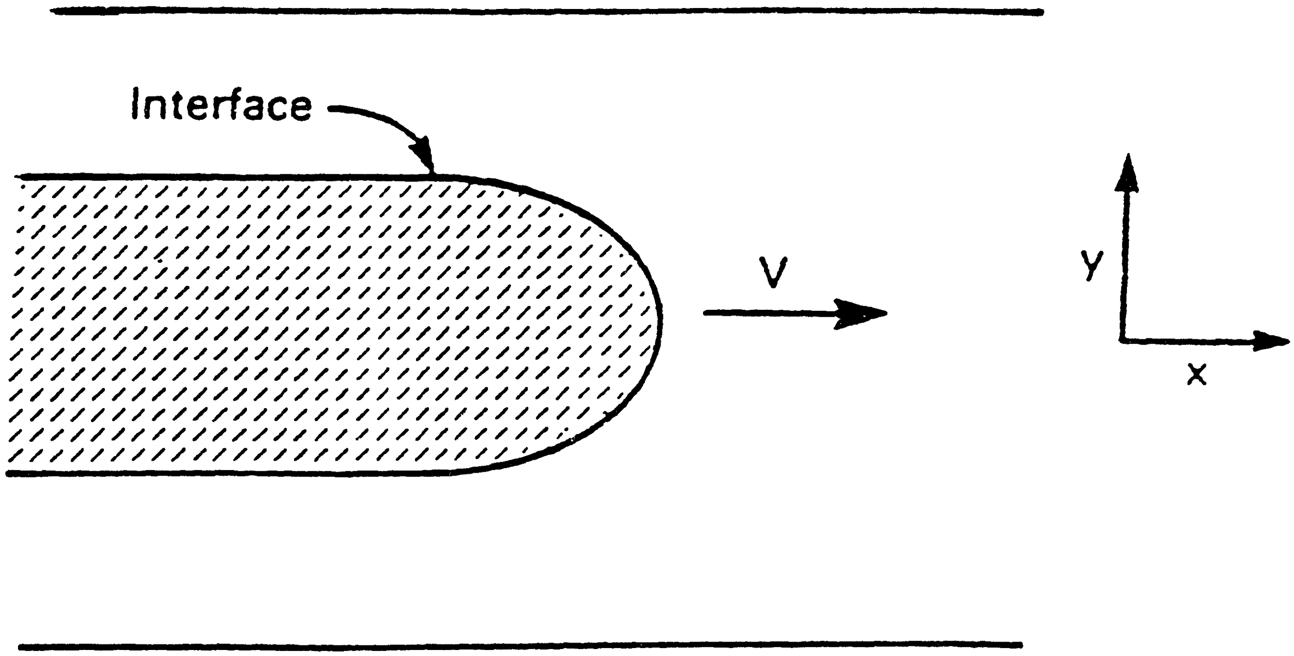

Figure 1.29: Schematic of the Geometry of the Saffman-Taylor problem of viscous fingering in a Hele-Shaw cell (from Kessler *et al.* 1988).

In the absence of surface tension this problem has a family of isobaric *Saffman-Taylor finger* solutions due to Saffman & Taylor (1958) in terms of a parameter λ defined as the ratio of the maximum finger thickness to the width of the Hele-Shaw cell. Experimentally, however, the finger width is a unique function of the surface tension and seems to approach the value $\lambda = \frac{1}{2}$ as $\tilde{\gamma}$ goes to zero. The stability analysis of the equations above indicates that the absence of selection in the theory is because the growth rate of possible perturbations with time is unbounded for $\tilde{\gamma} = 0$. It is believed that the problem is ill-posed in this limit (Kessler *et al.* 1988).

The steady-state width selection has since been studied by a number of researchers (McLean & Saffman 1981, Vanden-Broeck 1983, Kessler & Levine 1986a, Shraiman & Bensimon 1984). Perturbation methods do not work; the selection mechanism is absent to to all orders of perturbative corrections to the shape. Kruskal & Segur (1987), therefore, refer to their method as one that *goes beyond all orders*. Typically, one of the solution procedures reviewed in the previous subsubsection is applied to the defining equations (1.51)–(1.53) and the shooting method is applied to obtain a solvability condition for a finite surface tension $\tilde{\gamma}$; a solution exists when the magnitude of the cusp (the slope of the interface at the cell tip) is zero. A countably infinite number of discrete finger solutions is obtained, as represented in Fig. 1.30. Exactly as in the dendrite problem, only the first solution is found to be linearly stable.

1.5.2.3 Selection in Cellular Solidification

The analogy between the Saffman-Taylor problem and that of cellular solidification has been well-studied (Pelcé and Pumir 1985, Kessler & Levine 1986b, Mashaal *et al.* 1990). At low velocities, where a quasi steady-state approximation is valid, it is expected that the convection-like term in the field equations, which arises because of movement of the reference frame with the steady-state velocity, can be neglected. This leads to an equation set for directional solidification that resembles the Saffman-Taylor problem. Molho *et al.* (1990) conduct a similar comparison for dendritic growth in a rectangular capillary and try to estimate the velocities at which the solidification frame stops resembling the Saffman-

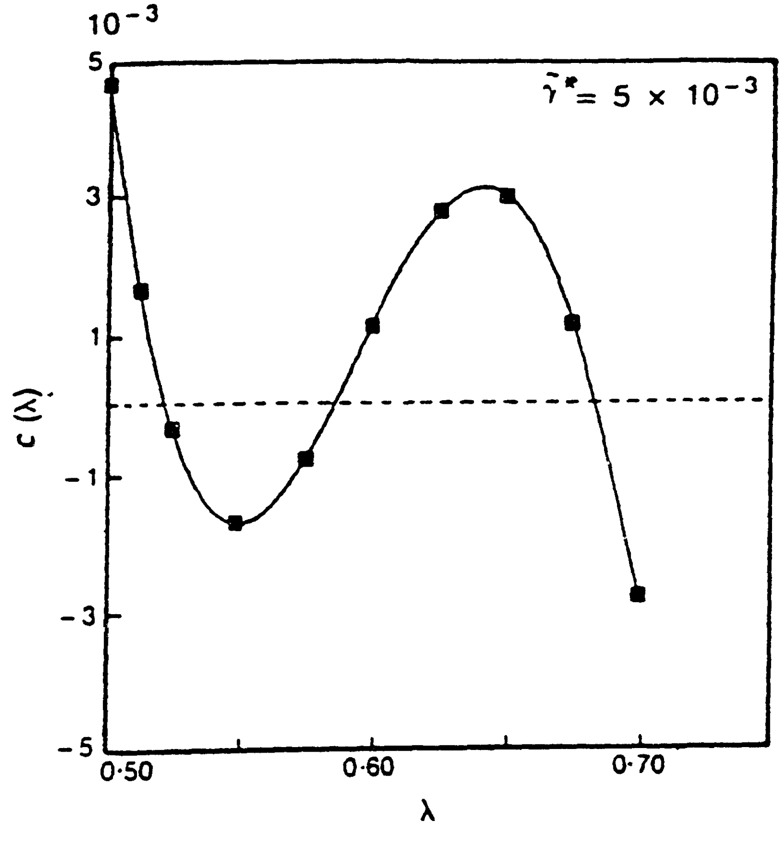

Figure 1.30: Variation of cusp magnitude c with relative finger width λ. Solutions exist when $c = 0$. (from Kessler *et al.* 1988)

Taylor finger and starts resembling the parabolic dendrite; they estimate that a Peclet number ($P_L = VL/\mathcal{D}$, where L is the largest transverse dimension of the channel) of $\mathcal{O}(1)$ represents the transition between these regimes. de Cheveigné *et al.* (1990) however find that comparisons of cell shapes with Saffman-Taylor profiles is not satisfactory.

Karma (1986) has tried to adapt the general approach used for dendritic solidification and viscous fingering for cellular solidification. Unfortunately, there is no zero-surface tension solution corresponding to the Ivantsov parabola or the Saffman-Taylor finger. Therefore, an asymptotic solution to the sidewall region of the groove is used to start the shooting method (Kessler & Levine 1988). Curvature (and hence the effect of surface tension) is neglected in this region. A perturbation expansion of the one-sided model equations for solute diffusion (diffusion in the solid is again neglected) in the limit of small segregation coefficient k yields the infinitely long slender region due to Scheil and Hunt (Hunt 1979) with cusp at an infinite distance

$$y + \frac{\mathcal{D}/V}{1-k} \sim x^{k-1} \tag{1.54}$$

where x is the distance from the center of the groove and y is the distance away from the cell tip. Karma (1986, 1987) has applied the solvability method to the above equations; the interface is computed by starting with the limiting solution far from the cell tip at $y = y_o$ and moving up towards the tip. Solutions exist when the shape satisfies the reflective symmetry condition at the cell tip. Using a Green's function formulation expanded in the limit of small Peclet numbers ($P = \lambda V/\mathcal{D}$, where λ is the cell spacing) Karma reports that surface tension is again necessary for solutions to exist. A single shape is selected at finite surface tension with a cell spacing that decreases as the growth rate is increased with the scaling $\tilde{\gamma} \propto V^{-0.5}$. Unlike the results for dendritic solidification, however, Karma finds that anisotropy of the surface tension is not necessary for selection; anisotropy only causes a shift in the cell spacing selected.

The results of this thesis (Chapter 3.5) will show that in fact selection of steady-states is not seen with such two-dimensional continuum models of cellular solidification; selection in Karma's work is possibly the result of some invalid assumption. First, as Kessler & Levine (1988) note correctly, any finite diffusivity would not allow an infinite cusp. In addition, the solution to the field equations in the above analysis shows that the concentration of solute increases linearly with distance from the tip. As the results of Chapter 3 will show, the solute diffuses away into the solid phase and the cusp closes at a finite distance. Furthermore, the assumption of small Peclet numbers (small growth rates) is suspect; the transition to deep cells in experiment happens at high growth rates. This again is borne out by the results of Chapter 3.

More recent studies agree with the numerical results of this thesis. For the same limit of small Peclet numbers, Dombre & Hakim (1987) show by analogy of the cell tip with the Saffman-Taylor finger that, in general, a continuous family of cells of varying wavelength should exist at any pull rate. This has also been confirmed by the numerical results of Ben-Amar & Moussallam (1988) who also argue that any reasonable steady-state model would yield a continuum of solutions and any selection mechanism is probably based on dynamic considerations. Karma & Pelcé (1986) performed a linear stability analysis of the one-sided model using the Green's function formulation in the small Peclet number limit and conclude that any perturbation to the position of the tip of a deep cell with a particular cell spacing will grow in an oscillatory way when the velocity exceeds a threshold value thus limiting the parameter range for which steady-state solidification can occur. This is not borne out by the calculations presented in this thesis (Chapter 3). It is likely that this is because the assumption of small Peclet numbers is invalid.

There are some fundamental differences between the cellular and dendritic solidification problems which probably cause the procedure for determining a selection criterion to fail in cellular solidification. First, in the analysis of dendritic solidification the domain is not limited in the direction perpendicular to growth. The analysis of Subsubsection 1.5.2.1 is for an individual dendrite in isolation; the effects of neighboring dendrites in a dendritic array on the temperature field are not considered. The effect of neighboring cells is an integral part of the formulation for cellular solidification; this effect is represented by the reflective symmetry boundary conditions along the center of the growing solid and the groove of the cell. In fact, even the selection mechanism for dendrites only selects the tip radius of an individual dendrite. There have been no satisfactory theoretical estimates yet of the primary spacing of dendrites. Warren & Langer (1990) address this problem. They argue that there is no reason to believe that there is any unique primary spacing at fixed growth conditions and that the selected state is probably dependent on the the sequence of events by which the system was set in motion. This is probably the case with cellular solidification as well. In addition, the zero-surface tension solution is approximate and does not satisfy the symmetry condition at the cell tip (unlike the Ivantsov and Saffman-taylor solutions).

In summary, the selection of cellular spacing in the experiments has not been explained satisfactorily. The possibilities for cellular selection are discussed below.

1.5.3 Possible Scenarios for Selection in Experimental System

Langer (1980) notes that wavelength selection in the experimental system may occur due to a variety of reasons. The following is a discussion of each of these possibilities and a look at how these effects can be modeled.

1. Selection via boundary conditions or introduction of other length scales.

A pattern may be selected so that its characteristic length scale is comparable to the length scales in the system. For example, the thermal-solutal model presented in Section 2.1 involves the effects of nine length scales. The wavelength of a selected pattern is probably dependent on one or more of these length-scales; the results of Chapter 3 based on the thermal-solutal model address this question. It is also possible that the wavelength is dependent on some length scale that is omitted in the modeling; this possibility is reviewed in Chapter 3.5.

It is conceivable that some experiment-related length scale may cause selection. For example, in the macroscale problem of breakup of jets of pure liquids, the most common length scale is the diameter of the nozzle. Saffman-Taylor viscous fingers seen in Hele-Shaw cells used to illustrate fluid flow in porous media have a wavelength that has been related to the distance between separating plates (McLean & Saffman 1981). However, it is unlikely that the distant boundaries in the solidification system play any role in selection. On the other hand, the smaller length-scale provided by the lateral distance between the two plates of a thin-film experimental system may cause selection. Most models do not take this lateral dimension into account. Caroli *et al.* (1986) address this issue for the morphological stability of weakly curved interfaces. Three-dimensional models which account for interface curvature in the plane perpendicular to the direction of cell growth are the only way of verifying this mechanism.

The analysis of Karma (1986) involves the addition of an extra length scale; this modification may be resulting in the selection mechanisms that they derive. In particular, the value of y_0 used to determine where the cusp region starts in Karma's model provides such a condition. This striking change which occurs on a seemingly minor alteration of the model for a deep cell leads us to believe that asymptotic analysis of the slender side-wall region of deep cells may provide better insight into the physics of the mechanism; the results of the asymptotic analysis are presented in Chapter 3.

2. Dynamic selection mechanism.

Selection is possible when out of a set of possible steady-states, only one of them is accessible from the initial experimental conditions. Nonlinear theory can be used to predict the fastest-growing wavelength but this does not compare well with the experimentally selected wavelength (de Cheveigné *et al.* 1986). It is hoped that a thorough stability analysis of the steady-state solutions will shed some light on any dynamic selection; time-dependent calculations presented in Chapter 3 address this possibility.

There is another, more complex case where dynamic selection is possible. This is when one cell interacts dynamically with one or more cells. Bennett (1988) has done a series of time-consuming computations for collections of shallow cells which show a myriad of possibilities including periodic and chaotic solutions, but no pattern selection was indicated. An added problem with the analysis for deep cells is the difficulty in finding a transformation which can be used to simulate an array of growing cells; the orthogonal curvilinear transformations of Tsiveriotis (1990) offer one solution. The number of equations to be solved to simulate a pool of even a few cells is large (in addition to the field variables of concentration and temperature and interface shape, the computations must simultaneously estimate the coordinate variables) and the sample size may have to be infinitely larger to simulate an "infinite" number of cells. Calculations such as these for deep cells have not been carried out.

3. Imposition of a variational or other condition.

Imposition of an extra condition on the system may be the cause of selection. It is possible, though unlikely, that the experimental system may operate to optimize some quantity, for example, the growth rate, the undercooling at the interface, or some thermodynamic quantity. Phenomenological models often incorporate such conditions; the low Peclet number limit in Karma's (1986) theory, the hypothesis of selection of the highest velocity among possible states by Nash & Glicksman (1971) and the marginal stability hypothesis of Langer & Müller-Krumbhaar (1978) might induce selection in the theoretical analysis through this mechanism. We do not believe that the first three assumptions have any physical basis to be studied further; the thermal-solutal model used in the computations presented in Chapter 3 incorporates the effect of anisotropy (see Section 2.1).

4. Noise-driven selection and other external mechanisms.

This is a possibility if all states indicated by stability theory are equally possible and the experiment selects based on unavoidable, external perturbations. There is no clear evidence that this is the case in directional solidification.

5. Selection caused by other physical effects

The thermal-solutal models that are generally employed to simulate transitions involving families of shallow cells are adequate to simulate similar transitions in deep cells as shown by the results of this thesis. Hence, there is no conclusive evidence that the modeling of deep cellular interfaces has to account for additional physical effects. However, it is possible that simple modifications of the commonly-used thermal-solutal model presented in Chapter 2 are necessary to accurately simulate the physics of deep cells in experimental systems; these modifications may provide a mechanism for wavelength selection. For example, it is possible that the small distance between the walls of the groove of deep cells results in surface effects of attraction or repulsion (Van der Waal's forces) that are not accounted for in the thermal-solutal models that are commonly employed. Fattinger *et al.* (1986) demonstrated that in dendritic growth, such forces affect the characteristics of the wetting of the interface with the wall in thin-film solidification and related the value of the critical spacing between the supporting plates for stable dendritic growth to the van der Waal's energy of the material.

6. No selection mechanism.

A final possibility is that there is in fact no pattern selection mechanism. This is believed to be true for shallow cells (Trivedi 1980, Karma 1986) but the wavelength of deep cells is believed to be selected. The volume of existing experimental evidence in the deep cellular regime is inadequate and the conclusion that deep cells are selected in experiments may indeed be erroneous.

Clearly, a better understanding of deep cellular interfaces is necessary to clarify the issues presented above. The extensive computations of deep cells presented in Chapters 3-5 are aimed at resolving these issues.

1.6 Thesis Outline

The review of previous research in the area of pattern formation in directional solidification that was presented in this chapter clearly shows the need for better understanding of the interfaces that are observed at conditions that are far from the planar-to-cellular transition. The onset of cellular solidification and the weakly nonlinear transitions of families of almost planar cells are well-characterized. The goal of this thesis is to fill the void in our understanding of large-amplitude interfaces. In particular, the evolution of deep cells, the question of wavelength selection and the transition to dendrites are addressed in the following chapters.

The mathematical models used in the calculations of deep cells in this thesis and the assumptions made in the development of these equations are described in Section 2.1. Numerical methods are necessary for the analysis of highly-deformed interfaces, as discussed in Section 1.4. The numerical techniques used for the calculations of deep cells are presented in Section 2.4.

Using these numerical methods, extensive computations are carried out for the solutal model to predict the transition from shallow cells to deep cells. These results of these calculations are presented in Chapter 3. The question of spatial wavelength selection of these interfaces is addressed and comparison of the numerical results with the experimental data for the CBr_4-Br_2 system is presented, in that chapter. Computations using the thermal-solutal model are described in Chapter 4; these calculations also focus on the evolution of deep cells and the question of wavelength selection of these patterns. An asymptotic analysis of the deep cell is performed using the solutal model, and is presented in Chapter 5. The results of the analysis are used to modify the numerical method to make possible the calculation of highly deformed interfaces with narrow grooves; these calculations are also presented in Chapter 5. Finally, the main conclusions of the thesis are summarized in Chapter 6.

Chapter 2

Modeling and Numerical Methods

This chapter describes the mathematical formulation of the free- and moving-boundary problems that are employed to model thin-film solidification of dilute binary alloys and the development of the numerical solution methods for the resulting equations. A general thermal-solutal model is developed in Section 2.1; the model accounts for the diffusion of solute and heat in the two phases solute segregation, freezing-point depression and the dependence of the melting point on the surface energy. The assumptions associated with this model are analyzed in Section 2.2. The results presented in Chapter 3 use either the thermal-solutal model or some simplification of it in which additional approximations have been made; commonly-used sub-models are discussed in Section 2.3. The equations describing these models are inherently nonlinear and numerical analysis of the problem is required to satisfactorily describe its solution. The numerical approximation used to solve these free- and moving-boundary problems is presented in Section 2.4; in essence, the unknown interface shape in the free- or moving-boundary problem is mapped to a fixed domain using a non-orthogonal transformation. The transformed equations are discretized using Galerkin finite element methods and the resulting set of nonlinear algebraic equations is solved by Newton's method to determine the field variables of temperature and concentration and the interface shape simultaneously.

2.1 Thermal-Solutal Model

As Mullins & Sekerka (1964) first demonstrated, models which include diffusion of heat and solute in the melt and solid, solute segregation at the interface between the two phases, freezing-point depression caused by the solute, and the dependence of the melting point on the surface energy through the curvature of the melt-solid interface capture the essence of one characteristic of microstructure formation in directional solidification - the onset of the instability of the planar interface. Such models have also been shown to simulate many of the other characteristics of directional solidification (Ungar 1984). Thermal-solutal models are continuum descriptions because the melt and solid are modeled as bulk phases and surface effects are only included as boundary conditions which treat the melt-solid interface as a Gibbs dividing surface (Woodruff 1973). This type of description assumes that the length scales for morphological instability are large enough so that local density variations in the bulk phases adjacent to the interface can be neglected. This assumption is valid since the patterns vary over tens of microns and density changes caused by the presence of the interface occur over a length scale of Angstroms.

The model equations at steady-state describe a free-boundary problem where the position of the interface has to be determined as part of the solution. The time-dependent model equations describe a moving-boundary problem where the solution similarly involves determination of the position of the interface shape as a function of time. In free- and moving-boundary problems, another boundary condition is required at the melt-solid interface to set its position, in addition to the boundary conditions along the interface that are necessary for the complete description of the differential equations for the field variables.

The equations for the thermal-solutal model are given below for a two-dimensional directional solidification system. The equations are presented in a coordinate frame fixed in space in which the melt is convected to the interface and solid is pulled away, both at the velocity of the interface V. Here the direction of solidification coincides with the y-coordinate direction. Corresponding equations for the three-dimensional system are available in McFadden *et al.* (1987).

2.1.1 Model Equations

Equations 2.1 - 2.20 define the thermal-solutal model (hereafter referred to as TSM). Written in dimensional form, the equations for the solute field in the melt and in the solid are

$$\begin{aligned} \frac{\partial \tilde{c}_m}{\partial \tilde{t}} &= \mathcal{D}_m \tilde{\nabla}^2 \tilde{c}_m + V \frac{\partial \tilde{c}_m}{\partial \tilde{y}} \quad , & (2.1) \\ \frac{\partial \tilde{c}_s}{\partial \tilde{t}} &= \mathcal{D}_s \tilde{\nabla}^2 \tilde{c}_s + V \frac{\partial \tilde{c}_s}{\partial \tilde{y}} \quad , & (2.2) \end{aligned}$$

where $\tilde{c}_m$ and $\tilde{c}_s$ are the concentrations of the solute in the melt and solid and $\mathcal{D}_m$ and $\mathcal{D}_s$ are the solute diffusivities in the melt and solid, respectively.

Similarly, the thermal field in the two phases is represented as

$$\begin{aligned} \frac{\partial \tilde{T}_m}{\partial \tilde{t}} &= \alpha_m \tilde{\nabla}^2 \tilde{T}_m + V \frac{\partial \tilde{T}_m}{\partial \tilde{y}} \quad , & (2.3) \\ \frac{\partial \tilde{T}_s}{\partial \tilde{t}} &= \alpha_s \tilde{\nabla}^2 \tilde{T}_s + V \frac{\partial \tilde{T}_s}{\partial \tilde{y}} \quad , & (2.4) \end{aligned}$$

where $\tilde{T}_m$ and $\tilde{T}_s$ are the temperature in the melt and solid and α_m and α_s are the thermal diffusivities in the melt and solid respectively.

Conservation of solute and heat are applied at the melt-solid interface:

$$\begin{aligned} \left[\hat{\mathbf{n}} \cdot \mathcal{D}_m \tilde{\nabla} \tilde{c}_m - \hat{\mathbf{n}} \cdot \mathcal{D}_s \tilde{\nabla} \tilde{c}_s = \left[\hat{\mathbf{n}} \cdot \hat{\mathbf{e}}_{(y)} \right] (1-k)\, c_m (V + V_e) \right]_{\text{interface}} \quad , & \quad (2.5) \\ \left[\hat{\mathbf{n}} \cdot \kappa_m \tilde{\nabla} \tilde{T}_m - \hat{\mathbf{n}} \cdot \kappa_s \tilde{\nabla} \tilde{T}_s = \left[\hat{\mathbf{n}} \cdot \hat{\mathbf{e}}_{(y)} \right] L (V + V_e) \right]_{\text{interface}} \quad , & \quad (2.6) \end{aligned}$$

where V_e is the vertical component of the dimensional interfacial velocity in excess of the growth rate V. Here k is the segregation coefficient, L is the latent heat of solidification, κ_m and κ_s are the thermal conductivities in the melt and solid respectively, and $\hat{\mathbf{n}}$ and $\hat{\mathbf{e}}_{(y)}$ are the unit outward normal and the unit vector in the direction of growth, respectively. Eq. (2.5) assumes local thermodynamic equilibrium at the melt-solid interface given by

$$[\tilde{c}_s = k \tilde{c}_m]_{\text{interface}} \quad , \qquad (2.7)$$

and thermal equilibrium at the interface is given by

$$\left[\tilde{T}_s = \tilde{T}_m \right]_{\text{interface}} \quad . \qquad (2.8)$$

The effect of concentration and curvature on the melting temperature of the interface is represented by the Gibbs-Thomson equation:

$$\left[\tilde{T} = \tilde{T}_o + \tilde{m}\tilde{c}_m + \tilde{\Gamma}\tilde{T}_o(2\tilde{\mathcal{H}})\right]_{\text{interface}} \quad . \tag{2.9}$$

In Eq. (2.9) $\tilde{T}_o$ is the melting point of the pure material at a planar interface, $\tilde{m}$ is the linearized liquidus slope, $\tilde{\mathcal{H}}$ is the mean curvature of the interface and $\tilde{\Gamma}$ is the capillary length, which is given as

$$\tilde{\Gamma} = \tilde{\Gamma}_o[1 - \epsilon_a \cos(4\theta)] \quad , \tag{2.10}$$

where $\tilde{\Gamma}_o$ is the isotropic capillary length and ϵ_a is the anisotropy in the capillary length. Away from the interface, the boundary conditions for the solute field in the melt and solid are

$$\lim_{\tilde{y}\to\infty} \tilde{c}_m \;\rightarrow\; c_\infty \quad , \tag{2.11}$$

$$\lim_{\tilde{y}\to-\infty} \tilde{c}_s \;\rightarrow\; c_\infty \quad , \tag{2.12}$$

where c_∞ is the bulk concentration of the solute. Eqs. (2.11) and (2.12) are both essential boundary conditions; the equation set for the concentration field is hence well-posed. It should be noted that as the concentration reaches the bulk value far field into the melt and solid, the concentration gradient in the y-direction simultaneously goes to zero. Thus equally appropriate boundary conditions on the far field solute concentration in the two phases are

$$\lim_{\tilde{y}\to\infty} \frac{\partial \tilde{c}_m}{\partial \tilde{y}} \;\rightarrow\; 0 \quad , \tag{2.13}$$

$$\lim_{\tilde{y}\to-\infty} \frac{\partial \tilde{c}_s}{\partial \tilde{y}} \;\rightarrow\; 0 \quad . \tag{2.14}$$

Using both Eqs. (2.13) and (2.14) results in natural boundary conditions everywhere along the boundary and the concentration field can be estimated only to an arbitrary constant.

The results of this thesis have been obtained using a combination of these boundary conditions. The concentration in the solid is forced to approach the bulk value far into the solid, but a mixed boundary condition is used far field in the melt; the boundary conditions used are

$$\lim_{\tilde{y}\to\infty} \left[\mathcal{D}_m \frac{\partial \tilde{c}_m}{\partial \tilde{y}} + V c_m\right] \;\rightarrow\; P \quad , \tag{2.15}$$

$$\lim_{\tilde{y}\to-\infty} \tilde{c}_s \;\rightarrow\; c_\infty \quad . \tag{2.16}$$

Equation 2.15 represents a mass balance in the melt far from the melt-solid interface where the concentration field should be invariant in the x-direction. Eq. (2.15) is clearly valid in the melt far from the interface; the solution to the one-dimensional version of the field equation (2.1) yields Eq. (2.15). The added advantage of using this equation is related to its application in the numerical procedure as described below. Eq. (2.15) is valid anywhere ahead of the interface where lateral concentration variation across the cell is zero and the concentration field is one-dimensional. As the computations of Chapters 3 and 4 will show, the variation in solute concentration across the domain in the x-direction often becomes negligible not far ahead of the interface. Eq. (2.15) can then be applied in the numerical procedure at a short distance from the interface; this reduces the size of the computational domain and, therefore, increases the accuracy of the computations for the same effort.

The conditions on the thermal field far from the interface are

$$\lim_{\tilde{y}\to\infty} \frac{\partial \tilde{T}_m}{\partial \tilde{y}} \rightarrow \tilde{G}_m \quad , \tag{2.17}$$

$$\lim_{\tilde{y}\to-\infty} \frac{\partial \tilde{T}_s}{\partial \tilde{y}} \rightarrow \tilde{G}_s \quad , \tag{2.18}$$

where $\tilde{G}_m$ and $\tilde{G}_s$ are temperature gradients far away from the interface in the melt and solid, respectively. However, the gradients cannot be independently specified at steady state as they are related according to

$$\kappa_m \tilde{G}_m - \kappa_s \tilde{G}_s = LV \quad . \tag{2.19}$$

This condition is simply an overall heat balance across the domain, assuming that no heat is lost through lateral boundaries. The condition that far from the interface in the solid the temperature in the solid is uniform across the cell is employed instead:

$$\lim_{\tilde{y}\to-\infty} \frac{\partial \tilde{T}}{\partial \tilde{x}} \rightarrow 0 \quad . \tag{2.20}$$

This condition states that temperature variations in the lateral direction are smoothed out by diffusion far from the cell. Condition (2.20) is actually implemented in the numerical method by setting the temperature to a constant at all points along a cross-section of the domain that is at a finite distance from the bottom of the cell. This distance is carefully chosen so that the error in the approximation is not large as discussed in Section 2.4.

However, the value of the temperature at this boundary is unknown. Hence, a new variable $\hat{T}$ is defined as

$$\hat{T} = \tilde{T} - \tilde{T}_b \tag{2.21}$$

where $\tilde{T}_b$ is the unknown temperature at the boundary of the computational domain and Equations (2.1)–(2.9) are rewritten in terms of $\hat{T}$. Since $\tilde{T}_b$ is a constant, the form the equations involving the temperature remain unchanged.

The computational domain considered here is $0 \leq \tilde{x} \leq \tilde{\lambda}/2$, where λ is the wavelength of the cell. Thus only cells with wavelength $\tilde{\lambda}$ or some integral fraction of this wavelength are allowed. Symmetry conditions are applied on the concentration and temperature fields in both phases and the interface shape at the lateral boundaries $\tilde{x} = 0$ and $\tilde{x} = \tilde{\lambda}/2$:

$$\left[\frac{\partial \tilde{c}_{m,s}}{\partial \tilde{x}} = 0\right]_{\tilde{x}=0,\tilde{\lambda}/2} \quad , \tag{2.22}$$

$$\left[\frac{\partial \tilde{T}_{m,s}}{\partial \tilde{x}} = 0\right]_{\tilde{x}=0,\tilde{\lambda}/2} \quad , \tag{2.23}$$

and

$$\left[\frac{\partial \tilde{h}}{\partial \tilde{x}} = 0\right]_{\tilde{x}=0,\tilde{\lambda}/2} \quad . \tag{2.24}$$

The equation set (2.1) - (2.24) above can be non-dimensionalized using a length scale $\tilde{\lambda}_{\text{ref}}$. Thus non-dimensional lengths are defined as

$$x = \frac{\tilde{x}}{\tilde{\lambda}_{\text{ref}}}; \quad y = \frac{\tilde{y}}{\tilde{\lambda}_{\text{ref}}}; \quad \text{and} \quad \lambda = \frac{\tilde{\lambda}}{\tilde{\lambda}_{\text{ref}}} \tag{2.25}$$

Scaling time with the diffusion time $\tau_d \equiv (\tilde{\lambda}_{\text{ref}})^2/\mathcal{D}_m$, temperatures with the melting temperature of pure solvent $\tilde{T}_o$, and concentrations with the bulk concentration of the alloy c_∞. Equations Eq. (2.1) - Eq. (2.20) are rewritten in dimensionless form as

$$\frac{\partial c_m}{\partial t} = \nabla^2 c_m + P\frac{\partial c_m}{\partial y} \quad , \tag{2.26}$$

$$\frac{\partial c_s}{\partial t} = R_m \nabla^2 c_s + P\frac{\partial c_s}{\partial y} \quad , \tag{2.27}$$

$$Le\frac{\partial T_m}{\partial t} = \nabla^2 T_m + P_t\frac{\partial T_m}{\partial y} \quad , \tag{2.28}$$

$$Le\frac{\partial T_s}{\partial t} = R\nabla^2 T_s + P_t\frac{\partial T_s}{\partial y} \quad , \tag{2.29}$$

$$\left[\hat{\mathbf{n}}\cdot\nabla c_m - R_m\,\hat{\mathbf{n}}\cdot\nabla c_s \;=\; \left(\hat{\mathbf{n}}\cdot\hat{\mathbf{e}}_{(y)}\right)(1-k)\,c_m\,(P+P_e)\right]_{\text{interface}} \quad , \tag{2.30}$$

$$\left[\hat{\mathbf{n}}\cdot\nabla T_m - R\,\hat{\mathbf{n}}\cdot\nabla T_s \;=\; \left(\hat{\mathbf{n}}\cdot\hat{\mathbf{e}}_{(y)}\right) St\,(P_t + LeP_e)\right]_{\text{interface}} \quad , \tag{2.31}$$

where P_e is the vertical component of the dimensionless interfacial velocity in excess of the dimensionless growth rate P. Also,

$$[c_s = kc_m]_{\text{interface}} \quad , \tag{2.32}$$

$$[T_s = T_m]_{\text{interface}} \quad , \tag{2.33}$$

$$[T = 1 + mc_m + (2\mathcal{H})\Gamma]_{\text{interface}} \quad , \tag{2.34}$$

$$\Gamma \equiv \Gamma_o[1 - \epsilon_a\cos(4\theta)] \quad , \tag{2.35}$$

$$\lim_{y\to\infty}\left[\frac{\partial c_m}{\partial y} + Pc_m\right] \;\to\; P \quad \text{, and} \tag{2.36}$$

$$\lim_{y\to-\infty} c_s \;\to\; 1 \quad , \tag{2.37}$$

$$\lim_{y\to\infty}\frac{\partial T_m}{\partial y} \;\to\; G_m \quad \text{, and} \tag{2.38}$$

$$\lim_{y\to-\infty}\frac{\partial T_m}{\partial x} \;\to\; 0 \quad . \tag{2.39}$$

For shallow cells the interface can be represented by the simple Mongé Cartesian representation $y = h(x,t)$ (Ungar 1984) where the mean curvature $\tilde{\mathcal{H}}$, in Eq. (2.9) is written as

$$2\tilde{\mathcal{H}} = \frac{\partial^2 h/\partial x^2}{\left[1 + (\partial h/\partial x)^2\right]^{3/2}} \quad ; \tag{2.40}$$

see Fig. 2.1. Using this representation, the gradient operator takes the form

$$\nabla = \hat{\mathbf{e}}_x\frac{\partial}{\partial x} + \hat{\mathbf{e}}_y\frac{\partial}{\partial y} \quad . \tag{2.41}$$

The outward pointing unit normal vector $\hat{\mathbf{n}}$ in Eqs. 2.5 and 2.6 is given by

$$\hat{\mathbf{n}} = \frac{\hat{\mathbf{e}}_y - h_x\hat{\mathbf{e}}_x}{(1 + h_x^2)^{1/2}} \quad , \tag{2.42}$$

where $\hat{\mathbf{e}}_{\mathbf{x}}$ and $\hat{\mathbf{e}}_{\mathbf{y}}$ are the unit vectors in the x and y coordinate directions, respectively, and $h_x \equiv \partial h/\partial x$.

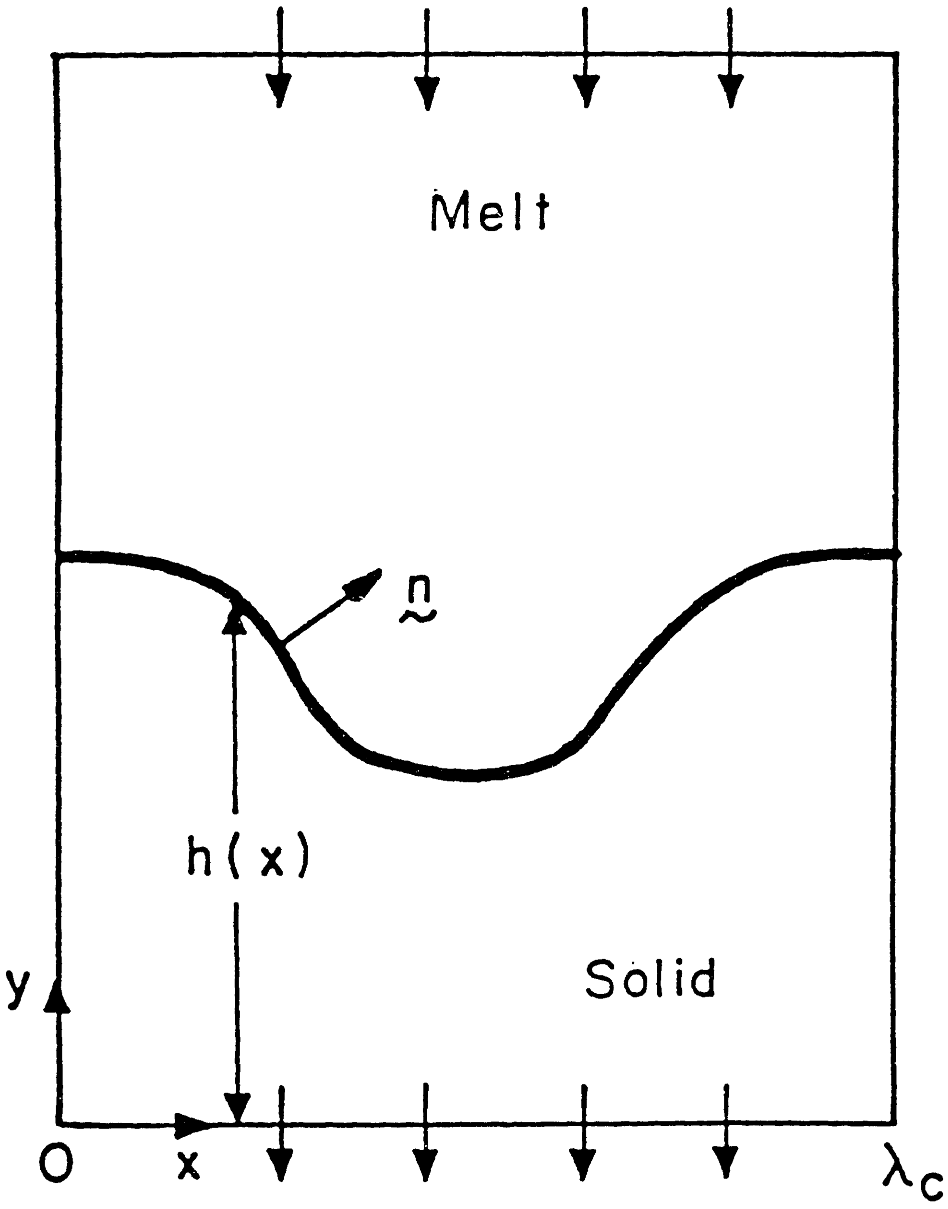

Figure 2.1: Schematic of the melt and solid regions considered in the models of directional solidification for shallow cells. The single-valued function $y = h(x,t)$ is used to represent the melt-solid interface. From Ungar *et al.* (1988).

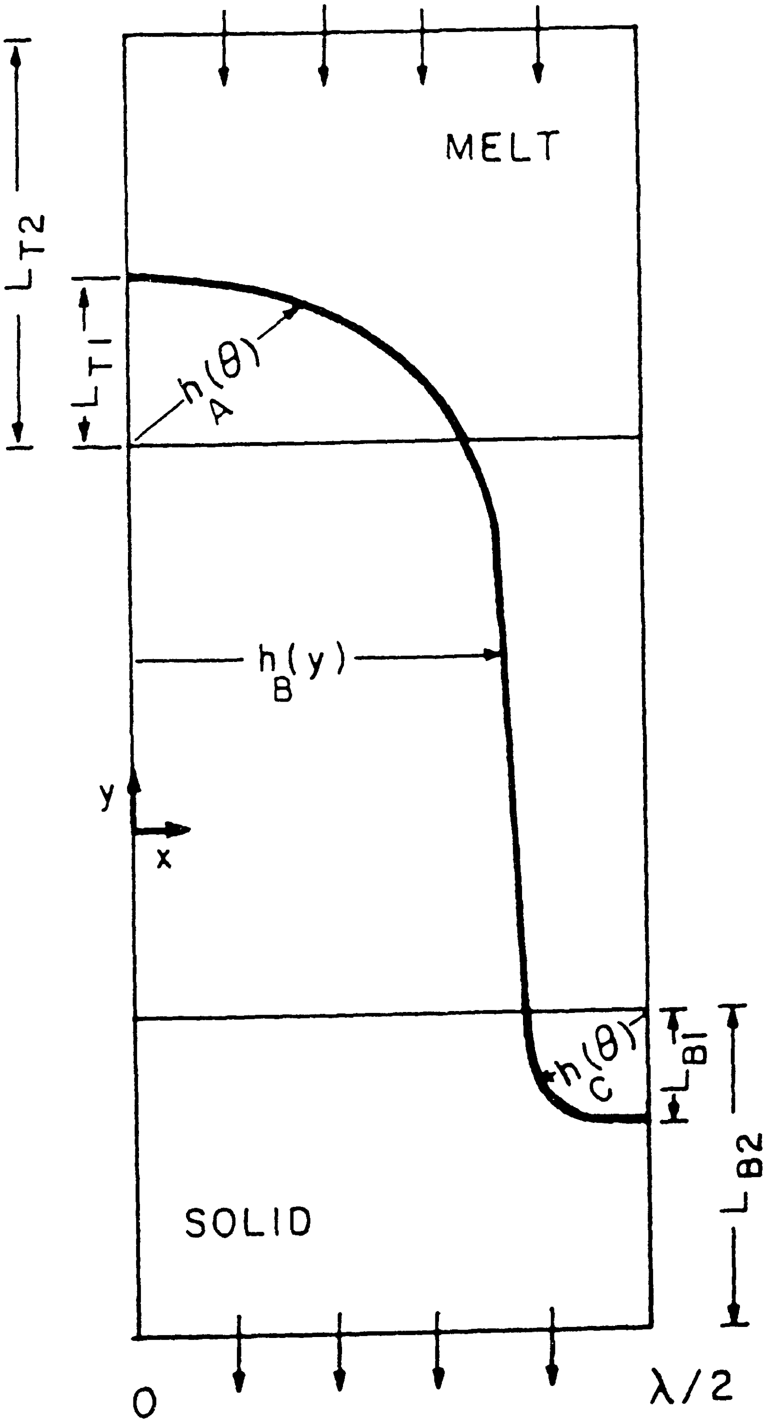

Figure 2.2: Schematic of the melt and solid regions considered in the models of directional solidification. A mixed coordinate system is used to represent the melt-solid interface in deep cells. From Ungar *et al.* (1988).

For deep cells, the Mongé representation fails since the reentrant grooves of such structures in this representation result in a multivalued function $h(x,t)$. For deep cells a mixed coordinate system developed by Ungar & Brown (1985) is employed; see Fig. 2.2. The melt and solid are divided into two cylindrical (A,C) regions and one Cartesian (B) region, where the cylindrical regions represent the tip and bottom of the cell and the rectangular region approximates the sidewall of the groove. In the two parts of the domain represented by cylindrical coordinates, the mean curvature, the gradient operator and the unit normal are

$$2\mathcal{H} = \frac{1}{\left[h^2 + {h_\theta}^2\right]^{1/2}} - \frac{1}{h}\frac{\partial}{\partial \theta}\left[\frac{h_\theta}{(h^2 + h_\theta^2)^{1/2}}\right] \quad , \tag{2.43}$$

$$\nabla = \hat{\mathbf{e}}_r \frac{\partial}{\partial r} + \left(\frac{1}{r}\right)\hat{\mathbf{e}}_\theta \frac{\partial}{\partial \theta} \quad , \tag{2.44}$$

$$\hat{\mathbf{n}} = \frac{h\hat{\mathbf{e}}_r - h_\theta \hat{\mathbf{e}}_\theta}{(h^2 + h_\theta^2)} \quad , \tag{2.45}$$

where $h = h(\theta, t)$ in regions A and C is the shape function for either the tip or bottom of the cell and the subscript θ denotes differentiation, i.e., $h_\theta \equiv \partial h/\partial \theta$. The unit basis vectors in the radial and azimuthal directions are $\hat{\mathbf{e}}_\mathbf{r}$ and $\hat{\mathbf{e}}_\theta$, respectively.

In the Cartesian part of the domain (B) $x = h(y,t)$, the mean curvature, the gradient operator and the unit normal are expressed as

$$2\tilde{\mathcal{H}} \equiv \frac{h_{yy}}{\left[1 + h_y^2\right]^{3/2}} \quad , \tag{2.46}$$

$$\nabla \equiv \hat{\mathbf{e}}_x \frac{\partial}{\partial x} + \hat{\mathbf{e}}_y \frac{\partial}{\partial y} \quad , \tag{2.47}$$

$$\hat{\mathbf{n}} \equiv \frac{\hat{\mathbf{e}}_x + h_y \hat{\mathbf{e}}_y}{\left(1 + h_y^2\right)^{1/2}} \quad , \tag{2.48}$$

where $h(y,t)$ is the single-valued function which represents the interface in region B and $\hat{\mathbf{e}}_\mathbf{x}$ and $\hat{\mathbf{e}}_\mathbf{y}$ again are the unit vectors in the x and y coordinate directions and $h_y \equiv \mathrm{d}h/\mathrm{d}y$.

As can be seen from Eqs. (2.26) - (2.34) the TSM is characterized by twelve dimensionless groups: $G_m \equiv \tilde{G}_m \tilde{\lambda}_{\mathrm{ref}}/\tilde{T}_o$, the dimensionless far field temperature gradient in the melt; $G_s \equiv \tilde{G}_s \tilde{\lambda}_{\mathrm{ref}}/\tilde{T}_o$, the dimensionless far field temperature gradient in the solid; k, the equilibrium partition coefficient; $m \equiv \tilde{m}c_\infty/\tilde{T}_o$, the dimensionless slope of the liquidus line; the Lewis number $Le \equiv \mathcal{D}_m/\alpha_m$, the ratio of the rates of solutal to thermal diffusion in the melt; the solutal Peclet number $P \equiv \tilde{\lambda}_{\mathrm{ref}} V/\mathcal{D}_m$, which scales solutal diffusive transport relative to the uniaxial convection of solute in the melt and solid; the thermal Peclet number $P_t \equiv \tilde{\lambda}_{ref}V/\alpha_m$, which scales thermal diffusive transport relative to the uniaxial convection of heat in the melt and solid; $R \equiv \alpha_s/\alpha_m$, ratio of thermal diffusivity in the solid to that in the melt; $R_m \equiv \mathcal{D}_s/\mathcal{D}_m$, ratio of solutal diffusivity in the solid to that in the melt; the Stefan number $St \equiv L/\rho c_p \tilde{T}_o$, ratio of the latent heat released along the interface to the sensible heat in the melt at the melting point; the capillary constant $\Gamma_o \equiv \tilde{\Gamma}_o/\tilde{\lambda}_{ref}$, the dimensionless form of isotropic surface free energy; and ϵ_a the anisotropy in the capillary length. It should be noted that the thermal Peclet number is the product of the solutal Peclet number and the Lewis number and the temperature gradients in the melt and solid are related by Eq. (2.19). Hence there are only ten independent dimensionless groups and ten independent natural length scales can be derived from the model. One choice of these length scales is the following: the four diffusive length scales $\mathcal{D}_m/V$, $\mathcal{D}_s/V$, α_m/V, α_s/V, two capillary length scales $\tilde{\Gamma}_o$ and $\epsilon_a\tilde{\Gamma}_o$, the two length scales based on the far field thermal conditions, $\tilde{T}_o/\tilde{G}_m$ and $\tilde{T}_o/\tilde{G}_s$, two length scales based on the concentration gradients, $\tilde{m}c_\infty/\tilde{G}_m$ and $k\tilde{m}c_\infty/\tilde{G}_m$. The length scale of the patterns that form during solidification are expected to be related to these lengths.

As described in Section 1.5, the smallest of these length scales is the capillary length and this length scale is considered paramount in determining the complexity of the patterns that form during directional solidification. Eq. (2.9) shows that the Gibbs-Thomson equation indicates that the melt-solid interface of a solid surrounded by melt ($2\tilde{\mathcal{H}} < 0$) will have a melting temperature lower than that of a flat interface and that the interface of a melt surrounded by solid ($2\tilde{\mathcal{H}} > 0$) will have a higher melting point than that of a flat interface. The capillary term of the Gibbs-Thomson equation (2.9) thus has a stabilizing effect. Clearly, the bottoms of the grooves between cells ($2\tilde{\mathcal{H}} > 0$) will have higher melting temperatures than they would have had without capillarity effects, and their position will be shifted up (in the y-direction) towards higher temperatures. Thus capillarity tends to shorten the lengths of cells. The smaller the wavelength of the cells the larger is the magnitude of the dimensionless capillary length ($\Gamma \equiv \tilde{\Gamma}/\lambda$) and hence the effect of capillarity is larger. This effect is responsible for the left boundary of the neutral stability diagram; see Fig. 1.14.

2.2 Assumptions Involved in the Formulation of the TSM

The formulation of the thermal-solutal model involves a few important assumptions; these are discussed below.

2.2.1 Negligible Convection

The convective terms in the TSM equations are a result of using the reference frame which moves with the steady-state growth rate V. The model neglects true convection which would result if there is an appreciable density change on solidification. A more elaborate model would include the equation for the conservation of momentum and the continuity equations (Ungar 1984):

$$\begin{aligned} \frac{Dv}{Dt} &= -\nabla p/\rho_o + [1 - \alpha(T - T_o) + \beta(c - c_o)]g + \nu \nabla^2 v \quad , & (2.49) \\ \nabla \cdot v &= 0 \quad , & (2.50) \end{aligned}$$

where the substantial derivative $\frac{D}{Dt}$ is defined as $\frac{\partial}{\partial t} + v \cdot \nabla$; ρ, ν, g and v represent density, kinematic viscosity, gravitational acceleration and mass average flow velocity. In the above Boussinesq equation, density has been assumed to be of the form

$$\rho = \rho_o[1 + \alpha(T - T_o) + \beta(c - c_o)] \tag{2.51}$$

in the expression for buoyancy. Other material properties are assumed to be constant. The only fluid motion relative to the interface is due to solidification. If the density change on solidification is neglected the fluid velocity must approach the average interface velocity v_i at the interface and there will be a region close to the interface where the flow is essentially at this velocity in both phases. We can assume a boundary layer of thickness δ where the velocity changes linearly from the interfacial value v_i to the bulk value v_b. If this boundary layer thickness is much larger than the scale of the morphological instability the bulk fluid flow and morphological stability are decoupled. Typically, fluid flow in a solidifying melt occurs with a characteristic scale about four orders-of-magnitude larger than that of the morphological stability. The assumption of negligible convection is thus valid.

The wide difference in these length scales also makes it impractical to do full numerical simulation of models which include both phenomena and these effects have only been examined by linear stability analyses. Coriell *et al.* (1980), Caroli *et al.* (1985a, 1985b) and McFadden *et al.* (1988) conducted linear stability analysis of systems with both morphological and convective instabilities. They concur that the characteristic scales of the two phenomena are disparate and the coupling of these phenomena at the onset of morphological instability is weak. They conclude that both phenomena are important for a small range of growth parameters far from onset of morphological instability where the unstable modes of the the phenomena are comparable.

As pointed out in Section 1.3, the thin-film solidification configuration is particularly indifferent to convective instabilities. In addition, using neutrally buoyant latex particles in these systems de Cheveigné *et al.* (1986) and Somboonsuk *et al.* (1984) observed no signs of convection. Thus comparison of the results with the TSM with thin-film experiments should be valid.

2.2.2 Equilibrium

The TSM assumes that the interface is near equilibrium, i.e., that the kinetics of interfacial phase change are very rapid compared to transport rates of solute and heat. The equilibrium assumption enters the model through the equilibrium segregation coefficient k, the liquidus slope m, which are both derived from the equilibrium phase diagram and the equlibrium melting temperature. The model assumes constant values for these properties, independent of growth rate; the variation of these parameters with growth conditions is discussed in the next Section 2.2.3. These constants are derived from a linearized version of the phase diagram for dilute alloys (near the solvent-rich end); see Fig. 1.12. The concentration of the solute in the melt c_m and the solid c_s at an interface which is at a temperature T_I is given by the equations for the liquidus and solidus lines

$$T_I = T_o + mc_m \quad , \tag{2.52}$$

$$T_I = T_o + m_s c_s \quad , \tag{2.53}$$

where m and m_s are the slopes of the liquidus and solidus lines, respectively. The concentrations in the two phases are related from Eqs. (2.52) and (2.53) by

$$\begin{aligned} c_s &= \left(\frac{m}{m_s}\right) c_m \quad , & (2.54) \\ &= k c_m \quad . & (2.55) \end{aligned}$$

The equilibrium partition coefficient is defined as

$$k \equiv \frac{c_s}{c_m} \quad . \tag{2.56}$$

Boettinger (1982) describes more general forms of Eqs. (2.7) and (2.9) which account for deviations from equilibrium as:

$$[\tilde{c}_s = k\ \tilde{c}_m g(V, \tilde{c}_m)]_{\text{interface}} \quad , \tag{2.57}$$

and

$$\left[\tilde{T} = \tilde{T}_o + \tilde{m}\tilde{c}_m + \tilde{T}_o\tilde{\Gamma}(2\tilde{\mathcal{H}}) - f(V, \tilde{c}_m)\right]_{\text{interface}} \quad , \tag{2.58}$$

where the function $f(V, \tilde{c}_m)$ is the kinetic undercooling. In the absence of solidification the function has a limiting equilibrium value of zero. The function $f(V, \tilde{c}_m)$ is found to vary approximately linearly with the growth velocity in experiments resulting in undercoolings of $0.1 - 1.0K$ degrees at growth velocities of the order of 1 cm/sec. Given that the solidification velocities in thin-film experiments are typically 3–4 orders-of-magnitude less, the effect of this kinetic undercooling can be safely neglected.

The function $g(V, \tilde{c}_m)$ has a limiting value of 1.0 in the absence of solidification corresponding to perfect equilibrium. For very large velocities this function has the limiting form (Boettinger 1982)

$$\lim_{V \to \infty} k\,\tilde{c}_m g(V, \tilde{c}_m) \to 1 \quad . \tag{2.59}$$

Here, the solute in the melt is entirely incorporated into the solid. This function is found experimentally to scale with $V\,l/\mathcal{D}_m$, where l is some characteristic length scale of the melt adjacent to the interface. For the low velocities of growth seen in our system this effect is again negligible.

2.2.3 Effects of Concentration, Temperature and Curvature

Variation of the thermophysical properties with concentration, temperature and curvature have been neglected. The dimensional properties $\mathcal{D}_m$, $\mathcal{D}_s$, α_m, α_s, L, $\tilde{m}$, $\tilde{\Gamma}$ are all assumed to be constants in the model. Simulations and experiments are usually carried out with small imposed temperature gradients; in addition, the size of the computational domain (and sample) are so small that the overall temperature variation of of the order of $10K$ degrees. The effect of temperature can thus be neglected.

The maximum concentration seen over the entire system in the simulations of Chapter 3 is of the order of c_∞/k. For typical segregation coefficients the maximum concentration would thus be an order-of-magnitude higher than the bulk value. If the bulk material is not dilute enough, this change in concentration could make the assumption of linear liquidus and solidus lines (and hence constant k) invalid. However, for the systems that have been studied in this thesis the bulk concentrations are of the order of 1 mole% and the assumption is valid.

The segregation coefficient is known to depend on the curvature of the interface and pressure (Flemings 1974); However, the precise effect of these parameters is unknown.

2.3 The Solutal Model and Other Simple Versions of the TSM

Analytical study of the complete thermal-solutal model is difficult because of the many disparate length and time scales and the large number of parameters that are included. In addition, for numerical simulation it is useful to have simplified models which reduce the number of unknown variables and, hence, reduce the cost of computation. Many simplified versions of the TSM have been derived; this section describes the salient features of the more widely-used versions.

2.3.1 The Solutal Model

The Solutal Modei (SM) assumes that the sample has an imposed linear temperature field which is independent of the solidification process. This approximation is the result of two assumptions: (i) equal thermal conductivities in the two phases ($R = 1$) and (ii) high thermal diffusivities in the two phases ($P_t \ll 1$, $Le \ll 1$). It should be noted that the second assumption automatically makes the effect of latent heat release also negligible ($P_t St \ll 1$). The Equations (2.28), (2.29) and (2.31) are approximated as

$$\begin{aligned} \nabla^2 T_m &= 0 \quad , && (2.60)\\ \nabla^2 T_s &= 0 \quad , && (2.61)\\ \Big[\nabla T_s &= \nabla T_m\Big]_{\text{interface}} \quad . && (2.62) \end{aligned}$$

The solution to this set of equations is simply

$$T(y) = T_{\text{ref}} + G_m\, y \quad , \tag{2.63}$$

where $G = G_m = G_s$ is a constant and the interface is positioned in the domain by setting the value of T_{ref}, a reference temperature.

The thermal and solutal equations are thus decoupled and the solutal model equations is rewritten in dimensionless form as

$$\begin{aligned} \frac{\partial c_m}{\partial t} &= \nabla^2 c_m + P\frac{\partial c_m}{\partial y} \quad , && (2.64)\\ \frac{\partial c_s}{\partial t} &= R_m \nabla^2 c_s + P\frac{\partial c_s}{\partial y} \quad , && (2.65) \end{aligned}$$

$$\left[\hat{\mathbf{n}}\cdot\nabla c_m - R_m\,\hat{\mathbf{n}}\cdot\nabla c_s = \left(\hat{\mathbf{n}}\cdot\hat{\mathbf{e}}_{(y)}\right)(1-k)c_m\left(P+\frac{\partial h}{\partial t}\right)\right]_{\text{interface}} \quad , \tag{2.66}$$

$$[c_s = k c_m]_{\text{interface}} \quad , \tag{2.67}$$

and

$$[T_{\text{ref}} + G\,y = 1 + m\,c_m + \Gamma(2\mathcal{H})]_{\text{interface}} \quad , \tag{2.68}$$

where anisotropy is incorporated into the capillary length Γ as

$$\Gamma = \Gamma_o[1 - \epsilon_a \cos(4\theta)] \quad , \tag{2.69}$$

along with

$$\lim_{y \to \infty} \left[\frac{\partial c_m}{\partial y} + P c_m \right] \rightarrow P \quad \text{, and} \tag{2.70}$$

$$\lim_{y \to -\infty} c_s \rightarrow 1 \quad . \tag{2.71}$$

The solutal model is characterized by seven dimensionless groups: $G_m \equiv \tilde{G}_m \tilde{\lambda}_{\text{ref}} / \tilde{T}_o$, the dimensionless far field temperature gradient in the melt; k, the equilibrium partition coefficient; $m \equiv \tilde{m} c_\infty / \tilde{T}_o$, the dimensionless slope of the liquidus line; the solutal Peclet number $P \equiv \tilde{\lambda}_{\text{ref}} V / \mathcal{D}_m$, which scales solutal diffusive transport relative to the uniaxial convection of solute in the melt and solid; $R_m \equiv \mathcal{D}_s / \mathcal{D}_m$, ratio of solutal diffusivity in the solid to that in the melt; the capillary constant $\Gamma_o \equiv \tilde{\Gamma}_o / \tilde{\lambda}_{\text{ref}}$, the dimensionless form of isotropic surface free energy; and ϵ_a the anisotropy in the capillary length. Seven independent length scales can be derived from the SM. One choice of these length scales is the following: the two diffusive length scales $\mathcal{D}_m / V$, $\mathcal{D}_s / V$, two capillary length scales $\tilde{\Gamma}_o$ and $\epsilon_a \tilde{\Gamma}_o$, the length scales based on the far field thermal conditions, $\tilde{T}_o / \tilde{G}_m$, and two length scales based on the concentration gradients, $\tilde{m} c_\infty / \tilde{G}_m$ and $k \tilde{m} c_\infty / \tilde{G}_m$. The length scale of the patterns that are predicted by the solutal model are expected to be related to these lengths.

The computational effort involved in solving the solutal model is approximately half of that involved in the TSM; the solutal model has therefore been widely used (Ungar 1984, Bennett 1990, Karma 1986, Langer 1980). Results for both the TSM and SM are presented in this thesis.

2.3.2 Other Models

Other simplifications that have been used are the one-sided TSM (Mullins & Sekerka 1964) and the one-sided SM (Hunt 1979, Ungar & Brown 1985) where diffusivity of solute in the solid is neglected. Neglecting solid diffusivity causes the solute conservation equation in the solid to become hyperbolic (Ungar 1984) and the numerical solution is considerably more complicated. However, researchers typically do not solve the equations in the solid phase; it is just assumed that the concentration in the solid at any point is exactly equal to the concentration of the solid at a point on the interface exactly upstream of the desired point.

In the Cartesian representation this is

$$c_s(x^*, y) = c_m\left[x^*, y = h(x^*)\right] \quad . \tag{2.72}$$

However, when the grooves of the cells start folding over, as shown in Fig. 1.21, the one-sided model is invalid. In this model the value of the concentrations at points A and B on Fig. 1.21 would be independently computed. However, the concentrations of solute in the melt at these two points ought to be the same since the solid is convected down from point A to point B before melting. Thus a two-sided model (with a small diffusion coefficient in the solid) is essential for the calculation of reentrant cells. Several researchers have noted that the results of the one-sided model cannot be obtained by setting $R_m \ll 1$ in the two-sided model (Nadarajah 1988, Kessler *et al.* 1989) since the $R_m = 0$ is a singular limit of the two-sided model. While this is obviously true for reentrant cells, Ungar & Brown (1985) showed that for shallow cells the results with the one-sided model and the two-sided model (with small solid diffusivity) were very close and the one-sided model was thus applicable. However, the results of Chapter 3 have been obtained using two-sided versions of the TSM and SM.

2.4 Numerical Methods

Linear stability analyses and weakly-nonlinear analysis of the models presented in the previous section have proved inadequate in explaining the complex behavior of the solidifying interface far from onset of the morphological instability. This is due to the complex nonlinear structure of the solutions. Nonlinear equations can rarely be solved analytically except in asymptotic limits of some parameter or about a known solution. These solutions, such as those discussed in Chapter 3, though useful for analysis of solution behavior in certain parameter ranges, have limited applicability. Numerical methods capable of solving these equations are therefore essential.

The free- and moving-boundary problem presented in the previous section is rewritten using a nonorthogonal transformation which is presented in Section 2.4.1. The finite element method that is used to discretize these equations is briefly described in the Section 2.4.2 and the solution of the resulting algebraic equation set by Newton's method is described in Section 2.4.5. Finally, the formulation for the time-dependent equations is discussed in Section 2.4.6.

The equations for the thermal-solutal model are rewritten here for convenience:

$$\frac{\partial c_m}{\partial t} = \nabla^2 c_m + P\frac{\partial c_m}{\partial y} \quad , \tag{2.73}$$

$$\frac{\partial c_s}{\partial t} = R_m \nabla^2 c_s + P\frac{\partial c_s}{\partial y} \quad , \tag{2.74}$$

$$Le\frac{\partial T_m}{\partial t} = \nabla^2 T_m + P_t\frac{\partial T_m}{\partial y} \quad , \tag{2.75}$$

$$Le\frac{\partial T_s}{\partial t} = R\nabla^2 T_s + P_t\frac{\partial T_s}{\partial y} \quad , \tag{2.76}$$

$$\left[\hat{\mathbf{n}}\cdot\nabla c_m - R_m\,\hat{\mathbf{n}}\cdot\nabla c_s = (1-k)\,c_m\left(P+\frac{\partial h}{\partial t}\right)\right]_{\text{interface}} \quad , \tag{2.77}$$

$$\left[\hat{\mathbf{n}}\cdot\nabla T_m - R\,\hat{\mathbf{n}}\cdot\nabla T_s = St\left(P_t + Le\frac{\partial h}{\partial t}\right)\right]_{\text{interface}} \quad , \tag{2.78}$$

$$[c_s = kc_m]_{\text{interface}} \quad , \tag{2.79}$$

and

$$[T = 1 + mc_m + \Gamma(2\mathcal{H})]_{\text{interface}} \quad , \tag{2.80}$$

where

$$\Gamma = \Gamma_o[1 - \epsilon_a \cos(4\theta)] \quad , \tag{2.81}$$

with

$$\lim_{y\to\infty} \left[\frac{\partial c_m}{\partial y} + Pc_m\right] \quad \to \quad P \quad , \quad \text{and} \tag{2.82}$$

$$\lim_{y\to-\infty} c_s \quad \to \quad 1 \quad , \tag{2.83}$$

and

$$\lim_{y\to\infty} \frac{\partial T_m}{\partial y} \quad \to \quad G_m \quad , \quad \text{and} \tag{2.84}$$

$$\lim_{y\to-\infty} \frac{\partial T_m}{\partial x} \quad \to \quad 0 \quad . \tag{2.85}$$

2.4.1 Mapping

The unknown melt-solid interface for the deep cell given by the mixed cylindrical-Cartesian mapping presented in Section 2.1 is projected to a fixed coordinate surface using a non-orthogonal coordinate transformation as described by Ungar (1984). In this formulation, similar to that of Ettouney & Brown (1983), the added complexity of the transformed equation set is counterbalanced by the alleviating the need for updating the mesh during the iteration scheme. The non-orthogonal transformation is shown in Fig. 2.3.

The computational domain is reduced to the region $0 \leq x \leq \lambda/2$ because only cells with wavelength λ are considered. Conditions of reflective symmetry are imposed at $x = 0$ and $x = \lambda/2$ in both phases for the field variables of concentration and temperature and the interface shape:

$$\left[\frac{\partial c_m}{\partial x} = 0\right]_{x=0,\lambda/2} \quad , \tag{2.86}$$

$$\left[\frac{\partial c_s}{\partial x} = 0\right]_{x=0,\lambda/2} \quad , \tag{2.87}$$

and

$$\left[\frac{\partial T_m}{\partial x} = 0\right]_{x=0,\lambda/2} \quad , \tag{2.88}$$

$$\left[\frac{\partial T_s}{\partial x} = 0\right]_{x=0,\lambda/2} \quad , \tag{2.89}$$

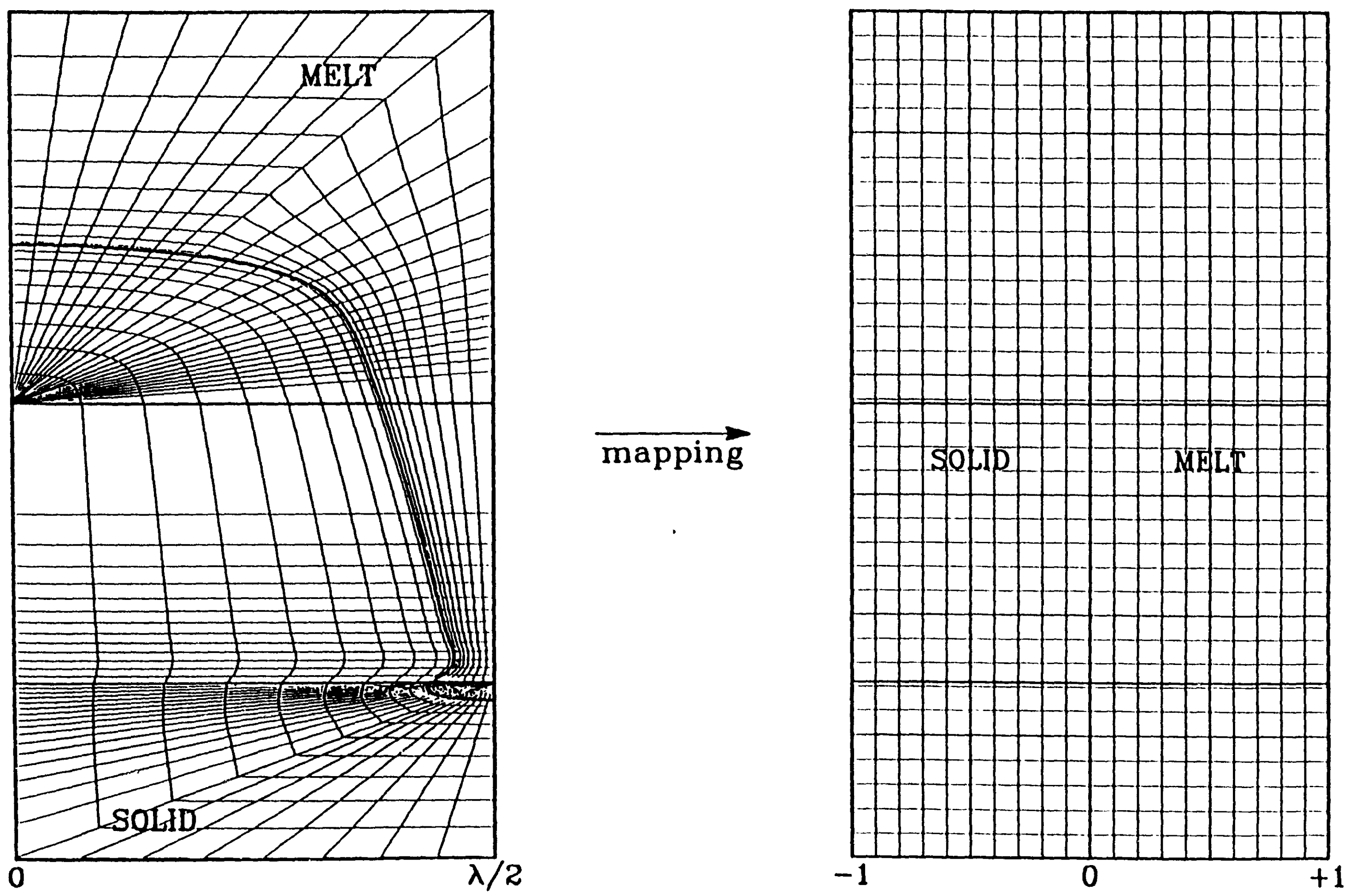

Figure 2.3: Schematic of the melt and solid regions considered in the models of directional solidification. A mixed coordinate system is used to represent the melt-solid interface in deep cells.

with

$$\left[\frac{\partial h}{\partial x} = 0\right]_{x=0,\lambda/2} \quad . \tag{2.90}$$

In addition, the mapping is constructed so that the top of the Cartesian region B is held at a fixed distance L_{T1} below the tip of the cell and the bottom of region B is held at a fixed distance L_{B1} above the bottom of the cell. The length of the sidewall region is determined as part of the solution. The Cartesian region elongates as the cell deepens so that arbitrarily deep cells can be calculated using the mapping.

The far field boundary conditions at the inlet where the melt flows in and the outlet where the solid is pulled out are applied at fixed distances L_{T2} and L_{B2} from the origins of the cylindrical coordinates. These distances are carefully chosen (significantly greater than the characteristic length of the dominating physical phenomena in these regions) so that boundary conditions applied at these limits of the computational domain do not influence conditions at the melt-solid interface.

In this formulation, the solid and melt domains in the three regions are projected to fixed domains in the transformed coordinates ξ and η as defined below.

Region A:

$$\text{solid}: -1 \le \xi \le 0 \quad \text{and} \quad 0 \le \eta \le 1$$
$$\text{melt}: 0 \le \xi \le 1 \quad \text{and} \quad 0 \le \eta \le 1$$

Region B:

$$\text{solid}: -1 \le \xi \le 0 \quad \text{and} \quad -1 \le \eta \le 0$$
$$\text{melt}: 0 \le \xi \le 1 \quad \text{and} \quad -1 \le \eta \le 0$$

Region C:

$$\text{solid}: -1 \le \xi \le 0 \quad \text{and} \quad -2 \le \eta \le -1$$
$$\text{melt}: 0 \le \xi \le 1 \quad \text{and} \quad -2 \le \eta \le -1$$

The free-boundary is projected to the coordinate surface $\xi = 0$. The transformations used to obtain the above projections are listed below. Separate transformations are used for the two phases.

Region A

Solid : $\xi \equiv \frac{r-h}{h} \qquad \eta \equiv \frac{2\theta}{\pi}$

Melt : $\xi \equiv \frac{r-h}{L_{T2}/\sin\theta - h}\,, \quad \eta \equiv \frac{2\theta}{\pi}$ in A1

$\xi \equiv \frac{r-h}{\lambda/2\cos\theta - h}\,, \quad \eta \equiv \frac{2\theta}{\pi}$ in A2

Region B

Solid : $\xi \equiv \frac{x-h}{h}\,, \quad \eta \equiv \frac{y-Y_t}{Y_t-Y_b}$

Melt : $\xi \equiv \frac{x-h}{\lambda/2-h}\,, \quad \eta \equiv \frac{y-Y_t}{Y_t-Y_b}$

where Y_t and Y_b are the y-coordinates of the origins of the cylindrical regions at the top and bottom.

Region C

Solid : $\xi \equiv \frac{h-r}{-\lambda/(2\cos\theta)-h}\,, \quad \eta \equiv 1 - \frac{2\theta}{\pi}$ in C1

$\xi \equiv \frac{h-r}{-L_{B2}/\sin\theta - h}\,, \quad \eta \equiv 1 - \frac{2\theta}{\pi}$ in C2

Melt : $\xi \equiv \frac{h-r}{h}\,, \qquad \eta \equiv 1 - \frac{2\theta}{\pi}$

The equation set (2.73)–(2.85) can be rewritten in terms of the transformed variables ξ and η using the relations above. In the transformed equation set, the interface shape does not set the shape of the computational domain and $h(x,t)$ reduces to a conventional nonlinear independent variable.

2.4.2 The Finite Element Method

The partial differential equations resulting from the analysis of the previous section are solved using the Galerkin finite element method (Strang & Fix 1972, Burnett 1987). The finite element method (FEM) is a numerical procedure for the solution of differential equations where the the domain is discretized into subregions or elements which allow for computationally efficient solution of the equations on computers.

In the FEM, the unknown function $u(x,t)$ is approximated by a trial solution $u_t(x,t)$ which is the sum of a weighted series of polynomial functions called trial or basis functions thus:

$$u(x,t) \approx u_t(x,t) = \sum_{i=1}^{N} \alpha_i(t)\phi_i(x) \quad , \tag{2.91}$$

where the weights or coefficients of these functions $\alpha_i(t)$ are to be determined. This representation is not unlike the Fourier series representation of a function in terms of basis functions (sines or cosines) except that finite element bases are simple algebraic functions which are zero outside of some local area (usually the area of the element) and that only a finite number of terms N of the series (equal to the number of elements) are retained. As the number N increases the error in approximating the function $u(x)$ decreases; as N approaches infinity the truncation error vanishes. Usually, quadratic polynomials are used as basis functions because of their simplicity and ability to approximate steep gradients (Strang & Fix 1973). Since the basis functions are local, a given basis function will only overlap with a few other basis functions (those that are in the vicinity). This characteristic of the finite element method is often referred to as compact support (Derby 1986) and allows for simple implementation on a computer.

The conditions used to determine the coefficients α_i are based on the differential equation and the boundary conditions; the procedure involves the optimization of some criterion which forces the trial function $u_t(x,t)$ to approximate the function $u(x,t)$. Most early finite element techniques used the Rayleigh-Ritz method where the optimization criterion is determined from the equations and boundary conditions using the calculus of variations (Finlayson 1972). The work of this thesis uses the method of weighted residuals which is more popular due to its universal applicability - this method can be applied even for problems where no variational principle exists (Finlayson 1972).

To illustrate this technique, we consider the steady-state two-dimensional solute transport equation in a domain D:

$$\nabla^2 c + P\frac{\partial c}{\partial y} = 0 \quad , \tag{2.92}$$

where $c(x,z)$ represents the solute concentration and P is the Peclet number that accounts for convection in the z-direction. The unknown function $c(z)$ is approximated as in Eq. (2.91)

$$c(z) \approx c_t(z) = \sum_{i=1}^{N} \alpha_i \phi_i(x,z) \quad , \tag{2.93}$$

where $c_t(x,z)$ is the trial solution. The basis functions $\{\alpha_i\}$ are determined by minimizing the *residual* $R(x,z)$ which is written as

$$R = \nabla^2 c_t + P\frac{\partial c_t}{\partial z} \quad . \tag{2.94}$$

If the trial solution is equal to the exact solution then the residual is exactly zero; thus, R represents the approximation error that results when $c_t \neq c$. The residual in Eq. (2.94) is multiplied by a set on N weighting functions $\{W_i(x,z)\}$ and integrated over the domain D; the resulting set of N *residual equations*

$$R_i = \int_D W_i \left[\nabla^2 \left\{ \sum_{i=1}^{N} \alpha_i \phi_i(x,z) \right\} + P\frac{\partial}{\partial y} \left\{ \sum_{i=1}^{N} \alpha_i \phi_i(x,z) \right\} \right] dA = 0 \quad , \; i = 1 \; , \; \ldots \; , \; N \quad , \tag{2.95}$$

are solved for the $\{\alpha_i\}$. Here dA is the differential area of the domain.

It is necessary that the weights $\{W_i\}$ are linearly independent so that the residual equations Eq. (2.95) are linearly independent. In this case the residual converges to zero in the mean and the trial solution approaches the exact solution (Strang & Fix 1972):

$$\lim_{n \to \infty} ||R(x,z)|| \; = \; 0 \quad , \tag{2.96}$$

$$\lim_{n \to \infty} ||c_t(x,z)|| \; = \; c(x,z) \quad . \tag{2.97}$$

The Galerkin FEM differs from other weighted residual methods in that the weights W_i are the same as basis functions: $W_i = \phi_i$. The main advantage of the Galerkin method is that for equations where a variational principle exists, the solution agrees exactly with the solution for the Rayleigh-Ritz formulation. Thus the method yields the optimal solution as derived from the variational principle. In addition, Galerkin's method can be applied to a larger class of problems. Furthermore, the Galerkin FEM has been shown to be consistently accurate for the same degree of computational effort when compared to other weighted residual methods (Burnett 1987).

The basis functions $\{\phi_i\}$ have to be chosen so that they have the continuity required by the partial differential equations. For example, the second-order terms in the field equation

Eq. (2.92) for mass transfer require that the trial functions be C^1 continuous, i.e. both the function and its first derivative should be continuous over the domain. However, the highest order derivatives in the residual equations are usually lowered by application of Green's theorem (Spiegel 1988) so that the simplest possible trial functions may be used. Integrals over the two-dimensional domain D are reduced to line integrals along the boundary ∂D of the domain:

$$\begin{aligned} \int\!\!\int \left[-\nabla\phi_i \cdot \nabla \left\{ \sum_{i=1}^{N} \alpha_i \phi_i(x,z) \right\} \right. &+ \left. P\ \phi_i \frac{\partial}{\partial z} \left\{ \sum_{i=1}^{N} \alpha_i \phi_i(x,z) \right\} \right] dA \\ &+ \int \phi \ \left[\hat{n} \cdot \nabla \left\{ \sum_{i=1}^{N} \alpha_i \phi_i(x,z) \right\} \right] ds = 0 \quad , \quad (2.98) \end{aligned}$$

where ds is the differential element along the boundary of the domain. The integral along the boundary, $\int \phi \ \left(\hat{n} \cdot \nabla \left[\sum_{i=1}^{N} \alpha_i \phi_i(x,z) \right] \right) ds$ is determined by applying the boundary conditions. The trial function in the *weak form* of the residual equations given in Eq. (2.98) have to be only C^0 continuous.

The algebraic equations represented by the equation set (2.98) are solved on a computer for the unknown weights $\{\alpha_i\}$ and the function $c(x,z)$ is determined from Eq. (2.93).

2.4.3 Finite Element Formulation

The finite element formulation follows that of Ettouney & Brown (1983). The field variables of concentration and temperature and the interface shape are all approximated using finite element discretizations and Galerkin's method is used to reduce the problem to a set of nonlinear algebraic equations. Ettouney & Brown examined applying either the Gibbs-Thomson isotherm condition along the equilibrium melt-solid interface or the interfacial energy balance as the *distinguished condition* for determining the interface shape at each iteration in the numerical algorithm. Calculations using the isotherm condition as the distinguished condition led to interface shapes computed to the same degree of accuracy as the field variable. Using the interfacial energy balance as the distinguished condition produced results of lesser accuracy. The larger error in the use of energy balance condition arises from the inaccuracies in the direct calculation of the normal derivative from the finite element approximations of the field variable at the interface; Lynch & Sullivan (1985) show that the use of self-consistent normal derivatives computed from the Galerkin residual equations at the interface eliminates these inaccuracies. The isotherm method has since been used successfully for accurate solution of a variety of solidification problems (Chang & Brown 1983, Derby 1986, Bennett 1990) and is the method of choice in this thesis.

Following Ungar (1984), the discontinuity in the concentration at the interface caused by the equilibrium segregation condition is accounted for by defining a new concentration variable $C(x, y)$ as

$$C(x,y) = \begin{cases} c_m(x,y,t) , & \forall (x,y) \in D_m \quad , \\ c_s(x,y,t)/k , & \forall (x,y) \in D_s \quad , \end{cases} \tag{2.99}$$

where k is the segregation coefficient and D_m and D_s are the melt and solid portions of the computational domain respectively. The temperature fields T_m and T_s in the two phases are also combined into a single variable $T(x, y, t)$. The new variables $C(x, y, t)$ and $T(x, y. t)$ are continuous over the entire computational domain (both phases) and are represented by standard finite element approximations.

The modified concentration field represented by Eq. (2.99) and the combined temperature field are represented in quadratic two-dimensional quadrilateral serendipity element bases $\Phi^i(\xi, \eta)$ and $\Xi^i(\xi, \eta)$ respectively (Burnett 1987). The interface shape is represented in Lagrangian quadratic finite element bases $\Psi^i(\xi)$. These representations are written as

$$C(\xi,\eta,t) = \sum_{i=1}^{N} a_i(t)\; \Phi^i(\xi,\eta) \quad , \tag{2.100}$$

$$T(\xi,\eta,t) = \sum_{i=1}^{N} b_i(t)\; \Xi^i(\xi,\eta) \quad , \tag{2.101}$$

$$h(\xi,t) = \sum_{i=1}^{M} c_i(t)\; \Psi^i(\xi) \quad , \tag{2.102}$$

where N and M are the number of coefficients in the corresponding expansion and (ξ, η) are the transformed coordinates defined by the mappings in Section 2.4.1. The coefficients $a_i(t)$, $b_i(t)$, and $c_i(t)$ are to be determined by the solution of the residual equations presented below.

2.4.4 The Residual Equations

The field equations for the solute concentration, Eqs. (2.73) and (2.74) and the interfacial solute balance equation Eq. (2.77) and the boundary conditions along the edge of the domain are combined to form a set of Galerkin weighted residual equations. On each domain, Eq. (2.73) or Eq. (2.74) is multiplied by the basis functions and integrated over the original domain. The weak form of the solute conservation equation is formed by summing these equations as

$$\begin{aligned} R_{1,i} \equiv & \int_{D_m} \Phi^i \frac{\partial C}{\partial t} dA + k \int_{D_s} \Phi^i \frac{\partial C}{\partial t} dA \\ & - P \int_{D_m} \Phi^i \frac{\partial C}{\partial y} dA - k P \int_{D_s} \Phi^i \frac{\partial C}{\partial y} dA \\ & + \int_{D_m} \nabla \Phi^i \cdot \nabla C \, dA + k R_m \int_{D_s} \nabla \Phi^i \cdot \nabla C \, dA \\ & - \int_{\partial D_m} \Phi^i (\hat{\mathbf{n}} \cdot \nabla C) \, dS - k R_m \int_{\partial D_s} \Phi^i (\hat{\mathbf{n}} \cdot \nabla C) \, dS \\ & + \int_{\partial D_i} \Phi^i \left(\hat{\mathbf{n}} \cdot \hat{\mathbf{e}}_{(y)} \right) (k-1) C \left(P + \frac{\partial h}{\partial t} \right) dS \quad , \end{aligned} \tag{2.103}$$

where dA is the differential area element of the domain, dS is the differential line element along the melt-solid interface, ∂D_i is the interface boundary, ∂D_m is the boundary of the melt not in contact with the solid, and ∂D_s is the boundary of the solid not in contact with the solid. The last five terms in Eq. (2.103) come from the application of Green's theorem to the Laplacian operator. The last term of Eq. (2.103) comes from the application of the natural boundary condition of the solute balance at the interface, Eq. (2.77), as an unconstrained boundary condition. Terms which arise at the boundaries $x = 0$ and $x = \lambda/2$ are set to zero following the application of the symmetry boundary condition

$$\left[\frac{\partial C}{\partial x} = 0 \right]_{x=0,\lambda/2} \quad . \tag{2.104}$$

The temperature field equations Eq. (2.75) and Eq. (2.76) in the two phases and the interfacial energy balance equation Eq. (2.78) and the boundary conditions along the edge of the domain are similarly combined to form another set of Galerkin residual equations

$$\begin{aligned} R_{2,i} \equiv & \int_{D_m} \Xi^i \frac{\partial T}{\partial t} dA + \int_{D_s} \Xi^i \frac{\partial T}{\partial t} dA \\ & - P_t \int_{D_m} \Xi^i \frac{\partial T}{\partial y} dA - P_t \int_{D_s} \Xi^i \frac{\partial T}{\partial y} dA \end{aligned}$$

$$
\begin{aligned}
&+ \int_{D_m} \nabla \Xi^i \cdot \nabla T \, dA \; + \; R \int_{D_s} \nabla \Xi^i \cdot \nabla T \, dA \\
&- \int_{\partial D_m} \Xi^i (\hat{\mathbf{n}} \cdot \nabla T) \, dS \; - \; R \int_{\partial D_s} \Xi^i (\hat{\mathbf{n}} \cdot \nabla T) \, dS \\
&+ \int_{\partial D_i} \Xi^i \left(\hat{\mathbf{n}} \cdot \hat{\mathbf{e}}_{(y)} \right) St \left(P + Le \frac{\partial h}{\partial t} \right) dS \quad , \qquad (2.105)
\end{aligned}
$$

where the reflective symmetry boundary condition

$$
\left[\frac{\partial T}{\partial x} = 0 \right]_{x=0,\lambda/2} \quad , \qquad (2.106)
$$

has been applied to eliminate terms that arise at the boundary $x = 0$ and $x = \lambda/2$. The term $\frac{\partial C}{\partial t}$ is transformed to the (ξ, η, τ) nonorthogonal coordinate system as

$$
\frac{\partial C}{\partial t} = \frac{\partial C}{\partial \tau} + \frac{\partial C}{\partial \eta} \frac{\partial \eta}{\partial t} \quad . \qquad (2.107)
$$

The contribution from the $\frac{\partial \eta}{\partial t}$ term which should be added to the mass matrix entries shown in Eq. (2.115), have been neglected, as in Ungar (1984), Ungar & Brown (1985), and Ungar *et al.* (1988). It is expected that the neglected terms will not significantly affect the results of the stability and dynamic behavior presented in Chapter 3, but could be significant in the simulation of the transition regime between deep cells and protodendrites; however, this has not been checked by calculations with these terms included.

The nonorthogonal mapping derived in Section 2.4.1 is applied on the weak form of the weighted residual equations Eqs. (2.103)–(2.105). Then the shape functions describing the melt-solid interface appear explicitly throughout the equation set, but not in the limits of the integration. The two-dimensional integrals are evaluated by nine-point Gaussian quadrature and the one-dimensional integrals are evaluated by three-point Gaussian quadrature defined on an isoparametric element (Burnett 1987).

Using the new concentration variable (2.99) and the combined temperature field, the weak form of the weighted residual equations for the Gibbs-Thomson relation, Eq. (2.80), is given by

$$
R_{3,i} \equiv \int_{\partial D_I} \left\{ \Psi^i [1 + mC - T] - \Gamma \frac{\partial \Psi^i}{\partial x} \frac{\partial h_B}{\partial y} \left[1 + \left(\frac{\partial h_B}{\partial y} \right)^2 \right]^{-1/2} \right\} dy \qquad (2.108)
$$

in the Cartesian region B, and by

$$
R_{3,i} \;\equiv\; \int_{\partial D_I} \left[\Psi^i \left\{ (1 + mC - T) h_{A,C} - \Gamma h_{A,C} \left[h^2 + \left(\frac{\partial h}{\partial \theta} \right)^2 \right]^{-1/2} \right\} \right. \qquad (2.109)
$$

$$- \quad \Gamma \frac{\partial \Psi^i}{\partial \theta} \frac{\partial h_{A,C}}{\partial \theta} \left\{ h^2_{A,C} + \left(\frac{\partial h_{A,C}}{\partial \theta} \right)^2 \right\}^{-1/2} \Bigg] d\theta$$

in regions A and C. The reflective symmetry boundary condition

$$\left[\frac{\partial h}{\partial x} = 0 \right]_{x=0,\lambda/2} \quad , \tag{2.110}$$

has been used to eliminate one of the terms generated by the integration by parts used to lower the order of the second order derivative occurring in the curvature term.

There is precedence for forming the residual equations as above to determine the shape of the melt-solid interface (Ungar *et al.* 1988). This weak form is analogous to the one derived for the Young-Laplace equation for liquid-fluid static surfaces with shapes dictated by a balance of surface energy and fluid effects (Brown 1979). Mittelman (1977) and others have shown that Lagrangian finite element methods are convergent for this type of nonlinear differential equation.

The weighted residual equations for the system represent a set of differential-algebraic equations for the coefficients $\{a_i, b_i, c_i\}$. These equations may be conveniently represented as:

$$\mathbf{M}\frac{d\mathbf{u}}{d\tau} \equiv \begin{bmatrix} \mathbf{M}_1(\mathbf{c}) & \mathbf{0} & \mathbf{M}_3(\mathbf{a},\mathbf{b},\mathbf{c}) \\ \mathbf{0} & \mathbf{M}_2(\mathbf{c}) & \mathbf{M}_4(\mathbf{a},\mathbf{b},\mathbf{c}) \\ \mathbf{0} & \mathbf{0} & \mathbf{0} \end{bmatrix} \frac{d}{d\tau} \begin{bmatrix} \mathbf{a} \\ \mathbf{b} \\ \mathbf{c} \end{bmatrix} = \mathbf{R} \equiv \begin{bmatrix} \mathbf{R}'_1(\mathbf{a},\mathbf{b},\mathbf{c}) \\ \mathbf{R}'_2(\mathbf{a},\mathbf{b},\mathbf{c}) \\ \mathbf{R}_3(\mathbf{a},\mathbf{b},\mathbf{c}) \end{bmatrix} \quad , \tag{2.111}$$

where the vector $\mathbf{u}$ is the array of the unknown nodal values $\mathbf{u}^T = (\mathbf{a}^T, \mathbf{b}^T, \mathbf{c}^T)$ and the mass matrix $\mathbf{M}$ is composed of the matrices $\mathbf{M}_1 \in \mathcal{R}^{N \times N}$, $\mathbf{M}_2 \in \mathcal{R}^{N \times N}$, $\mathbf{M}_3 \in \mathcal{R}^{N \times M}$ and $\mathbf{M}_4 \in \mathcal{R}^{N \times M}$. The elements of these matrices are given by

$$M_{1\,ij} = \int_{D_m} \Phi^i \, \Phi^j dA + k \int_{D_s} \Phi^i \, \Phi^j dA \quad , \tag{2.112}$$

$$M_{2\,ij} = \int_{D_m} \Xi^i \, \Xi^j dA + \int_{D_s} \Xi^i \, \Xi^j dA \quad , \tag{2.113}$$

$$M_{3\,ij} = \int_{\partial D_I} \Phi^i \left(\hat{\mathbf{n}} \cdot \hat{\mathbf{e}}_{(y)} \right) (k-1) \Psi^j \left(\sum_k a_k \Phi^k \right) dS \quad , \tag{2.114}$$

and

$$M_{4\,ij} = \int_{\partial D_I} \Xi^i \left(\hat{\mathbf{n}} \cdot \hat{\mathbf{e}}_{(y)} \right) St \; Le \Psi^j dS \quad , \tag{2.115}$$

where, because of the nonorthogonal mapping, both dA and dS are functions of the interface shape nodal unknowns, $\mathbf{c}$. The vector $\mathbf{R}_3(\mathbf{a},\mathbf{b})$ is given by Eq. (2.108). The vectors $\mathbf{R}'_1(\mathbf{a},\mathbf{b},\mathbf{c})$ and $\mathbf{R}'_2(\mathbf{a},\mathbf{b},\mathbf{c})$ are given by $-\mathbf{R}_1$ and $-\mathbf{R}_2$ from Eq. (2.103) and Eq. (2.105), with expansions for the trial solutions (Eq. (2.100), Eq. (2.101) and Eq. (2.102)) substituted in, and the time derivative terms set to zero.

2.4.5 Newton's Method

The $(2N + M)$-dimensional set of residual equations describing the free-boundary problem for steady-state solidification are obtained by setting $d\mathbf{u}/dt = \mathbf{0}$ in Equations (2.103), (2.105) and (2.108). These are

$$\mathbf{R}(\mathbf{u}) \equiv \begin{bmatrix} \mathbf{R}'_1(\mathbf{a},\mathbf{b},\mathbf{c}) \\ \mathbf{R}'_2(\mathbf{a},\mathbf{b},\mathbf{c}) \\ \mathbf{R}_3(\mathbf{a},\mathbf{b},\mathbf{c}) \end{bmatrix} = \mathbf{0} \quad , \tag{2.116}$$

Because this problem is nonlinear due to the interaction between the free-boundary shape and the concentration field, an iterative solution scheme must be used to solve for the $(2N + M)$ unknowns $\mathbf{u}^T \equiv (\mathbf{a},\ \mathbf{b}\ ,\mathbf{c})$. Ettouney & Brown (1983) showed that a Newton's method is superior to a successive approximation scheme for solution of finite element equations for free-boundary problems in crystal growth. A Newton-Raphson scheme is used here to simultaneously solve for both concentration unknowns and interface shape unknowns.

Newton's method for the solution of the nonlinear equation $\mathbf{R}(\mathbf{u}) = \mathbf{0}$ involves an iterative scheme starting with an initial guess, a solution vector $\mathbf{u}^{(0)}$, where the superscript 0 indicates this is the solution vector before the first Newton iteration has been performed. This solution vector is then improved after each iteration thus:

$$\mathbf{u}^{(i+1)} = \mathbf{u}^{(i)} + \boldsymbol{\delta}^{(i)} \quad , \tag{2.117}$$

where $\mathbf{u}^{(i)}$ is the solution vector after i Newton iterations, $\mathbf{u}^{(i+1)}$ is the solution vector after $i + 1$ Newton iterations, and $\boldsymbol{\delta}^{(i)}$ is the ith *correction vector.* The correction vector is calculated by solving the linear set of equations

$$\mathbf{J}\left(\mathbf{u}^{(i)}\right)\boldsymbol{\delta}^{(i)} = -\mathbf{R}\left(\mathbf{u}^{(i)}\right) \quad , \tag{2.118}$$

where $\mathbf{J}$ is the *Jacobian matrix* and represents the sensitivity of the equation set $\mathbf{R}(\mathbf{u})$ to changes in the unknowns. The entries of $\mathbf{J}$ are given by

$$J_{ij} = \frac{\partial R_i}{\partial u_j} \quad . \tag{2.119}$$

are computed by explicit differentiation of $\mathbf{R}(\mathbf{u})$.

As discussed earlier, a given basis function will only overlap with a few other basis functions that are in the vicinity. The value of $\frac{\partial u_i}{\partial u_j}$ for basis functions that do not overlap is zero. This feature leads to most terms of the Jacobian matrix being zero and the matrix $\mathbf{J}$ is a sparse matrix. When the nodal unknowns are globally numbered so that nodes in common have close element numbers, the Jacobian matrix is typically a banded matrix. The rows and columns from the distinguished condition for the interface shape, however, involve the concentration and temperature variables in addition to the interface shape variables and hence do not fit into the banded structure. This results in the Jacobian matrix for Eq. (2.116) having an arrow-like structure; this is shown schematically in Fig. 2.4. At each Newton iteration the equation set Eq. (2.118) is solved with the special software developed by Thomas & Brown (1987) which takes advantage of this banded structure; Gaussian elimination is used to solve the set of equations rather than actually forming the inverse of the matrix. Quadratic convergence is attained whenever a solution is successfully located from a particular initial guess (Dahlquist & Björk 1974, Finlayson 1980).

Continuation methods (Brown *et al.* 1980, Ungar & Brown 1982, Ungar & Brown 1984a) are used to generate accurate starting guesses using known solutions that are close by in parameter space. The initial guess for a parameter p at the value $p_0 + dp$ slightly different from the value p_0 where the solution is known is given as

$$\mathbf{u}^{(0)}(p_0 + dp) = \mathbf{u}(p_0) + \mathbf{u}_p dp \quad , \tag{2.120}$$

where $\mathbf{u}_p$ is calculated by solving the linear equation set

$$\mathbf{J}\mathbf{u}_p = -\mathbf{R}_p \quad , \tag{2.121}$$

where all terms all evaluated at $p = p_0$.

Bifurcation points are located by monitoring the value of the determinant *det*($\mathbf{J}$) along the solution family (Ungar 1984). Limit points are tracked by arc-length continuation;

details of these techniques are given in Ungar & Brown (1982), Ungar &Brown (1984a), Yamaguchi *et al.* (1984) and Seydel (1988).

2.4.6 Time-dependent Equations

The set of transient equations for the thermal-solutal model, can be represented as

$$\mathbf{M}(\mathbf{u})\frac{d\mathbf{u}}{d\tau} = \mathbf{R}(\mathbf{u}) \quad , \tag{2.122}$$

where $\mathbf{u}$ represents the set of all unknowns, the nonlinear vector function $\mathbf{R}(\mathbf{u})$ is the Galerkin finite element discretization of the steady-state solutal model equations, and $\mathbf{M}(\mathbf{u})$ is the *mass matrix*. The mass matrix $\mathbf{M}(\mathbf{u})$ for these equations is singular because the condition for thermal equilibrium at the melt-solid interface, the Gibbs-Thomson equation, is independent of time. Thus, the weighted residuals for this equation (Eq. (2.108)) have no time derivative. This type of formulation leads to nonlinear algebraic constraints and to coupled differential/algebraic equations (DAEs) (Petzold 1982) which are difficult to solve numerically because they are infinitely stiff. The singularity of the mass matrix prevents the use of explicit time integration methods. Following Ungar *et al.* (1988), a predictor-corrector time-integration scheme is used based on an Adams-Bashforth predictor step and an Adams-Moulton corrector step for implicit integration of the DAEs. This scheme is fully implicit when the nonlinear equation set arising from the Adams-Moulton method (Eq. (2.128)) is solved to a specific error tolerance at each time step. The scheme was initially developed by Gresho *et al.* (1980) for the case where the mass matrix is not a function of time, and it was generalized for the case of $\mathbf{M}(\mathbf{u})$ being a function of time by Ungar (Ungar 1984a, Ungar *et al.* 1988).

The second-order accurate scheme requires information from two previous times. This is generated by starting with two implicit backward Euler time steps. At successive steps $\frac{d\mathbf{u}}{d\tau}$ is calculated using the finite difference formula

$$\mathbf{M}(\mathbf{u}_{n+1})[\mathbf{u}_{n+1} - \mathbf{u}_n] - \Delta\tau_n \mathbf{R}(\mathbf{u}_{n+1}) = \mathbf{0} \quad , \tag{2.123}$$

where the subscripts n and $n+1$ refer to quantities at the nth and $(n+1)$st time step and $\Delta\tau_n \equiv \tau_{n+1} - \tau_n$; for the first two time steps $n = 0, 1$. The initial condition $\mathbf{u}_0 \equiv \mathbf{u}(0)$

comes from a solution to the steady-state problem. The Eq. (2.123) is used as the residual for Newton's method:

$$\mathbf{J}'\boldsymbol{\delta}^{\,i+1} = -\mathbf{M}\left(\mathbf{u}_{n+1}^{(i)}\right)\left[\mathbf{u}_{n+1}^{(i)} - \mathbf{u}_n\right] + \Delta\tau_n \mathbf{R}\left(\mathbf{u}_{n+1}^{(i)}\right) \quad , \tag{2.124}$$

which is solved first for $\mathbf{u}_1$ and then for $\mathbf{u}_2$. The entries for the Jacobian matrix $\mathbf{J}'$ are computed in closed form by differentiating each term, including the mass matrix, which is time dependent through the function $\mathbf{u}_{n+1}^{(i)}$. This Jacobian has the form:

$$\mathbf{J}' = \left[\mathbf{M} + \frac{\partial \mathbf{M}}{\partial \mathbf{u}}\mathbf{u} - \Delta\tau_n \frac{\partial \mathbf{R}}{\partial \mathbf{u}}\right] \quad . \tag{2.125}$$

The Jacobian $\mathbf{J}'$ again has an arrow-like structures allowing the use of the special arrow solver software (Thomas & Brown 1987).

The second-order accurate Adams-Bashforth formula is used to predict the solution at the following time step:

$$\mathbf{u}_{n+1}^{\text{pred}} = \mathbf{u}_n + \frac{\Delta\tau_n}{2}\left\{2\left(\frac{d\mathbf{u}}{d\tau}\right)_n + \frac{\Delta\tau_n}{\Delta\tau_{n-1}}\left[\left(\frac{d\mathbf{u}}{d\tau}\right)_n - \left(\frac{d\mathbf{u}}{d\tau}\right)_{n-1}\right]\right\} \quad , \tag{2.126}$$

for $n \geq 2$. $d\mathbf{u}/d\tau$ is calculated using a second-order backward difference formula:

$$\left(\frac{d\mathbf{u}}{d\tau}\right)_n = \frac{2\left(\mathbf{u}_n - \mathbf{u}_{n-1}\right)}{\Delta\tau_{n-1}} - \left(\frac{d\mathbf{u}}{d\tau}\right)_{n-1} \quad . \tag{2.127}$$

The time-dependent equation set Eq. (2.122) is discretized in time using a second-order accurate Adams-Moulton formula; the predicted solution vector $\mathbf{u}^{\text{pred}}$ is used as the starting guess in solving these equations

$$\mathbf{M}\left(\mathbf{u}_{n+1}\right)\left[\frac{2\left(\mathbf{u}_{n+1} - \mathbf{u}_n\right)}{\Delta\tau_n} - \frac{d\mathbf{u}_n}{d\tau}\right] - \mathbf{R}\left(\mathbf{u}_{n+1}\right) = \mathbf{0} \quad . \tag{2.128}$$

For all time steps after the first two Eq. (2.128) is taken as the residual equation for Newton's method:

$$\mathbf{J}''\boldsymbol{\delta}^{\,(i+1)} = \mathbf{M}\left(\mathbf{u}_{n+1}^{(i)}\right)\left[\frac{d\mathbf{u}_n}{d\tau} - \frac{2\left(\mathbf{u}_{n+1}^{(i)} - \mathbf{u}_n\right)}{\Delta\tau_n}\right] + \mathbf{R}\left(\mathbf{u}_{n+1}^{(i)}\right) \quad , \tag{2.129}$$

where the entries for the Jacobian matrix $\mathbf{J}''$ are again computed in closed form by differentiating each term including the mass matrix. This Jacobian has the form:

$$\mathbf{J}'' = \left[\frac{2}{\Delta\tau_n}\mathbf{M} + \frac{\partial \mathbf{M}}{\partial \mathbf{u}}\frac{d\mathbf{u}}{d\tau} - \frac{\partial \mathbf{R}}{\partial \mathbf{u}}\right] \quad . \tag{2.130}$$

The Jacobian $\mathbf{J}''$ of Eq. (2.129) also has an arrow-like structures; the arrow solver (Thomas & Brown 1987) is therefore employed.

After the first two time steps are taken using the backward Euler method, a variable time step scheme is used. The size of the next time step is chosen according to the relation developed by Gresho *et al.* (1980),

$$\Delta\tau_G = \Delta\tau_n \left[\frac{\epsilon_t F_t}{\Delta\mathbf{u}_{\text{norm}}}\right]^{1/3} \quad , \tag{2.131}$$

where the time factor F_t is given by

$$F_t = 3\left(1 + \frac{\Delta\tau_{n-1}}{\Delta\tau_n}\right) \quad , \tag{2.132}$$

and $\Delta\mathbf{u}_{\text{norm}}$ is a norm of the difference between the predicted solution vector and the converged solution vector,

$$\Delta\mathbf{u}_{\text{norm}} = \frac{||\mathbf{u}_n - \mathbf{u}_n^p||_2}{||\mathbf{u}_n||_\infty} \quad , \tag{2.133}$$

and ϵ_t is an error criterion that here was typically chosen to be 1×10^{-3} so that the error at each time step is of that order. Equation 2.131 was derived by Gresho *et al.* (1980) so as to minimize the truncation error at the next time step. In practice, however, it was found that the formula often produced a $\Delta\tau$ which was too large, so that the Newton-Raphson iterations did not converge. This behavior is not surprising, for the derivation of Eq. (2.131) assumes that $\Delta\tau$ is less than one; whereas, for the work done here $\Delta\tau$ is typically $\mathcal{O}(10^1)$. To adjust for this fact, the following criterion is used for the selection of the next time step, $\Delta\tau_{n+1}$:

$$\begin{array}{llll}
\text{if} & \Delta\tau_G < 0.8\Delta\tau_n & \text{then} & \Delta\tau_{n+1} = \Delta\tau_G \quad , \\
\text{if} & 0.8\Delta\tau_n \le \Delta\tau_G \le \Delta\tau_n & \text{then} & \Delta\tau_{n+1} = \Delta\tau_n \quad , \\
\text{if} & \Delta\tau_n < \Delta\tau_G \le \Delta\tau_{\max} & \text{then} & \Delta\tau_{n+1} = \Delta\tau_G \quad , \\
\text{if} & \Delta\tau_G > \Delta\tau_{\max} & \text{then} & \Delta\tau_{n+1} = \Delta\tau_{\max} \quad ,
\end{array}$$

where $\Delta\tau_n$ is the time step used in obtaining the last converged solution and the value $\Delta\tau_{\max}$ is chosen from experience to be of the order of the largest step size for which Newton's method is expected to converge.

To decrease the computational cost of the time-integration scheme an *adaptive Newton* method is employed. The computational time within each Newton iteration is controlled by the time for the LU decomposition of the Jacobian matrix. In the adaptive-Newton scheme, once a Jacobian matrix, Eq. (2.130), has been LU decomposed, this LU is stored and used repeatedly in the left hand side of Eq. (2.129) based on heuristic rules; thus only the components on the right hand side of Eq. (2.129) are evaluated at each iteration for an adaptive time step during the calculation of $\boldsymbol{\delta}^{(i+1)}$. Although this causes the asymptotically quadratic convergence of the pure Newton-Raphson method to be lost, the computational effort for using all pure Newton iterations for integration over a time interval is about 10 times the effort using the mixed iterations of the adaptive scheme. Thus considerable savings in computational effort are realized by using the adaptive-Newton method.

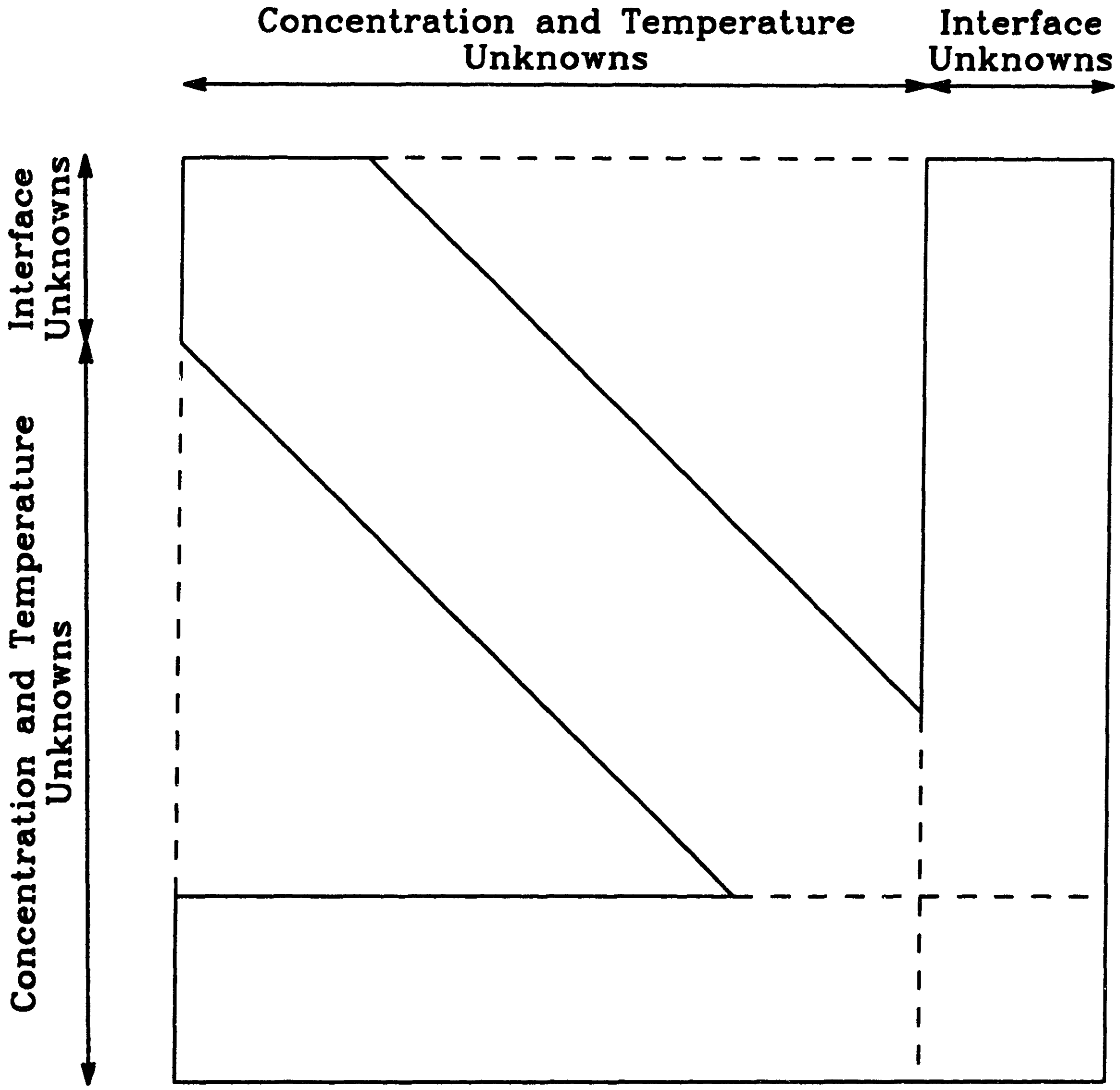

Figure 2.4: Arrow-like structure of the Jacobian matrix for the free-boundary problem.

Chapter 3

The Solutal Model

The bulk of the finite element calculations in this thesis were done using the solutal model. This chapter deals with the results from these computations while Chapter 4 details the results of the analysis using the full thermal-solutal model. The following section discusses the generic characteristics of the deep cells predicted by the steady-state computations. The accuracy of the numerical method is verified in Section 3.2. Steady-state calculations showing the evolution of deep cells with increasing growth rate are discussed in Section 3.3 using a bifurcation theory approach; results describing the evolution of these morphologies with changes in other parameters is presented in Section 3.4. Pattern selection is looked at in Section 3.5 and a comparison of numerical results with experimental data is presented in Section 3.6. Time-dependent calculations are described in Section 3.7. Finally, the results of the chapter are summarized and discussed in Section 3.8.

Finite element calculations were performed for the values of thermophysical properties that are representative of a Pb-Sb alloy, but with the solute diffusivity in the solid set to be equal to that in the melt, i.e. the diffusivity ratio R_m is set to 1.0 instead of the small values ($1 \times 10^{-2} - 1 \times 10^{-4}$) that would be more appropriate. This was done to facilitate comparison with the calculations of Ungar & Brown (1985) who worked with the same system. Besides, a parametric study of the effect of R_m on the neutral stability curve by Bennett (1990) shows that although the lowering of R_m makes the system more unstable by moving the neutral stability curve down towards lower growth rates, the curvature at the bottom of the curve was not altered substantially (even for a change of R_m from 1.0 to 1×10^{-5}). The nonlinear transitions for the system with $R_m = 1.0$ are therefore expected to be qualitative similar to those expected for more realistic values of R_m.

The values of the thermophysical properties and operating conditions for the Pb-Sb are listed in Table 3.1. All the results presented in this Chapter were obtained using this set of properties, with the exception of Section 3.6 where comparison of the results of the numerical procedure with experimental data are presented for the CBr_4-Br_2 system used by de Cheveigné *et al.* (1985, 1986). In the parametric studies presented in Sections 3.4 a single parameter is modified while the other parameters and operating conditions are maintained constant at the values listed in Table 3.1.

Property	Symbol	Value
Temperature Gradient	$\tilde{G}$	$27°K/\text{cm}$
Melting Temperature of Pure Solvent	$\tilde{T}_o$	$600.0K$
Liquidus Slope	$\tilde{m}$	$-5.0K/\text{wt}\ \%$
Solute Concentration	c_∞	0.2 wt %
Solute Diffusivity in the Melt	$\mathcal{D}_m$	$2.0 \times 10^{-5}\text{cm}^2/\text{sec}$
Solute diffusivity in the Solid	$\mathcal{D}_s$	$2.0 \times 10^{-5}\text{cm}^2/\text{sec}$
Capillary Length	$\tilde{\Gamma}$	$8.2 \times 10^{-9}\text{cm}$
Segregation Coefficient	k	0.4
Reference Length Scale	λ_{ref}	$100.0\mu\text{m}$

Table 3.1: Thermophysical properties and operating conditions used in the calculations for the Pb-Sb alloy system.

The most important feature of this set of parameters is the length scale associated with the surface energy $\tilde{\Gamma}$ which is two orders-of-magnitude smaller than the length scales for the temperature field $\mathcal{O}(\tilde{T}_o/\tilde{G})$ and the solute diffusion layer $\mathcal{O}(\mathcal{D}_m/V)$. Because the surface energy is the primary mechanism for selecting the lateral scale for the interface structure, the mechanism for determining this structure is expected to be weak.

The marginal stability curve $V_c(\tilde{\lambda})$ predicted by linear stability analysis is shown in Fig. 3.1 for the set of parameters listed in Table 3.1. The dimensional growth rate at which the first cellular form is predicted to grow is $V = 5.55\mu\text{m/sec}$ and the wavelength that corresponds to this form is predicted to be $\tilde{\lambda}_c = 459\mu\text{m}$. An important feature of the curve is its flatness at the bottom; this is most evident when compared with similar curves that describe wavelengths at onset for other instabilities. The lower portion of the curve is otherwise qualitatively similar to ones corresponding to the mathematical problems governing transitions in other transport systems. For example, when the dimensionless wavelength $\lambda^* = \tilde{\lambda}/\tilde{\lambda}_c$ is plotted against a measure of the relative deviation of the control parameter from the critical for cellular solidification and Rayleigh-Bénard instability for fluid flow between parallel shear-free surfaces, the neutral stability curve for directional solidification is seen to be 2 orders of magnitude flatter than the curve for the fluid mechanical system. A comparison between these systems for typical parameter values has been conducted by Bennett (1990) and is reproduced in Fig. 3.2. In Fig. 3.2 the marginal stability curve for directional solidification is plotted with λ^* as a function of $\epsilon \equiv \frac{P_c(\tilde{\lambda})-P_c(\tilde{\lambda}_c)}{P_c(\tilde{\lambda}_c)}$ and the corresponding curve for Rayleigh-Bénard convection is plotted with λ^* as a function of $\epsilon \equiv \frac{\mathcal{R}(\tilde{\lambda})-\mathcal{R}(\tilde{\lambda}_c)}{\mathcal{R}(\tilde{\lambda}_c)}$, where $\mathcal{R}(\tilde{\lambda})$ is the Rayleigh number – a dimensionless measure of the temperature difference across the fluid layer.

The small value of the surface energy $\tilde{\Gamma}$ for the directional solidification system (see Table 3.1) is ineffective as a mechanism for stabilizing perturbations to the interface except for spatial wavelengths that are much smaller than the critical wavelength $\tilde{\lambda}_c$ (the left border of the neutral stability curve); the curve is thus extremely flat for wavelengths near $\tilde{\lambda}_c$. Qualitatively, this flatness results in a large band of wavelengths becoming unstable at nearly the same value of the growth rate. This result impacts the nonlinear interactions between families of cells as brought out in Section 3.3.

The dimensionless parameters that appear in the solutal model equations can be easily derived from the thermophysical properties and operating conditions listed in Table 3.1 and the values of these parameters are listed in Table 3.2. Here, a reference length scale $\lambda_{\text{ref}} = 100\mu\text{m}$ has been used in the estimates; the value of the dimensionless parameter

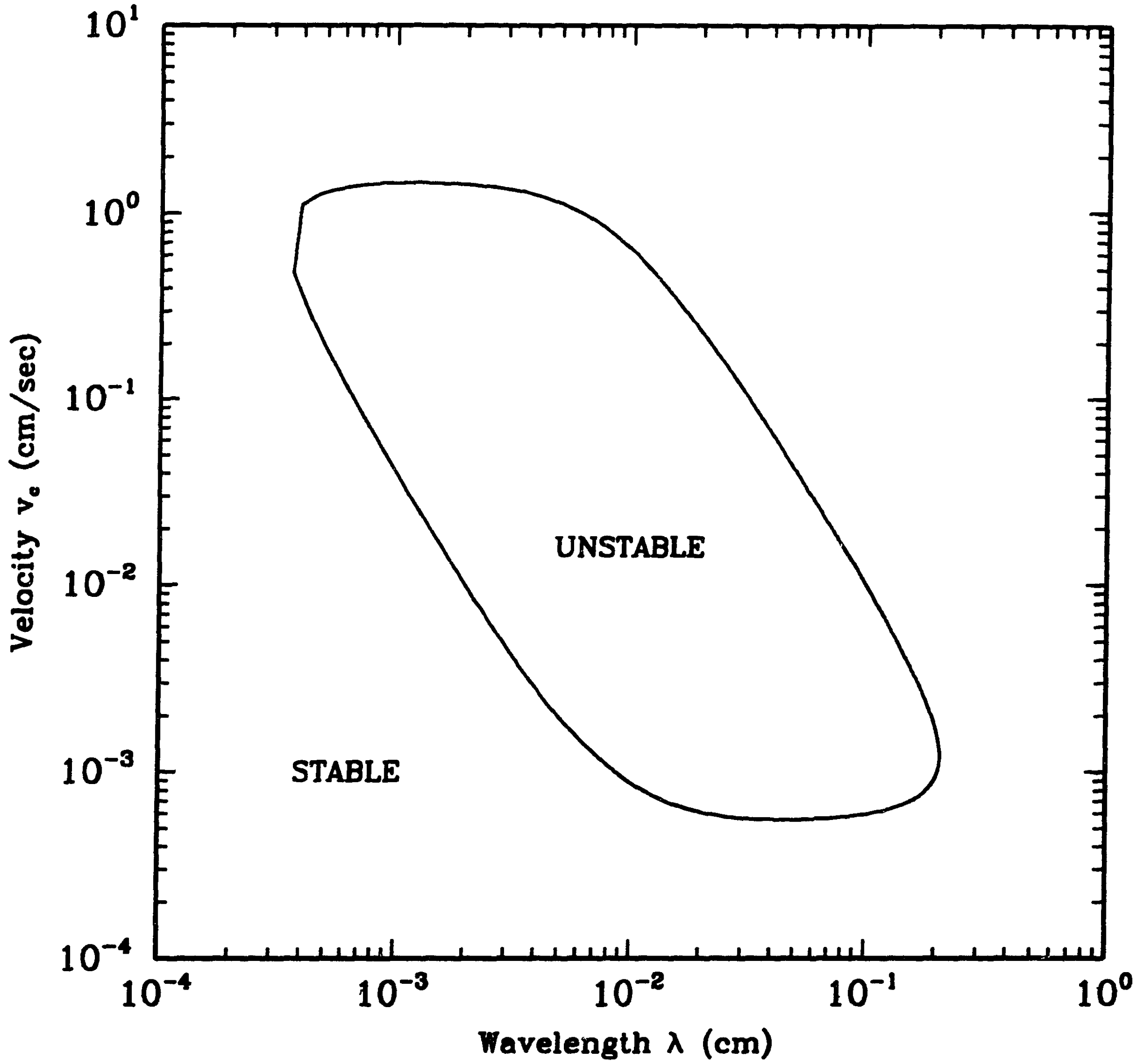

Figure 3.1: The neutral stability curve derived from linear stability analysis for the Pb-Sb system parameters listed in Table 3.1 showing regions of stability and instability of the planar interface.

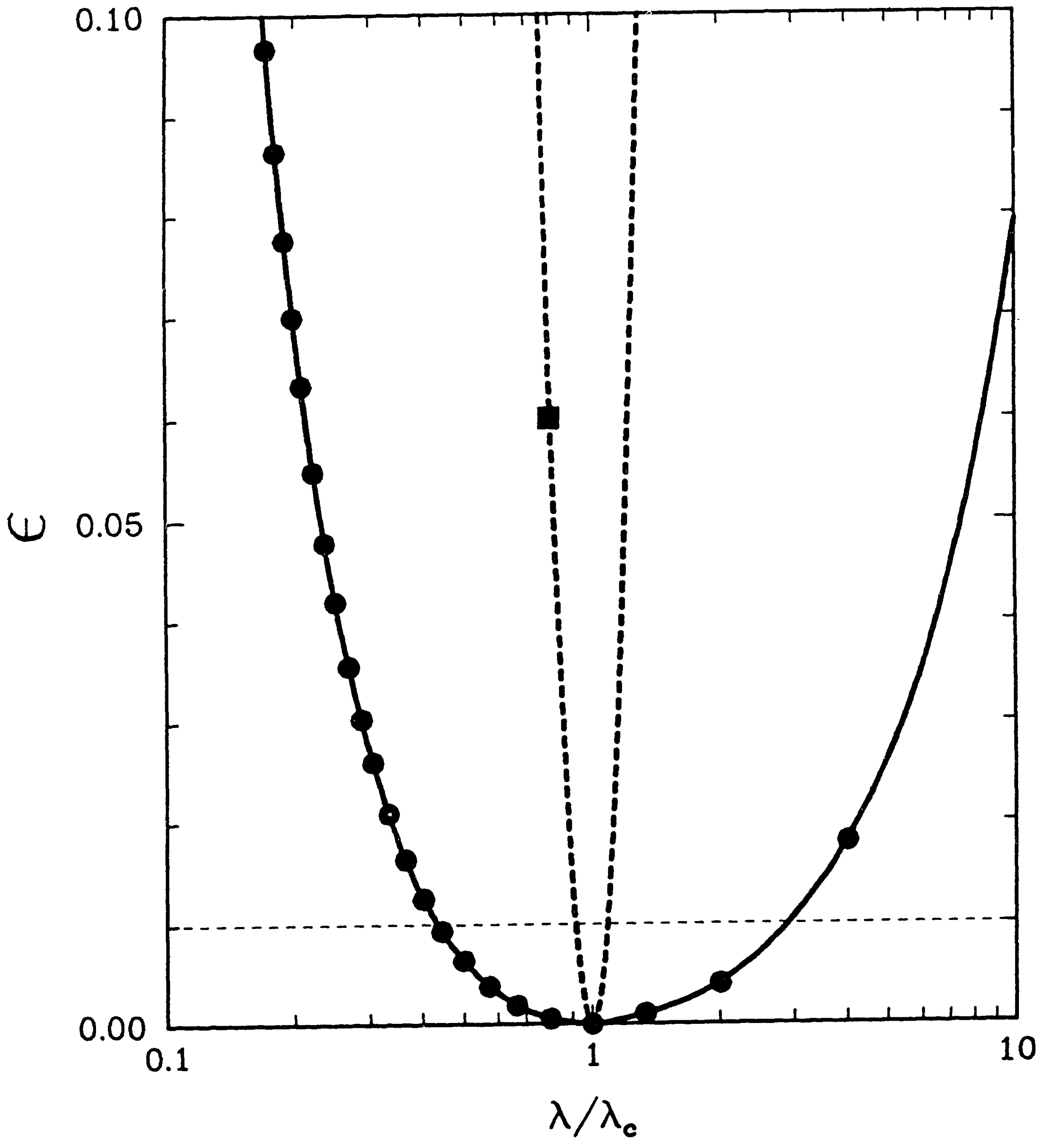

Figure 3.2: Comparison of the neutral stability curves for directional solidification (solid curve —) and Rayleigh-Bénard convection (dashed curve - - -) from Bennett (1990). The percent change from the critical value of the control parameter ϵ is defined as $\epsilon \equiv (P_c(\lambda) - P_c(\lambda_c)/P_c(\lambda_c)$ for the directional solidification curve and $\epsilon \equiv (\mathcal{R}(\lambda) - \mathcal{R}(\lambda_c)/\mathcal{R}(\lambda_c)$ for the Rayleigh-Bénard curve.

actually used in a particular calculation depends on the wavelength λ of the desired cellular solution.

3.1 The Deep Cell

The deep cells computed at steady-state using the numerical procedure have three main distinct regions: the cell tip region, the sidewall region and the cell bottom region. A typical deep cell predicted using the solutal model is shown in Fig. 3.3. The parameters used in the calculation correspond to those listed in Table 3.2 with a Peclet number $P =??$. A generic feature is the reentrant nature of the transition region that connects the sidewall to the cell bottom. Fig. 3.4a illustrates the concentration field predicted by the computations for the cell in Fig. 3.3 in terms of the concentration contours in the two phases. To maintain continuity across the interface, the solute concentration in the solid has been scaled using the segregation coefficient k. Fig. 3.4b shows the discretization used in the computation. The cell shapes in Fig. 3.4 have been expanded in the x-direction for clarity.

The concentration field can be more easily understood by analyzing Fig. 3.5 where the variation in concentration along three lines has been plotted. Fig. 3.5a is a plot of the variation in concentration along the center of the cell. The concentration profile along the interface is shown in Fig. 3.5b and the change in concentration along the center of the groove between cells is shown in Fig. 3.5c. Again, continuity of the concentration field is maintained by dividing the solute concentration in the solid by k.

Ahead of the rounded cell tip (Fig. 3.5a) is an exponential diffusion layer caused by the rejection of solute at the interface during solidification. The solute concentration decays from a high value at the cell tip to the bulk concentration uniformly across the melt far ahead of the interface.

Along the almost linear sidewall (Fig. 3.5b) is a slow variation in concentration that corresponds to the low thermal gradient G employed in the calculations. As Fig. 3.3 shows, the curvature of the interface in this region is small and the effect of surface energy Γ in

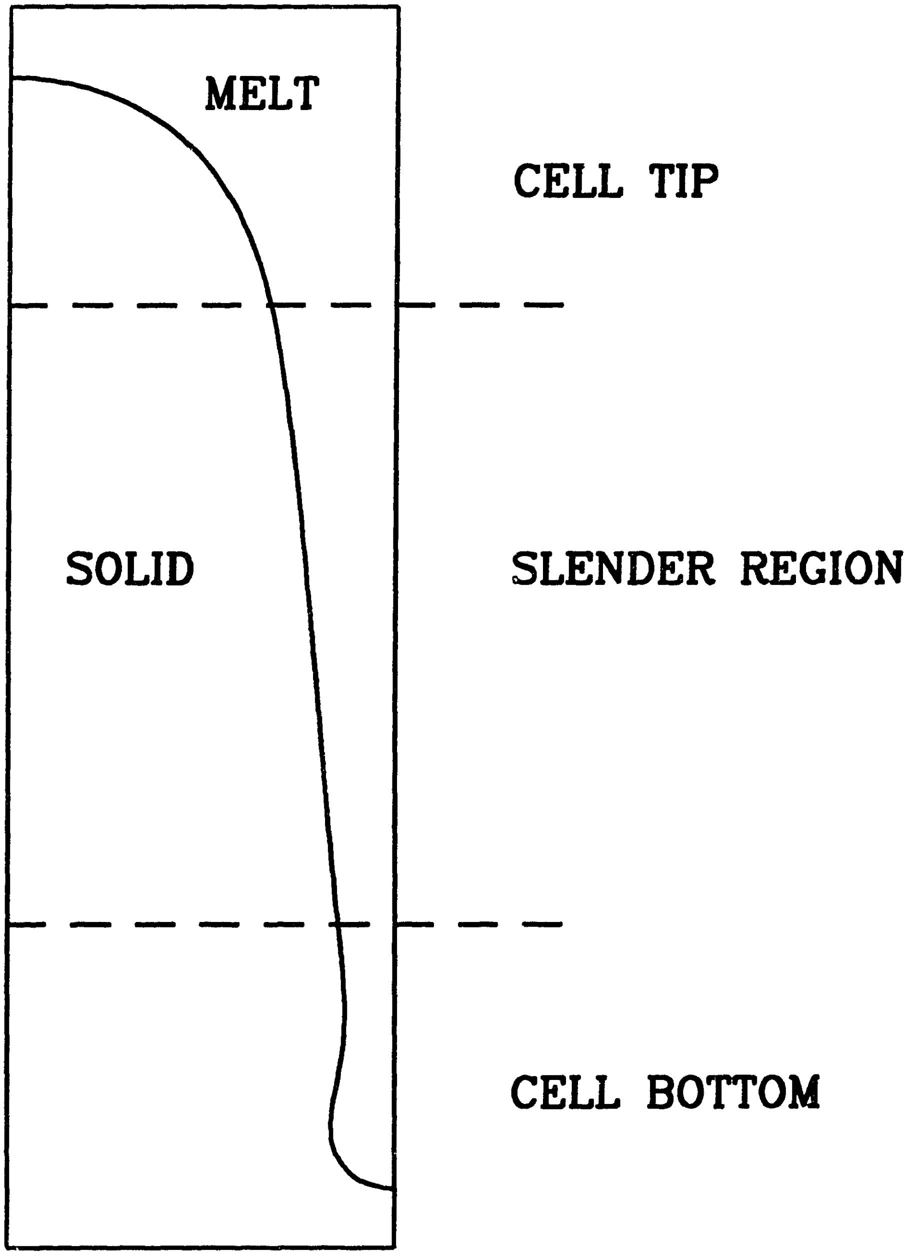

Figure 3.3: A typical deep cell computed using the solutal model.

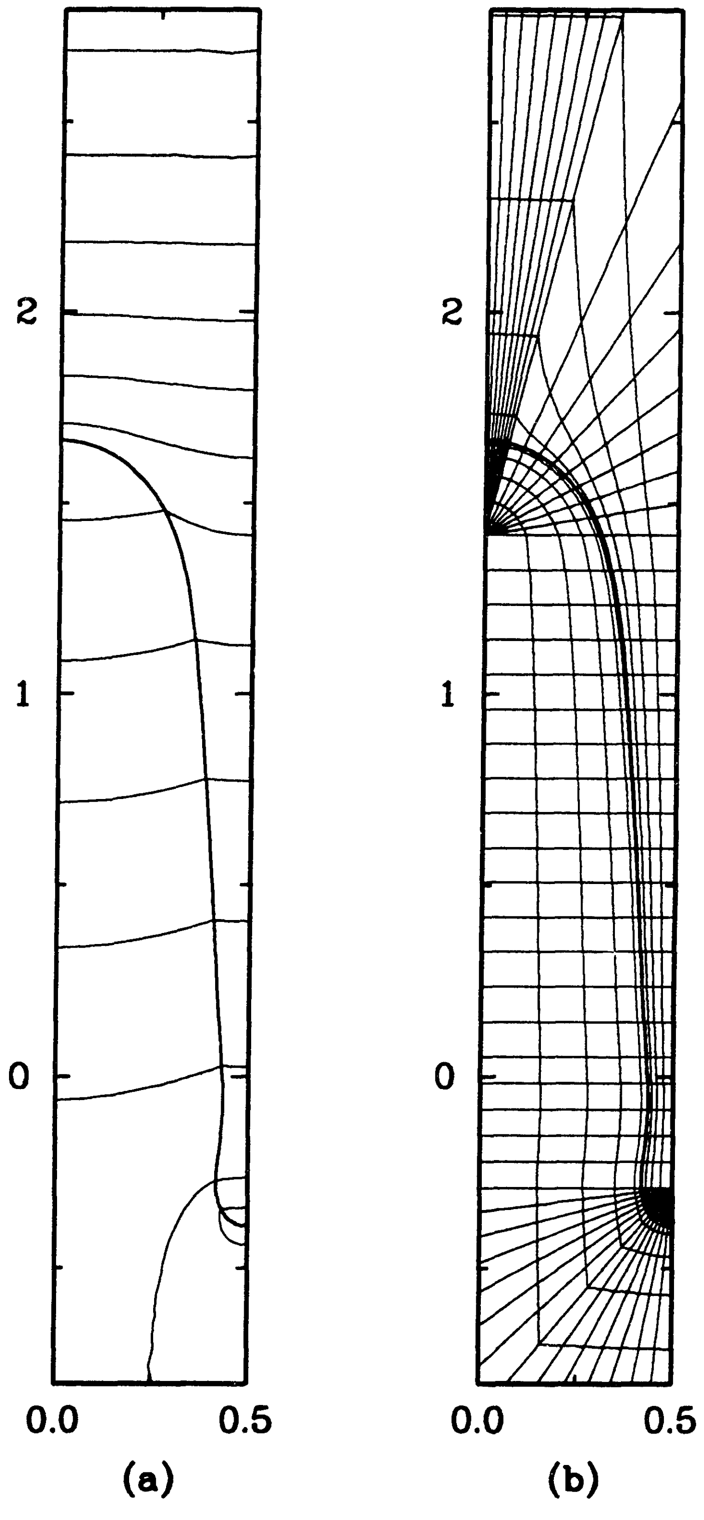

Figure 3.4: (a) Contour plot of the concentration field around the deep cell in Fig. 3.3 and (b) the discretization used in the computations.

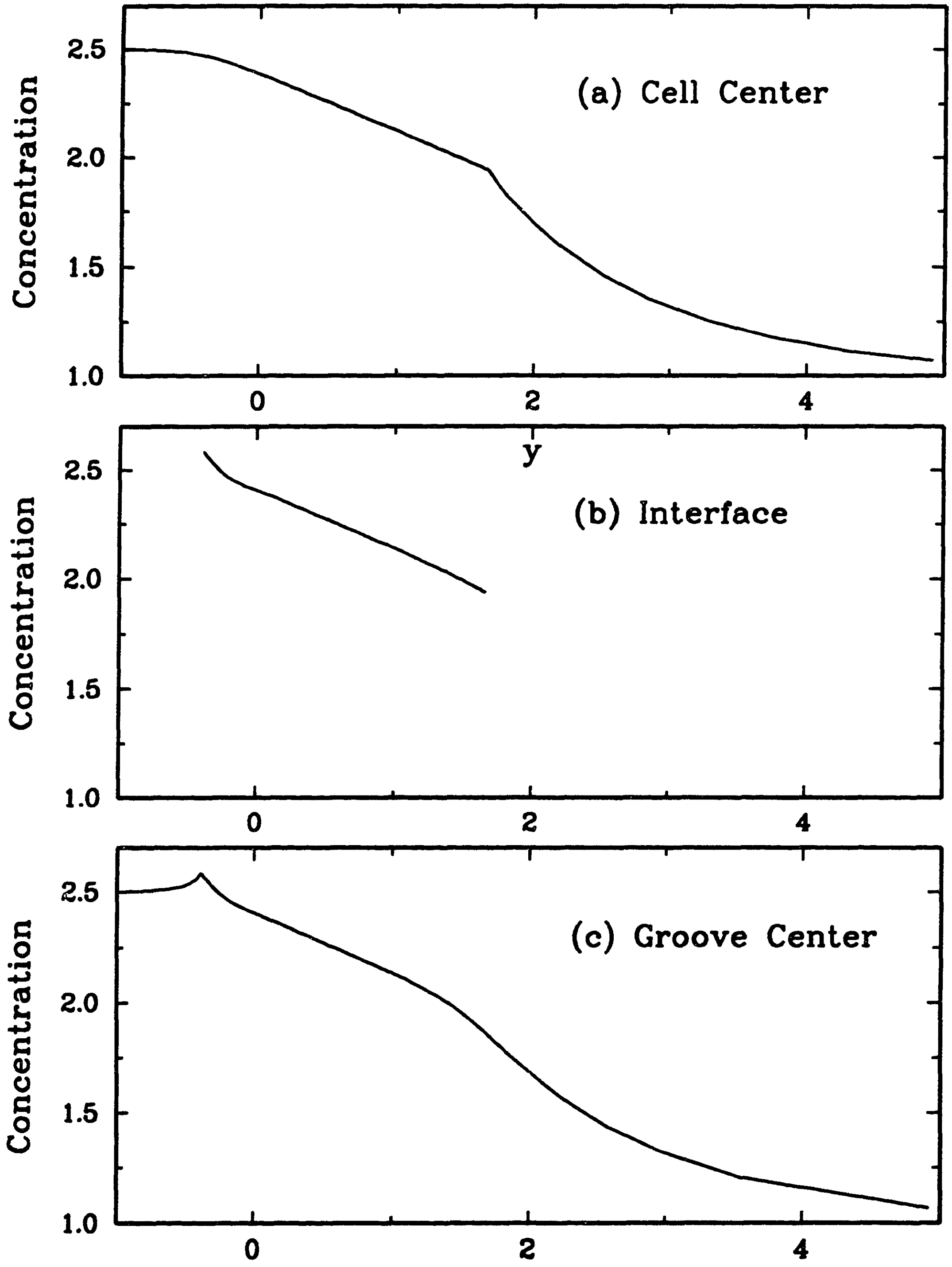

Figure 3.5: Variation in concentration along the (a) center of the cell, (b) the interface, and (c) the center of the groove, for the deep cell shown in Fig. 3.3.

the Gibbs-Thomson equation,

$$[T_{\rm ref} + G\,y = 1 + m\,c_m + \Gamma(2\mathcal{H})]_{\rm interface} \quad , \tag{3.1}$$

can be neglected. The variation in concentration across the cell also is minimal, as seen from the almost horizontal contours in Fig. 3.4 in this region. These features of the sidewall region are predicted by the asymptotic analysis presented in Chapter 5.

The sidewall region is attached to a pendant bottom through a transition regime (see Fig. 3.3) where the interface is reentrant; the curvature increases in this region from the negligible value in the sidewall region to the appreciable values that are applicable for the cell bottom. The sharp increase in the curvature along the interface in the cell bottom region is compensated by the a corresponding sharp increase in the solute concentration; these effects balance each other somewhat in the Gibbs-Thomson equation Eq. (3.1) so that the temperature field remains linear. The solute concentration in the melt is again independent of the x-coordinate. In the solid, however, is a gradual diffusion of solute away from the cell bottom (see Fig. 3.5b) and the concentration becomes uniform across the solid far downstream of the cell bottom with a value of $1/k$ which correspond to a dimensionless solute concentration of 1.0.

3.2 Accuracy of Numerical method

Deep cellular interfaces and the corresponding concentration fields were computed for a series of ten meshes $M(i,j)$ listed in Table 3.3. The parameters used correspond to the values listed in Table 3.2. The results of this Section correspond to a wavelength of $\tilde{\lambda} = 100\mu$m at a Peclet number $P = 0.8$. The aspect ratio of the cell A, the locations of the cell tip (l_{tip}) and bottom (l_{bot}), and the concentrations in the melt at the tip (c_{tip}) and bottom (c_{bot}) are listed in Table 3.4. Here, the aspect ratio is defined as

$$A = \frac{\tilde{\Delta}}{\tilde{\lambda}} \quad , \tag{3.2}$$

where $\tilde{\lambda}$ is the wavelength of the cell in the calculation. The five quantities listed in Table 3.4 were employed as measures of the solution to monitor the accuracy of the numerical method.

Increasing the resolution of the mesh in either direction increased the accuracy of the calculations as seen from the values of these solution measures. In addition, the convergence rate of the solution measures listed in Table 3.4 is at least as good as the $\mathcal{O}(h^3)$ rate expected with the quadratic finite element approximations used for the concentration field and the interface shape. The convergence rate is estimated by comparing the results for the meshes $M(1,1)$, $M(2,2)$ and $M(3,3)$, which represent systematic refinement of the discretization in both directions. Taking the solution $M(3,3)$ to be close to the exact result shows that the error in the solution for mesh $M(2,2)$ is smaller than the error for mesh $M(1,1)$ by more than the expected factor of 8.

The finite element meshes mapped back to the Cartesian system are shown in Fig. 3.6 along with the interface shapes and contours of the concentration field. As before, the solute concentrations in the solid have been divided by the segregation coefficient k to make the contours continuous across the interface. The coarsest meshes have highly distorted elements in the melt ahead of the interface and in the solid behind it. Some wiggles in the approximate concentration field are caused by these elements. Refining the mesh leads to very smooth approximations for the concentration and the interface, as seen in Fig. 3.6c.

3.3 Evolution of Deep Cells

The growth parameters that are most easily modified in experiment to illustrate the evolution of cellular interfaces from the planar state are the pull rate and the imposed temperature gradient. Most experiments (see Section 1.3) use the growth rate as the control parameter and V (and P) has hence been chosen as the primary parameter for following the evolution to deep cells in this thesis. In this section, results with changing growth rate are presented. Section 3.4 deals with the modifications in the morphology with changes in other parameters.

The transition from the planar interface to deep cells for a specific wavelength is exemplified by calculations for the most dangerous dimensionless wavelength $\lambda = \lambda_c = 4.59$ predicted by linear stability theory. As in Chapter 2, the dimensionless spatial wavelength

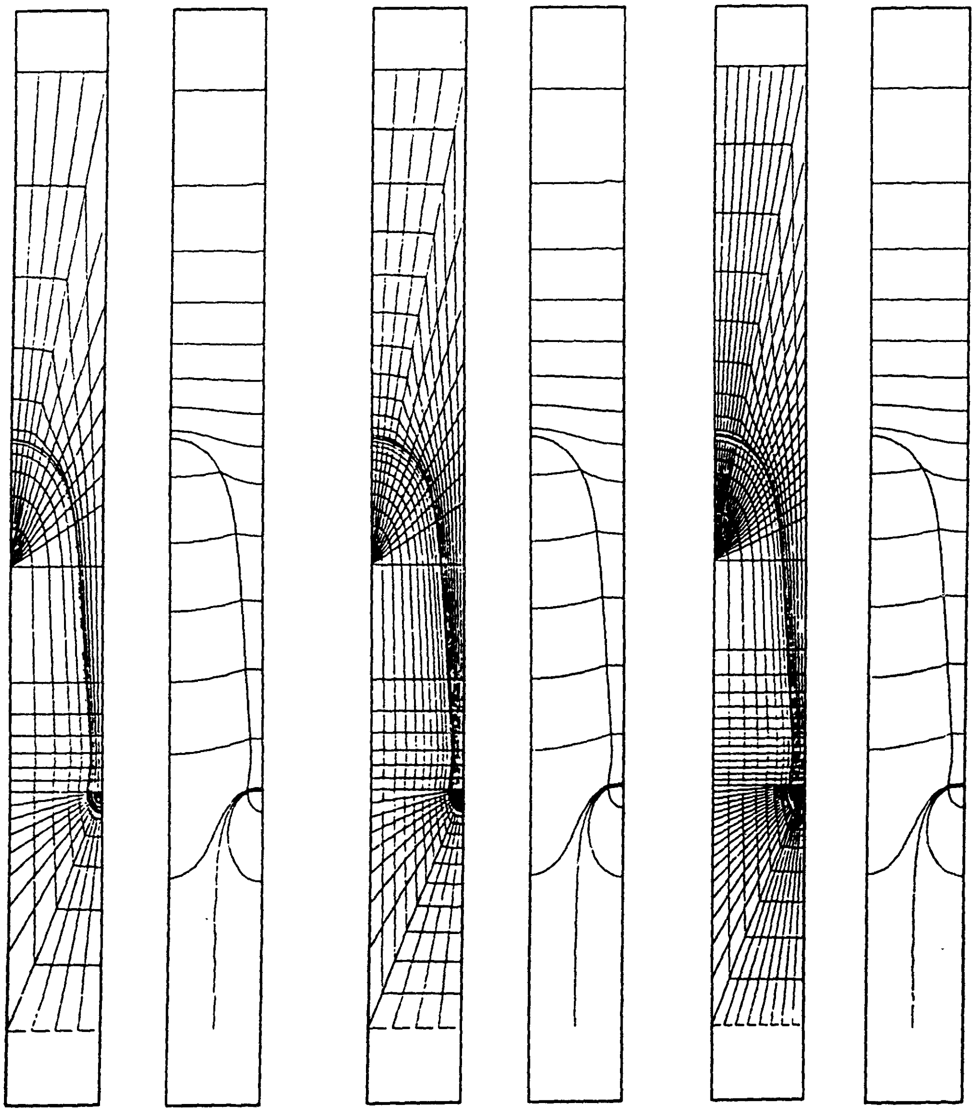

Figure 3.6: Finite element meshes projected into the original coordinate system and half-cell shapes and concentration fields for meshes (a) $M(1,1)$, (b) $M(2,2)$, and (c) $M(3,3)$.

λ is defined in terms of a reference wavelength $\tilde{\lambda}_{\text{ref}} = 100\mu\text{m}$ thus:

$$\lambda \equiv \frac{\tilde{\lambda}}{\tilde{\lambda}_{\text{ref}}} \tag{3.3}$$

The deep cell calculations are a continuation of the work done with the shallow cell formulation using the Mongé representation that are detailed in Ramprasad *et al.* (1987). The calculations were performed using a computational domain of $\lambda_c/2 = 2.295$ so that cells with wavelengths that are integer submultiples of λ_c, i.e., $\lambda = \frac{\lambda_c}{n+1}$, $n = 0, 1, \cdots$, are admissible solutions. In this domain, families of cellular shapes with wavelengths $\{\lambda_c,\ \lambda_c/2,\ \lambda_c/4, \cdots\}$ bifurcate from the planar state at critical values of the Peclet number $\{P_c(\lambda_c),\ P_c(\lambda_c/2),\ P_c(\lambda_c/4), \cdots\}$. These shapes are represented in Fig. 3.7 by the dimensionless amplitude of the cell defined as

$$\Delta \equiv \frac{\tilde{\Delta}}{\tilde{\lambda}_{\text{ref}}} \quad , \tag{3.4}$$

where $\tilde{\Delta}$ is the dimensional value of the cell depth.

The three families of shapes shown in Fig. 3.7 bifurcate from the planar state with dimensionless wavelengths λ_c, $\lambda_c/2$, and $\lambda_c/4$. These families were computed by tracking these solution curves from the corresponding critical points along the planar family. Two secondary bifurcation points were located that connect two of the solution families. Each is expected because of a codimension-two bifurcation point that exists at another wavelength between the two interacting cell shapes as discussed in Section 1.4. Cells with wavelength λ_c on the λ_c family of solutions were computed only up to the secondary bifurcation point where the family joined one with shapes of wavelength $\lambda_c/2$. This shape family evolved with P through a turning point $P = P_1 = 2.12$ and is connected to the family of cells with spatial wavelength $\lambda_c/4$ through another secondary bifurcation point. Deep cellular interfaces along the $\lambda_c/4$ family were then computed to higher P. Sample interface shapes from each family are shown in Fig. 3.8. The shape in the λ_c family shows the development of an indentation in the tip at very low amplitude as the beginning of the mechanism for tip-splitting. and formation of cell shapes in the $\lambda/2$ family. A similar evolution of the tip shape occurs in the shapes of the $\lambda_c/2$ family. The shapes in the $\lambda_c/4$ family get progressively reentrant for the range of P shown in Fig. 3.7. For $P > 2$, the cells have rounded tips, approximately linear side-walls, and rounded bottoms. The bottom and side-wall regions are connected

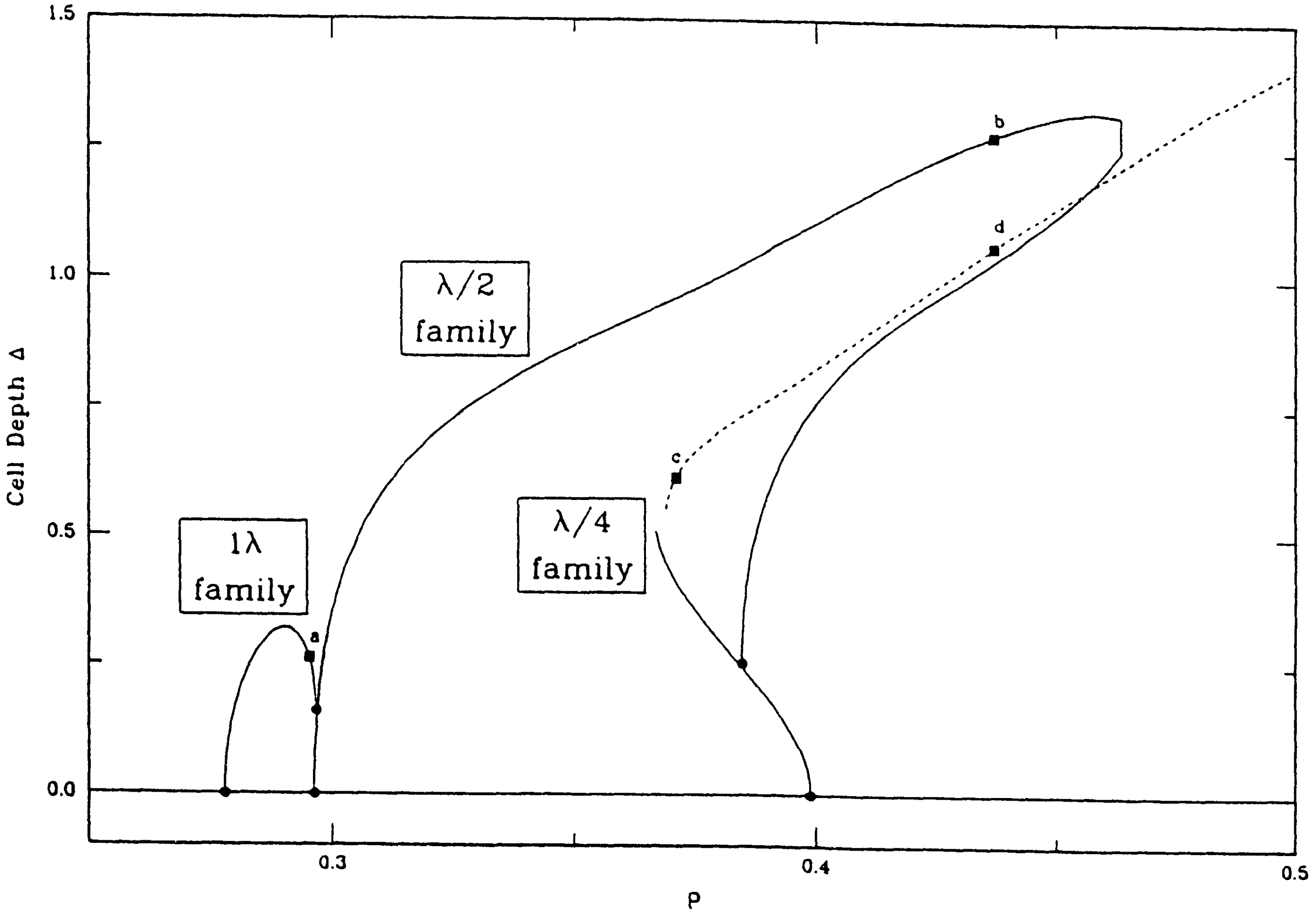

Figure 3.7: Families of steady-state cellular shapes with spatial wavelengths that are integer fractions of λ_c as computed by the finite element method plotted as a function of P.

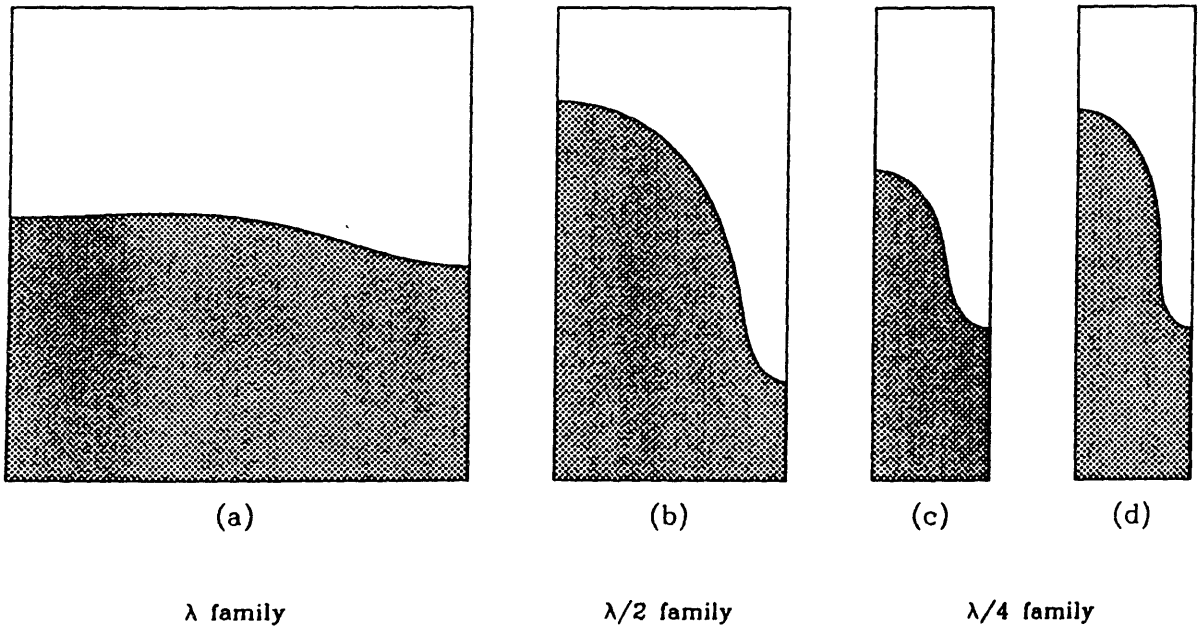

Figure 3.8: Sample half-cell shapes in each of the three shape families shown in Fig. 3.7. Letters correspond to points shown in that figure.

through a transition regime where the interface becomes reentrant so that solid melts into the bottom.

An important feature of this bifurcation diagram is the rapid change in the apparent spatial wavelength of the cells with increasing growth rate. Cells with the critical value are only possible for a narrow range of P and the wavelength splits to $\lambda_c/4$ within less than a 50% increase in P. The proximity of the value of P for these secondary transitions compared to the value of P for the onset of cellular solidification is a consequence of the flatness of the neutral stability curve $P = P_c(\lambda)$. Calculations with the same parameter value, but $R_m = 0$ show that these transitions occur in an even smaller range of growth rates (Ungar & Brown 1984).

The calculations shown in Fig. 3.7 for $\lambda = \lambda_c$ can be repeated for a range of wavelengths with only small changes in the connectivity of the bifurcation diagram. The bifurcation diagram computed for $\lambda = 1$ is shown in Fig. 3.9. The family of cells that bifurcate from the planar state with the fundamental wavelength $\lambda = 1$ become deep and reentrant before any secondary bifurcation is detected. Cells with the dimensionless wavelength $\lambda = 1$ (the λ family of solutions) exist only up to the turning point shown in Fig. 3.9. The shapes in the reverse portion of this family evolve to lower values of P until a secondary bifurcation occurs which splits the wavelength to $\lambda = 1/2$. Sample shapes in the λ family are shown in Fig. 3.10. The deep cell representation can only be used to compute cell shapes for which the tip region is single valued in the cylindrical polar coordinate representation for that region; so the entire process of wavelength splitting cannot be calculated. The cells shown in Fig. 3.10 calculated along the reverse portion of the λ family develop flat tips and become slightly indented as P is decreased. These cells are still long and have narrow grooves and reentrant bottoms; however, the the details of the cell bottom are changing with P. The $\lambda/2$ family similarly bifurcates off the planar state at the critical value of P dictated by linear stability analysis and cells become increasingly deeper with increasing P as shown in Fig. 3.9. The sample shapes with this wavelength are similar to those of the λ family, except that the bottom is enlarged due to the larger importance of the surface energy and the grooves are narrower. The computations had to be discontinued beyond a value of P when the grooves between cells became too narrow and the discretization in the melt region

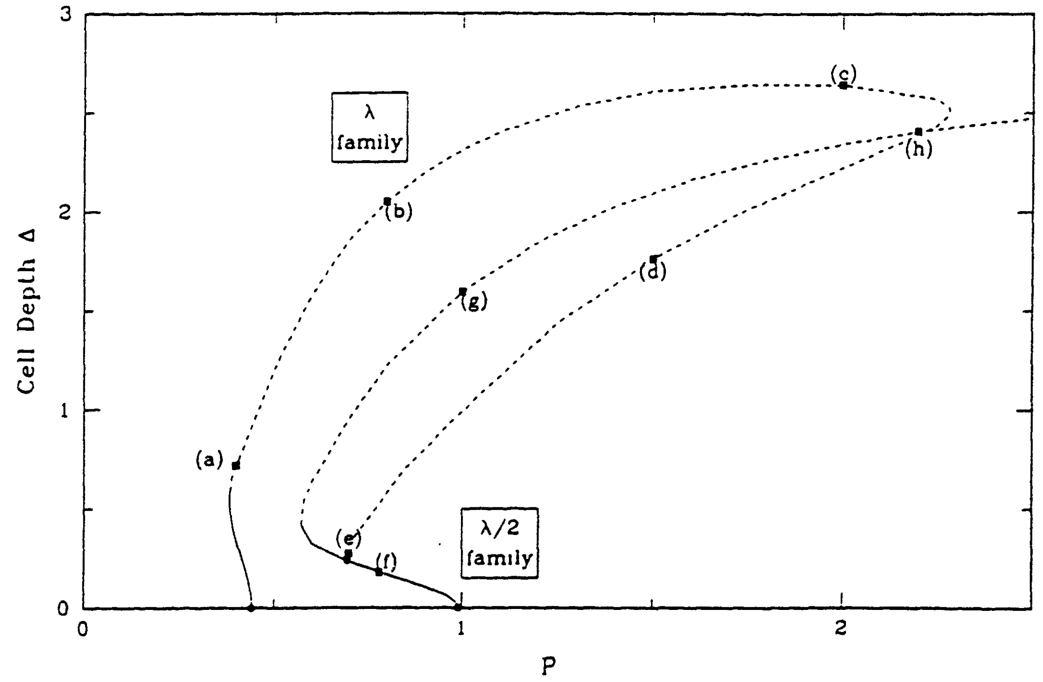

Figure 3.9: Families of steady-state cellular shapes with spatial wavelengths that are integer fractions of $\lambda = 1$ as computed by the finite element method plotted as a function of P.

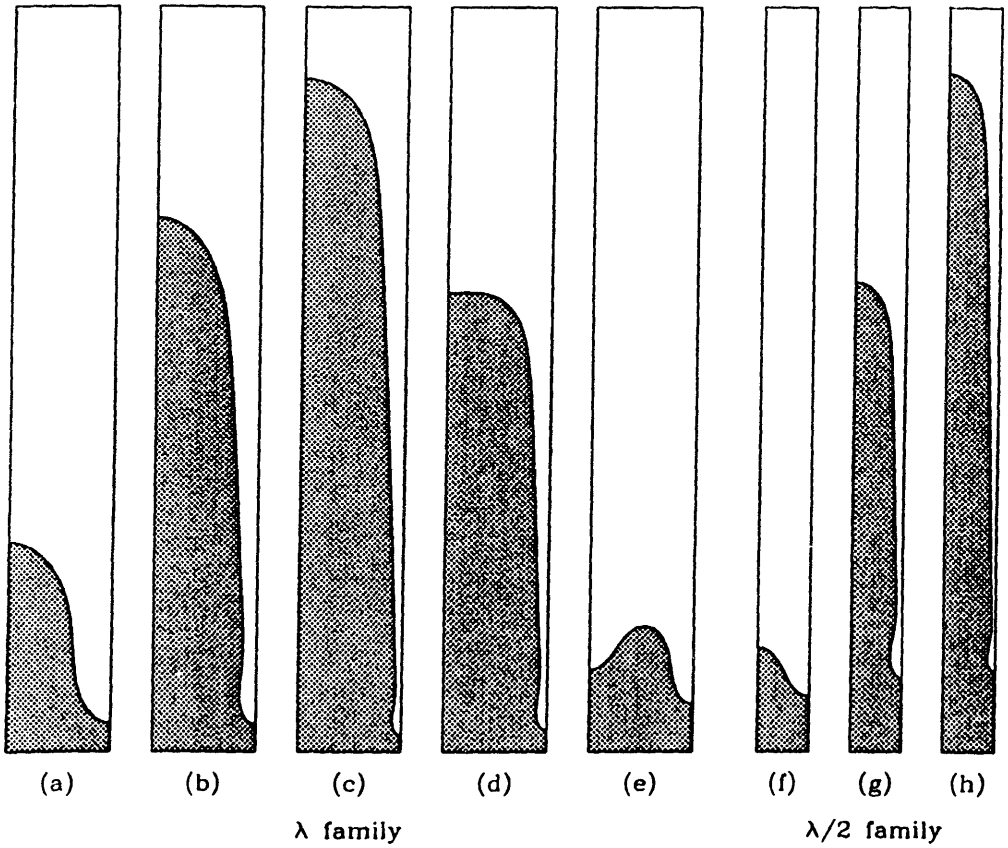

Figure 3.10: Sample half-cell shapes in each of the two shape families shown in Fig. 3.9. Letters correspond to points shown in that figure.

between adjacent cells became highly distorted. No limit point was detected in this family for the range of growth rates computed.

The problem of narrowing of the groove between cells is always seen when the cells get very deep. Solution of the equations beyond this point was only possible when the finite element method was modified using the results of an asymptotic analysis of the sidewall region. The results of these computations are presented in Chapter 5.

3.4 Effect of Various Parameters

The results of a parametric study of the change in the interface shape to variations of temperature gradient, surface energy, segregation coefficient, solute diffusivity ratio, liquidus slope and anisotropy of the surface energy are described here.

3.4.1 Effect of Temperature Gradient G

While most experiments of directional solidification look at the evolution of interface morphologies with changing growth rate, the evolution of cells from the planar interface is also sometimes followed using the temperature gradient $\tilde{G}$ as the control parameter. This is because $\tilde{G}$ can often be easily changed in the experimental system by moving the heating and cooling unit that are place on either side of the sample. Unlike the growth rate, a *decrease* in the temperature gradient causes the morphological instability as can be readily deduced from the constitutional supercooling criterion Eq. (1.20). The effect of the temperature gradient on cell shape was studied by calculations with cells of dimensionless wavelength $\lambda = 1$ using three values of the dimensionless temperature gradient: $G = 4.5 \times 10^{-5}$, $G = 3.0 \times 10^{-5}$, and $G = 2.0 \times 10^{-5}$. All the other dimensionless parameters were maintained at the values listed in Table 3.2. The Peclet number in all three calculations was 0.8. The cell shapes computed are shown in Fig. 3.11 along with the concentration contours. The cells are all deep with reentrant interfaces. The aspect ratio increases rapidly as G is decreased. This is to be expected as the parameters move further away from critical as G is decreased. Both the interface and the concentration variation in

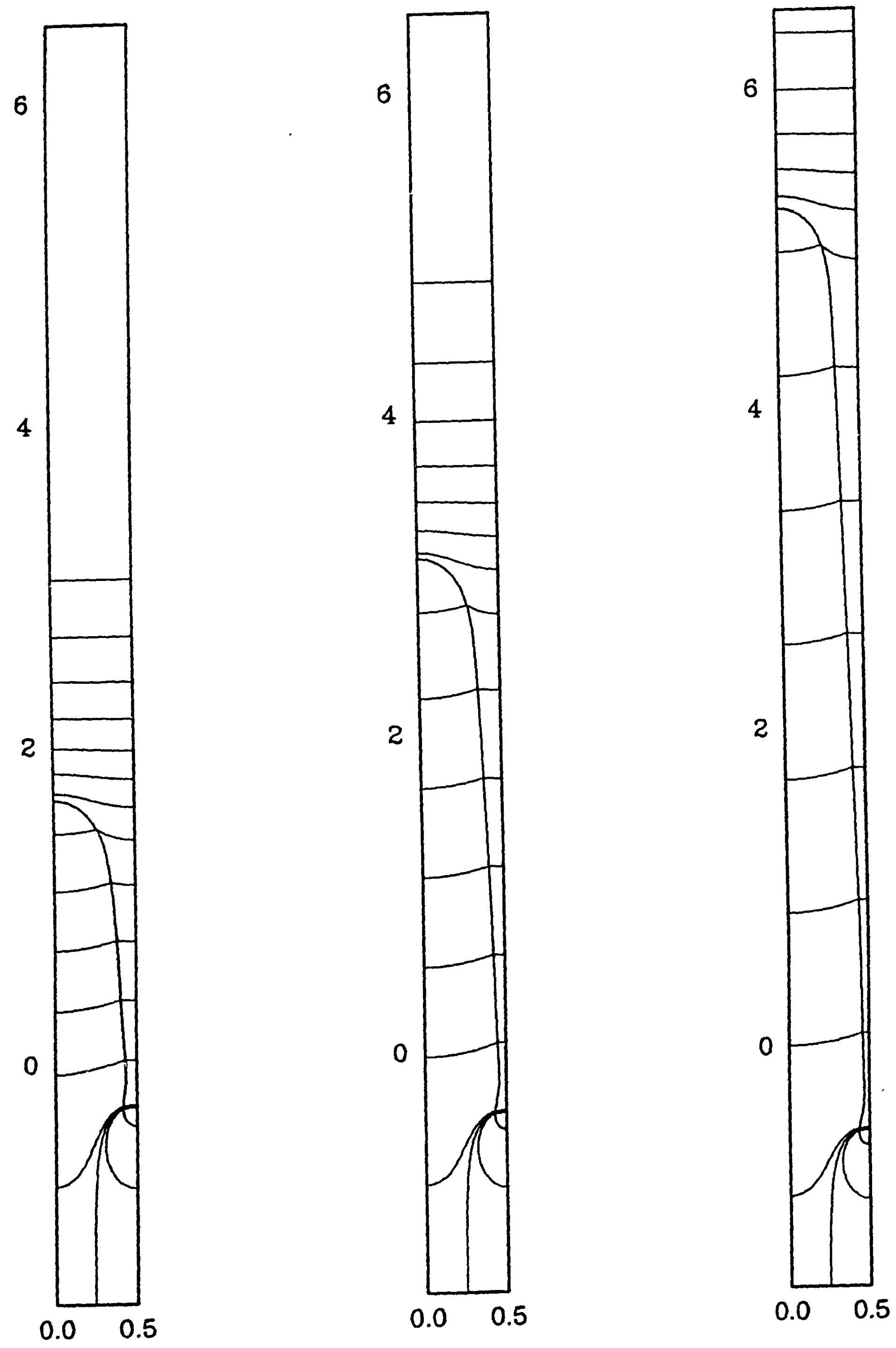

Figure 3.11: Half-cell shapes showing the dependence of interface shape on the dimensionless temperature gradient G: (a) $G = 4.5 \times 10^{-5}$, (b) $G = 3.0 \times 10^{-5}$, and (c) $G = 2.0 \times 10^{-5}$. All three cells were computed for $\lambda = 1$ and $P = 0.8$.

the y-direction in the sidewall region vary linearly linearly with G. This effect is accurately predicted by the asymptotic analysis in Chapter 5.

3.4.2 Effect of Surface Energy Γ

Bennett (1990) has shown that increasing Γ makes the planar interface more stable to low wavelength perturbations and moves the left border of the neutral stability curve towards higher wavelengths and growth rates. The neutral stability curve is also less flat at the bottom thereby reducing the likelihood of nonlinear interactions between families of cells at higher Γ. The effect of Γ on deep cells, however, is not well characterized. As already noted, the sidewall region has negligible curvature and the effect of Γ is hence minimal. The surface energy is clearly important in the cell bottom and probably helps to determine the shape of the tip of the cell. Calculations were performed by varying Γ while keeping the other dimensionless parameters in Table 3.2 constant to study the influence of the surface energy on the three regions. The results are presented in Fig. 3.12 and Fig. 3.13. In Fig. 3.12 the interface shapes computed by the numerical algorithm have been plotted for cells of the same spatial wavelength growing at identical growth rates into the same temperature gradient but having different surface energies. Fig. 3.13 is a plot of the variation of cell depth as a function of Γ for the cells shown in Fig. 3.12. Clearly, the slope of the slender region is independent of surface energy. In addition, the cell does not shift relative to the temperature field. The cell tip and bottom, however, change with the value of Γ used in the calculations. As the surface energy is decreased, the curvature of the cell bottom increases and the bottom becomes larger and more pendant. The cell depth, however, shows no monotonic change with the surface energy. As the surface energy is decreased along the top portion of the curve in Fig. 3.13 the cell aspect ratio A remains relatively uniform. A limit point in the curve is found where the surface energy has attained a value below which no steady cellular interfaces of the particular chosen wavelength exist. On the lower portion of the curve as the surface energy is increased, the cell gets rapidly shorter as the cell tip gets flatter. This cell then splits and the curve of solutions then intersects a second curve at a bifurcation point. This curve represents the family of cells having a spatial wavelength half that of the first family. These nonlinear interactions between families of cells are similar

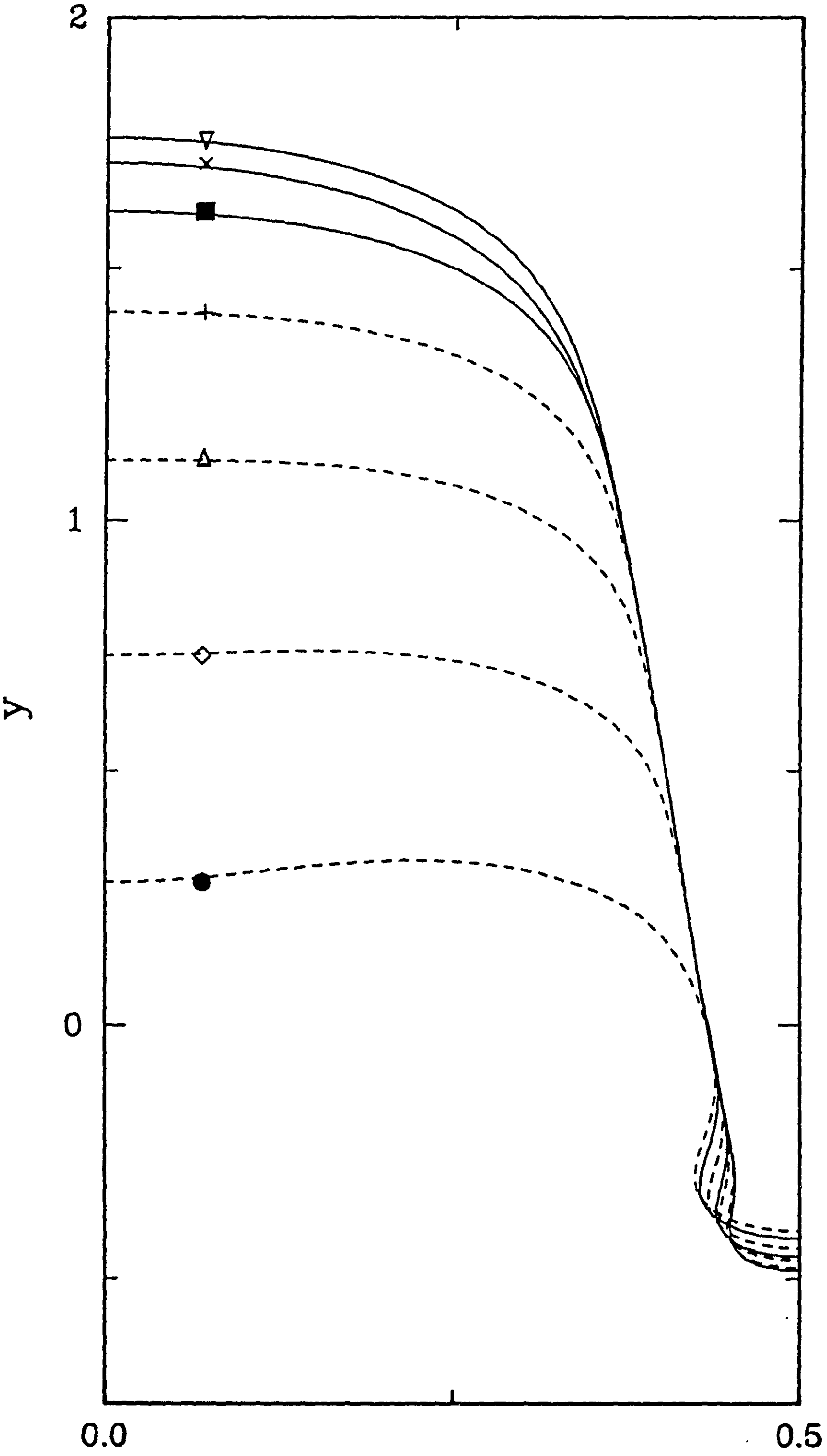

Figure 3.12: Sample half-cell shapes showing the dependence of interface shape on Γ. Letters correspond to solutions listed in Fig. 3.13. All other parameters were maintained at the values listed in Table 3.2.

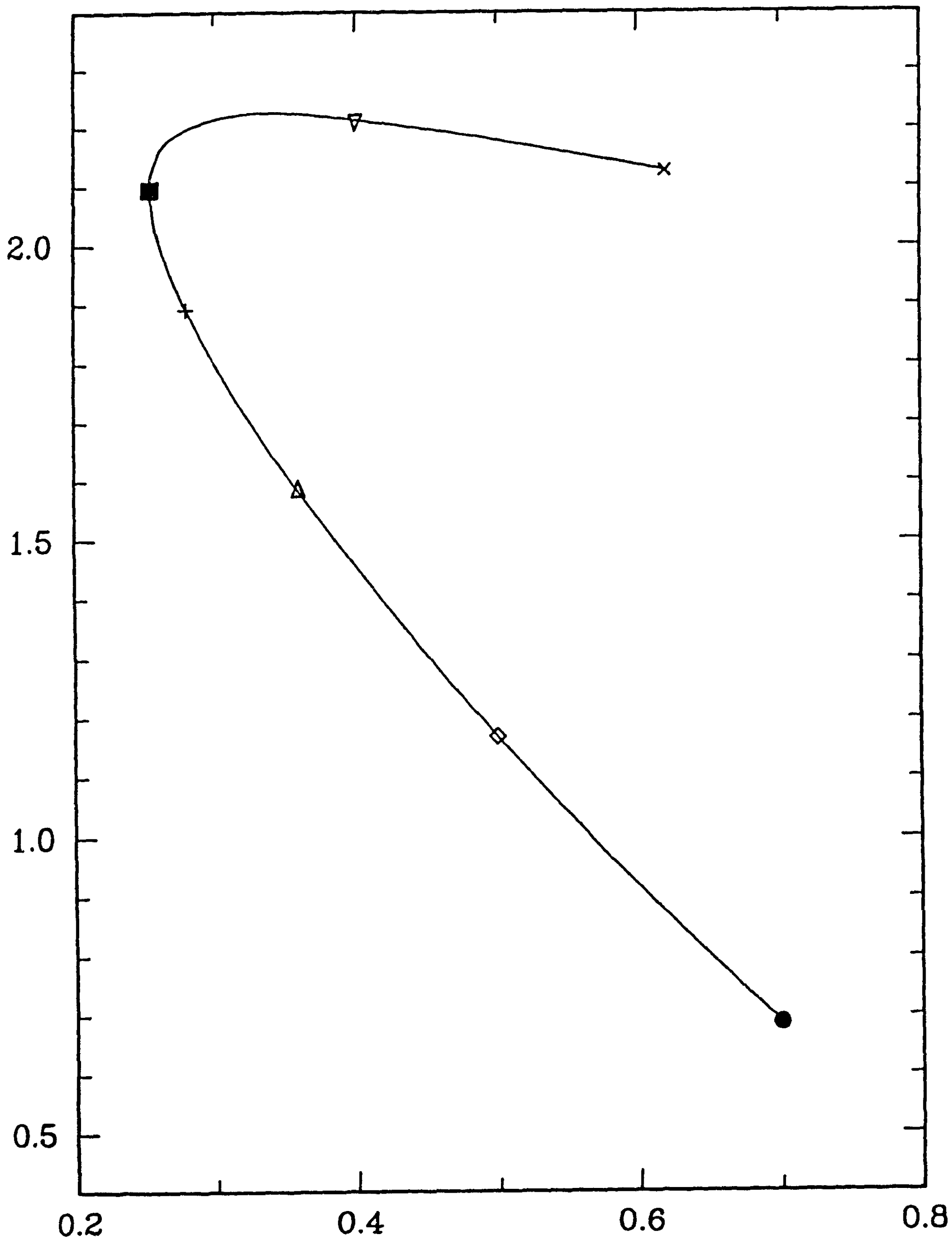

Figure 3.13: Dependence of cell aspect ratio A on surface energy $\dot{\Gamma}$. All other growth parameters are maintained constant at the values listed in Table 3.2.

to those seen for the evolution of cells with increasing growth rate (see Section 3.3). The shortening of cells with changing Γ takes place primarily through two mechanisms. First, as the cell bottom gets wider, the matching of the bottom with the sidewall takes place at a point where the groove between cells is also correspondingly wider, i.e., at a higher point along the sidewall. This effect tends to shorten the cell. Second, and more importantly, the tip gets progressively flatter and the matching of the cell tip with the sidewall takes place further down on the sidewall, thus reducing the length of the cell.

3.4.3 Effect of Segregation Coefficient k

Calculations were performed using the solutal model for different values of the segregation coefficient with all the other dimensionless parameters maintained constant at the values listed in Table 3.2. The results of these calculations are illustrated in Fig. 3.14 where the aspect ratio of the cells A is plotted as a function of k. The cells become increasingly smaller as the segregation coefficient is increased. The computation was discontinued beyond $k < 0.6$ as the cells became too small for the mixed Cartesian-cylindrical representation to be valid. In Fig. 3.15 sample interfaces from the family of solutions in Fig. 3.14 have been plotted. For small k the cells are extremely deep with a distinct slender sidewall region whose slope decreases as k is increased. Besides, the groove between cells becomes wider as the segregation coefficient is increased. The point along the cell near the bottom where the interface turns around approximately marks one end of the sidewall region; this point moves away from the center of the groove as k is increased. In addition, the cell moves down towards lower temperatures.

These characteristics of the sidewall are predicted by the asymptotic analysis presented in Chapter 5. As discussed in that chapter, the concentration at the cell bottom approximately equals $1/k$ and the increase in the aspect ratio of the cell as the segregation coefficient is increased is due to the corresponding increase in the solute concentration at the cell bottom.

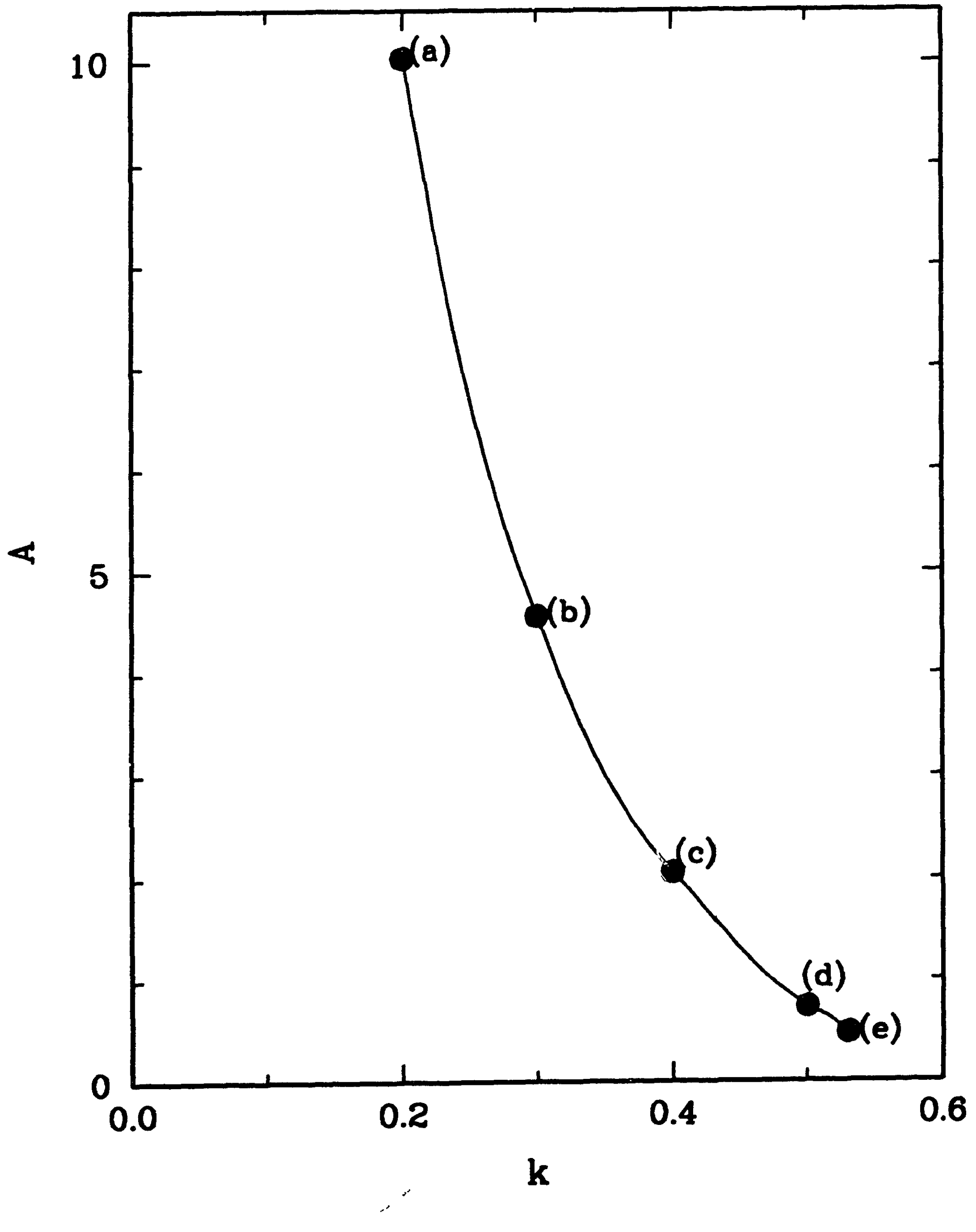

Figure 3.14: Dependence of cell aspect ratio A on segregation coefficient k. All other growth parameters were maintained constant at the values listed in Table 3.2.

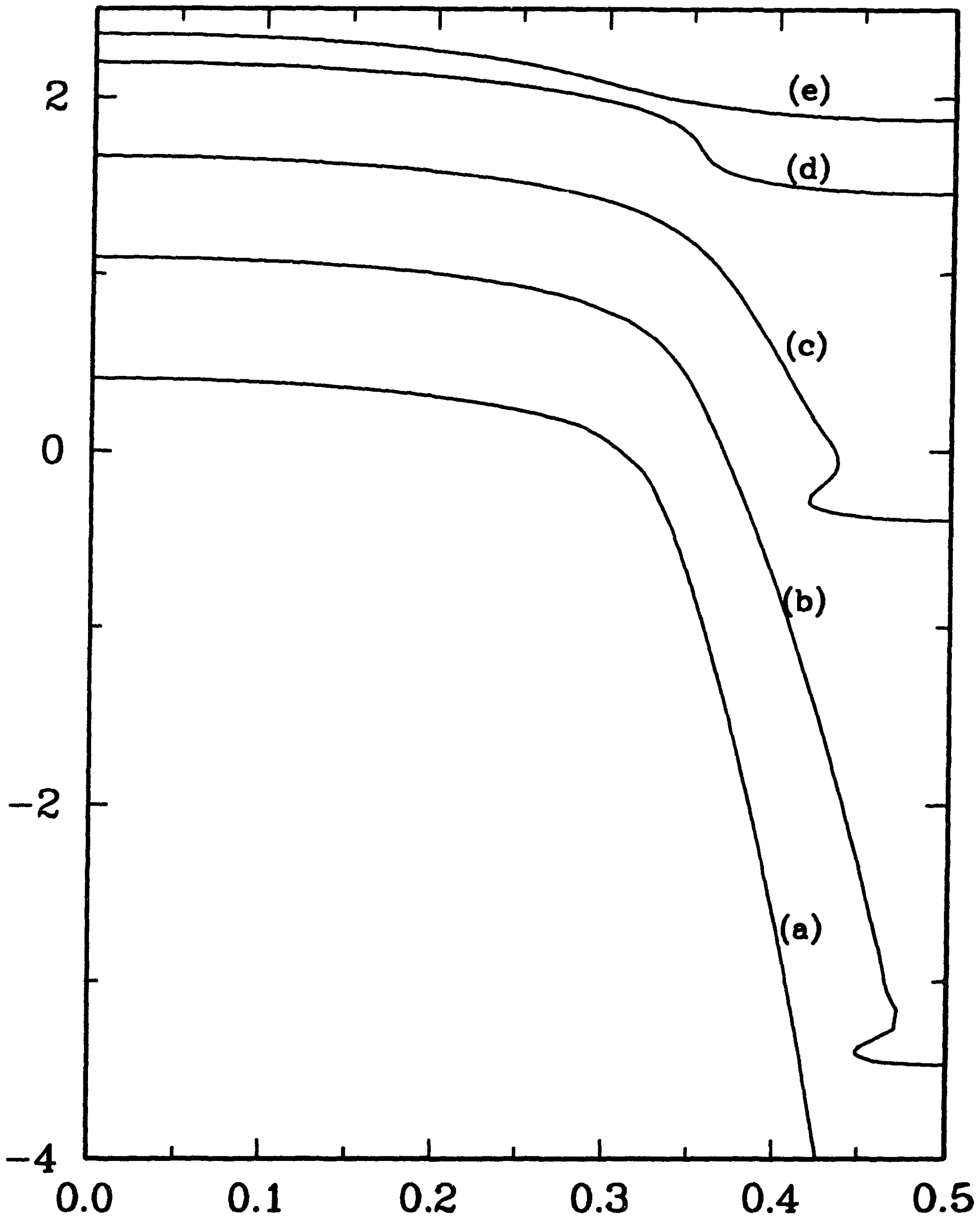

Figure 3.15: Sample hallf-cell shapes showing the dependence of interface shape on k. Letters correspond to solutions listed in Fig. 3.14.

3.4.4 Effect of Solute Diffusivity Ratio R_m

Among the parameters listed in Table 3.1, the solute diffusivity is the least accurately known. In fact, $\mathcal{D}_s$ is typically neglected when comparisons of experimental data with theory are made. While the solute diffusivity in metallic solids may well be small in comparison with the diffusivity in the liquid form (so that R_m can be neglected), for organic alloys it may not. As indicated in Section 1.3 estimates of R_m vary from $\mathcal{O}(10^{-1})$ to $\mathcal{O}(10^{-4})$ for organic alloys near their melting points. The study of the effect of the diffusivity ratio R_m on cell shape is therefore important.

To study the effect of R_m on the cell shape, finite element calculations were performed with changing R_m; all the other parameters were maintained constant at the values listed in Table 3.2. As R_m is decreased from the aspect ratio of the cell A increases linearly at first as shown in Fig. 3.16. When $R_m \ll 1.0$ there is a sharp increase in the length of the cell. Fig. 3.17 shows sample shapes from the family of solutions shown in Fig. 3.16. The groove between cells grows narrower and the cell bottom is attached to the sidewall at a much lower point as R_m is decreased. However, the slope of the sidewall remains constant. This is in agreement with the predictions of the asymptotic analysis presented in Chapter 5.

The increase in the aspect ratio of the cell as R_m is decreased can also be explained in another way. As mentioned before in this chapter, decreasing R_m is known to destabilize the system further by lowering the neutral stability curve towards lower growth rates. Thus any given growth velocity is moved further away from the critical value and the cell can be expected to be more nonlinear as shown in Fig. 3.16.

3.4.5 Effect of Liquidus Slope and Anisotropy

It is readily obvious from the solutal model equations Eqns. (2.64)-(2.71) that both the dimensionless liquidus slope m and the temperature gradient G affect the solution only through the Gibbs-Thomson equation Eq. (2.68). Indeed for regions of the cell where the interface curvature is small, the two parameters can be combined since the Gibbs-Thomson

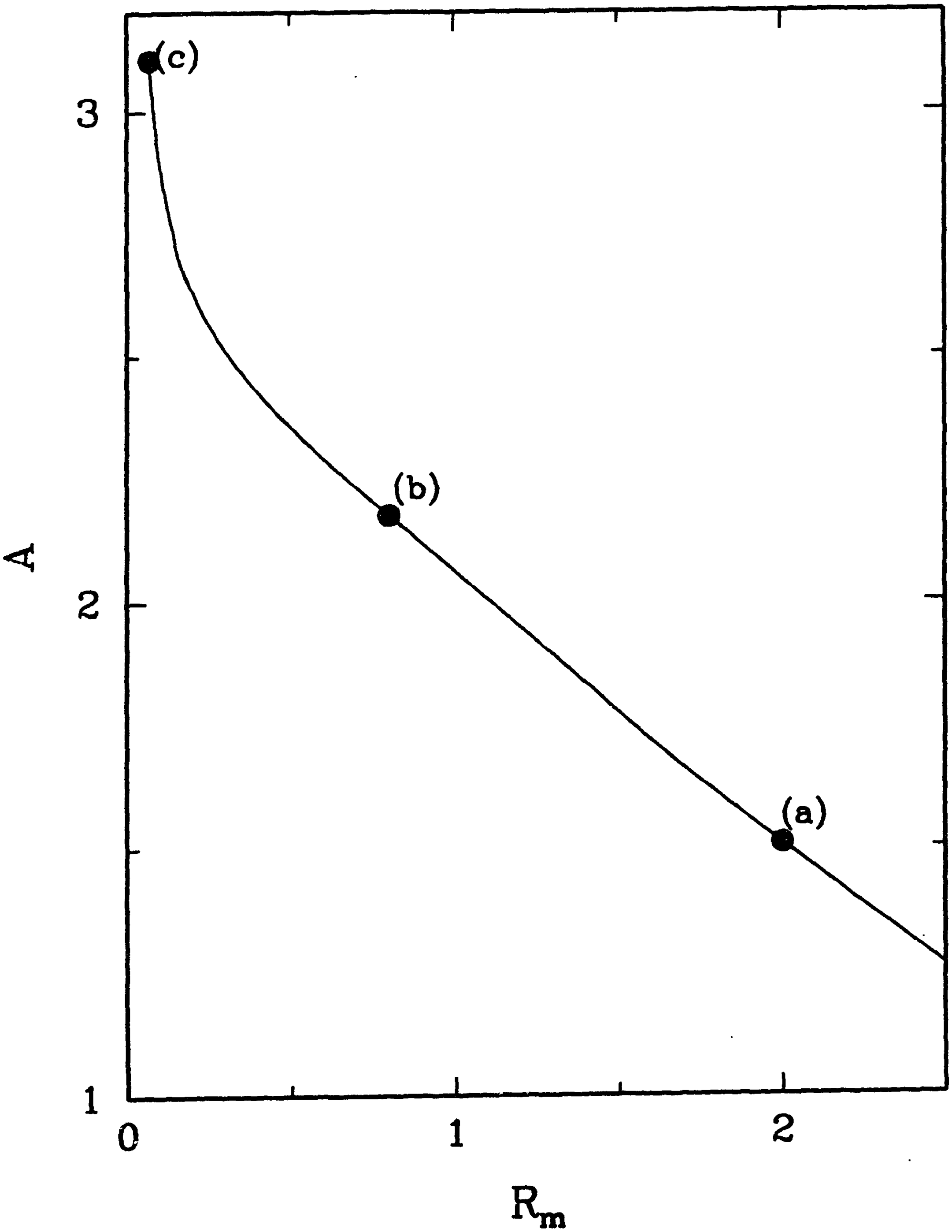

Figure 3.16: Dependence of cell aspect ratio A on solute diffusivity ratio R_m. All other growth parameters are maintained constant at the values listed in Table 3.2.

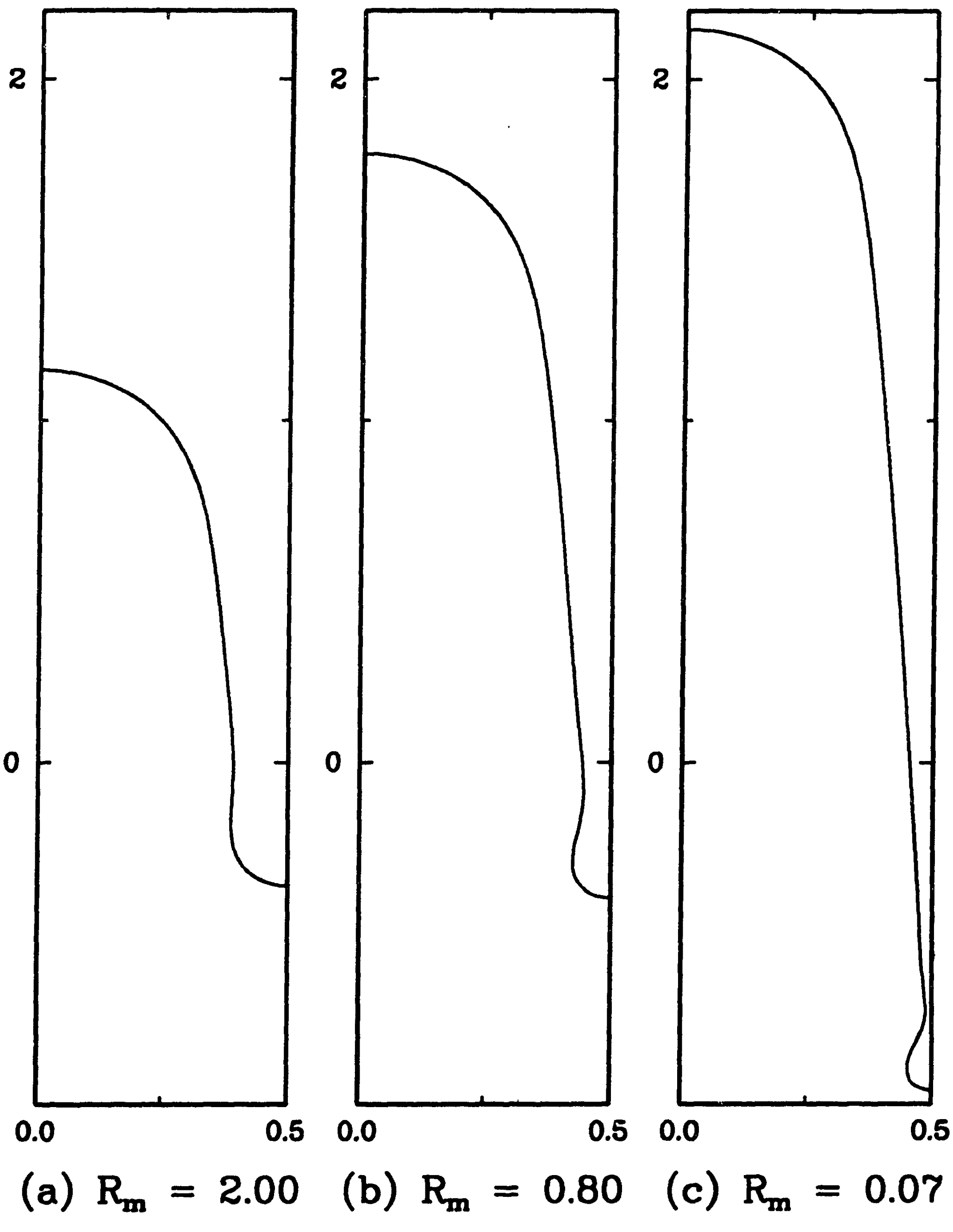

Figure 3.17: Sample half-cell shapes showing the dependence of interface shape on R_m. Letters correspond to solutions listed in Fig. 3.16.

equation can be rewritten simply as

$$\left[c_m = c_o + \frac{G}{m}y\right]_{\text{interface}} \quad , \tag{3.5}$$

where c_o is a reference solute concentration given in terms of the reference temperature T_{ref} as

$$c_o = \frac{T_{\text{ref}} - 1}{m} \quad . \tag{3.6}$$

Thus the length of the cell is primarily determined by the ratio G/m and it is expected that the parametric study of the dimensionless temperature gradient in Subsection 3.4.1 can be extended to the dimensionless liquidus slope m; any effect of G on the length of the cell can be essentially duplicated by a reciprocal change in m.

The effect of anisotropy of the surface energy ϵ_a on the cell shape is more complex. Calculations show that the at higher values of the anisotropy the range of allowed growth rates at a fixed wavelength is increased. These calculations could be continued only when the finite element method was modified to circumvent the problem caused by the narrowing of the grooves between cells that was alluded to in Section 3.3. These results are presented in Chapter 5.

3.5 Pattern Selection

Calculations were performed with specific values of the dimensional growth rate V, measured in units of the critical value $V = V_c(\tilde{\lambda}_c)$ and the dimensional wavelength $\tilde{\lambda}$. When the growth rate is constant, the dimensionless value of the pull rate given by the Peclet number P and the dimensionless temperature gradient G increase proportionally as the wavelength $\tilde{\lambda}$ is increased. On the other hand, the dimensionless capillary length Γ decreases as the inverse of $\tilde{\lambda}$.

Continuous families of cell shapes were computed for a range of wavelengths at each growth rate. These families of cells are plotted in Fig. 3.18 as a function of the dimensionless cell depth Δ for various dimensionless wavelengths λ at various growth rates, measured in units of $V_c(\tilde{\lambda}_c)$. For any growth rate there is a deepest cell computed by the finite element

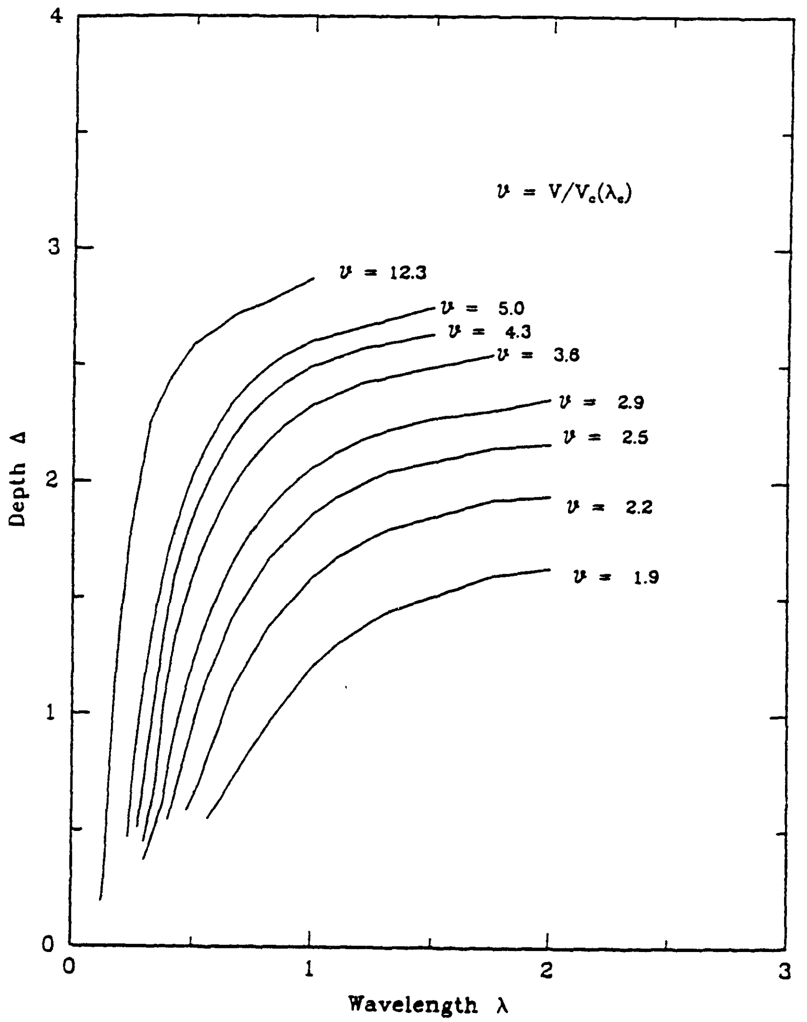

Figure 3.18: Dependence of dimensionless cell depth Δ on dimensionless spatial wavelength λ for specific values of the growth rate (in units of $V_c(\tilde{\lambda}_c)$) for the system parameters listed in Table 3.1.

algorithm. The wavelength of this form decreases from the value λ_c for $V = V_c(\tilde{\lambda}_c)$ at the onset of solidification to values that are close to the left side of the neutral stability curve.

With increasing V, finite amplitude cells are only seen for wavelengths below a decreasing maximum value. For the calculations examined here and those presented in Section 3.6, the termination of the curves at the largest wavelengths corresponds to the limit points observed in the calculations at constant λ and increasing P like those in Fig. 3.9. Near this limit the cellular form is nonunique; shorter cells exist on the branch with decreasing λ that was not computed.

The maximum in cell depth is more dramatically illustrated in Fig. 3.19 where the the curves on Fig. 3.18 have been replotted as a function of the aspect ratio of the cell for each calculation. The aspect ratio is defined as

$$A \equiv \frac{\tilde{\Delta}}{\tilde{\lambda}} \quad , \tag{3.7}$$

where $\tilde{\lambda}$ is the wavelength of the cell in the particular calculation. The peak of the curves $A = A(\lambda, v)$ sharpen with increasing V and move towards the left boundary of the neutral stability curve. Fig. 3.20 is a plot of the conditions in $V - \tilde{\lambda}$ space where cells with the maximum aspect ratio exist. The marginal stability curve is plotted for comparison. The reason that a portion of the curve connecting these peaks falls outside the marginal stability curve can be traced to the subcritical bifurcation of solution families from the planar state; thus, some cellular solutions actually exist at growth rates that are below critical for that wavelength. An ad hoc assumption of selection of the deepest cells at any wavelength would result in a selection curve as shown in Fig. 3.20. Another assumption is that of Nash & Glicksman (1971) who propose that the interface growing at the greatest velocity is the one selected among possible states at any wavelength. This corresponds to the set of limit points. This assumption is discussed in greater detail with reference to the CBr_4-Br_2 system in Section 3.6. It should be pointed out that there is no theoretical or physical basis to support either of these criteria.

The existence of a true asymptotic limit in which P and Δ tend to infinity as λ tends to a limiting value is impossible because of the closed shape of the neutral stability curve. Bennett *et al.* (1987) have shown that the restabilization of the planar interface for high

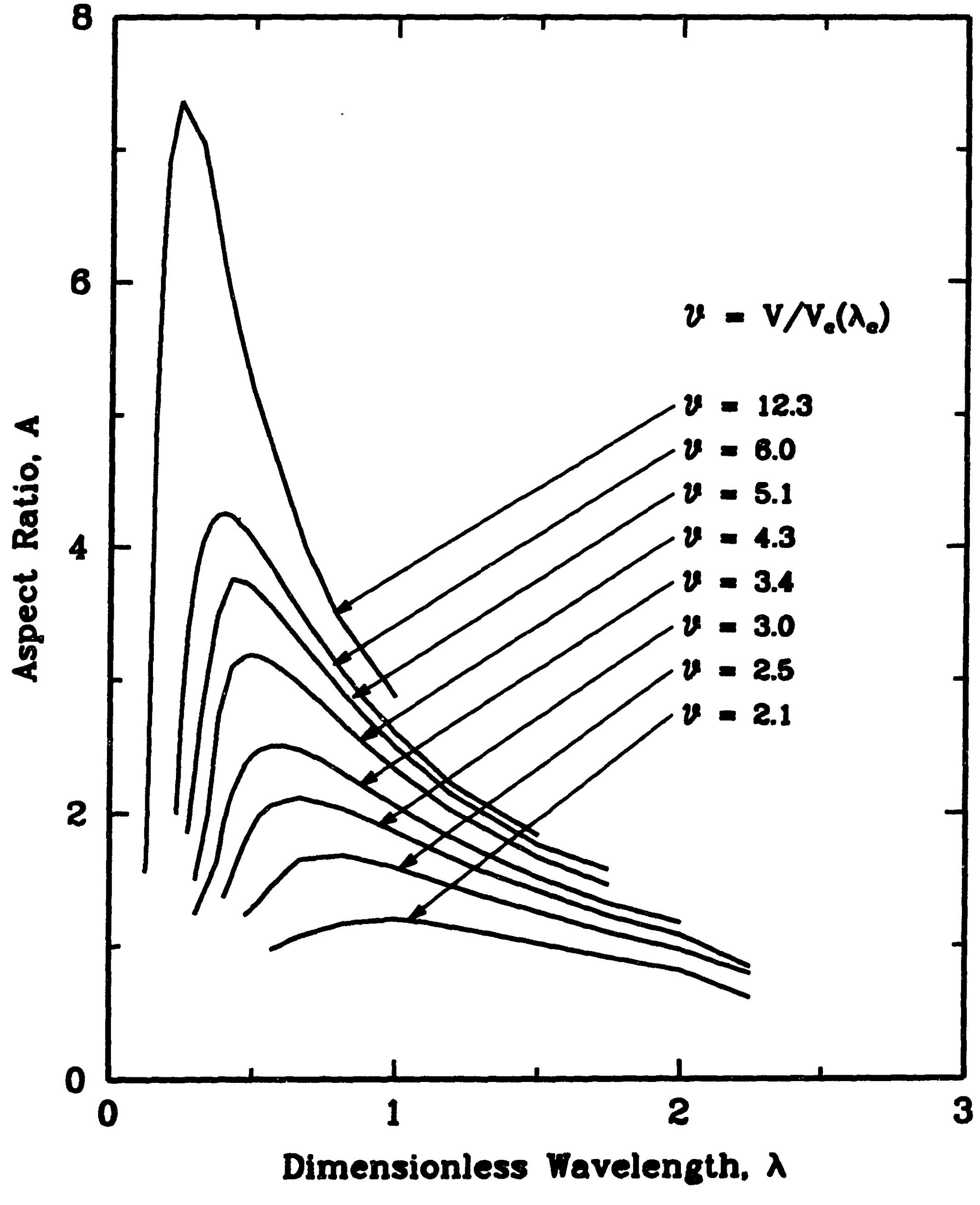

Figure 3.19: Dependence of cell aspect ratio A on dimensionless spatial wavelength λ for specific values of the growth rate (in units of $V = V_c(\tilde{\lambda}_c)$).

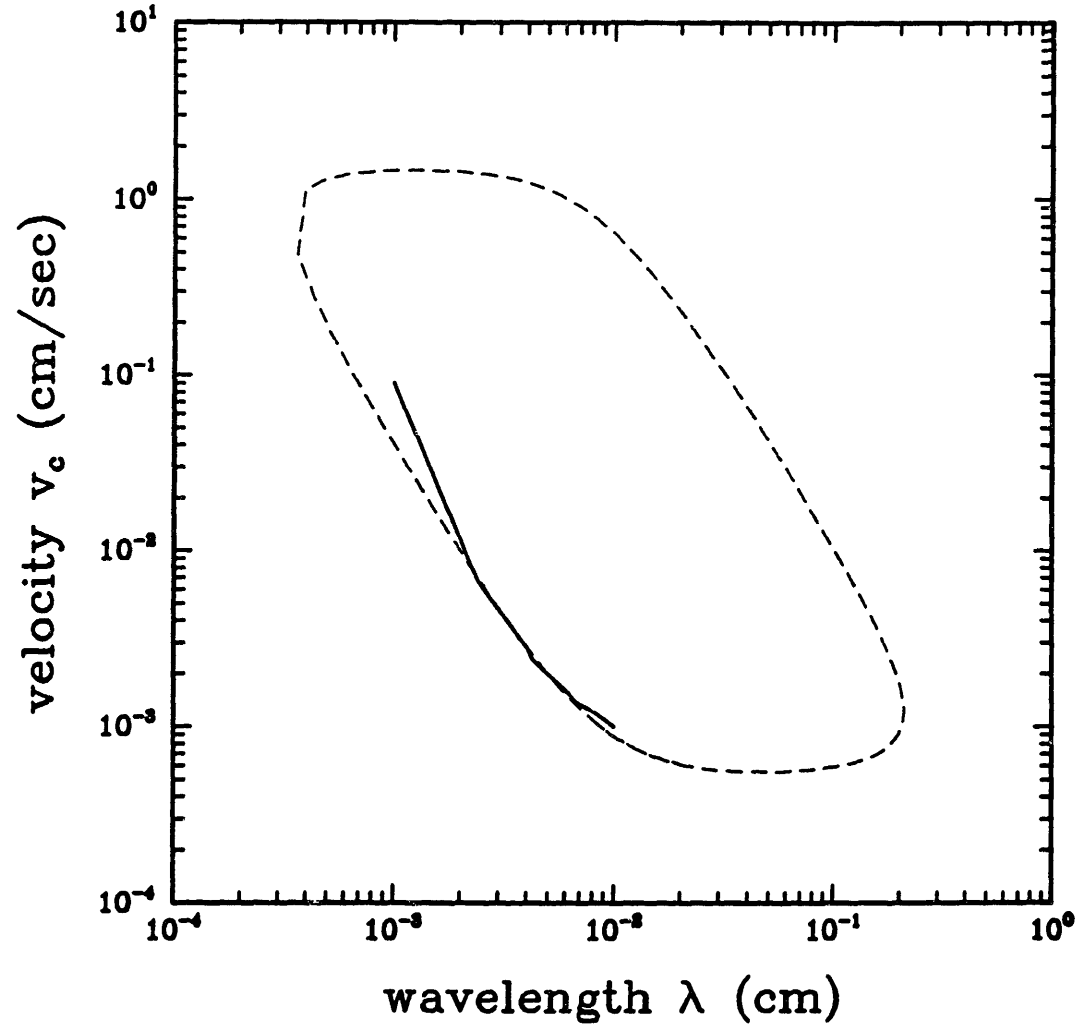

Figure 3.20: Curve of cells with the maximum aspect ratio plotted in $V - \bar{\lambda}$ space along with the marginal stability curve.

Peclet numbers leads to shape families for finite amplitude cells for given λ that bifurcate from the planar form at the lower critical value of P and reconnect at the upper one. Then cells with smooth bottoms will not tend to infinite depth, no matter what wavelength is considered.

Sample cell shapes computed along the curve for $V = 2.3V_c(\tilde{\lambda}_c)$ are shown in Fig. 3.21. Cell shapes with the smallest wavelengths have bulbous bottoms caused by the increasing value of Γ. The depth of the cell decreases with decreasing λ as the thickness and length of the groove between cells are adjusted to accommodate the matching of the tip and enlarging bottom of the cell. Cell shapes computed with the largest wavelengths have small bottoms connected to thin grooves so as to accommodate the small value of Γ. The increasing value of the temperature gradient with increasing λ increases the slope of the sidewall region as shown in Chapter 5 and the groove of the cell can thus be narrowed over a shorter length of the cell; the length of the cell thus decreases at higher wavelengths. The shape of the cell tip varies very little with the varying wavelength. The maximum wavelength for calculations at a specific growth rate is caused by the envelope of turning points $P_1 = P_1(\lambda)$ in the families of deep cells illustrated in Fig. 3.7 and Fig. 3.9. When plotted on Fig. 3.18 the results illustrated in these figures corresponds to vertical slices at the corresponding wavelengths.

Sample shapes in the family of cells for $V = V_c(\tilde{\lambda}_c)$ are shown in Fig. 3.22 as examples of some of the deepest cells computed in this study. The structure of the cells described above also holds good for this growth rate. The greater length of the cells at higher growth rate is a result of the changes in the structure of the cell bottom and cell tip as noted in the calculations shown in Fig. 3.10 for changing P with fixed λ.

3.6 Comparison with Experiments

Numerical calculations were performed using the solutal model for comparison to the data of de Cheveigné *et al.* (1986) for the CBr_4-Br_2 alloy system. This data set was selected because it addresses two important issues: the initial development of cellular morphologies from the planar state and the evolution of cellular wavelength with increasing growth rate.

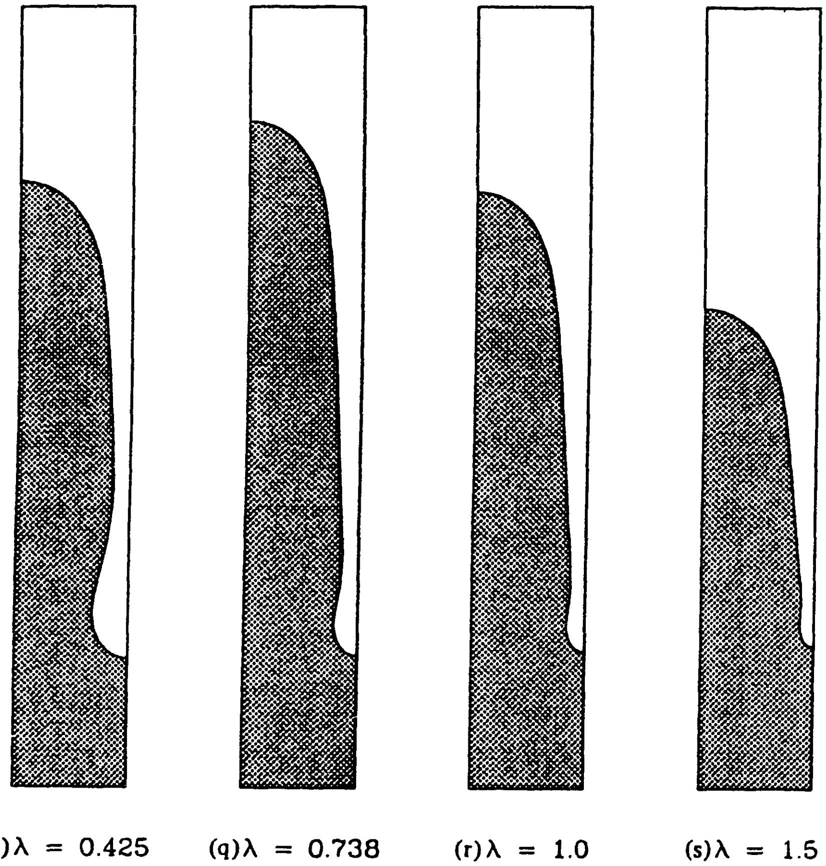

Figure 3.21: Sample half-cell shapes for representative calculations from Fig. 3.19 and $V = 2.9V_c(\lambda_c)$. The letters correspond to points shown there. The wavelength has been normalized so that the aspect ratio of the cells A can be compared directly.

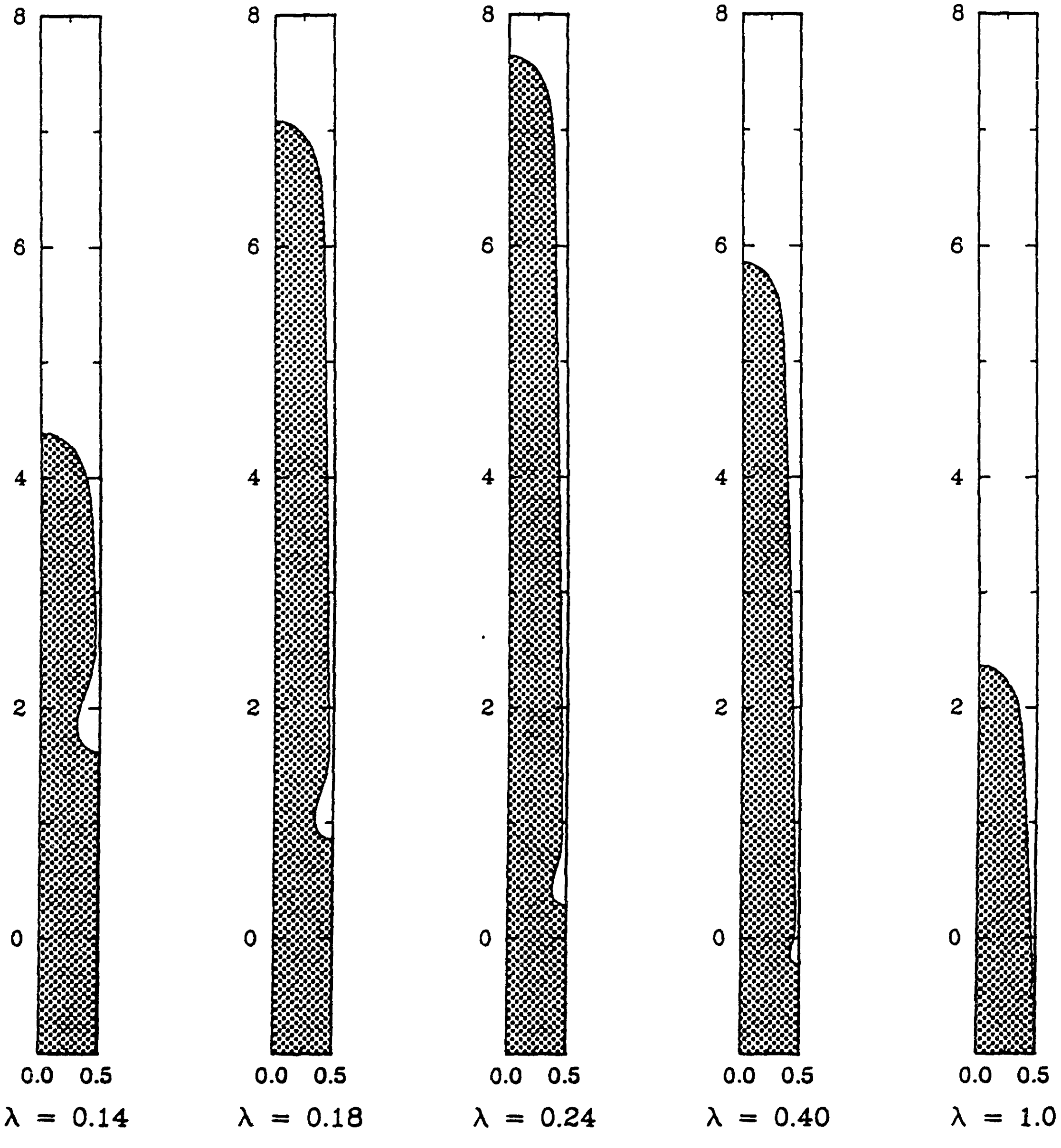

Figure 3.22: Sample half-cell shapes for representative calculations from Fig. 3.19 and $V = 12.3V_c(\lambda_c)$. The letters correspond to points shown there. The wavelength has been normalized so that the aspect ratio of the cells A can be compared directly.

Also, this data set was used in a similar comparison by Kessler & Levine (1989) with calculations performed using boundary integral numerical methods. Unfortunately, some of the thermophysical properties needed to describe the solutal model in the CBr_4-Br_2 are not accurately known. Bromine is generated *in situ* by spontaneous photo-decomposition of CBr_4 and the actual composition of the alloy can therefore not be determined with accuracy. In addition, the solid phase solute diffusivity is not known. However, the data on evolution of deep cellular interfaces and the selection of the spacing of these morphologies in the work of de Cheveigné *et al.* (1986) is the most extensive and has therefore been selected. The results of the comparison in the deep cellular regime are presented here; the examination of the results near the stability limit have been detailed in Ramprasad *et al.* (1991).

The thermophysical properties used in the analysis are listed in Table 3.5 and are those suggested by de Cheveigné *et al.* (1986), except for the value of the solute diffusivity $\mathcal{D}_s$ in the solid; $\mathcal{D}_s$ was chosen to be (1/20)th of the value in the melt ($R_m = 0.05$) in the calculations to reproduce the diffusionless behavior of a diffusionless solid while retaining the important mechanism for transporting solute through the solid phase and back into the melt by melting in the bottom of the grooves; see the discussion in Section 2.3.

The neutral stability results shown in Fig. 3.23 are in reasonable agreement with similar calculations by de Cheveigné *et al.* (1986) shown in Fig. 3.24. The neutral stability curves $V = V_c(\lambda)$ predicted for the values of the two temperature gradients $\tilde{G} = 120°K/\mathrm{cm}$ and $\tilde{G} = 70°K/\mathrm{cm}$ used by de Cheveigné *et al.* are plotted in Fig. 3.23.

Finite element calculations were conducted for the constant temperature gradient $\tilde{G} = 70°K/\mathrm{cm}$ for which the most dangerous wavelength was predicted by linear analysis to be $\lambda_c = 201.64\mu\mathrm{m}$ and the corresponding value of the growth rate is $V = V_c(\tilde{\lambda}_c) = 4.760\mu\mathrm{m/sec}$. It is important to note the flatness of these neutral stability curves about $\lambda = \lambda_c$. As with the system discussed in Section 3.5 over a decade of wavelengths are destabilized with only a small percentage increase in the growth rate above $V = V_c(\tilde{\lambda}_c)$. As discussed before this flatness leads to codimension two bifurcations for small increases in the growth rate which split single cells into two; this effect is demonstrated again below.

The data from de Cheveigné *et al.* for the evolution of the wavelength of finite amplitude

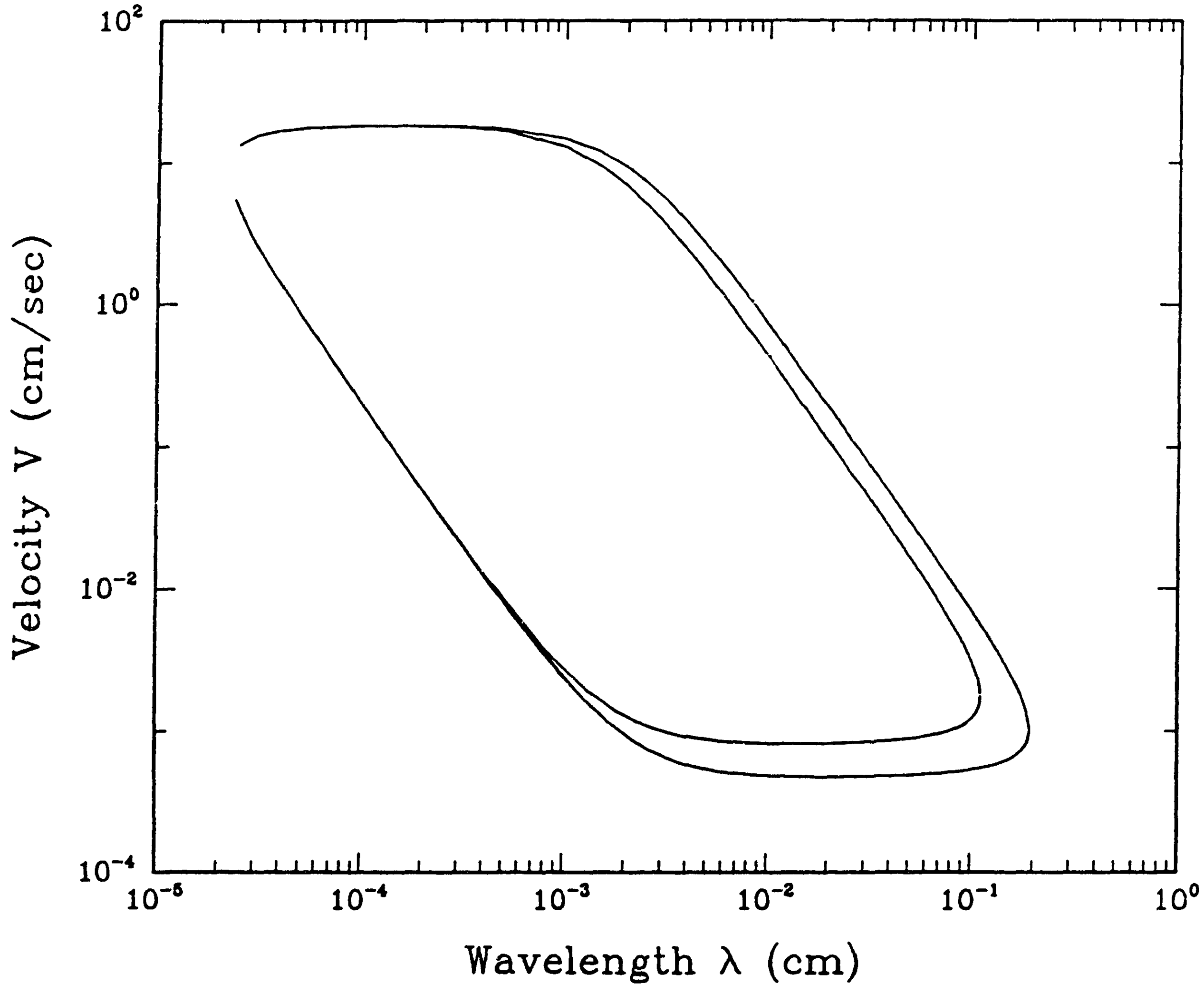

Figure 3.23: The marginal stability curves computed from linear theory for the CBr_4-Br_2 alloy system for the two temperature gradients, $\tilde{G} = 120°K/\text{cm}$, and $\tilde{G} = 70°K/\text{cm}$. The corresponding curves reported by de Cheveigné *et al.* (1986) are shown in Fig. 3.24.

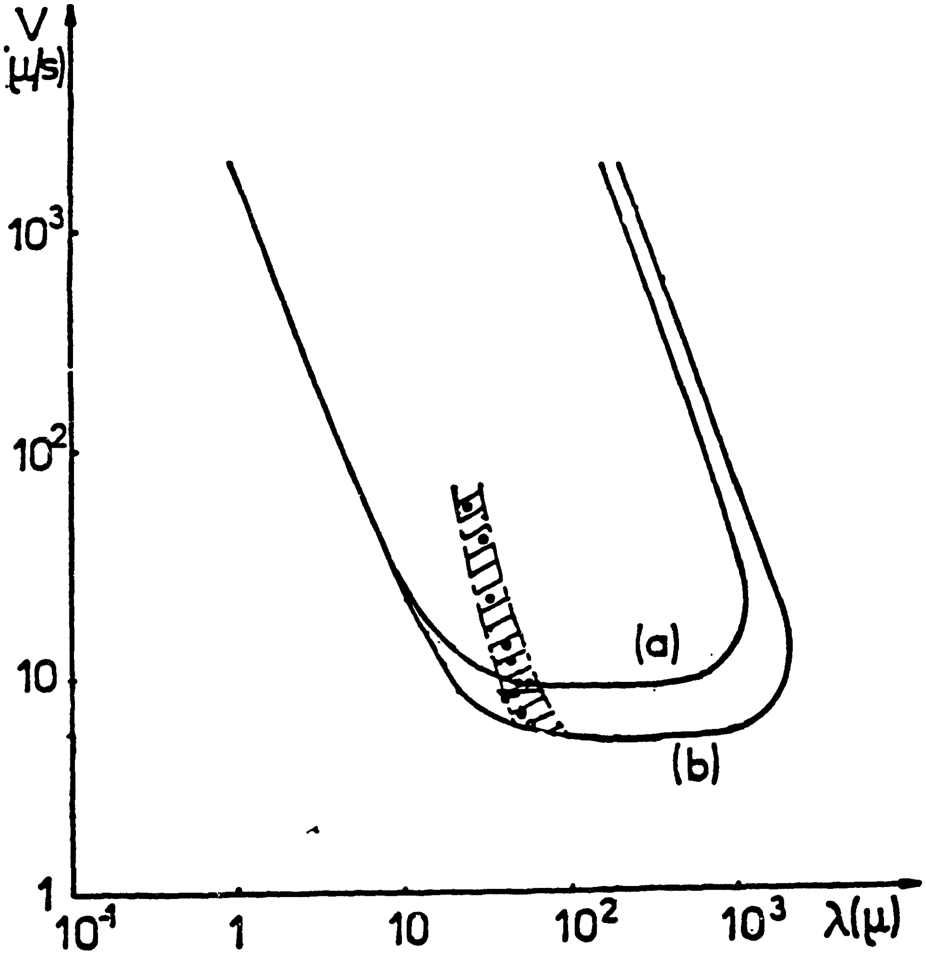

Figure 3.24: Experimentally observed wavelength as a function of in experiments with a CBr_4-Br_2 alloy. The full curves are the marginal stability curves for two temperature gradients. (a) and full circles: $\tilde{G} = 120°K/\mathrm{cm}$, (b) and empty circles: $\tilde{G} = 70°K/\mathrm{cm}$ (from de Cheveigné *et al.* 1986, p. 2099).

cells with increasing V (Fig. 3.24) shows that no observations for either gradient falls near the critical wavelength. For each gradient the wavelength of the cell measured at the lowest growth rate was approximately two times smaller than the value predicted by linear theory; we return to this observation below.

Finite element calculations of steady state interfaces were performed for discrete values of the spatial wavelength with varying growth rate; this variation was achieved by changing the dimensionless growth rate, $P = V\tilde{\lambda}/D$. As described in Section 3.5, families of cellular interface shapes with spatial wavelengths that are integer submultiples of the selected value bifurcate from the planar state at particular values of P that correspond to points on the neutral stability curve. This evolution of the steady state families with increasing P is shown schematically in Fig. 3.25 by a plot of the cell depth D as a function of P. Sample interface shapes are included as inserts in this figure. The shallow cellular interface solutions were obtained by us (Ramprasad *et al.* 1991) using the Mongé representation of the interface applied by Bennett (1990).

As with the system discussed in Section 3.5, steadily solidifying cells with wavelength equal to λ_c only exist for values of P between the critical value and the value of a secondary bifurcation point $P = P_2$ where this family (the λ_c-family) joins to one composed of cells with half the spatial wavelength (the $\lambda_c/2$-family); along the λ_c family of solutions the cells get increasingly indented at the tip near the bifurcation point and split into two cells at the value $P = P_2$. This narrow interval of existence of cells with the wavelength predicted by linear theory (expressed in terms of the growth rate as $4.76\mu\text{m/sec} \leq V \leq 4.88\mu\text{m/sec}$) leads to serious doubt whether these cells have been seen experimentally, since the stated accuracy of the growth rate in the experimental system is at best $\pm 0.1\mu\text{m/sec}$ (de Cheveigné *et al.* 1986).

The splitting of the spatial wavelength continues with increasing growth rate. Cells with the wavelength $\lambda_c/2$ do not exist beyond a limit point at which the family of solutions reverses to decreasing values of P before joining the family of cells with a wavelength $\lambda_c/4$ at another bifurcation point. As the growth rate is increased towards the limit point, the cells again become deeper and flatter at the top. After the solution family turns around at the limit point, the cells are seen to have an indentation at the tip that leads to tip-splitting.

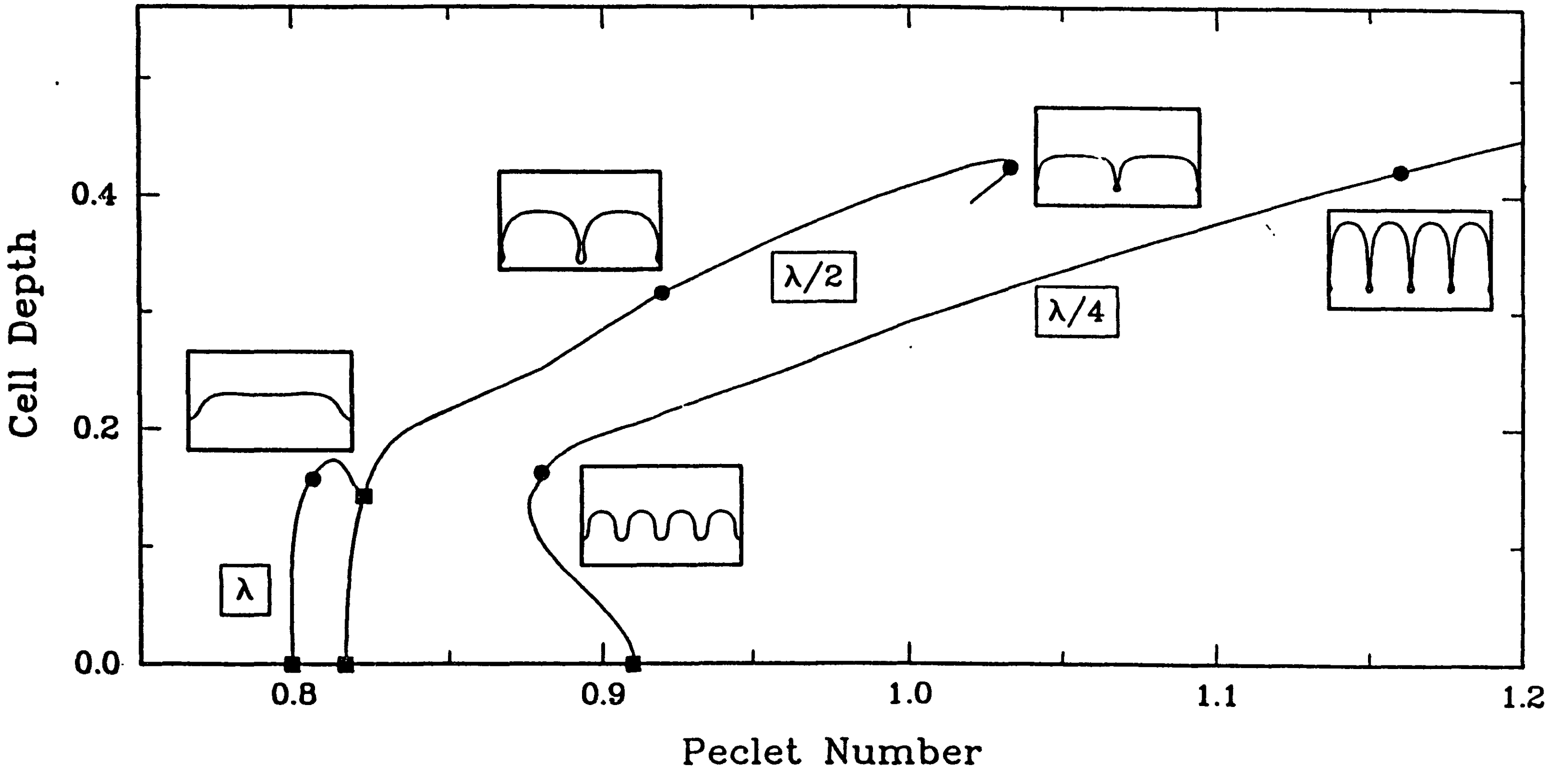

Figure 3.25: Families of steady-state cellular shapes with spatial wavelengths that are an integer fraction of the critical value predicted by linear theory λ_c, as a function of the cell aspect ratio in experiments with CBr_4-Br_2 alloy. Sample half-cell shapes are included for reference.

The limit point occurs at a growth rate less than 25% above the value at onset $V = V_c(\tilde{\lambda}_c)$.

In agreement with the results of Section 3.5, the computations with the CBr_4-Br_2 alloy system also show that deep two-dimensional interfaces are possible for a range of spatial wavelengths at any value of the growth rate; no selection of the primary spacing of steady-state shapes is seen. Sample families of cells were computed with continuously varying the wavelength at a fixed growth rate for the thermophysical properties listed in Table 3.5 and are displayed in Fig. 3.26. Each family is terminated at the highest wavelength by a limit point, such as shown in Fig. 3.25, that exist as a two-dimensional fold in the solution family in the two-dimensional parameter space spanned by growth rate and wavelength. Cells with low wavelengths (near the left border of the marginal stability curve in Fig. 3.23) were difficult to compute because the amplitude of the cell decreased rapidly as the stability curve was approached. Unlike Section 3.5, no attempt was made here to complete these calculations.

The predictions for the evolution of the continuous band of cellular wavelengths with increasing growth rate are compared with the experimental data of de Cheveigné *et al.* (1986) on Fig. 3.24. The result of this comparison is shown in Fig. 3.27. The solid curve is the curve of limit points that terminates the curves for fixed V and varying λ. The dashed curve marks the calculations performed with the lowest wavelength. The reason that the calculations could be continued for values of λ and V outside the neutral stability curve is the existence of subcritical states along the portion of the neutral stability curve that bounds low wavelengths. We have discussed the subcritical bifurcation from the planar state for low wavelengths in detail in Ramprasad *et al.* (1991).

The curve of limit points evolves with increasing V approximately as $V^{-1/2}$, as predicted by Kessler & Levine (1989) for their calculations for the CBr_4-Br_2 system. The location of this curve for the temperature gradient $\tilde{G} = 70°K/\mathrm{cm}$ does not agree with experimental data, contrary to the calculations reported by Kessler & Levine with the higher temperature gradient $\tilde{G} = 120°K/\mathrm{cm}$ which fit the data well. It is important to note that the calculations show a distinct dependence of the solution structure on the temperature gradient $\tilde{G}$ that is not present in the experimental data of de Cheveigné *et al.* (1986).

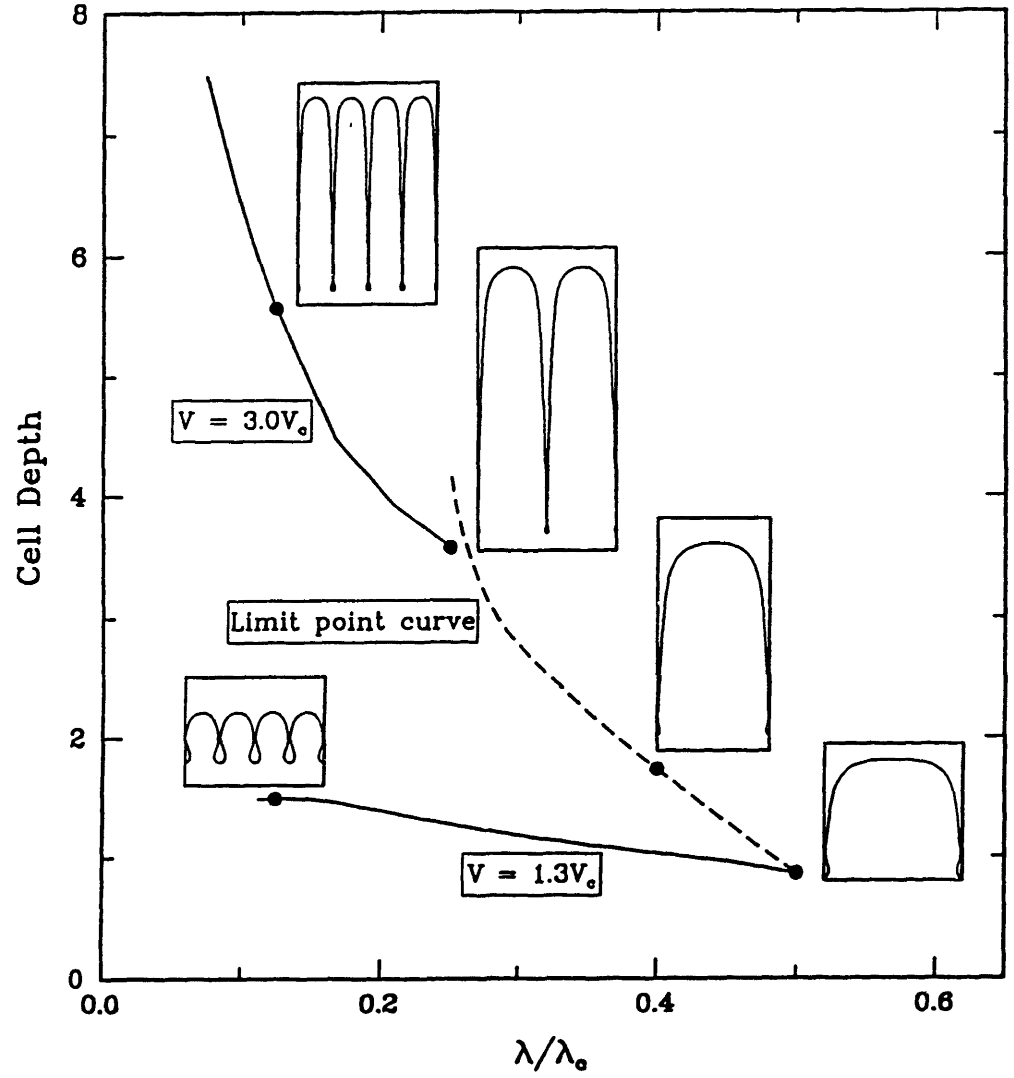

Figure 3.26: Representation of continuous band of wavelengths as a function of λ/λ_c and the cell aspect ratio at selected fixed growth rates in experiments with the CBr_4-Br_2 alloy. Sample half-cell shapes are shown for reference.

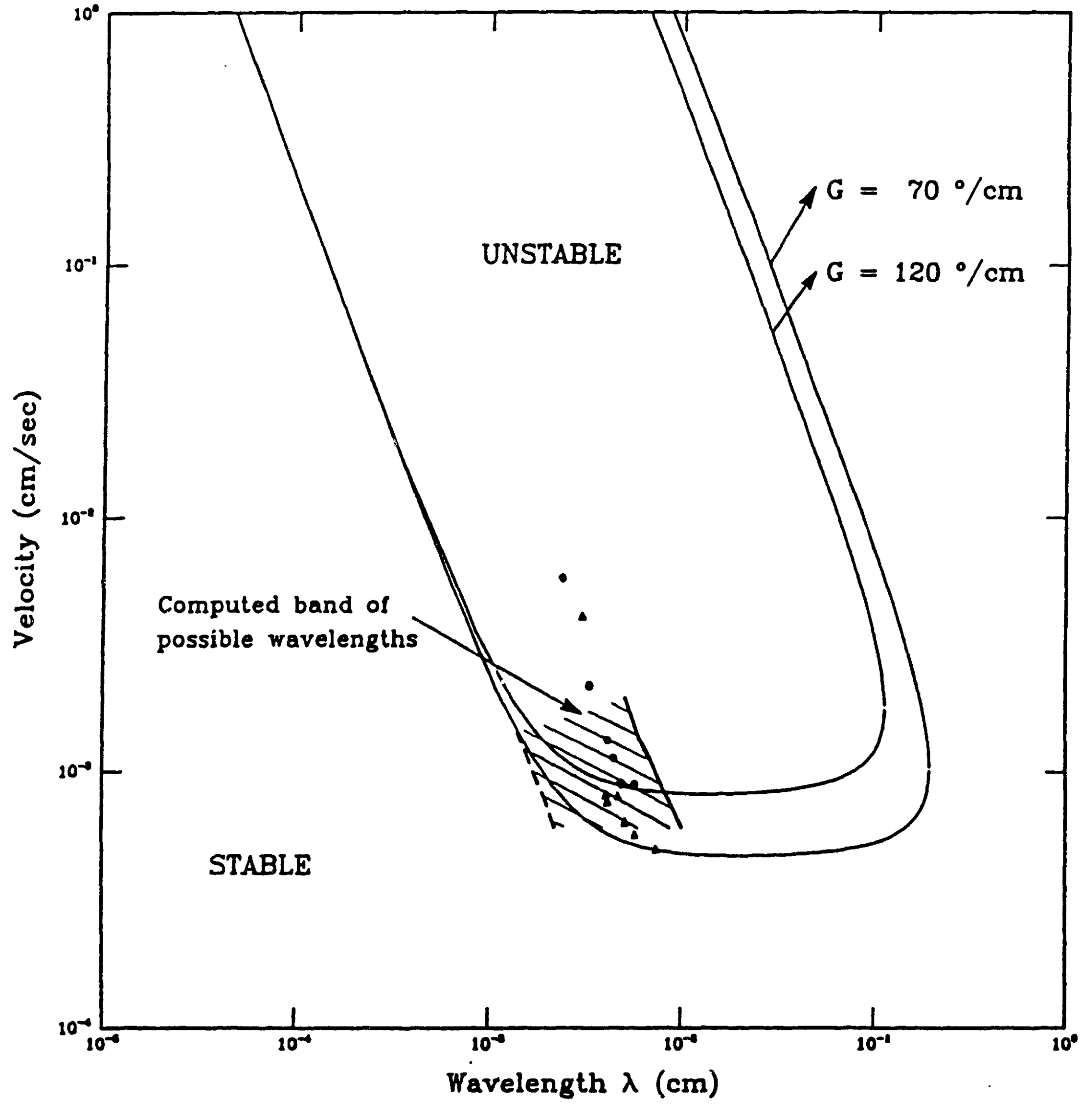

Figure 3.27: Comparison of continuous band of wavelengths with experimental data for the CBr_4-Br_2 alloy.

Sample interface shapes with varying wavelengths and and fixed growth rates are shown as inserts in Fig. 3.26. The increased importance of the surface energy on the curvature of the bottom of the deep cell is obvious at both growth rates shown. An attempt was made to compare these cellular shapes directly to those observed by de Cheveigné *et al.* (1986). This comparison is shown in Fig. 3.28 for cells with a wavelength of $\lambda = 50\mu$m and $V = 3.0V_c(\tilde{\lambda}_c)$. The computed cell shape is shown along with a picture taken from the experiment. The overall shape predicted by the calculations is in reasonable agreement with the experiments everywhere, except in the groove. The aspect ratio of the cell predicted by the analysis is 3.57 compared to 4.10 measured from the picture. This difference may result from a difference in the phase behavior of the alloy in the groove or from errors in the thermophysical properties used in the analysis.

For example, the depth of the cell is sensitive to the value of the diffusivity ratio R_m, which sets the rate of solute transfer from the groove into the surrounding solid. Decreasing R_m from 0.05 to 0.025 increased the aspect ratio of the cell to 4.20 which matches well with the experiment. In addition, a real alloy may form a eutectic in the groove where the composition of the alloy becomes high. Then an interlamellar phase forms between the adjacent cells instead of the finite length groove predicted by the analysis which neglects the eutectic.

The comparison of cells for similar growth conditions seems extremely promising; however, other points of comparison clearly indicate the still considerable gaps in the understanding of the evolution of cellular microstructures. Although the evolution of the wavelength with increasing growth rate has the same functional form that describes the behavior of the limit point of the band of wavelengths, the insensitivity to the temperature gradient seen in the experiments is not described by such a theory (see Section 3.4). Justification that this system operates at this maximum wavelength as a mechanism for wavelength selection from the continuous band must wait for comparison with other alloys and for a rigorous theory based on the stability of cellular forms. Presently, there is no physical evidence to suggest that this criterion is valid; see Section 1.5.

COMPUTED SHAPE

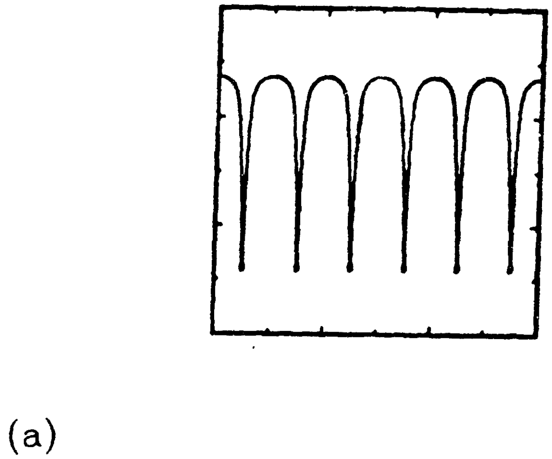

EXPERIMENTAL SHAPE

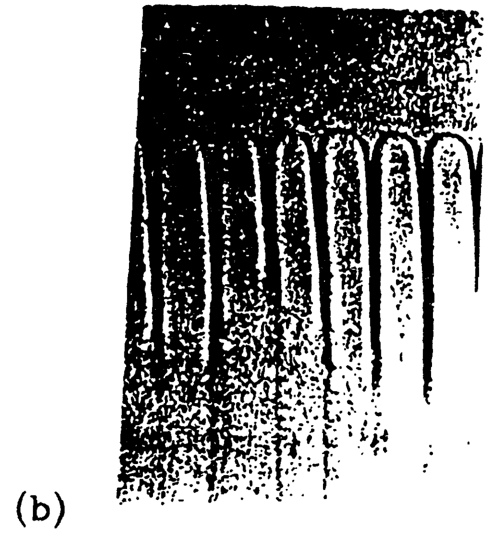

Figure 3.28: Half-cell shape (a) computed for $V = 3.0V_c(\tilde{\lambda}_c)$ for $\lambda = 50\mu m$ for direct comparison to the photograph (b) taken from de Cheveigné *et al.* (1986).

3.7 Time-dependent Calculations

The stability of the steady-state solutions described in Sections 3.3 - 3.6 were checked by calculations with the solutal model using the time-dependent numerical procedure described in Chapter 2. The stability of steady-states is important because some of the wavelength selection theories that have been derived for pattern formation in other systems like dendritic solidification (Bensimon *et al.* 1987, Kessler & Levine 1986a, 1986b and Tanveer 1987) and Saffman-Taylor fingering (Kessler & Levine 1986a, Shraiman & Bensimon 1984) have been based on the stability of the steady-state patterns; in these theories, out of a continuum of possible steady solutions, a single pattern of a particular wavelength is uniquely stable at given operating conditions. In addition, the transition to dendrites is expected to be a dynamic phenomenon, and can only be tested by a time-dependent calculation. Further, drop-shedding, a feature that is often seen in experiment is a time-periodic phenomenon, as shown in Fig. 1.18, and can only be simulated with such calculations.

Steady-state cellular solutions with a range of wavelengths were found, as described in Sections 3.3 - 3.6, and displayed in Figs. 3.19 and 3.26. This range of steady-state solutions was also found to be stable; the stability of the steady-state solutions is illustrated by calculation of the transient between the two steady-state solutions for the temperature gradients of $G = 0.45 \times 10^{-4}$ ($\Delta = 2.032$) and $G = 0.30 \times 10^{-4}$ ($\Delta = 3.568$). The stable steady-state solution for the higher value of G was used as the initial state and the temperature gradient was instantaneously lowered. The lowering of the temperature gradient is a change towards conditions that are further away from the critical, and cause an increase in the nonlinearity of the cell, as shown below.

The history of the interface deflection predicted with a maximum step size of $\Delta t = 0.01$ and initial time steps of 0.005 and 0.010 are shown in Fig. 3.29 for short times. In both cases the time step evolved quickly to the maximum value and continued there until the calculations were terminated. The only structure in the transient was the overshoot in the interface deflection.

The overshoot in the total interface deflection is a result of the response of the bottom

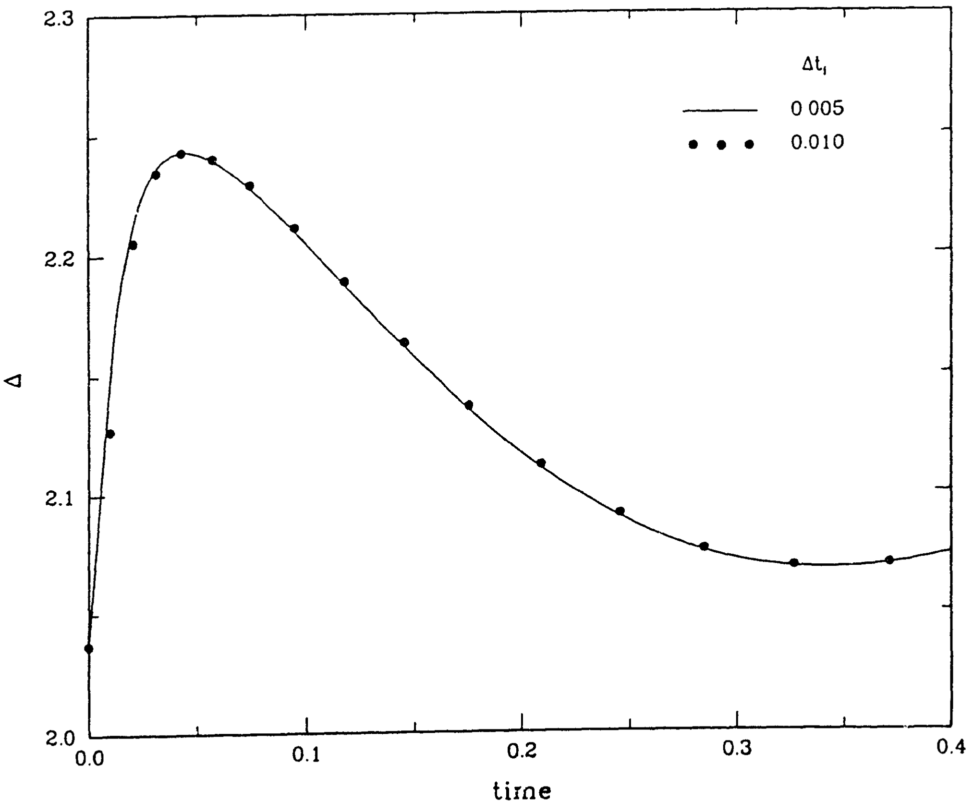

Figure 3.29: Short time history of cell depth predicted by implicit method for transition from steadily growing deep cellular interfaces for $G = 4.5 \times 10^{-5}$ and $G = 3.0 \times 10^{-5}$ with a step increase in G. results are shown for maximum step sizes of 0.005 and 0.010.

of the cell which overshoots and oscillates about its final steady-state value. The response of the cell depth Δ is plotted in Fig. 3.30 for long times; the letters on this figure indicate the times corresponding to the sample interfaces plotted on Fig. 3.31. The oscillation in the position of the cell bottom is clearly visible and may be preliminary to an instability that pinches off the cell bottom, causing drop-shedding, and thereby marking the end to steady-state growth. Brattkus (1989) used a linear stability analysis of thin three-dimensional axisymmetric roots between the cells to show that the roots are always unstable due to surface energy and the resulting oscillatory instability causes drop-shedding; however, corresponding two-dimensional calculations revealed no such instability.

The cell tips in this calculation do not get significantly more pointed as the cells get deeper. No indication of a transition to protodendritic patterns is indicated in this calculation. While drop-shedding is believed to caused by a cusp or cell bottom instability, dendrites are expected to be the result of an oscillatory instability of the tip (Langer 1986, Ben-Jacob *et al.* 1983, Kessler *et al.* 1988). A more thorough examination of the change in the cell shape with a change in growth rate, rather than temperature gradient, is required before any conclusions can be drawn about the transition to protodendritic forms.

3.8 Discussion

The finite element methods described in Chapter 2 are seen to be effective for accurate solution of the steady-state and time-dependent problems arising from the solutal model. The combination of the Galerkin finite element discretization and the nonorthogonal mapping leads to accurate descriptions of the deep cellular interfaces and field variables.

The results of the finite element calculations of deep cellular interfaces with the solutal model presented in this chapter predict the characteristics of the deep cells with narrow grooves that are seen in experiment by systematically continuing the predictions for small amplitude cells near the onset of cellular growth.

The calculations confirm that the small value of surface energy appropriate for a melt-solid system leads to complex nonlinear transitions. These transitions have been previously

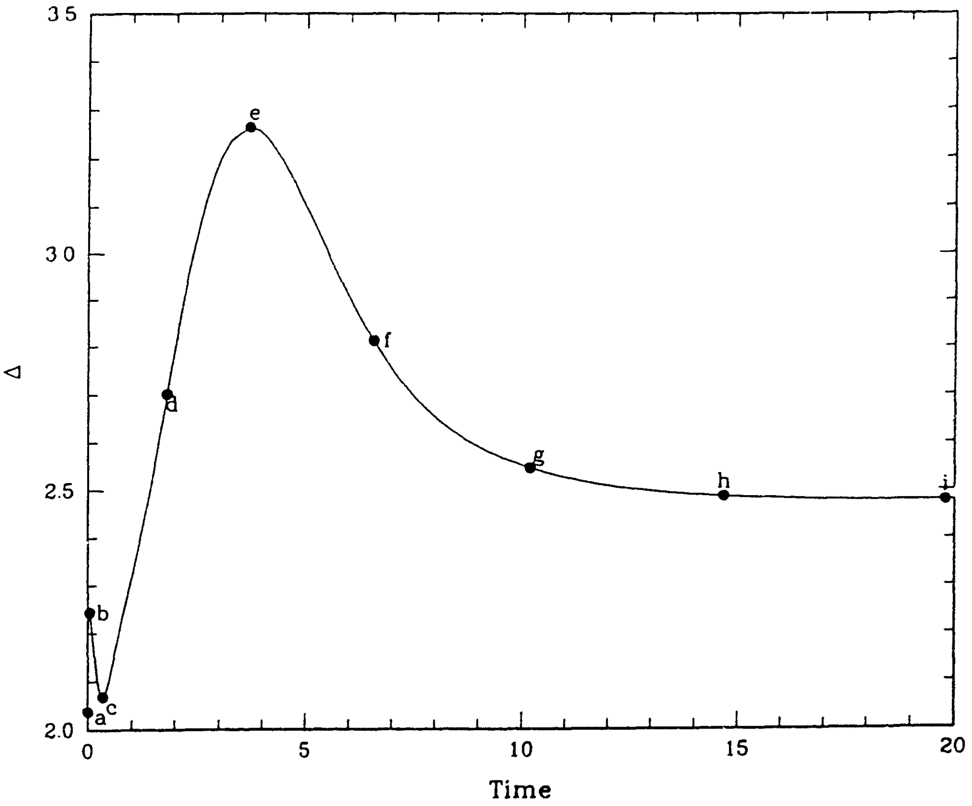

Figure 3.30: Long time history of cell depth predicted by implicit method for transition described in Fig. 3.29. The letters denote times for sample interface shapes shown in Fig. 3.31.

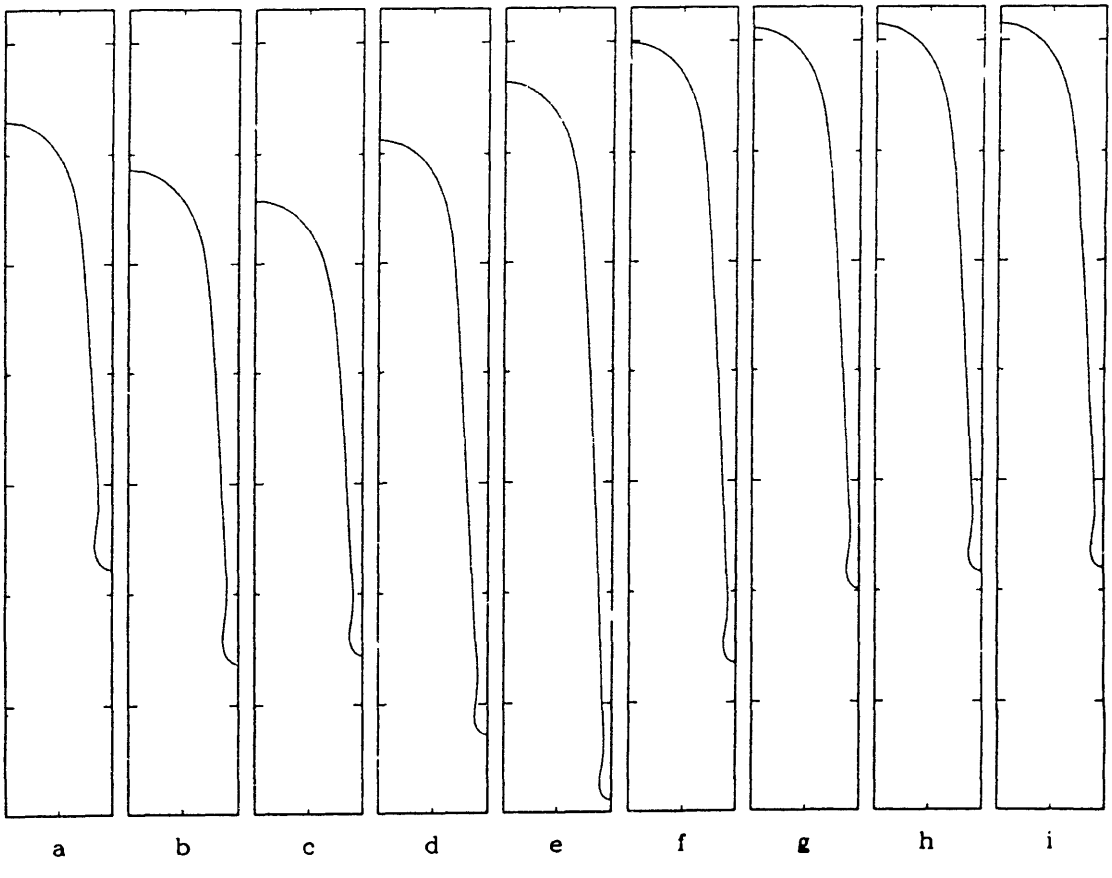

Figure 3.31: Sample half-cell shapes taken during the transition described in Fig. 3.29 and Fig. 3.30. Letters correspond to points shown in Fig. 3.30.

characterized for cells near the onset of the instability of the planar state remain qualitative unchanged for conditions far from critical. For a small increase in growth rate shallow cells are shown to undergo tip-splitting to deep cells with rounded tips connected to pendant bottoms through a long, slender sidewall and a transition region near the bottom where the cell is reentrant. Tip-splitting by secondary bifurcation is not limited to shallow cells. It is observed for deep cells; however, the family of cells passes through a limit point and evolves to lower values of the growth rate before the splitting takes place.

The deep cell can be analyzed in terms of three primary regions – the cell tip, the slender sidewall, and the cell bottom. The sidewall is seen to set the length of the cell as cell tip and bottom regions have lengths of $\mathcal{O}(1)$. The matching of the cell tip to the sidewall is important in this context; the bottom does not move significantly with respect to the temperature field except for small values of Γ as discussed below.

The slope of the sidewall is highly dependent on the temperature gradient G, the segregation coefficient k and the Peclet number P and relatively independent of the solute diffusivity ratio R_m and the surface energy Γ. An asymptotic analysis of the sidewall region is presented later (see Chapter 5). The cell tip is not significantly influenced by k and G and a change in these parameters increases the depth of the cell primarily by modifying the slope of the sidewall region. The effect of the growth rate is more complex; the sidewall and cell tip regions are both modified and the matching of these regions leads to a complex variation of cell depth with P. The surface energy is seen to affect the shape of the cell tip and is paramount in setting the shape of the bottom and transition zone between it and the sidewall. Indeed, the small length scale of the cell bottom makes the curvature correction the dominant term in the Gibbs-Thomson equation Eq. (3.1). The minimal effect of surface energy on the sidewall suggests that the cell tip and bottom regions are not intricately linked. Thus, propagation of any small effect of surface energy from the cell bottom region to the cell tip is unlikely.

The most important conclusion that can be reached from the calculations is that spatially-periodic steadily-growing, two-dimensional cells with smooth shapes exist for ranges of growth rates *and* wavelengths so that *no mechanism for selection* of a particular wavelength at a given growth rate is found. At any growth rate, cells exist for a range of wavelengths bounded on the left by the left border of the neutral stability curve and on the right by a curve of limit points that corresponds to the set of turning points in calculations with a fixed wavelength and increasing growth rate. The aspect ratio of the cell attains a maximum at a point in this range.

This thesis is the first of its kind to conclusively prove the absence of a selection mechanism using a solute diffusion model of directional solidification. Thus, this study disproves the results of the analysis of Karma (1986); the main difference between the analyses is that smooth cell bottoms and finite cells are predicted here for a range of velocities and wavelengths. Recently other theoretical (Dombre & Hakim 1987) and numerical studies (Ben-Amar & Moussallam 1988, Kessler & Levine 1989) have reached the same conclusions. It is possible that the extra length scales that are included in the thermal-solutal model could cause selection of the primary spacing of the morphology. Numerical computations presented in Chapter 4 investigate this possibility.

The steady-state calculations presented here suggest the picture shown in Fig. 3.32. Along the neutral stability curve there is a region of growth rates and spatial wavelengths in which at least one steadily solidifying cell exists. An enclosed region of wavelengths and growth rates is excluded. Tip-splitting of shapes at constant wavelength and increasing growth rate leads to a loss of existence of shapes with these wavelengths. A portion of the curve separating the regions has been identified by the calculations presented here to be associated with limit points in the family of solutions for the particular wavelength. The form of the bifurcation diagrams may evolve so that the secondary bifurcation from the shapes with a given wavelength $\tilde{\lambda}$ to its harmonic $\tilde{\lambda}/2$ sets the bound on the existence of shapes.

Another result of the calculations is that no transition to dendrites is seen. As discussed in Chapter 1 dendrites are believed to be dynamically changing three-dimensional structures but it is expected that cells undergo a transition to two-dimensional steady-state protodendritic interfaces that have sharp parabolic tips. Such morphologies have been reported in experiment; see Section 1.3. The calculations reveal that the nonlinear transition to cells with a smaller spacing is a generic phenomenon seen for families of cells of all wavelengths so that no transition to protodendritic morphologies is predicted at least within the range

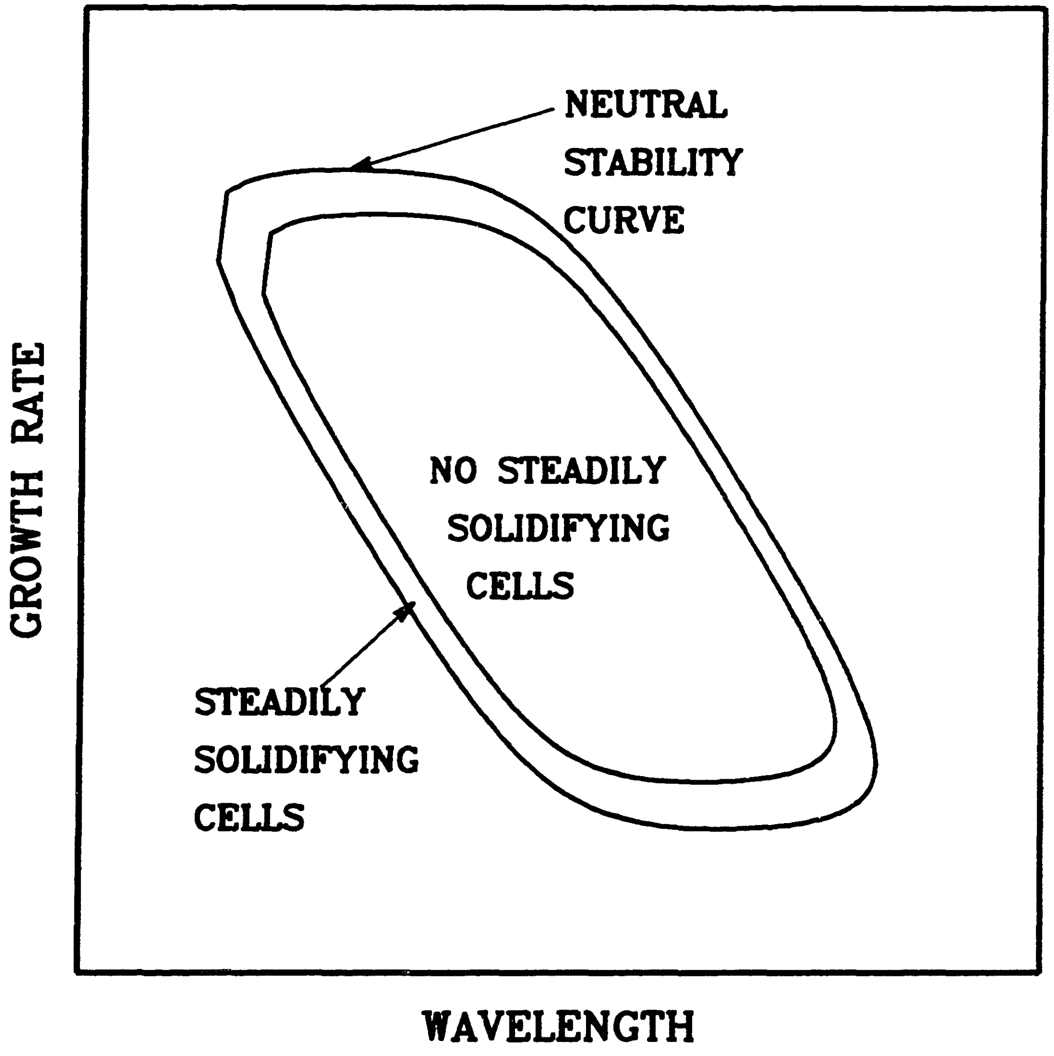

Figure 3.32: Schematic representation of the region of existence of steadily solidifying cells suggested by calculations and bifurcation analysis

of growth rates computed. Any attempt to achieve higher growth rates in the calculations is thwarted by the narrowing of the groove between cells, a problem that is encountered almost always during the computations of very deep cells in this study. Continuation of the calculations beyond such a point is discussed in Chapter 5 where an asymptotic analysis of the steady-state solutal model equations is used to show that the cell tip and bottom regions can be analyzed separately; a solution procedure applicable only to the cell tip and sidewall regions is employed to eliminate the problem of thin grooves.

Most theoretical simulation of dendritic solidification by previous studies (see Section 1.5.2.1 for a discussion) employ a purely thermal model where the effect of solute segregation is entirely neglected; the influence of latent heat generation and thermal convection are included in these models. The numerical analysis of thermal-solutal model for the Pb-Sb system presented in Chapter 4 deals with these effects.

The results of the numerical procedure compare well with the experimental data of de Cheveigné *et al.* (1986) for the CBr_4-Br_2 system. The nonlinear transitions seen in the Pb-Sb system are qualitatively very similar to those for the CBr_4-Br_2 alloy. Wavelength reduction by repeated tip-splitting and absence of selection are confirmed. The range of predicted wavelengths at a given growth rate is shown to bracket the experimentally seen wavelengths. The computed and experimental cell shapes at a given growth rate and wavelength compare favorably.

The curve of limit points (also the curve of maximum wavelengths at any velocity) is shown to have the same scaling of λ versus V as the experimental data. However, the data points indicate cells of a clearly smaller wavelength at any velocity. It is possible that the experimentally selected wavelength is dependent on the specific experimental apparatus or procedure; consistent reproducible experimental data is not yet available. It is likely that any selected wavelength is likely to be a statistically averaged quantity.

Dimensionless Group	Symbol	Value
Solute Diffusivities Ratio	$R_m \equiv \frac{\mathcal{D}_s}{\mathcal{D}_m}$	1.0
Dimensionless Temperature Gradient	$G \equiv \frac{\tilde{G}\tilde{\lambda}_{ref}}{\tilde{T}_o}$	4.5×10^{-3}
Dimensionless Liquidus Slope	$m \equiv \frac{\tilde{m}c_{\infty}}{\tilde{T}_o}$	-1.67×10^{-4}
Dimensionless Capillary Length	$\Gamma \equiv \frac{\tilde{\Gamma}}{\tilde{\lambda}_{ref}}$	8.2×10^{-7}
Segregation Coefficient	k	0.4

Table 3.2: Dimensionless values of the thermophysical parameters and operating conditions used in the calculations with the solutal model.

Mesh	Number of Elements in each direction						Number of unknowns
	Cell tip		Sidewall		Bottom		
	ξ	η	ξ	η	ξ	η	
$M(1,1)$	12	6	7	6	12	6	698
$M(1,2)$	12	12	7	12	12	12	1268
$M(1,3)$	12	18	7	18	12	18	1838
$M(1,4)$	12	24	7	24	12	24	2408
$M(2,1)$	24	6	14	6	24	6	1380
$M(2,2)$	24	12	14	12	24	12	2508
$M(2,3)$	24	18	14	18	24	18	3638
$M(3,1)$	36	6	21	6	36	6	2062
$M(3,2)$	36	12	21	12	36	12	3748
$M(3,3)$	36	18	21	18	36	18	5434

Table 3.3: Meshes used in calculations with mixed Cartesian-cylindrical representation.

Mesh	A	l_{bot}	l_{tip}	c_{bot}	c_{tip}
$M(1,1)$	2.063034	0.387131	1.675903	2.584211	1.939394
$M(1,2)$	2.052700	0.388481	1.664219	2.584895	1.942571
$M(1,3)$	2.051721	0.388591	1.663130	2.584936	1.942870
$M(1,4)$	2.051542	0.388613	1.662929	2.584945	1.942926
$M(2,1)$	2.061981	0.387200	1.674781	2.585429	1.939694
$M(2,2)$	2.061709	0.388519	1.663190	2.586074	1.942888
$M(2,3)$	2.060798	0.388622	1.662176	2.586121	1.943167
$M(3,1)$	2.061719	0.387199	1.674520	2.585521	1.939759
$M(3,2)$	2.061554	0.388513	1.663044	2.586160	1.942930
$M(3,3)$	2.060658	0.388615	1.662043	2.586208	1.943205

Table 3.4: Cell aspect ratios (A), locations of the cell tip (l_{tip}) and bottom (l_{bot}), and solute concentrations at the cell tip (c_{tip}) and bottom (c_{bot}) predicted for the meshes listed in Table 3.3.

Property	Symbol	Value
Temperature Gradient	$\tilde{G}$	$70°K/\text{cm}$
Melting Temperature of Pure CBr_4	$\tilde{T}_o$	$366.45K$
Liquidus Slope	$\tilde{m}$	$-2.9K/\text{mole }\%$
Br_2 Concentration	c_∞	0.12 mole %
Solute Diffusivity in the Melt	$\mathcal{D}_m$	$1.2 \times 10^{-5}\text{cm}^2/\text{sec}$
Solute diffusivity in the Solid	$\mathcal{D}_s$	$6.0 \times 10^{-7}\text{cm}^2/\text{sec}$
Capillary Length	$\tilde{\Gamma}$	2.03 cm
Segregation Coefficient	k	0.16
Melt Density	ρ	$3.42\ \text{g/cm}^3$
Reference Length Scale	λ_{ref}	$100.0\mu\text{m}$

Table 3.5: Thermophysical properties and operating conditions used in the calculations for the CBr_4-Br_2 alloy system.

Chapter 4

The Thermal-Solutal Model

The results of the numerical computations using the Solutal Model (SM) that are described in Chapter 3 predict many of the characteristics of melt-solid interface in steady-state directional solidification experiments. The onset of the morphological instability of the planar interface producing cellular morphologies and the transition to large-amplitude cells are qualitatively predicted by the solutal model. Some of the other important features of interfaces that form during directional solidification are not predicted by calculations with the solutal model, as outlined below; the computations using the Thermal-Solutal Model (TSM) presented in this Chapter aim to simulate these features of solidification microstructure. investigate this possibility.

Spatial wavelength selection of deep cells is believed to occur in experiments, as discussed in Section 1.5.1. This selection of the spacing of highly deformed cellular interfaces is not predicted by the calculations. As discussed in Section 3.8, it is possible that the extra length scales included in the TSM could cause wavelength selection. The computations described in this Chapter involve the TSM and attempt to check this possibility.

In addition, apparently two-dimensional protodendritic structures with parabolic tips are seen in experiment; see Fig. 1.15. These structures, which are believed to be steadily growing, are considered to be a transition state before dynamically changing three-dimensional dendrites are formed, as discussed in Section 1.3. The transition to these structures is also not predicted by the computations in Chapter 3. Dendritic solidification has been theoretically simulated in previous theoretical studies by using a purely thermal model where the effect of solute segregation is neglected; see Section 1.5.2 for a discussion. Is is therefore possible that the effects of latent heat generation and thermal convection are important to the transition from cellular interfaces to protodendritic shapes.

The calculations presented in this Chapter employ the dimensionless parameters listed in Table 4.1 which are representative of the Pb-Sb system discussed in Chapter 3. The values listed in Table 4.1 are identical to Table 3.2 except for two additions; the thermal diffusivity ratio R and the Stefan number St. The reference wavelength $\tilde{\lambda}_{\mathrm{ref}} = 100\mu\mathrm{m}$ again is used to calculate the parameters in Table 4.1 and is used elsewhere in this Chapter to scale the depth of cellular solutions.

Dimensionless Group	Symbol	Value
Solute Diffusivities Ratio	$R_m \equiv \frac{\mathcal{D}_s}{\mathcal{D}_m}$	1.0
Thermal Diffusivities Ratio	$R \equiv \frac{\alpha_s}{\alpha_m}$	1.87
Dimensionless Temperature Gradient	$G \equiv \frac{\tilde{G}\tilde{\lambda}_{\mathrm{ref}}}{\tilde{T}_o}$	4.5×10^{-3}
Dimensionless Liquidus Slope	$m \equiv \frac{\tilde{m}c_{\infty}}{\tilde{T}_o}$	-1.67×10^{-4}
Dimensionless Capillary Length	$\Gamma \equiv \frac{\tilde{\Gamma}}{\tilde{\lambda}_{\mathrm{ref}}}$	8.2×10^{-7}
Segregation Coefficient	k	0.4
Stefan Number	$St \equiv \frac{L}{\rho c_p \tilde{T}_o}$	0.29

Table 4.1: Dimensionless values of the thermophysical parameters and operating conditions used in the calculations with the thermal solutal model.

The linear stability analysis of the one-sided thermal-solutal model was first conducted by Mullins & Sekerka (1964). As described in Section 1.2.5, the analysis for this model and for simpler versions involves the quasi-steady-state assumption. Typically, the steady-state solution for the base case of a planar interface is first determined. In the case of the two-sided TSM that is employed in this section, the mathematical statement of the model is given by Eqs. (2.1)–(2.20) and the steady-state solution for the case of the planar interface is as follows:

$$
\begin{aligned}
\tilde{c}_m^{ss}(\tilde{x},\tilde{y}) &= c_\infty\left[1+\left(\frac{1-k}{k}\right)\exp(-\frac{V\tilde{y}}{\mathcal{D}_m})\right] \quad , & (4.1)\\
\tilde{c}_s^{ss}(\tilde{x},\tilde{y}) &= c_\infty \quad , & (4.2)\\
\tilde{T}_m^{ss}(\tilde{x},\tilde{y}) &= \tilde{T}_i+\tilde{G}_m\tilde{y} \quad , & (4.3)\\
\tilde{T}_m^{ss}(\tilde{x},\tilde{y}) &= \tilde{T}_i+\tilde{G}_s\tilde{y} \quad , & (4.4)
\end{aligned}
$$

where $\tilde{G}_s$ is related to $\ddot{G}_m$ by

$$\kappa_m\tilde{G}_m - \kappa_s\tilde{G}_s = LV \quad . \tag{4.5}$$

In the linear stability analysis of Mullins & Sekerka, the solution of the field equations for the case of an infinitesimally perturbed interface

$$\tilde{h}h(\tilde{x},\tilde{t}) = \epsilon\sin(\omega\tilde{x})\exp(\sigma\tilde{t}) \tag{4.6}$$

is then postulated so that the steady-state field equations and far field boundary conditions are still satisfied; the time-dependence is only retained in the equations for the mass and energy balance at the interface, Eqs. (2.5) and (2.6). Typically, the solutions $\tilde{c}_{m,s}^{per}$ and $\tilde{T}_{m,s}^{per}$ have the form

$$
\begin{aligned}
\tilde{c}_{m,s}^{per}(\tilde{x},\tilde{y},\tilde{t}) &= \tilde{c}_{m,s}^{ss}(\tilde{x},\tilde{y})+\epsilon\;\hat{c}_{m,s}\sin\omega\tilde{x}\;\,f(\omega,\tilde{y}) \quad , & (4.7)\\
\tilde{T}_{m,s}^{per}(\tilde{x},\tilde{y},\tilde{t}) &= \tilde{T}_{m,s}^{ss}(\tilde{x},\tilde{y})+\epsilon\;\hat{T}_{m,s}\sin\omega\tilde{x}\;\,f(\omega,\tilde{y}) \quad , & (4.8)
\end{aligned}
$$

where $f(\omega,\tilde{y})$ has the form that satisfies the field equations and far field boundary conditions.

For the case of far field boundary conditions of the form of Eqs. 2.38 and 2.39, where the temperature field is bounded at both extremities, no such solution can be postulated for the temperature field. The neutral stability curve for the thermal-solutal model was hence not computed for the model used in the calculations presented here.

The accuracy of the computations using the TSM is verified in Section 4.1. The effect of the ratio of thermal diffusivities in the two phases on the interface is discussed in Section 4.2 and the effect of thermal convection and latent heat generation is considered in Section 4.3. Wavelength selection is investigated in Section 4.4. The results are summarized in Section 4.5.

4.1 Accuracy of Numerical Method for the Thermal-Solutal Model

Steadily growing deep cellular interfaces and the corresponding concentration and temperature fields were computed for a series of eight meshes $M(i,j)$ listed in Table 4.2 using the

Mesh	Number of Elements in each direction						Number of unknowns
	Cell tip		Sidewall		Bottom		
	ξ	η	ξ	η	ξ	η	
$M(1,1)$	7	8	7	8	7	8	1171
$M(1,2)$	7	16	7	16	7	16	2211
$M(2,1)$	14	8	14	8	14	8	2305
$M(2,2)$	14	16	14	16	14	16	4353
$M(2,3)$	14	24	14	24	14	24	6401
$M(3,1)$	21	8	21	8	21	8	3439
$M(3,2)$	21	16	21	16	21	16	6495
$M(3,3)$	21	24	21	24	21	24	9551

Table 4.2: Meshes used in calculations with mixed Cartesian-cylindrical representation for the thermal-solutal model.

Thermal-Solutal Model (TSM). The cellular shapes correspond to the $\lambda = 1$ family used in Chapter 3 where λ is the non-dimensional wavelength defined by

$$\lambda = \frac{\tilde{\lambda}}{\tilde{\lambda}_{ref}} \quad , \tag{4.9}$$

The parameters used in the computations are those that are listed in Table 4.1 along with a solutal Peclet numbers $P = 0.8$ and a thermal Peclet number $P_t = 1.7 \times 10^{-4}$.

The aspect ratio of the cell A and the temperature at the bottom of the computational domain T_b are listed in Table 4.3. The two quantities listed in Table 4.3 were employed as measures of the solution to monitor the accuracy of the numerical method. Increasing the resolution of the mesh in either direction increased the accuracy of the calculations as seen from the values of these solution measures. In addition, the convergence rate of the solution measures listed in Table 4.3 is at least as good as the $\mathcal{O}(h^3)$ rate expected with the quadratic finite element approximations used for the concentration and temperature fields and the interface shape, as shown below. The convergence rate is estimated by comparing the results for the meshes $M(1,1)$, $M(2,2)$ and $M(3,3)$, which represent systematic refinement of the discretization in both directions. Taking the solution $M(3,3)$ to be close to the exact result shows that the error in the solution for mesh $M(2,2)$ is smaller than the error for mesh $M(1,1)$ by approximately the expected factor of eight.

The finite element meshes mapped back to the Cartesian system are shown in Fig. 4.1 along with the interface shapes and contours of the concentration and temperature fields. As before, the solute concentrations in the solid have been divided by the segregation coefficient k to make the contours continuous across the interface. The coarsest meshes have highly distorted elements in the melt ahead of the interface and in the solid behind it. Some wiggles in the approximate concentration field are caused by these elements. Refining the mesh leads to very smooth approximations for the solute concentration and temperature fields and the interface, as seen in Fig. 4.1c.

4.2 Effect of Thermal Diffusivity Ratio R

To check the effect of thermal diffusivity ratio on cell shape, steady-state computations were performed with cells of a specific wavelength and increasing thermal diffusivity ratio. The parameters used correspond to the Pb-Sb system and are those listed in Table 4.1 except R which was varied from the value 1.0. The chosen cellular family had the wavelength $\lambda = 1$ and the solutal Peclet number for the calculations was 0.8; the thermal Peclet number was maintained zero as in the solutal model calculations.

The results of the computations is presented in Fig. 4.2 where the cell aspect ratio A is plotted as a function of R. The cell aspect ratio increases linearly with R. The solution

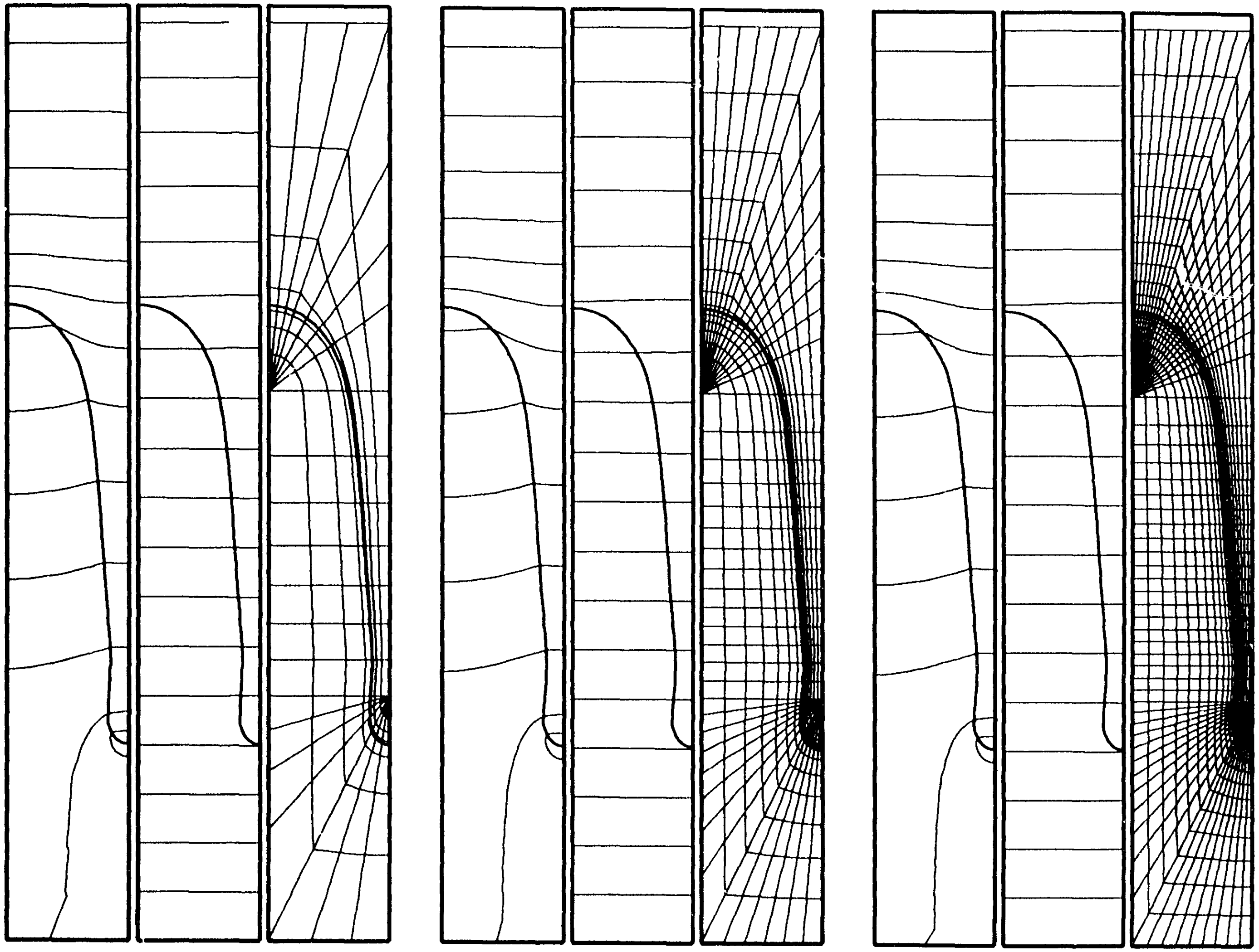

(a) (b) (c)

Figure 4.1: Interface shapes, concentration and temperature fields for meshes (a) $M(1,1)$, (b) $M(2,2)$, and (c) $M(3,3)$ along with finite element meshes projected into the original coordinate system.

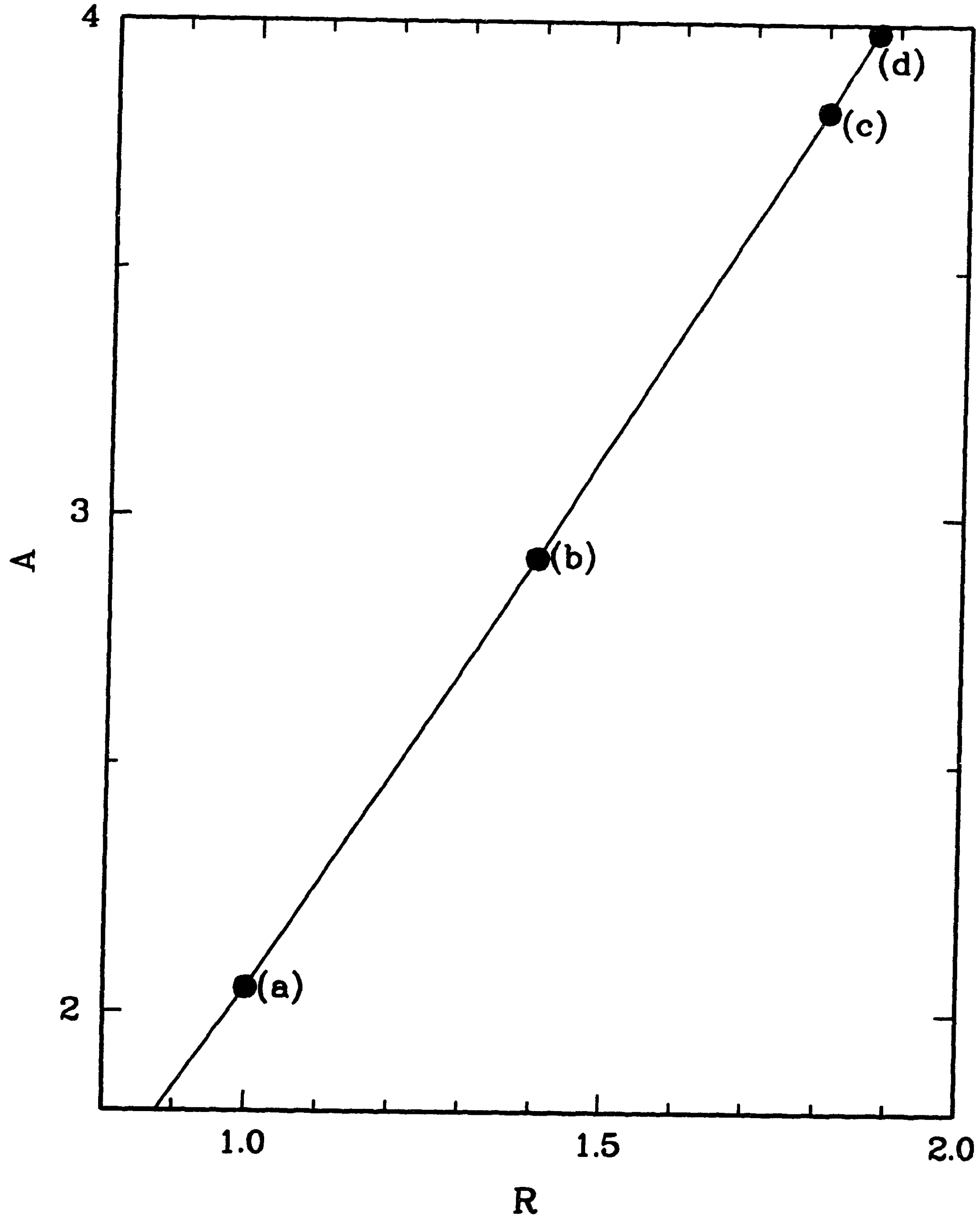

Figure 4.2: Dependence of cell aspect ratio A on thermal diffusivity ratio R. All other growth parameters were maintained constant at the values listed in Table 4.1.

at point (a) on Fig. 4.2 was computed at a value $R = 1.0$. This corresponds to point (b) on Fig. 3.9 where the calculation was done with the solutal model. The solution at point (d) on Fig. 4.2 was calculated with $R = 1.87$, which is correct for the Pb-Sb system. Sample half-cell shapes for three solutions from Fig. 4.2 are plotted in Fig. 4.3 along with the corresponding concentration and temperature profiles. The solute concentration in the solid has again been scaled by the segregation coefficient to make the contours continuous across the interface.

The temperature gradient far field in the melt in all three cases is equal to the imposed value. The heat that leaves the domain far field in the solid is equal in all three cases so that an increase in R (which correspond to an increase in thermal diffusivity in the solid) is accompanied by a corresponding decrease in the temperature gradient as seen in Fig. 4.3. Most of the decrease in the temperature gradient along the interface occurs near the cell tip. This is because the tip region occupies over half the width of the cell and most of the latent heat generated in this region. The amount of latent heat released along the sidewall is comparatively negligible, so that diffusion of the latent heat away from the interface is not a major effect, as indicated by the almost flat temperature contours in this region. The gradual decrease in the temperature gradient along the sidewall is accompanied by a slower variation in the solute concentration at the interface as dictated by the Gibbs-Thomson Equation Eq. (2.34); this is also indicated in Fig. 4.3 by the widening of the space between the concentration contours with increasing R. The results of the asymptotic analysis of the solutal model presented in Chapter 5 will show the concentration gradient along the interface is of utmost importance in determining the slope of the sidewall. The decreasing concentration gradient along the sidewall decreases the slope of the sidewall, resulting in a deeper cell.

4.3 Effect of Thermal Convection and Latent Heat Release

The combined effect of thermal convection and latent heat release was studied by performing computations where steadily growing deep cells of a specific wavelength were calculated with

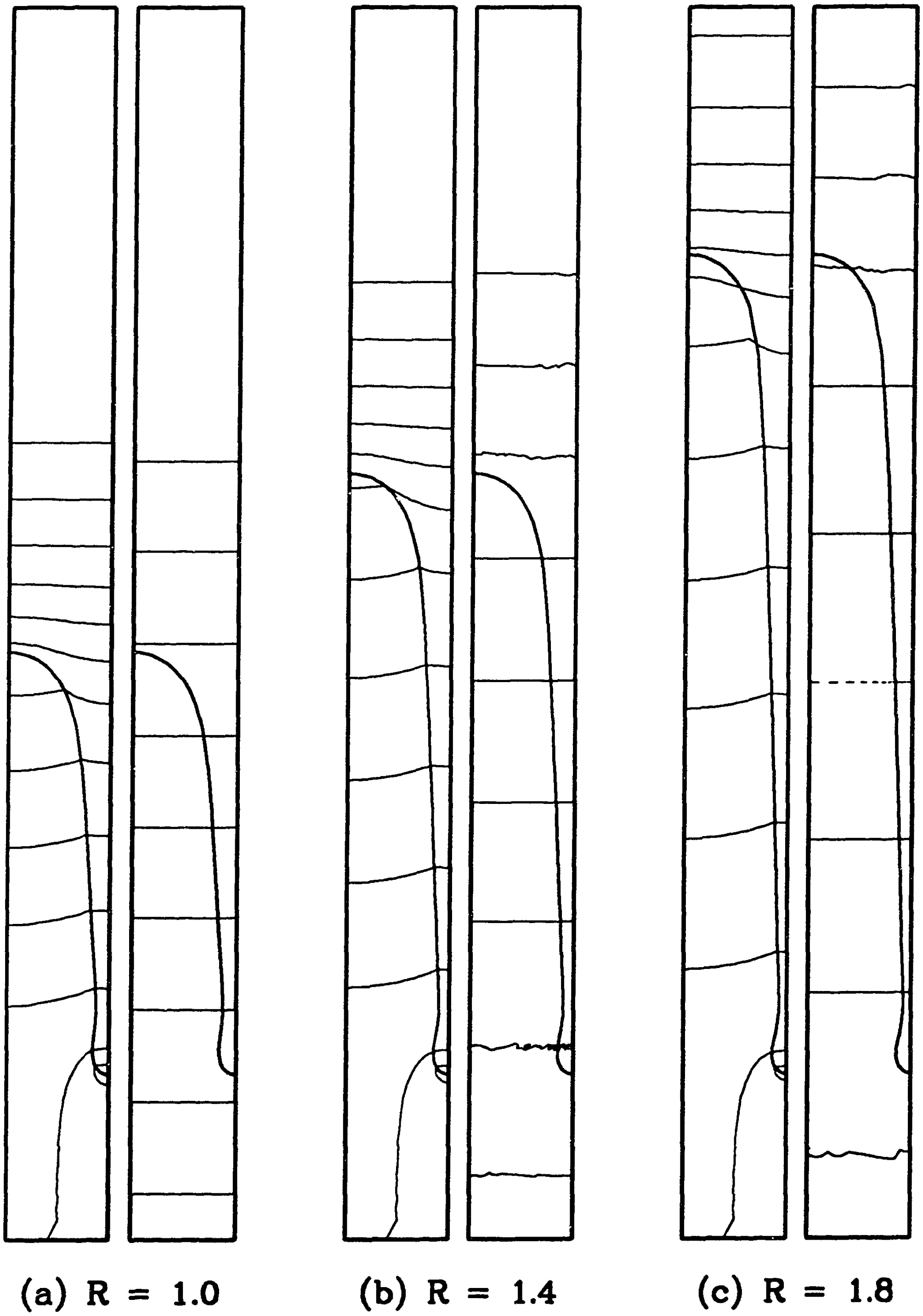

Figure 4.3: Sample half-cell shapes showing the dependence of interface shape on R. Letters correspond to solutions listed in Fig. 4.2. Concentration contours are plotted on the left and temperature contours are plotted on the right.

changing P_t. The parameters used again correspond to the Pb-Sb system and are listed in Table 4.1. The chosen family is again the $\lambda = 1$ family and the solutal Peclet number was maintained at $P = 0.8$. Eq. (2.31) shows that latent heat release influences the solution only for nonzero values of the thermal Peclet number since the Stefan number St (which is a measure of the latent heat release) is multiplied by P_t in its only occurance in the equation set describing the thermal-solutal model. This is because the amount of latent heat released is in direct proportion to the amount of melt converted into solid. The importance of latent heat release is measured by the ratio of the amount of latent heat to the amount of heat entering the system far field in the melt, i.e., the ratio P_tSt/G_m. For these calculations the ratio is exactly one for $P_t \approx 1.5517 \times 10^{-4}$.

Clearly, as P_t is increased both thermal convection and latent heat release become more important. This is seen in Fig. 4.4 where the aspect ratio of the cells A has been plotted as a function of P_t. The solution at point (a) corresponds to point (d) in Fig. 4.2 where $P_t = 0$. As P_t is increased, A decreases so that for thermal Peclet numbers as small at 2×10^{-4} the cell is only as long as it is wide. This effect can be seen in Fig. 4.5 where three sample cell shapes from the solution family in Fig. 4.4 have been plotted along with the corresponding solute concentration and temperature fields. While the temperature gradient in all three cases is equal to the imposed value far field into the melt, the amount of latent heat released increases with P_t. Thus the temperature contours further down the cell are closer for larger P_t. It is interesting to note that for a value of P_t between 1.0 and 2.0, the temperature contours in the bulk of the domain are equally spaced. This happens when the increase in energy leaving the system (as compared to the amount of energy entering it) due to latent heat is compensated exactly by the ratio of thermal diffusivities, i.e., when

$$\frac{P_tSt + G_m}{G_m} = R = 1.87 \quad \Longrightarrow \quad P_t = 1.35 \times 10^{-4} \quad . \tag{4.10}$$

As in the previous section, the narrowing of the space between tempearture contours is accompanied by a correspondingly closer solute concentration contours as dictated by the Gibbs-Thomson Equation Eq. (2.34); consequently, the cells are shorter.

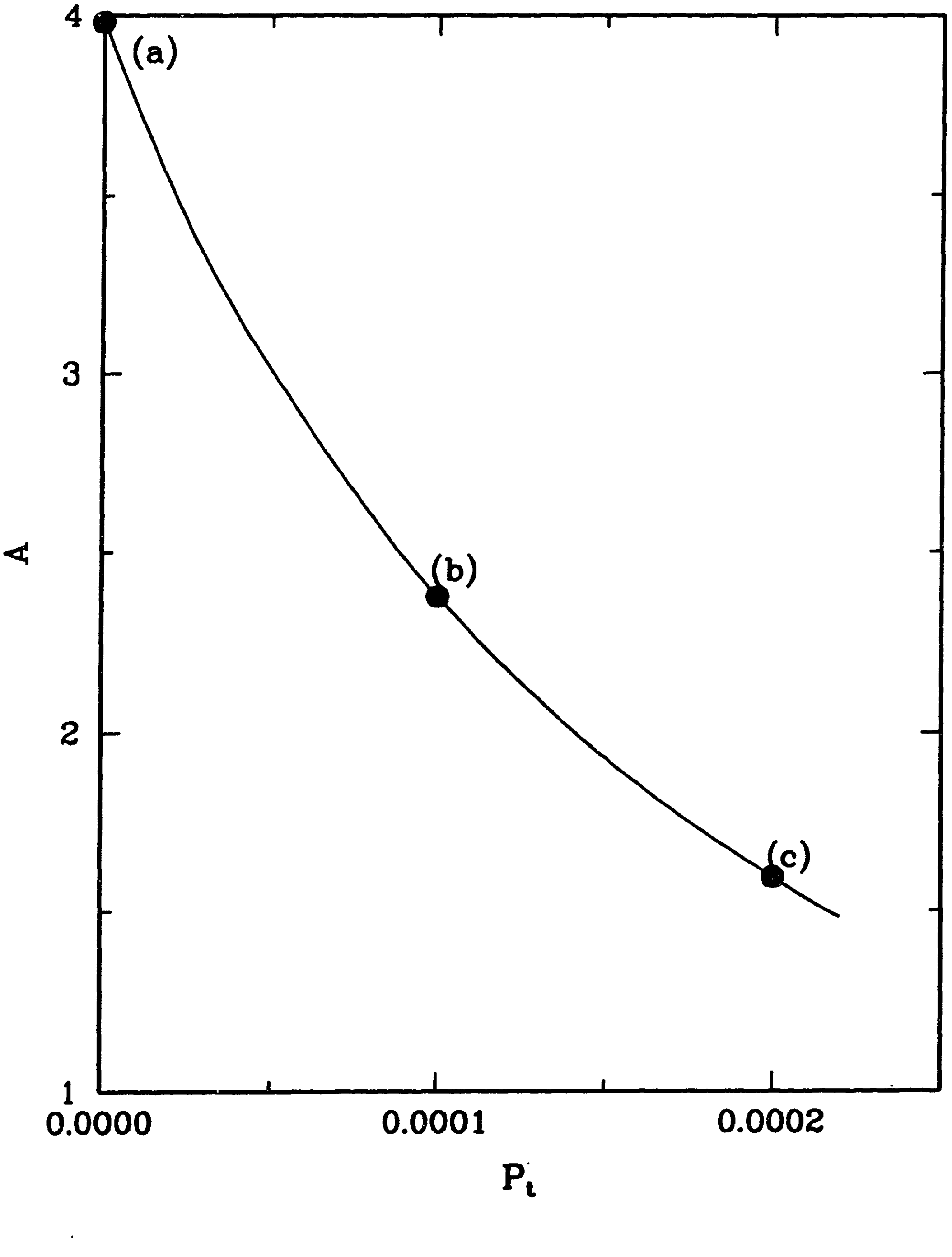

Figure 4.4: Dependence of cell aspect ratio A on P_t. All other growth parameters were maintained constant at the values listed in Table 4.1.

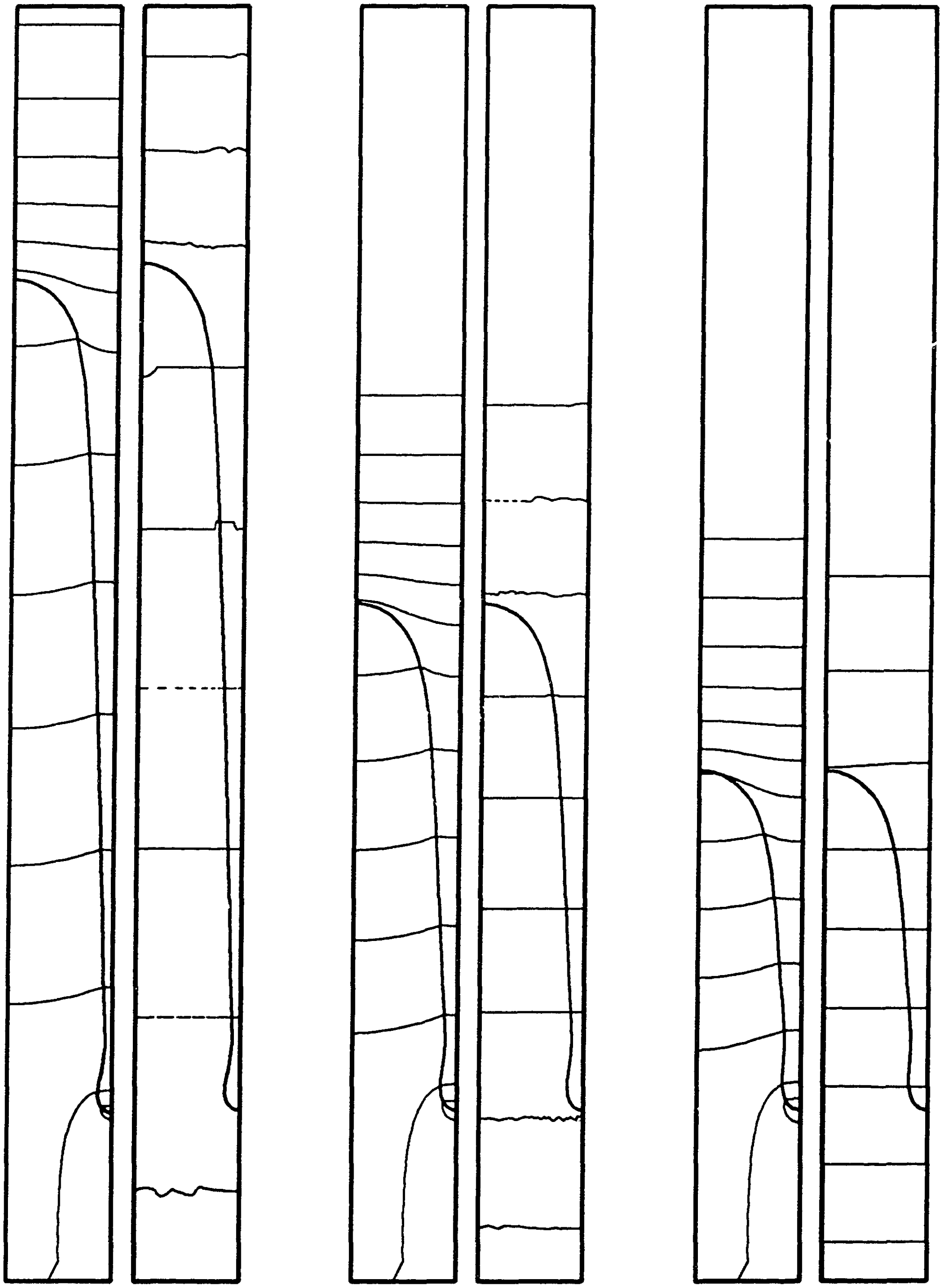

Figure 4.5: Sample half-cell shapes showing the dependence of interface shape on P_t. Letters correspond to solutions listed in Fig. 4.4. Concentration contours are plotted on the left and temperature contours are plotted on the right.

4.4 Wavelength Selection

Calculations were performed for the specific value of the dimensional growth rate V with varying dimensional wavelengths $\tilde{\lambda}$. The growth rate was fixed so that for $\lambda = 1.0$, the Peclet numbers had the values $P = 0.8$ and $P_t = 2.0 \times 10^{-4}$. The dimensional wavelength was varied by varying four parameters for each calculation: P, G_m, Γ, and P_t. While P, P_t and G_m are directly proportional to the dimensional wavelength, Γ in inversely proportional to $\tilde{\lambda}$.

A continuous family of cell shapes was computed over a range of wavelengths at this growth rate. This family of cells is plotted in Fig. 4.6 as a function of the dimensionless cell depth Δ for various dimensionless wavelengths λ at the specified growth rate. Thus, *no selection* of the spacing of steady-state cellular interfaces is seen with computations using the TSM. Finite amplitude cells are only seen for wavelengths below a maximum value. This behavior is very similar to that seen in calculations with the solutal model; see Section 3.5. It is expected that the termination of the curve at the largest wavelength again corresponds to the limit points in the calculations at constant λ and increasing growth rate like those in Fig. 3.9 for the solutal model. No attempt was made to perform these calculations for the TSM. This limit point also shows that arbitrarily large Peclet numbers cannot be attained in the calculations; therefore it is unlikely that sharp parabolic protodendritic structures can be simulated.

As in Section 3.5, the specified growth rate there is a deepest cell computed by the finite element algorithm. This maximum in cell depth is more dramatically illustrated in Fig. 4.7 where the the curve on Fig. 4.6 has been replotted as a function of the aspect ratio of the cell for each calculation. It is expected that the dramatic decrease in the aspect ratio at low values of λ is a result of the proximity of the left border of the neutral stability curve.

Sample shapes from the calculation are shown in Fig. 4.8. As in the previous section, the increase in P_t caused by the increasing wavelength makes the temperature and concentration contours come closer and has the effect of increasing the slope of the sidewall. This effect is compounded by the increase in the imposed temperature gradient. At high values of λ

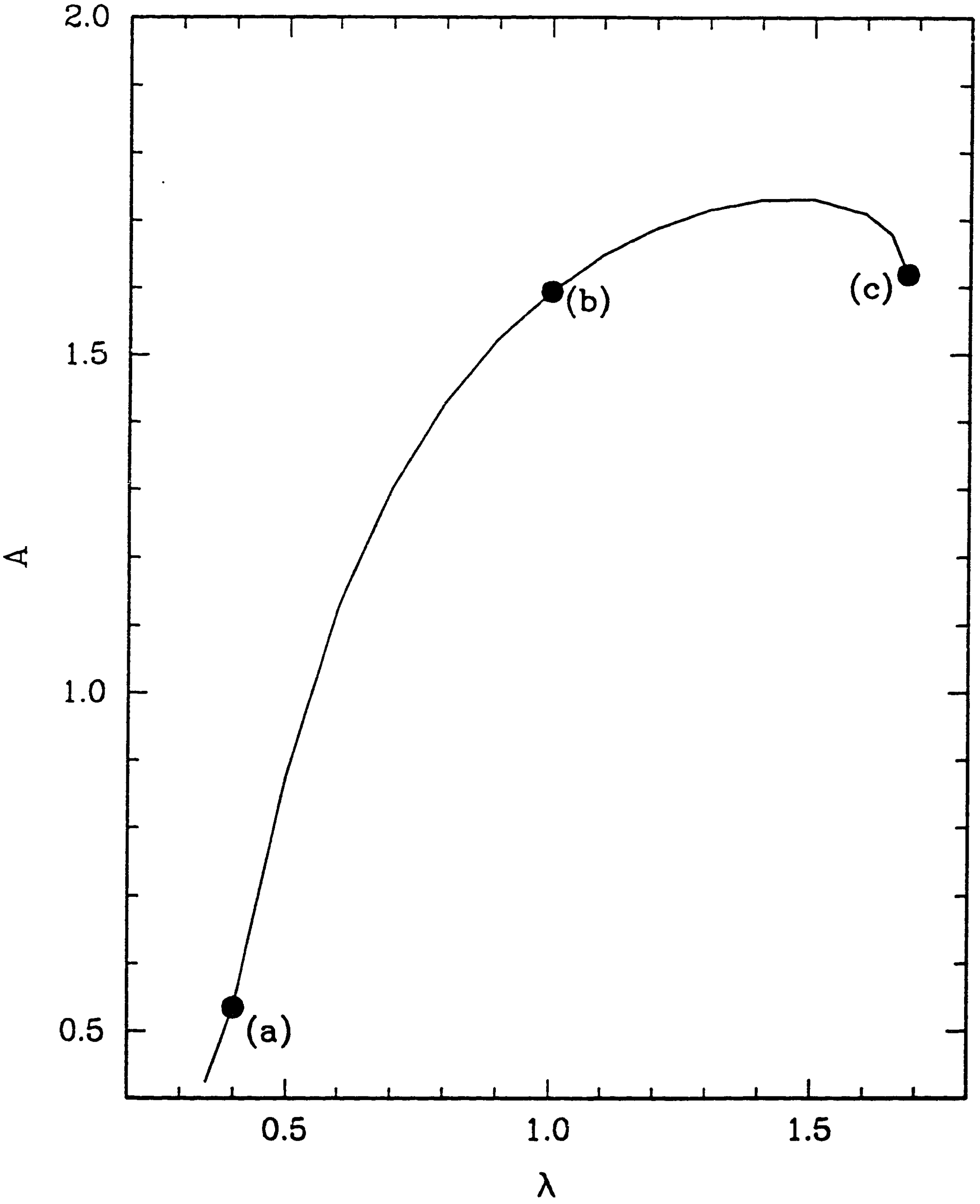

Figure 4.6: Dependence of dimensionless cell depth Δ on dimensionless spatial wavelength λ for specific value of the growth rate for the system parameters listed in Table 3.1.

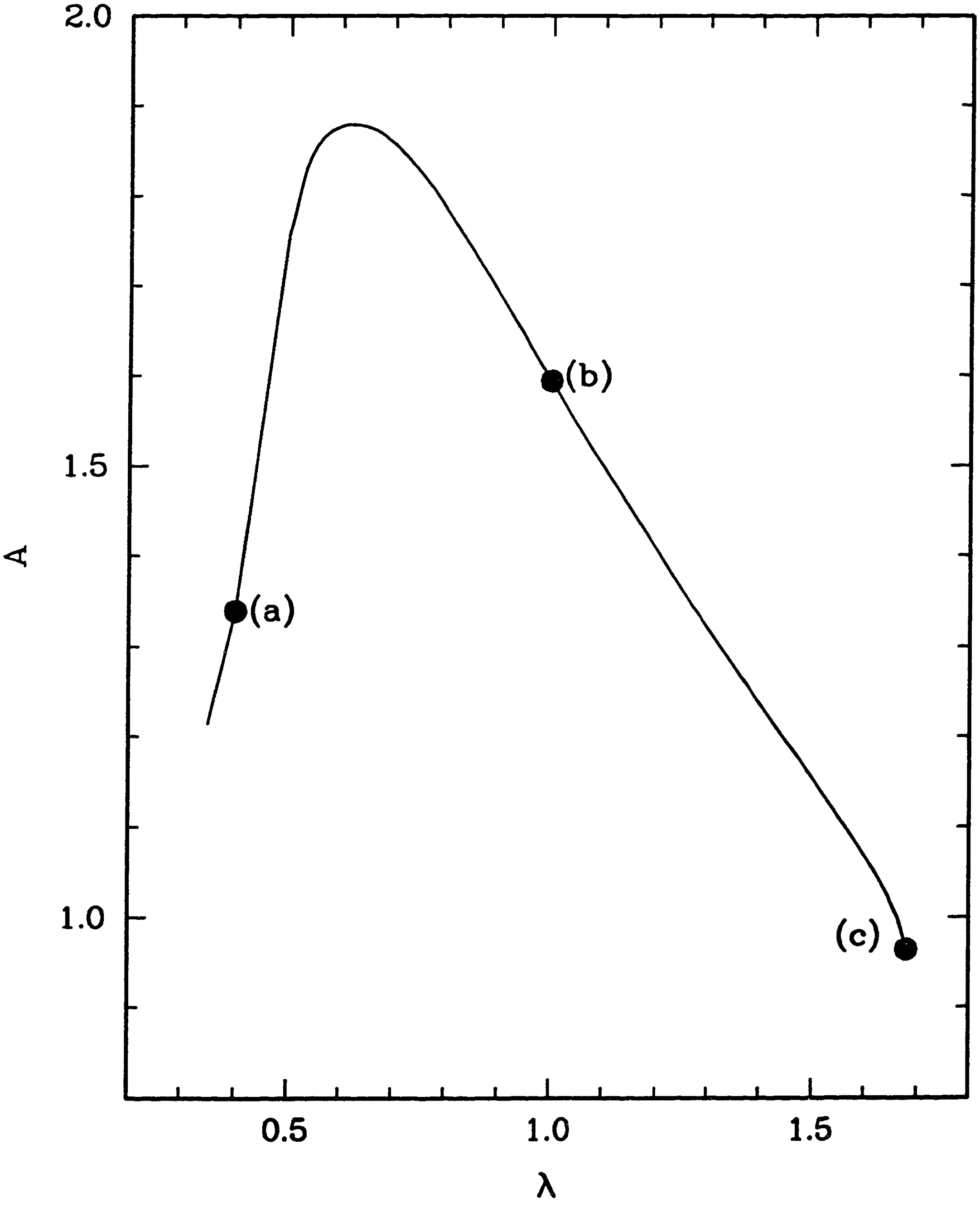

Figure 4.7: Dependence of cell aspect ratio A on dimensionless spatial wavelength λ for specific values of the growth rate.

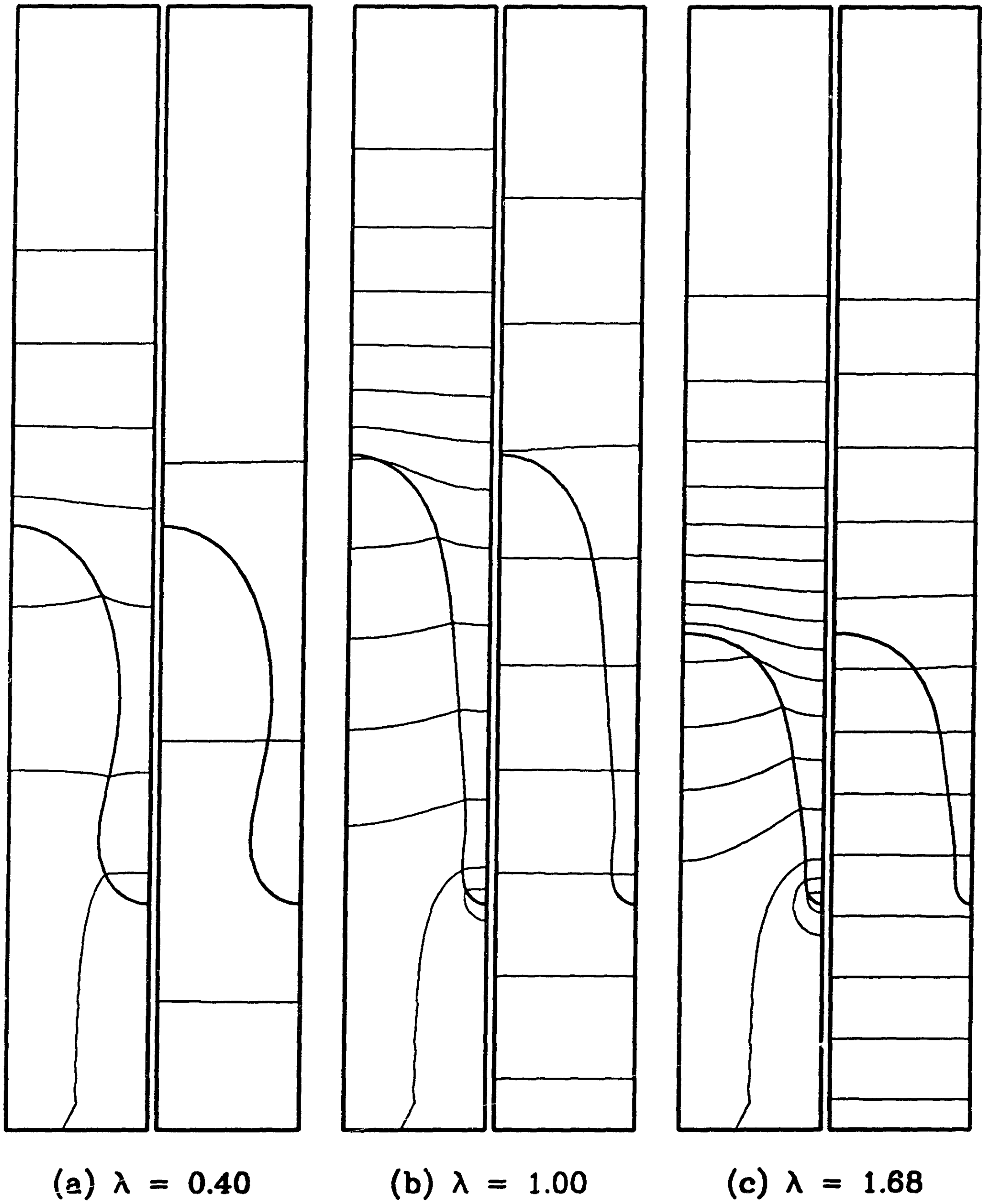

Figure 4.8: Sample half-cell shapes for calculations from Fig. 4.6 and Fig. 4.7. The letters correspond to points shown there. The wavelength has been normalized so that the aspect ratio of the cells A can be compared directly. Concentration contours are plotted on the left and temperature contours are plotted on the right.

this effect lowers the of the cell. For small λ, the bottom is more bulbous because of the increasing value of Γ; the matching of the bottom to the sidewall in this regime results in short cells.

4.5 Discussion

The finite element methods described in Chapter 2 are shown to be effective for accurate solution of the steady-state problems arising from the thermal-solutal model. The combination of the Galerkin finite element discretization and the nonorthogonal mapping is used to obtain accurate descriptions of the deep cellular interfaces and the concentration and temperature field variables.

The results of finite element calculations of steadily growing deep cellular interfaces presented in this Chapter confirm some of the characteristics of these morphologies that were predicted using the solutal model in Chapter 3. The effect of the additional parameters - the thermal diffusivity ratio and thermal Peclet number - are predicted by the calculations. In particular, the effect of latent heat release and the mechanism for the transport of this energy are discussed.

Selection of cellular solutions of a particular wavelength for a specific set of operating parameters is not indicated; steadily growing deep cells exist for a range of wavelengths for a specific growth rate. This confirms the findings of Chapter 3 using the solutal model and strengthens our belief that the wavelength selected in an experimental system depends on the particular experiment so that the resulting interface is a function of the time history of the experiment; any wavelength that can be specified for an interface has to be a quantity that is statistically averaged over time and across the interface.

As with the solutal model calculations, no transition to protodendritic morphologies is seen in steady-state calculations. It is possible that time-dependent calculations are necessary to simulate these structures or that three-dimensional calculations are important.

Finally, while the thermal-solutal model can be used to specifically study the effect of latent heat release or thermal convection, steadily growing deep cells can be qualitatively studied quite effectively using the solutal model itself. The solutal model has the advantage that the computational effort is much smaller for the same accuracy in the concentration field and interface shape.

Mesh	Aspect ratio A	T_b
$M(1,1)$	1.781463	0.999539026
$M(1,2)$	1.780124	0.999539011
$M(2,1)$	1.786076	0.999538830
$M(2,2)$	1.783658	0.999538817
$M(2,3)$	1.783508	0.999538816
$M(3,1)$	1.786479	0.999538812
$M(3,2)$	1.784104	0.999538801
$M(3,3)$	1.783956	0.999538800

Table 4.3: Cell aspect ratios (A) and temperature at the bottom of the computational domain (T_b) predicted for the meshes listed in Table 4.2.

Chapter 5

Asymptotic Analysis of Deep Cellular Interfaces

Numerical computations using the two-dimensional Solutal Model of directional solidification of a dilute binary alloy show the gradual evolution of steady-state cellular melt-solid interface morphologies from the planar interface as the growth rate is increased. As the results of Sections 3.3-3.6 show, these cells became very deep, with aspect ratios of up to 10 for various values of the determining parameters. The interface shapes for the deep cells computed with the finite element method have three distinct regions, as shown in Fig. 5.1 for a typical deep cell:

(i) a rounded *cell tip* which is attached to

(ii) an almost linear *sidewall* which stretches down between adjacent cells and terminates in

(iii) a smooth, pendant *cell bottom.*

As discussed in Chapter 2, the shape of the steadily growing cell is determined by the interaction between the seven length scales that are included in the solutal model. The length scales are very disparate so that it is possible that the important characteristics of the deep cell are influenced only by some of these scales. An asymptotic analysis of the different regions of the deep cell for limiting values of these parameters is expected to clarify the effects of each of these scales. In addition, it is hoped that the results of the perturbation analysis

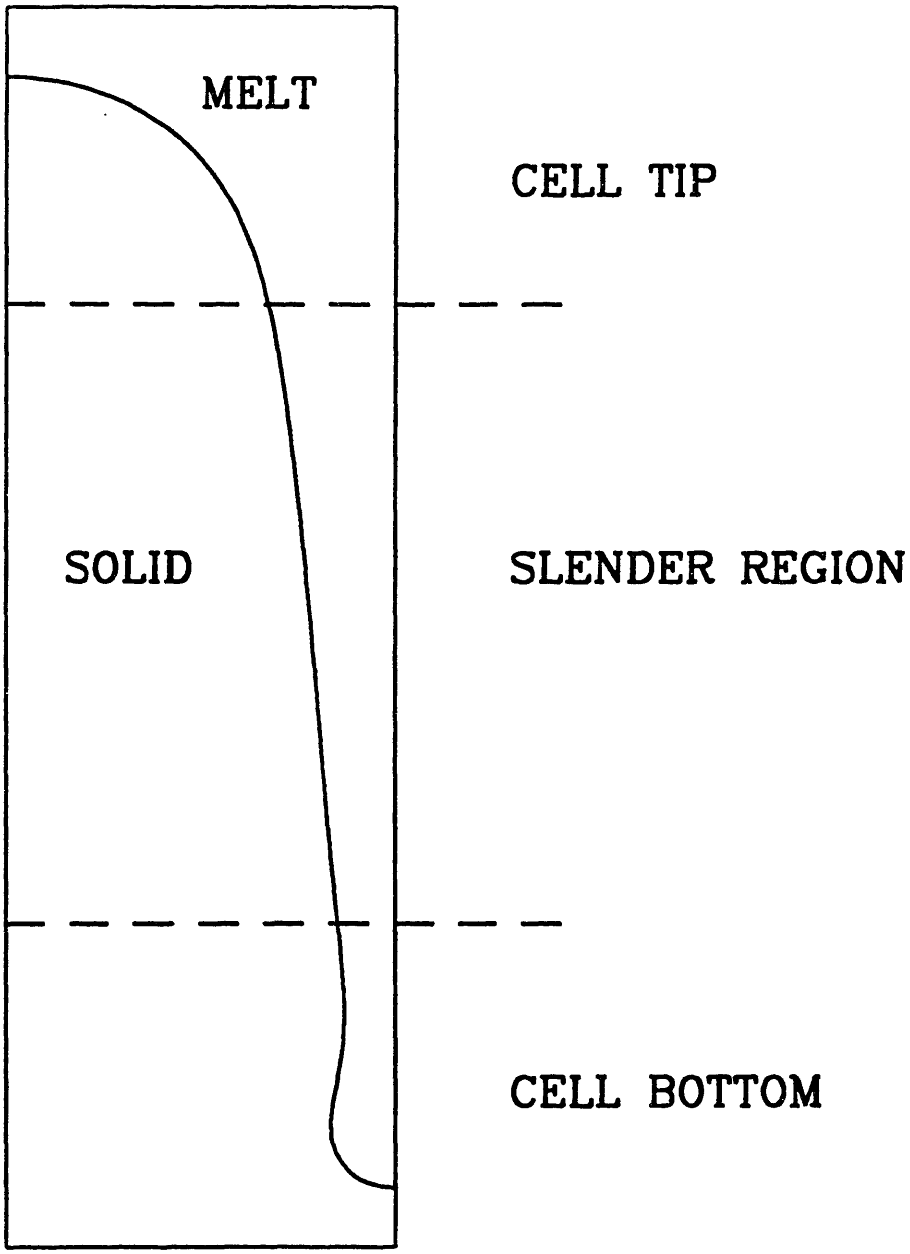

Figure 5.1: Schematic of a deep cell showing three distinct regions, (a) an rounded cell tip, (b) an almost linear sidewall and (c) a pendant bottom.

will relieve some of the difficulties encountered during the finite element computation of very deep cells as described in Section 3.8.

In this Chapter an asymptotic study of the solutal model for steadily solidifying deep cells is presented and an explanation of some of the characteristics of these interfaces using the asymptotics is attempted. The choice of the perturbation parameter used to characterize deep cells is discussed in Section 5.1. The analyses of the sidewall, cell bottom and cell tip regions are separately described in Sections 5.2-5.4. The application of the results of the asymptotic analysis to numerical computation of highly deformed interfaces with narrow grooves is detailed in Section 5.5. The effect of the anisotropy of the surface energy is studied using the modified numerical procedure in Section 5.6. The results are summarized and discussed in Section 5.7.

The steady-state solutal model equations are reproduced here for convenience:

$$\nabla^2 c_m + P\frac{\partial c_m}{\partial y} = 0 \quad , \tag{5.1}$$

$$\frac{\partial c_s}{\partial t} R_m \nabla^2 c_s + P\frac{\partial c_s}{\partial y} = 0 \quad , \tag{5.2}$$

$$\left[\hat{\mathbf{n}} \cdot \nabla c_m - R_m \, \hat{\mathbf{n}} \cdot \nabla c_s = \left(\hat{\mathbf{n}} \cdot \hat{\mathbf{e}}_{(y)}\right) P(1-k)c_m\right]_{\text{interface}} \quad , \tag{5.3}$$

$$[c_s = k c_m]_{\text{interface}} \quad , \tag{5.4}$$

$$[T_{\text{ref}} + G\,y = 1 + m\,c_m + \Gamma(2\mathcal{H})]_{\text{interface}} \quad , \tag{5.5}$$

$$\lim_{y \to \infty} c_m \to 1 \quad , \quad \text{and} \tag{5.6}$$

$$\lim_{y \to -\infty} c_s \to 1 \quad . \tag{5.7}$$

5.1 Choice of Perturbation Parameter

A central problem involved in the asymptotic analysis of a deep cell is the choice of the parameter ϵ, with limiting values that results in the large aspect ratio of the cell. It is expected that this parameter can be determined by estimating the length of the cell. Clearly, the the sidewall region contributes most to the length of the cell; the cell tip and bottom are $\mathcal{O}(1)$ regions when scaled with the wavelength, and the length of the cell can be estimated by analyzing the sidewall region, as shown below.

The sidewall is a region where the curvature is small and the effect of surface energy is negligible. The concentration gradient along a portion of the interface with negligible curvature reduces to a constant. The Gibbs-Thomson equation Eq. (5.5) relates the melt concentration at the interface to the temperature gradient and the surface energy, and can be rewritten explicitly for the concentration as

$$\left[c_m = c_o + \frac{G}{m}y - \frac{\Gamma}{m}(2\mathcal{H})\right]_{\text{interface}} \quad , \tag{5.8}$$

where c_o is a reference solute concentration given in terms of the reference temperature T_{ref} as

$$c_o = \frac{T_{\text{ref}} - 1}{m} \quad . \tag{5.9}$$

Neglecting the last term in Eq. (5.8) which corrects the interfacial solute concentration for the curvature of the interface, the concentration gradient along the interface is given simply by the ratio of the temperature gradient G and the liquidus slope m as

$$\left[G_c = \frac{G}{m}\right]_{\text{interface}} \quad , \tag{5.10}$$

or

$$G_{c,i} = \frac{G}{m} \quad , \tag{5.11}$$

where $G_{c,i} = G/m$ is the concentration gradient along the sidewall of the deep cellular interface.

The length of the sidewall region is dependent on the difference in the solute concentration in the melt between the cell tip and the cell bottom and the concentration gradient along the interface:

$$l = \frac{c_{tip} - c_{bot}}{G_{c,i}} \quad , \tag{5.12}$$

where l is the approximate length of the cell, c_{tip} and c_{bot} are the concentrations of the solute in the melt at the cell tip and cell bottom respectively, and $G_{c,i}$ is the solute concentration gradient in the melt along the interface. Eq. (5.12) may be written only because $G_{c,i}$ is a constant as shown in Eq. (5.11).

The solute concentration in the melt at the cell tip is bounded by the far field concentration $c_m = 1.0$, or

$$c_{tip} \geq 1.0 \quad . \tag{5.13}$$

The solute concentration in the melt at the cell bottom is approximated by the value of the melt concentration that is in equilibrium with the solid concentration far into the solid. Using the segregation coefficient k, this value is determined as

$$c_{bot} \approx \frac{1}{k} \quad . \tag{5.14}$$

Substituting Eqns 5.11, 5.13, and 5.14 into Eq. (5.12) the maximum length of the cell is estimated to be

$$l_{\max} = \frac{1-k}{k}\frac{m}{G} \quad . \tag{5.15}$$

From Eq. (5.15) it is obvious that cell may be deep if k is small; here, the concentration variation across the length of interface is large. The deep cell in Fig. 5.2a has been calculated for the CBr_4-Br_2 system with $k = 0.16$ and $G_{c,i} = (G/m)$ of $\mathcal{O}(1)$. The other thermophysical properties and operating conditions for this calculation are listed in Table 3.5.

Secondly, the cell can be deep if the concentration gradient is small. This occurs when $G_{c,i}$ is small. Fig. 5.2b shows a cellular interface calculated using a segregation coefficient of 0.4 but with $(G/m) = 0.18 \ll 1.0$. This corresponds to the parameter set representative of the Pb-Sb alloy listed in Table 3.1. It is clear that the the deep cell is characterized by both parameters. The small parameter used in this analysis accounts for both effects and is defined as

$$\begin{aligned} \epsilon &= \frac{1}{Pl_{\max}} \quad , & (5.16)\\ &= \frac{k}{P(1-k)}\frac{G}{m} \quad . & (5.17) \end{aligned}$$

This parameter has also been used by Young & Davis (1986) in their studies of directional solidification in systems with small segregation coefficients, and by Langer (1980) in his small-amplitude analysis. It is interesting that the parameter $M \equiv \epsilon^{-1}$ is also the measure of the constitutitional supercooling that was introduced in Subsection 1.2.5. Thus the constitution supercooling criterion presented in Section 1.2 can be rewritten in terms of ϵ

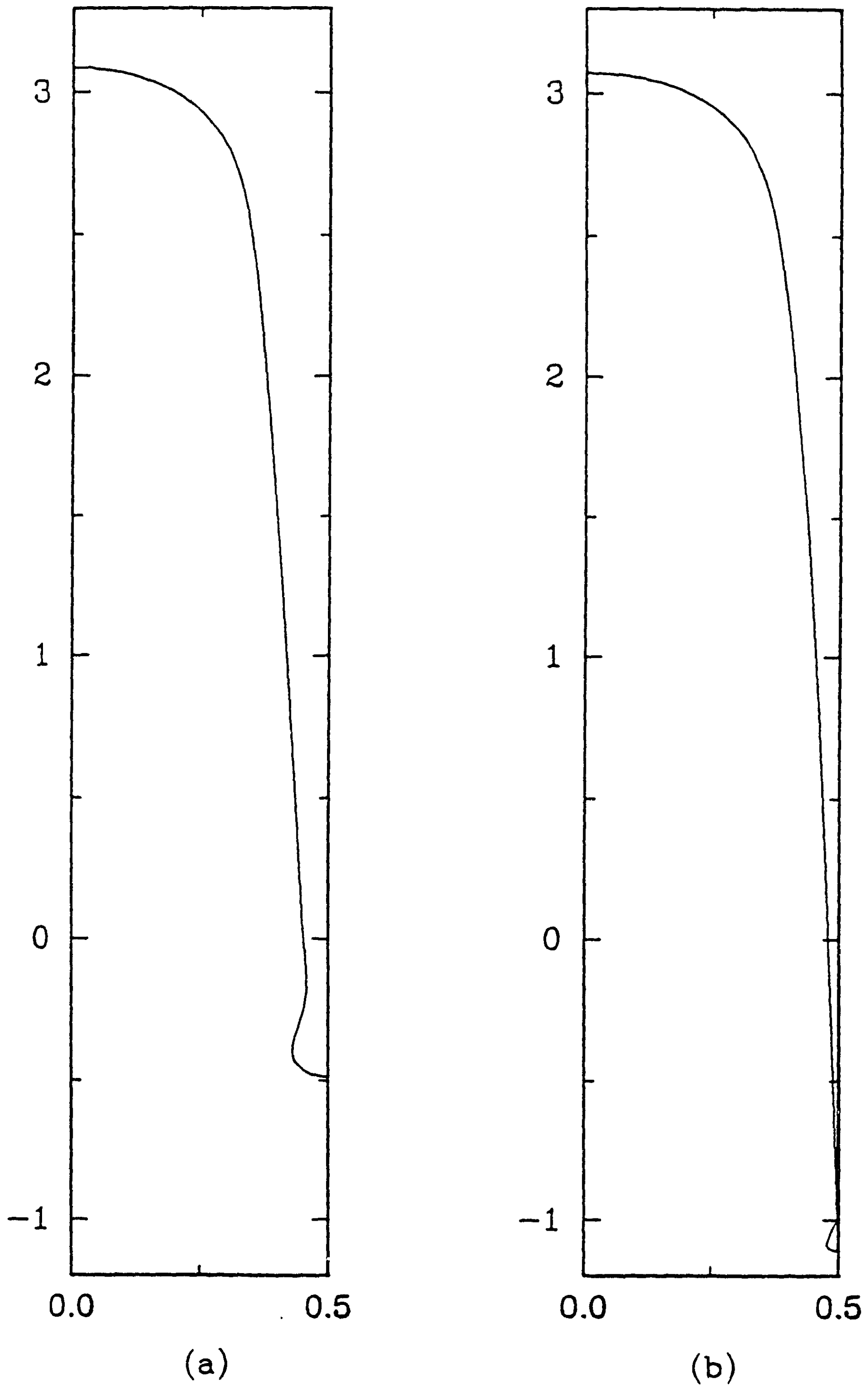

Figure 5.2: Computed deep cells for (a) $G_{c,i} = G/m = 0.18$ and $k = 0.4$, and (b) $G_{c,i} = G/m = 1.1$ and $k = 0.16$.

simply as

$$\epsilon < 1.0 \tag{5.18}$$

for the morphological instability to occur. Thus, ϵ is clearly a measure of the degree of deviation from the stable planar interface and appears to be a good choice for the perturbation parameter; for deep interfaces ϵ is expected to be very small.

The parameter ϵ can also be written as

$$\epsilon \equiv \frac{G/m}{G_{c,p}} \quad , \tag{5.19}$$

where $G_{c,p}$ is the concentration gradient in front of the planar interface. It is thus a ratio of the temperature and solute concentration length scales. Using ϵ as the perturbation parameter, the appropriate scalings for the variables in the three regions can now be determined by balancing the relevant terms in the Gibbs-Thomson equation 5.8.

5.2 Sidewall Region

We analyze this region of negligible curvature as a slender body. The ordinate is scaled by $\delta = \epsilon^{1/2}$ and all lengths are rewritten in terms of the diffusion length:

$$Y \equiv yP\delta \quad , \tag{5.20}$$

$$X \equiv \left(\frac{1}{2} - x\right) P \quad , \tag{5.21}$$

$$H \equiv \left(\frac{1}{2} - h\right) P \quad , \tag{5.22}$$

where Y is a compressed ordinate that is $\mathcal{O}(1)$ everywhere along the interface. Fig. 5.3 is a schematic representation of the deep cell showing the original and scaled variables. X and H are measured from the center of the groove as shown in Fig. 5.3. The melt concentration is scaled by k to be of the same order as the solid concentration so that the new concentration variables are equal at the interface:

$$\phi = \frac{kc_m}{1-k} \quad , \tag{5.23}$$

$$\psi = \frac{c_s}{1-k} \quad , \tag{5.24}$$

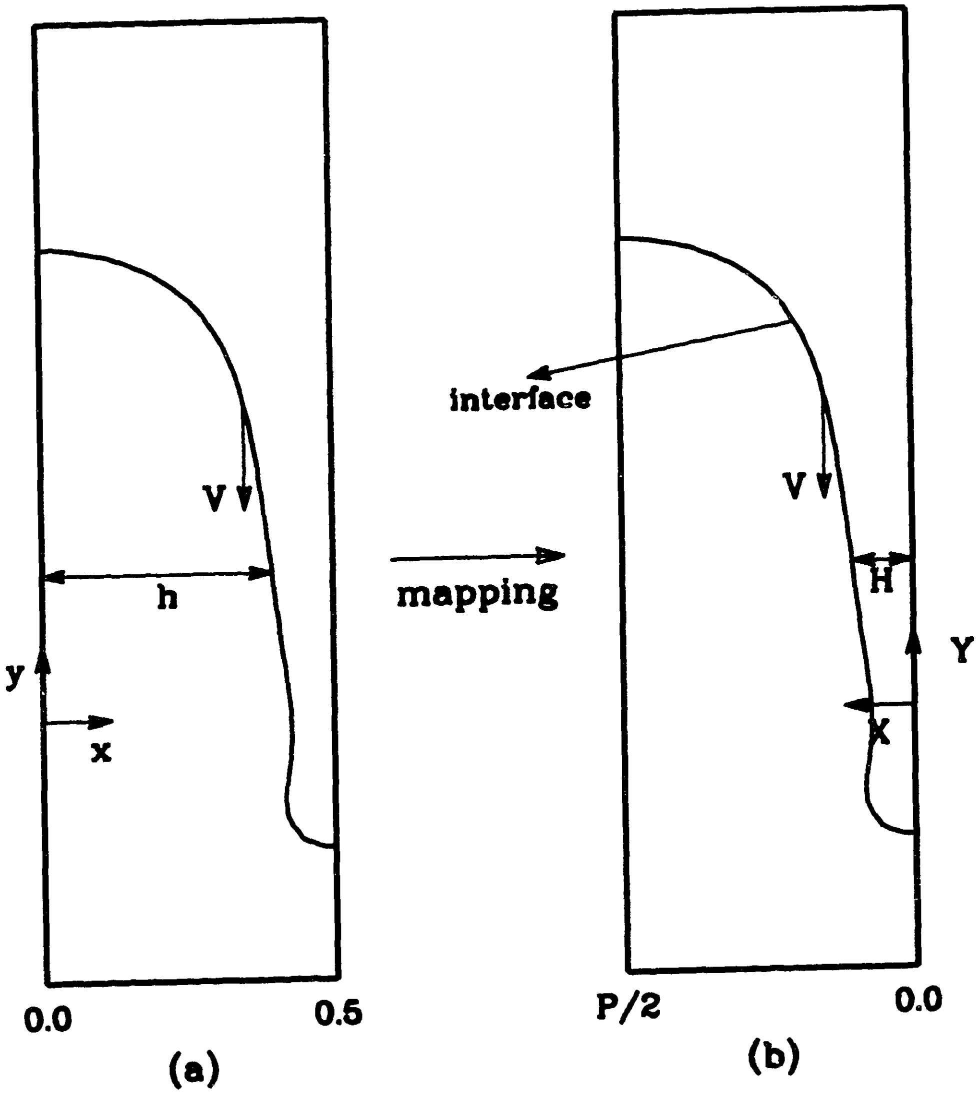

Figure 5.3: Schematic of a deep cell showing the scalings used in the asymptotic analysis of the sidewall region. x, y and h are the original independent variables and X, Y and H are the scaled variables.

where $\phi(X,Y)$ and $\psi(X,Y)$ are the scaled solute concentrations in the melt and solid respectively. The solutal model equations at steady-state can be rewritten in terms of the scaled variables as follows:

$$\begin{aligned} \phi_{XX} + \delta^2 \phi_{YY} + \delta \phi_Y &= 0 \quad , & (5.25) \\ \psi_{XX} + \delta^2 \psi_{YY} + \frac{\delta}{R_m} \psi_Y &= 0 \quad , & (5.26) \end{aligned}$$

$$\left[(\phi_X - \delta^2 H_Y \phi_Y) - (kR_m)(\psi_X - \delta^2 H_Y \psi_Y) = \delta(1-k)\phi H_Y \right]_{X=H(Y)} \quad , \qquad (5.27)$$

$$[\phi = \psi]_{X=H(Y)} \quad , \qquad (5.28)$$

$$\left[\phi = \psi = \phi_r - \delta Y - \frac{\Gamma P^2}{G} \delta^3 \frac{H_{YY}}{\{1 + (H_Y)^2\}^{3/2}} \right]_{X=H(Y)} \quad , \qquad (5.29)$$

where

$$\phi_r = \frac{kC_o}{1-k} \qquad (5.30)$$

is the reference concentration cast in terms of the scaled variables. Also,

$$\begin{aligned} \lim_{Y \to \infty} \phi &\to \frac{k}{1-k} \quad , \text{ and} & (5.31) \\ \lim_{Y \to -\infty} \psi &\to \frac{1}{1-k} \quad , & (5.32) \end{aligned}$$

and

$$[\phi_X = \psi_X = 0]_{X=0,\frac{P}{2}} \quad , \qquad (5.33)$$

The melt concentration and solid concentrations and the interface shape are functions of the parameter δ. When $\delta = 0$ the domain of the free-boundary problem defined above has a simple shape. The equations above can be solved easily to obtain the concentration field and interface profile

$$\begin{aligned} \phi^0 &= \psi^0 = \phi_r \quad , & (5.34) \\ H^0 &= D = \text{constant} \quad , & (5.35) \end{aligned}$$

where the supercript '0' denotes the fact that these solutions can be viewed as the $\mathcal{O}(\delta^0)$ terms of a regular perturbation expansion in δ. Thus, in the absence of a temperature gradient an infinitely long cell of constant width is indicated. The solute concentration is uniform along the interface at the value c_o. The constant D, which can be viewed as the limit of the melt and solid domains for $\delta = 0$, is determined by an overall mass balance as shown in the Appendix. In essence, a total solute balance is performed across the cross-section of the cell at any Y yielding

$$D = \frac{Pk/2}{1-k}\left[\frac{1-kc_o}{kc_o}\right] \quad . \tag{5.36}$$

In the absence of an imposed temperature gradient a continuum of solutions to the sidewall region exist where the groove thickness depends on the value of the solute concentration at the interface c_o. The corresponding dimensionless cell half-width is given by

$$w(c_o) = \frac{1}{2(1-k)}\left(1 - \frac{1}{c_o}\right) \quad . \tag{5.37}$$

Fig. 5.4 is a plot of the cell width w as a function of the solute concentration in the melt at the interface for the Pb-Sb system of Table 3.1; $k = 0.4$. The half-width of the cell grows from a minimum value of zero when the concentration at the interface equals the bulk concentration ($c_o = 1$) to a maximum value of $1/2$ when the interfacial concentration reaches the value $1/k$. Fig. 5.4 shows that cellular solidification is indeed very similar to both dendritic solidification and Saffman-Taylor fingering in the absence of a temperature gradient; in all three cases a continuum of infinitely long solutions exist in the absence of surface energy. It is hence possible for a microscopic solvability criterion such as that described in Section 1.5 to be applicable so that a single solution is selected from this continuum upon the introduction of surface energy into the problem. Clearly, the presence of a finite, although small, temperature gradient breaks this continuum of solutions by bounding the length of the slender region. This dependence on the temperature gradient is borne out by higher-order terms of the perturbation analysis.

Higher-order corrections are determined by converting the domain of the full free-boundary problem defined by Eqs. 5.25-5.33 to the simple domain defined by D by applying the coordinate transformations

$$\text{melt} : \eta \equiv \frac{XD}{H} \quad , 0 \le \eta \le D \quad , \tag{5.38}$$

$$\text{solid} : \mu \equiv \frac{(P/2 - X)E}{G} \quad , 0 \le \mu \le E \quad , \tag{5.39}$$

and

$$\xi = Y \quad , \tag{5.40}$$

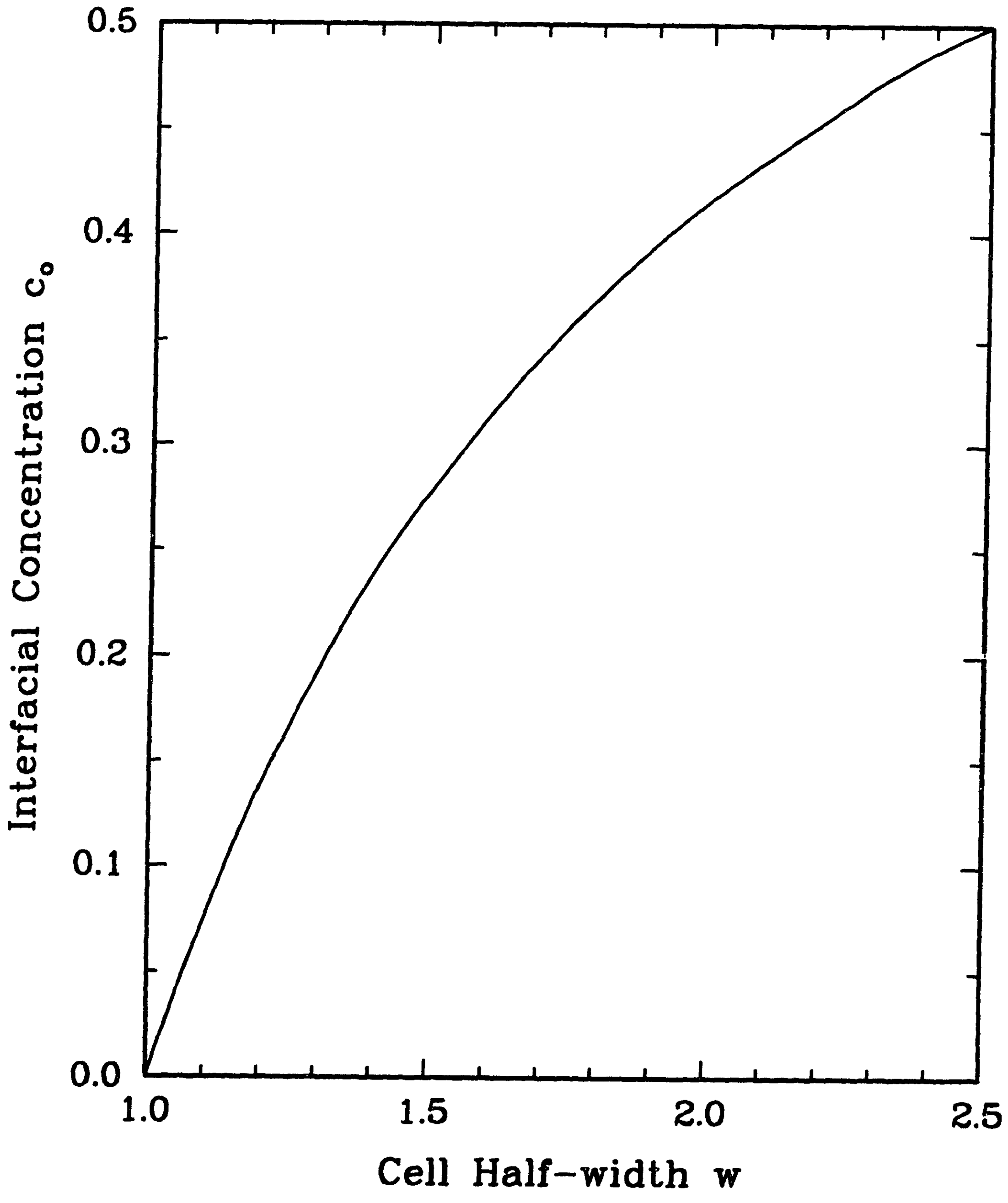

Figure 5.4: Variation of cell half-width w with interface concentration c_o in the absence of an imposed temperature gradient.

where $E \equiv P/2 - D$ and $G \equiv 1/2 - H$. With this change of coordinates, the free-boundary problem becomes

$$\begin{aligned} &\left\{\frac{D^2}{H^2}\right\}\phi_{\eta\eta} - \delta\left[\left\{\frac{\eta H_\xi}{H}\right\}\phi_\eta + \phi_\xi\right] \\ &+\delta^2\left[\left\{\frac{\eta H_\xi{}^2}{H}\right\}\phi_{\eta\eta} + 2\left\{\frac{\eta H_\xi}{H}\right\}\phi_{\eta\xi} + \phi_{\xi\xi} + \eta\phi_\eta\left\{2\frac{H_\xi{}^2}{H} - \frac{H_{\xi\xi}}{H}\right\}\right] = 0 \quad , \end{aligned} \tag{5.41}$$

$$\begin{aligned} &\left\{\frac{E^2}{G^2}\right\}\psi_{\mu\mu} - \delta\left[\left\{\frac{\mu G_\xi}{R_m G}\right\}\psi_\mu + \frac{\psi_\xi}{R_m}\right] \\ &+\delta^2\left[\left\{\frac{\mu G_\xi{}^2}{G}\right\}\psi_{\mu\mu} - 2\left\{\frac{\mu G_\xi}{G}\right\}\psi_{\mu\xi} + \psi_{\xi\xi} + \mu\psi_\mu\left\{2\frac{G_\xi{}^2}{G} - \frac{G_{\xi\xi}}{G}\right\}\right] = 0 \quad , \end{aligned} \tag{5.42}$$

The transformed equation set 5.41-5.42 is not a free-boundary problem any more but rather a problem with three explicit variables, the solute concentrations in the two phases and the interface shape. The equations for these variables are now coupled.

We now perform a regular perturbation on the transformed domain near the known limiting solution; $\delta = 0$. The dependent variables are assumed to be expressible as power series in δ. The problem is solved accurate to the required order in δ. The results of this procedure up to $\mathcal{O}(\delta^2)$ are given below. Details of this procedure are presented in the Appendix.

$$\begin{aligned} \mathcal{O}(0) \quad &: \quad \phi^0 = \psi^0 = \phi_r \quad , & H^0 &= D \quad , \\ \mathcal{O}(1) \quad &: \quad \phi^1 = \psi^1 = -\xi \quad , & H^1 &= \tfrac{P}{2kc_o^2}\xi + D_1 \quad , \\ \mathcal{O}(2) \quad &: \quad \phi^2 = \tfrac{1}{2}\left[\eta^2 - D^2\right] \quad , & & \\ & \quad\;\; \psi^2 = \tfrac{1}{2R_m}\left[\mu^2 - E^2\right] \quad . & & \end{aligned}$$

The constants D and D_1 in these expressions are estimated by performing an overall material balance across a representative cross-section of the cell correct to the required order in δ and the results are rewritten in terms of the original dimensionless variables; the analysis is detailed in the Appendix. The shape of the interface correct to $\mathcal{O}(\delta^2)$ is determined as

$$h(y) = \frac{k/2}{1-k}\left[\frac{1-kc_o}{kc_o}\right] + \left(\frac{G}{m}\right)\left\{\frac{1}{2(1-k)c_o^2}\right\} y \quad . \tag{5.43}$$

A convenient choice of the reference concentration is $c_o = 1/k$. The interface is then written as

$$h(y) = \left(\frac{G}{m}\right)\left\{\frac{k^2}{2(1-k)}\right\} y \quad . \tag{5.44}$$

The slender region is essentially linear as expected. The concentration profile is also linear with a quadratic term showing a drop in concentration away from the interface. This interface shape has been plotted along with the corresponding computed shape in Fig. 5.5. The asymptotic shape clearly matches the result of the numerical method in the slender region. A key feature of the sidewall region is that its position is completley fixed in the temperature field accurate to $\mathcal{O}(\delta)$. Thus the cell tip and bottom can be matched to this entirely determined shape. It is thus unlikely that the cell bottom affects the shape of the cell tip or vice-versa. The free-boundary problems in the cell tip and botton can be decoupled. Matching of the slender region variables with those of the cell tip and/or bottom were not required here because the overall material balance served the same purpose.

The cell bottom is seen to match the sidewall approximately where $y = 0$ and the interface concentration reaches the value $1/k$. Thus, the depth of the cell is affected only by the slope of the sidewall region and the matching of the cell tip; the matching of the cell bottom does not significantly affect the depth of the cell.

In the special case of the one-sided model ($R_m = 0$) the equation set has to be solved again because the solution for the two-sided model is singular in R_m; the solution can hence not be determined by setting $R_m = 0$ in the solution to the full problem. The solution in this case is that obtained by Scheil and reproduced by Kessler & Levine(1989). The solution procedure is described in detail in the Appendix. The sidewall is infinitely long and is described by

$$h(y) = \frac{A}{(\phi_r - y)^{\frac{1}{1-k}}} \quad . \tag{5.45}$$

where A is a constant that can be determined by an overall material balance. Eq. (5.45) was also used by van Sarloos & Weeks (1988) as the outer solution in their efforts to match a consistent cell tip shape and groove shape to obtain a criterion for the selection of the cell tip. Their effort is discussed further in Section 5.4.

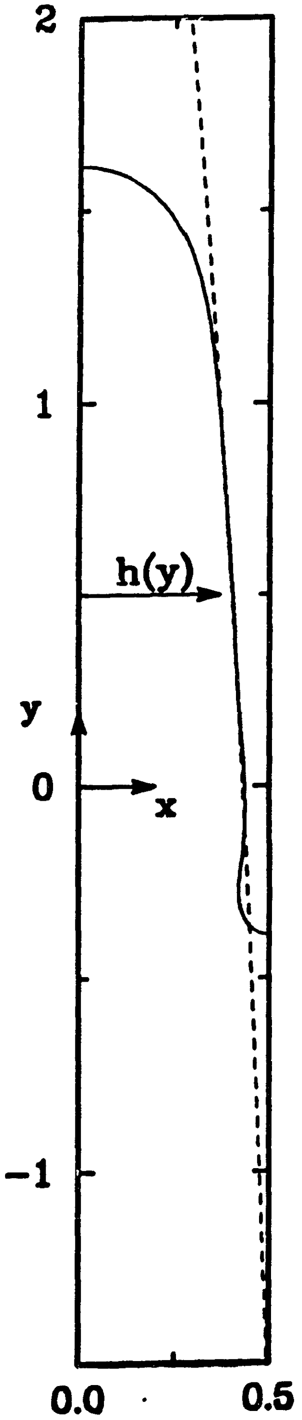

Figure 5.5: Comparison of numerically computed interface (solid line) and asymptotically predicted sidewall (dashed line).

5.3 Cell Bottom

The cell bottom is a treated as a region of high curvature; this assumption is borne out by the results of the calculations presented in Section 3.4. Thus the surface energy term in the Gibbs-Thomson equation is of a significant magnitude. Matching relevent terms of the Gibbs-Thomson equation to attain different balances yields a plausible set of scalings for the variables in this region, but the field equations in the solid cannot be simplified; the partial differential equation in this phase has to be solved in its entirety because the length scales in this region are both of $\mathcal{O}(1)$.

Instead, an alternative approach has been used to simulate the cell shape and its characteristics. An averaged equation is employed for the cell bottom. The concentration is assumed independent of the x-direction in both phases. The variation of cell shape and concentration with the y-direction are retained. A one-dimensional equation for the interface shape is derived; this approach is similar to analyses that have been conducted for other problems like flow in circular jets (Weber 1931) and coating flows

(Bob...I don't know where I read saw such an approach...Some papers, books, you gave me. Can you help me?)

An overall material balance at a given cross-section of the cell under these assumptions yields

$$\left[h(1-k)+\frac{k}{2}\right]Pc_i+\left[h(1-kR_m)+\frac{kR_m}{2}\right]\frac{dc_i}{dy}=\frac{P}{2} \quad , \tag{5.46}$$

where $c_i(y)$ is the assumed concentration profile everywhere in the domain. Here, the solute leaving the cell at the cross-section at the ordinate y has been matched with the amount entering far-field ($y \to \infty$). Eq. (5.46) is assumed to be valid at any cross-section of the cell. The concentration and the gradient are determined from the Gibbs-Thomson equation as

$$c_i(y)=c_o-\frac{G}{m}y-\frac{\Gamma}{m}(2\mathcal{H}) \quad , \tag{5.47}$$

where the curvature $2\mathcal{H}$ is written interms of the interface $x=h(y)$ as

$$2\mathcal{H}=\frac{\frac{d^2h}{dy^2}}{\left[1+\left(\frac{dh}{dy}\right)^2\right]^{3/2}} \quad . \tag{5.48}$$

Substituting for c_i and dc_i/dy from Eq. (5.47) and for the interface curvature from Eq. (5.48) into Eq. (5.46) yields a nonlinear third-order ordinary differential equation in the interface shape.

This equation is solved using the Runge-Kutta method with the boundary conditions: At $y = y_o$ (the cell bottom)

$$2\mathcal{H} = \mathcal{K}_b \quad , \tag{5.49}$$

$$h = \frac{1}{2} \quad , \tag{5.50}$$

$$\frac{dh}{dy} = -\infty \quad , \tag{5.51}$$

where $\mathcal{K}_b$ is the curvature at the bottom of the cell. Calculations were performed with parameters representative of the Pb-Sb system shown in Table 3.2. The reference concentration used is $c_o = 1/k$and the Peclet number is $P = 0.8$. Both $\mathcal{K}_b$ and y_o can be arbitrarily specified to start the calculation, but only one choice of $\mathcal{K}_b$, for a given y_o, results in a slender sidewall for high values of y. Using the boundary conditions above, the interface is computed upwards towards the cell tip. Three sample interfaces computed by the algorithm are shown in Fig. 5.6 along with the finite element solution to the solutal model equations. The cell bottom regions are blown up and compared in Fig. 5.7. Three different combinations of $\mathcal{K}_b$ and y_o have been used. The interface shapes qualitatively predict the reentrant nature of the transition region between the cell bottom and sidewall regions. The predicted sidewall also compares well with the finite element calculation. Several solutions to the cell bottom are predicted. This is to be expected since the diffusion equations in the two phases have not been solved so that the boundary conditions far downstream in the solid have not been satisfied. However, the simple overall balance is enough to model the characteristics of the cell bottom qualitatively.

The integral equation technique cannot be applied to the case of the one-sided model as any reentrant portion of the cell shape has an interface concentration equal exactly to the concentration at the interface directly above it. This is because solute is convected without diffusion in the solid. This is not accounted for in the averaging procedure.

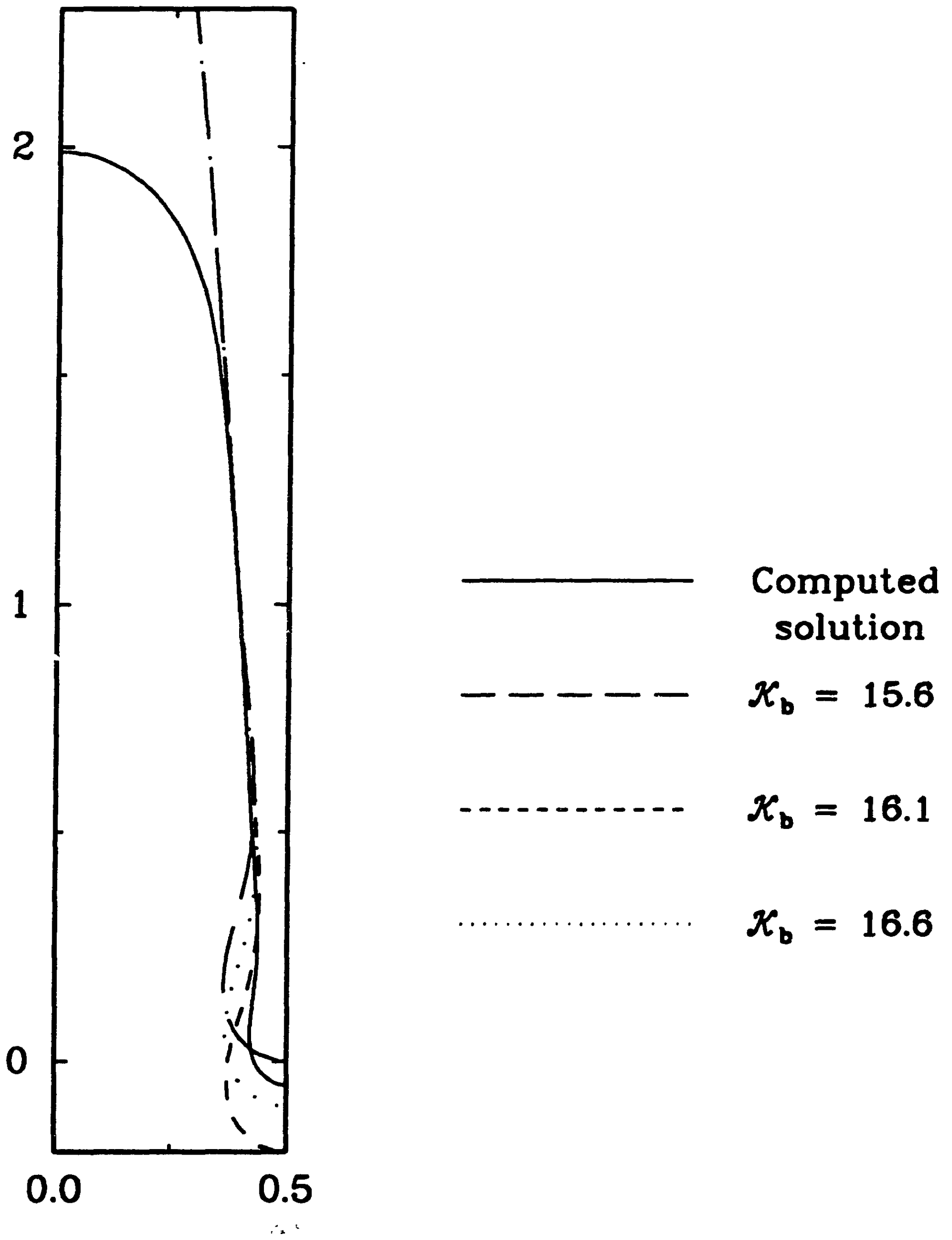

Figure 5.6: Three interfaces computed by solution of the averaged equation along with the cell computed by the finite element procedure. The curvature at the cell bottom $\mathcal{K}_b$ in each case is listed in the figure.

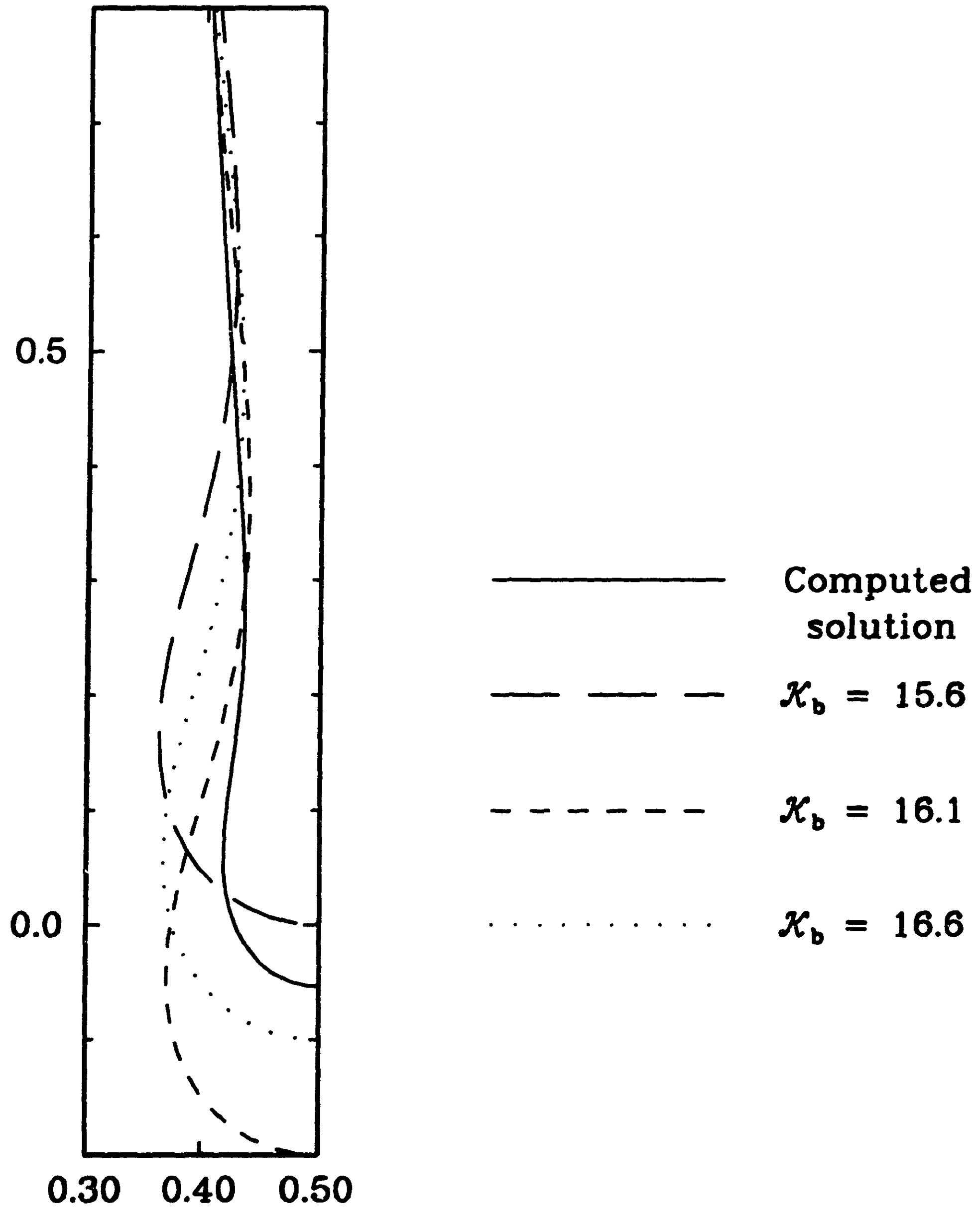

Figure 5.7: Cell bottoms for the three interfaces computed by the solution of the averaged equation listed in Fig. 5.6 along with the cell bottom computed by the finite element procedure. The curvature at the cell bottom $\mathcal{K}_b$ in each case is listed in the figure.

5.4 Cell Tip

The cell tip region is comparatively more complicated. The length scales in this region appear to be of $\mathcal{O}(1)$ in both phases. Thus no scaling conditions can be derived. The concentration field equations in the two phases have to be solved fully.

At high growth rates, a boundary layer builds up in front of the interface, so that a boundary layer scaling of the y-coordinate with P is valid; However, the effect of adjacent cells, as represented by the lateral symmetry boundary conditions are still important, as shown in the following section; thus a simple asymptotic solution could not be found.

As seen in Fig. 3.12, the surface energy is important in this region though the curvature is small. This is because the concentration here changes very little over the entire region, so that the change in concentration could balance the small effect of curvature in the Gibbs-Thomson equation. The importance of a small parameter, the surface energy, in selecting the shape of the cell tip is similar to the Microscopic Solvability conditions which arise in other fluid systems such as dendritic solidification and Saffman-Taylor fingering in Hele-Shaw cells. Unlike in these systems, where the overall dimension is selected by this criterion, in directional solidification it appears that such criteria are possible only for the selection of the shape of the cell tip characterized by the dimensionless radius of the cell tip.

5.5 Computation of Deep Cells Using the Results of the Asymptotic Analysis

As mentioned in Chapter 3, a problem that is frequently encountered during the calculation of deep cells using the solutal model is the narrowing of the groove between adjacent cells. Accurate computation is made impossible by distortions that result in the discretization in the narrow portion of the groove so that accurate solution of the deep cellular shape families could not be completed. In particular, computation of the bifurcation diagrams with increasing growth rate in Section 3.3 could not be completed using the numerical procedure outlined in Chapter 2. This restricts the analysis of any transition to dendrites as explained below.

Any transition from deep cells with rounded tips protodendritic forms which have sharp parabolic tips is only expected at high P where the concentration field is expected to wrap around the cell tip in a boundary layer so that the effect of adjacent cells is negligible. The analysis then reduces to that of an isolated single finger growing in an infinite medium ahead of it; this resembles the configuration that is generally assumed in the simulation of dendrites; see Section 1.5.

The asymptotic results of the sidewall presented in Section 5.2 provide a means of overcoming the difficulty posed by the narrow grooves. The analysis of the slender region shows that the sidewall is entirely determined by an overall mass balance and can be located in the domain independent of the cell tip and bottom regions. This result is used to eliminate the need for the computation of the narrow melt regions near the bottom. Only the cell tip and sidewall regions are computed. The extent of the sidewall that is computed is also adjusted so that the groove is not too narrow. The discretization used in the computations is shown in Fig. 5.8. As in Chapter 2, a Cartesian representation is used for the sidewall region and a cylindrical polar coordinate system is employed for the cell tip region. The discretization can again be independently graded in the η-direction (towards or away from the interface) and ξ-direction in both regions in either phase. As before, the length of the Cartesian region is allowed to vary so that cells of arbitrary lengths can be calculated.

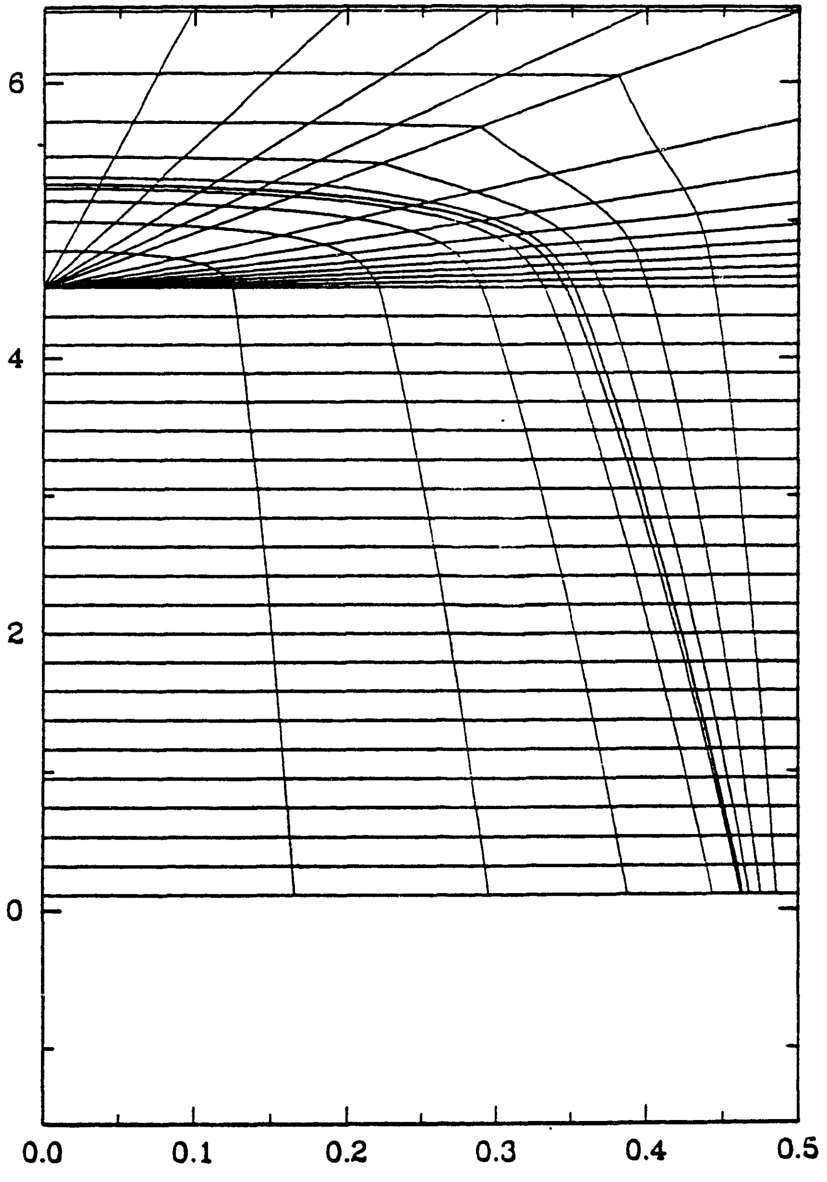

Figure 5.8: Schematic of the deep cell showing the discretization used in the computations with the asymptotic sidewall. Cartesian coordinates are employed for the sidewall region and a cylindrical polar coordinate system is employed for the sidewall region.

Appropriate boundary conditions derived from the asymptotic analysis of the sidewall are employed at the bottom of the Cartesian region. The concentration profile and interface slope predicted by the asymptotic analysis are specified as follows:

$$\frac{dh}{dy} = \left(\frac{G}{m}\right)\left\{\frac{k^2}{2(1-k)}\right\} \quad , \tag{5.52}$$

$$c_m(x, y_b) = c_o - \frac{G}{m}y_b - \frac{\Gamma}{m}(2\mathcal{H}) \quad , \tag{5.53}$$

where y_b is teh position of the bottom of the new domain. No condition is specified on the size of the groove and $h(y)$ is determined by the numerical procedure.

Comparison of the results of the calculation with the bottom retained, with the results of the above formulation, is plotted in Fig. 5.9; the cell shapes and the corresponding discretizations in the two methods are shown in the figure. The shapes of the cell tip and sidewall regions are reproduced accurately by the procedure using the asymptotic sidewall. In addition this technique has the advantage that for the same accuracy the computational effort is decreased because the number of unknowns is lower. Further, for cells that have narrower grooves the computation can be stopped higher up along the sidewall so that the discretization is not distorted. The technique is used effectively for computation of cell shapes of higher nonlinearity, as demonstrated in the following section.

The comparison of these methods is continued in the followins section, where deep cells were computed with both methods, as the anisotropy of the surface energy was varied.

5.6 Effect of Anisotropy of Surface Energy

Estimates for the anisotropy of the surface energy for organic alloys range from 0.075 for SCN to 0.75 for pivalic acid (Huang & Glicksman 1981). Typical values for most organic alloys lie near the lower end of this range. Even for small values of ϵ_a, the effect on the interface shape is significant as demonstrated below.

The effect of anisotropy of the surface energy of the interface shape is examined by calculations of deep cells with a constant spatial wavelength but varying ϵ_a. Calculations

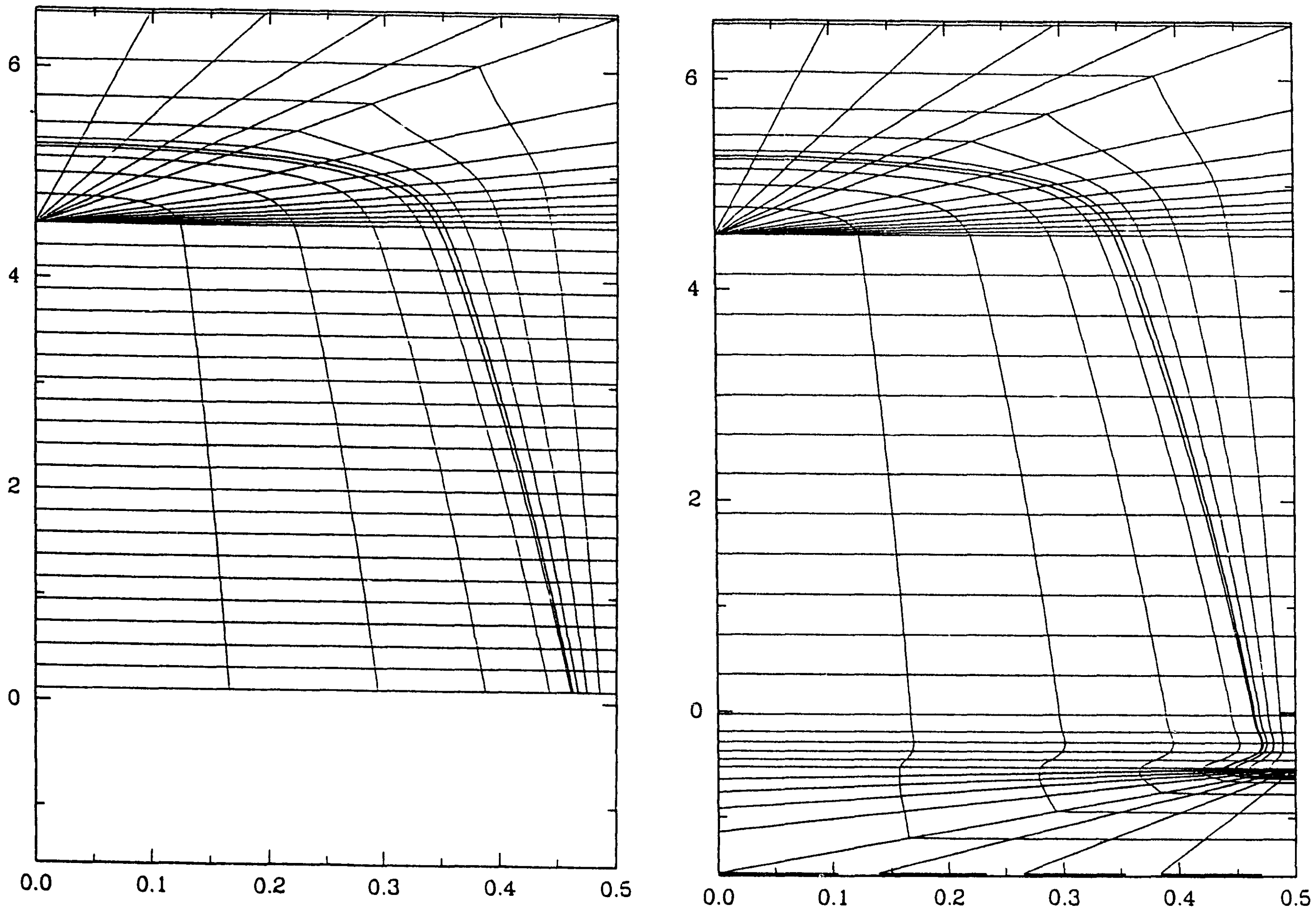

Figure 5.9: Comparison of the interface computed using the asymptotic sidewall with the shape of the cell computed by solution of the solutal model in all regions of the cell. The discretization employed in each case is also shown.

were done using the parameters listed in Table 3.1 which are representative of a Pb-Sb system. The growth rate was maintained constant so that $P = 2.3615$. This value corresponds to the limit point with increasing growth rate in the $\lambda = 1/2$ family shown in Fig. 3.9. Calculations were done, both with the bottom retained, and with the modified technique described in the previous technique.

As the anisotropy was increased two families of cells were computed. These families of cells are shown with the position of the cell tip (y_{tip}) as a function of ϵ_a in Fig. 5.10. The solid curve represents the results of the calculations with the bottom retained, and the points represent the procedure with the asymptotic sidewall. As Fig. 5.10 indicates, the two procedures compare well for the calculations presented here.

As discussed in Section 3.7, y_{tip} can be used as an approximate measure of the the length of the cell since for a reference concentration $c_o = 1/k$ the $\mathcal{O}(1)$ cell bottom attaches itself to the sidewall approximately at $y = 0$. Fig. 5.10 can thus be directly compared with the bifurcation diagrams plotted in Section 3.3; Figs 3.7 and 3.9. The two families are joined at $\epsilon_a = 0$. This point represents the limit point shown in Fig. 3.9 for the $\lambda = 1/2$ family with increasing P for $\epsilon_a = 0$. Sample shapes from the two families in Fig. 5.10 are plotted in Fig. 5.11. Along the lower family, cells have decreasing lengths as ϵ_a is increased. The cells get increasingly flat at the tip and undergo tip-splitting as ϵ_a is increased. It is expected that the family of solutions connects to another family with wavelength $\lambda = 1/4$ through a secondary bifurcation. This behavior is similar to the tip-splitting of the $\lambda_c/2$ family in Fig. 3.7 and the $\lambda = 1/2$ family in Fig. 3.9 as the Peclet number is increased (see Section 3.3). No attempt was made to compute the $\lambda = 1/4$ family.

No limit point with increasing ϵ_a was detected in the upper family of cells for the range, $0 \leq \epsilon_a \leq 1$. As discussed in Section 1.2, $\epsilon_a > 1.0$ leads to faceted interfaces; attempts at numerical computation of cells in this regime were not successful.

To check if the cells were getting more pointed and parabolic as an indication of a transition to protodendrites the radius of curvature of the cell tip was estimated for the shapes corresponding to the computations in Fig. 5.10. The results are plotted in Fig. 5.12 with the radius of curvature at the cell tip r_{tip} plotted as a function of ϵ_a for the two

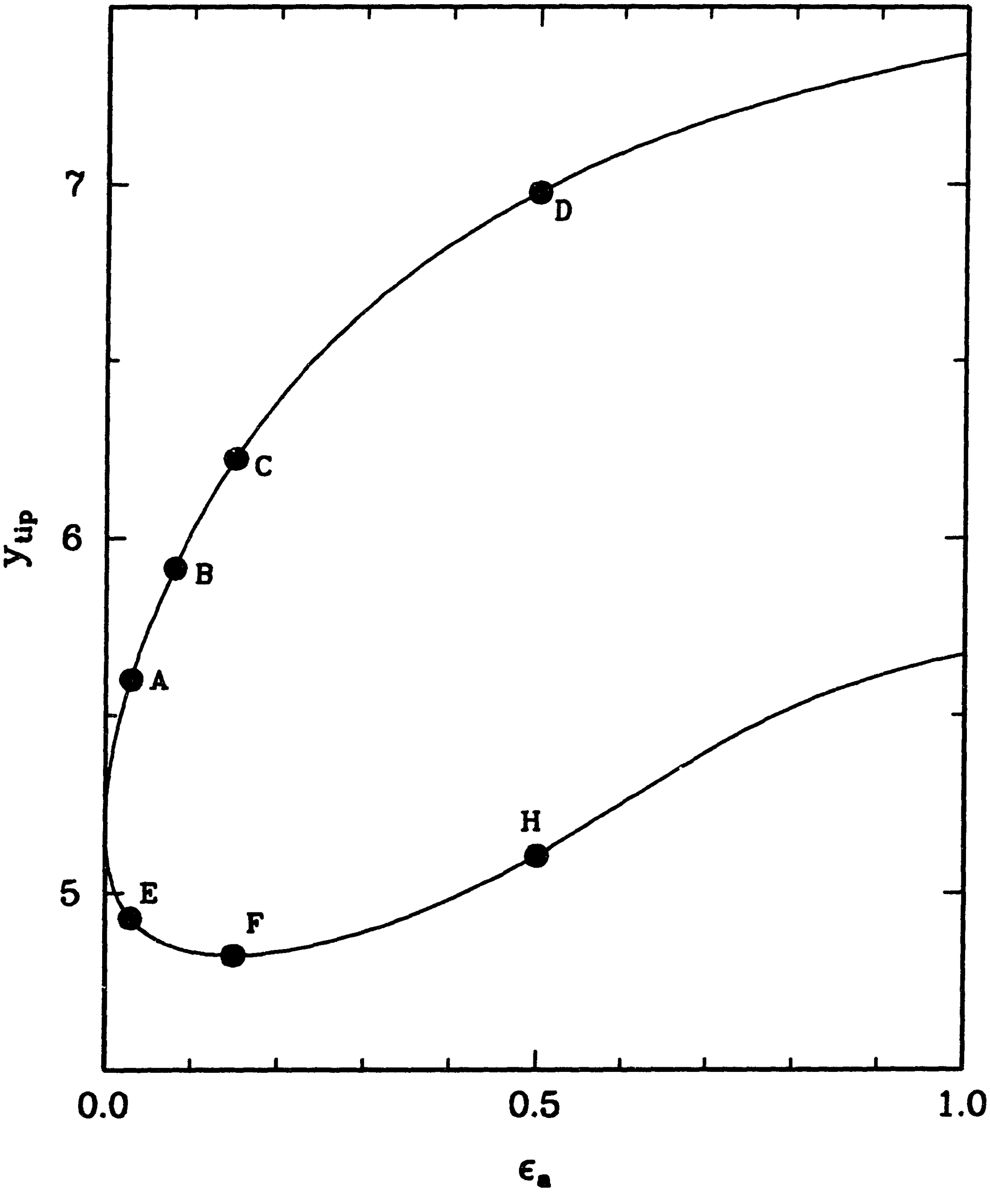

Figure 5.10: Variation of the position of the cell tip y_{tip} with the anisotropy of the surface energy ϵ_a. All other parameters were maintained at the values listed in Table 3.2.

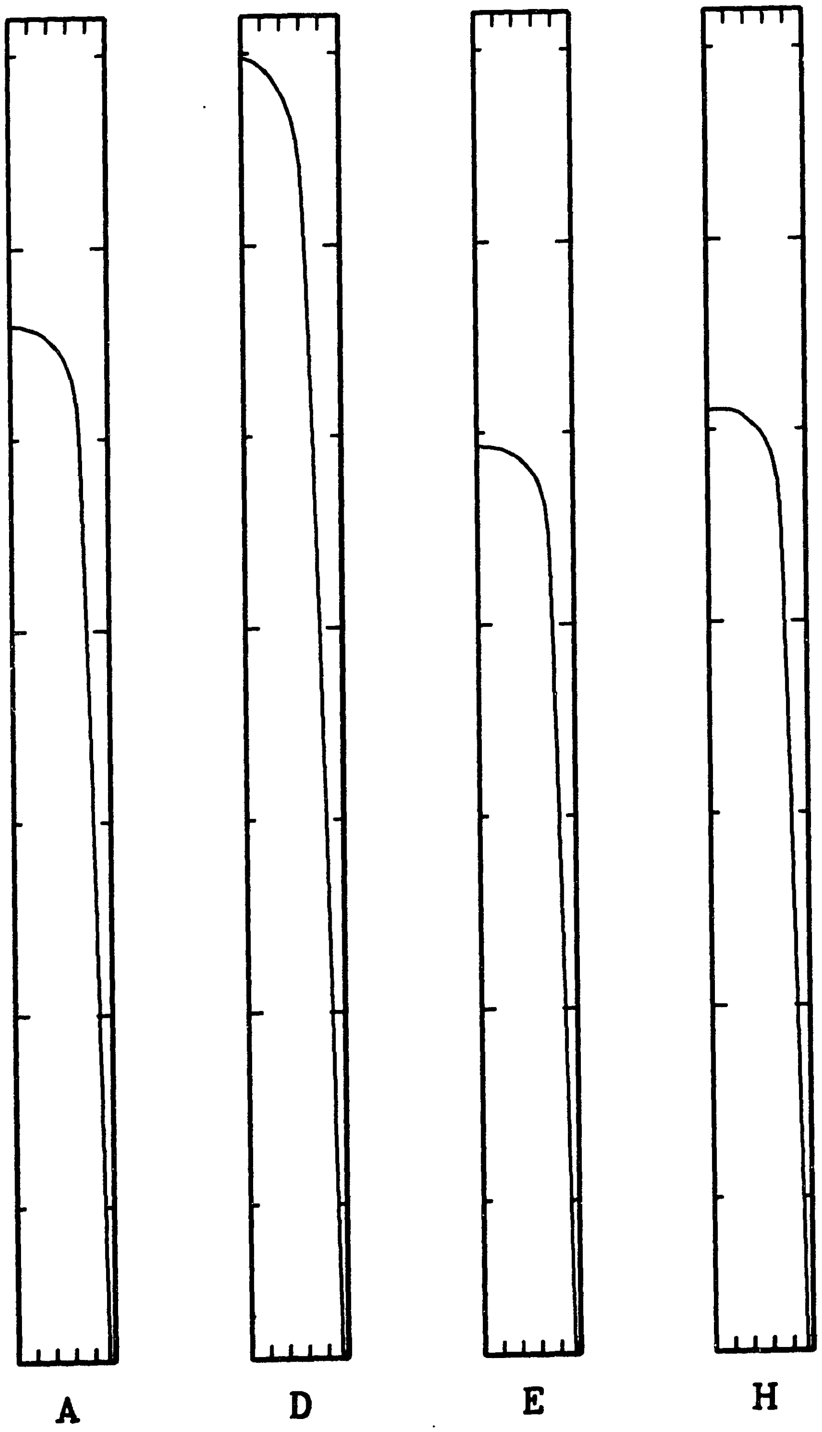

Figure 5.11: Sample interfaces showing the effect of ϵ_a of the cell shape. Letters correspond to solutions listed in Fig. 5.10. All other parameters were maintained at the values listed in Table 3.2.

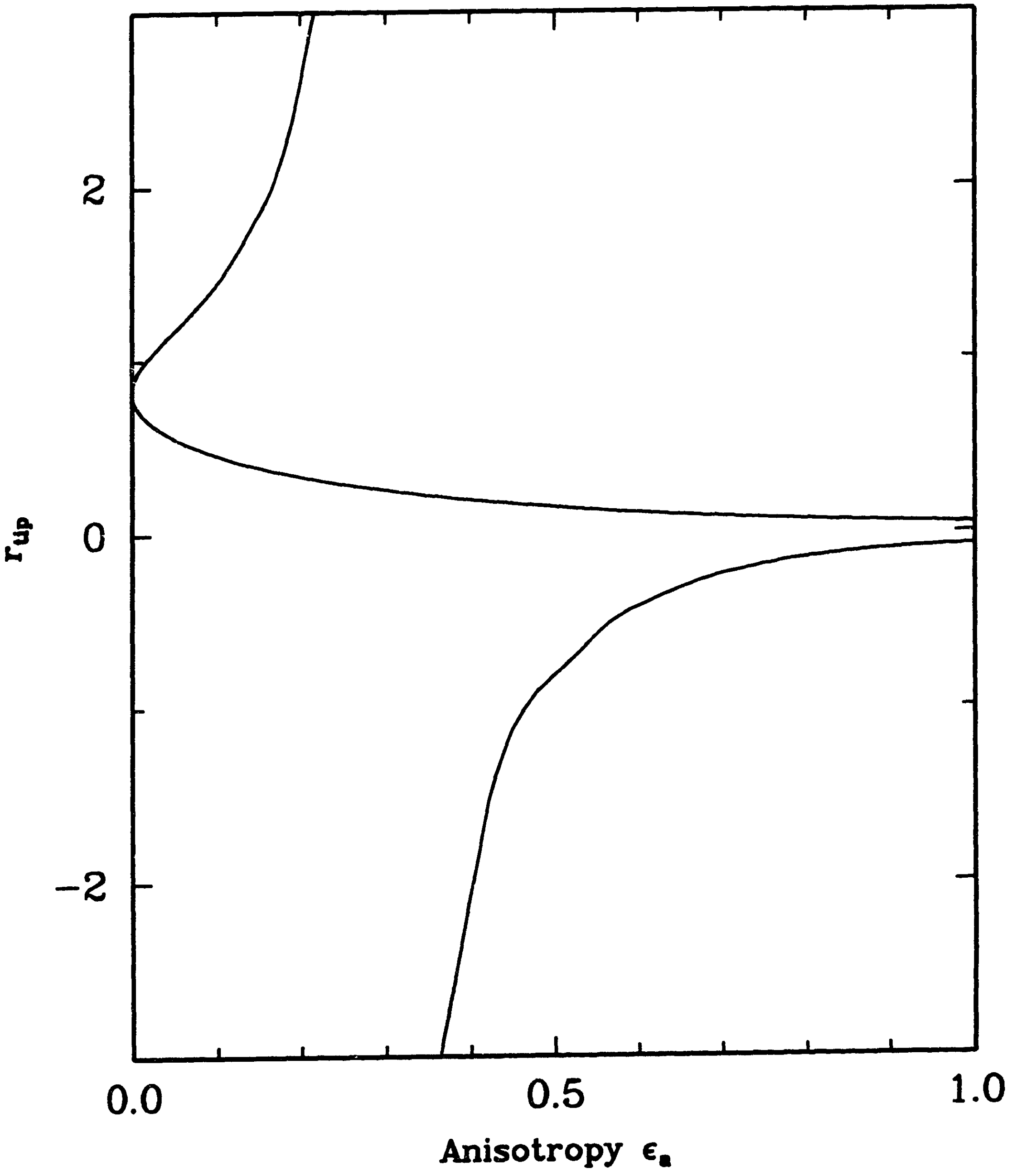

Figure 5.12: Dependence of the radius of curvature at the cell tip $r_{\rm tip}$ on ϵ_a. The solutions families are the same as those shown in Fig. 5.10.

families shown in Fig. 5.10. Along the lower family the radius increases rapidly as ϵ_a is increased as the cell tip gets flatter. The radius reaches an infinite value when the cell tip is planar just before tip-splitting. Cells computed beyond this value of ϵ_a have indented tips as indicated by the negative radius of curvature. The indentation gets deeper and is more pointed as indicated by the increasing radius of curvature. The tip-splitting phenomenon is very similar to that which occurs with increasing growth rate as described in Section 3.3. Along the upper family of solutions the cells gets increasingly pointed as the anisotropy is increased.

While the radius of curvature of the cell tip decreases with increasing ϵ_a on the upper family, the cell tip is flatter than a circle or a parabola with the same radius at the tip. This is shown in Fig. 5.13 where the computed cell shape has been compared with a circle and a parabola with the same radius of curvature at the tip as the deep cell for a value $\epsilon_a = 0.10$. No transition to protodendritic shapes with an increase in ϵ_a is indicated.

To check if any transition to protodendritic shapes is seen with increasing growth rate and nonzero anisotropy, calculations were also performed with increasing P for cells of a constant wavelength for four values of the anisotropy of the surface energy: $\epsilon_a = 0.03$, 0.08, 0.15, and 0.5. The Peclet number was increased in each case from $P = 2.3615$. The starting points corresponds to points A, B, C and D on the upper family of Fig. 5.10. The results of the calculations are plotted in Fig. 5.14 with the position of the cell tip (y_{tip}) plotted as a function of P. Sample shapes from these families are plotted in Fig. 5.15. Steadily solidifying cells were calculated up to a limit point $P = 2.5248$ for $\epsilon_a = 0.03$. This maximum Peclet number steadily increases as ϵ_a is increased as shown in Fig. 5.16 with P_{limit} as a function of ϵ_a, where $P_{\text{limit}}(\epsilon_a)$ is the maximum Peclet number of steadily solidifying cells of wavelength $\lambda = 1/2$ with the specified anisotropy of the surface energy. The limit point in the calculations with increasing P is predicted to move towards higher values of P as ϵ_a is increased. Thus, the range of possible growth rates is widened.

It is expected that all the families of solutions in Fig. 5.14 turn around at their respective limit points towards lower values of P with cells shapes that undergo tip-splitting as the solution family finally intersects the $\lambda = 1/4$ family at a secondary bifurcation point. This continuation of the solution family towards lower values of P is illustrated by calculations

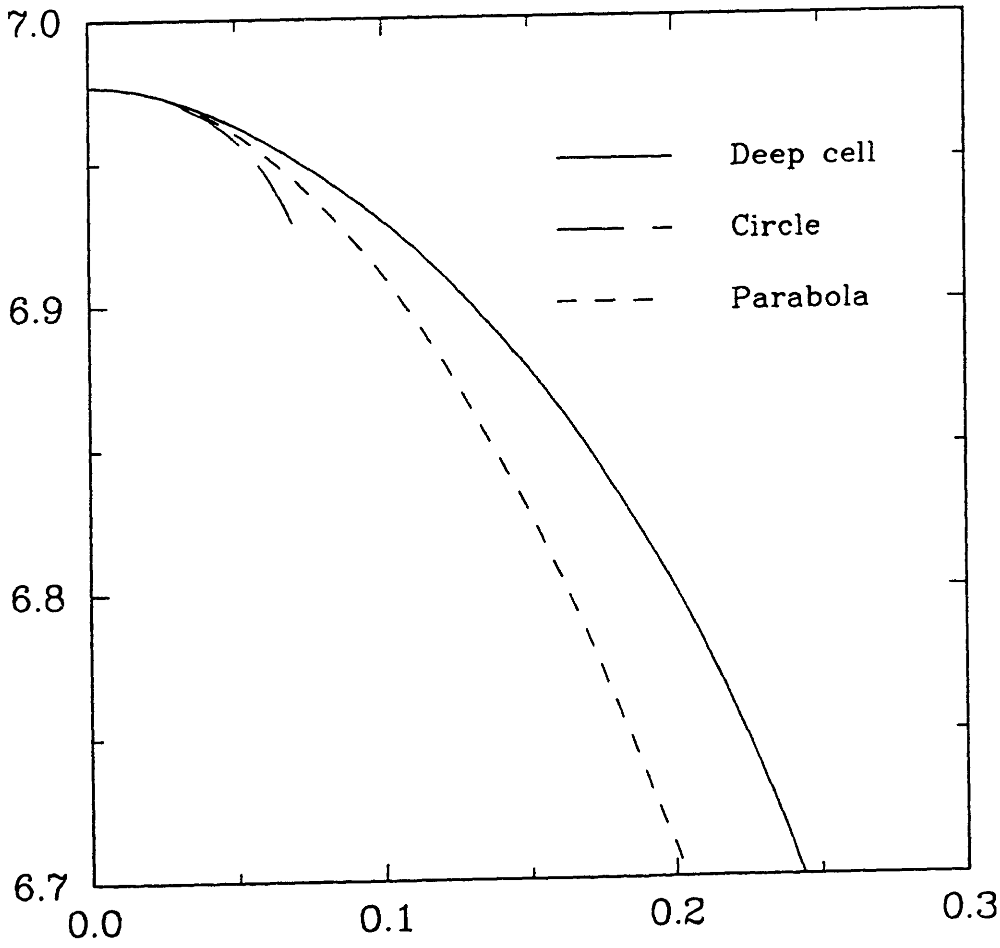

Figure 5.13: Comparison of the shape of the cell tip for $\epsilon_a = 0.1$ with a circle and a parabola with the same radius of curvature at the tip as the deep cell.

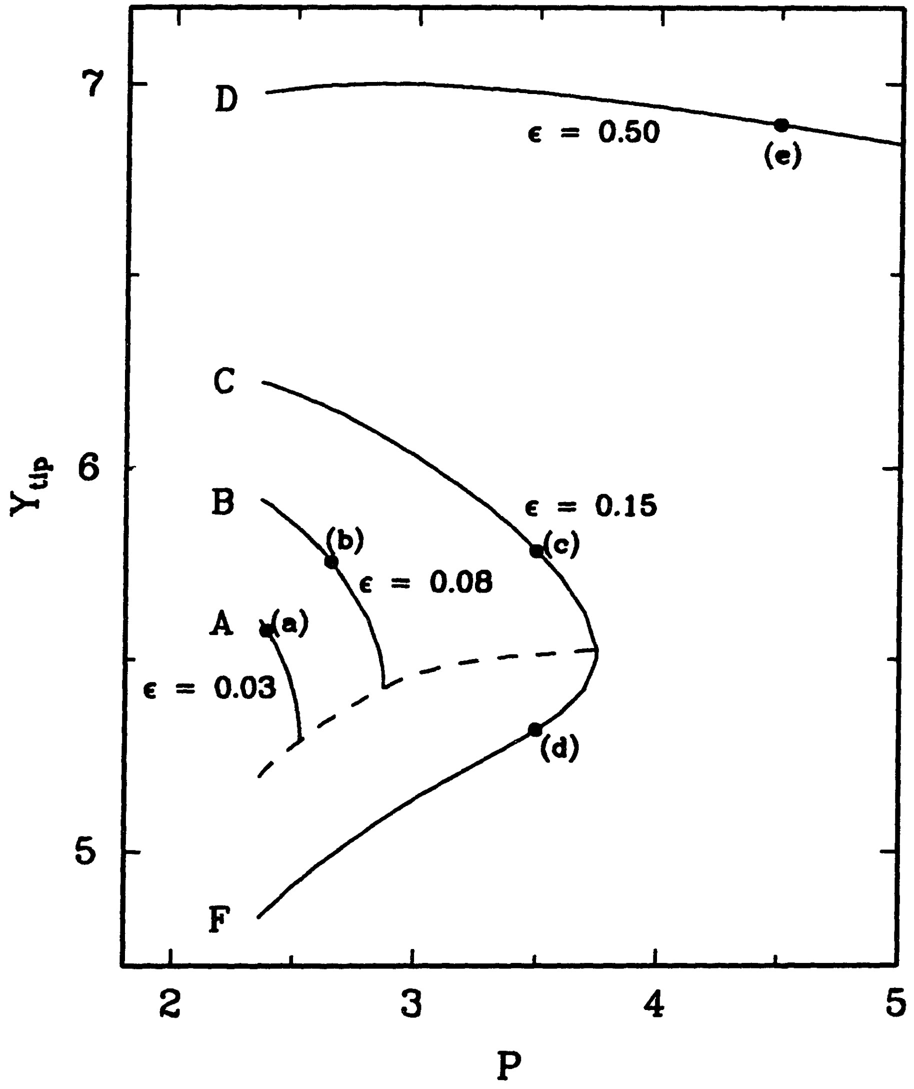

Figure 5.14: Evolution of cells with P for non-zero ϵ_a represented with the position of the cell tip y_{tip} plotted as a function of P. The dashed line is the curve of limit points. Capital letters correspond to points on Fig. 5.10.

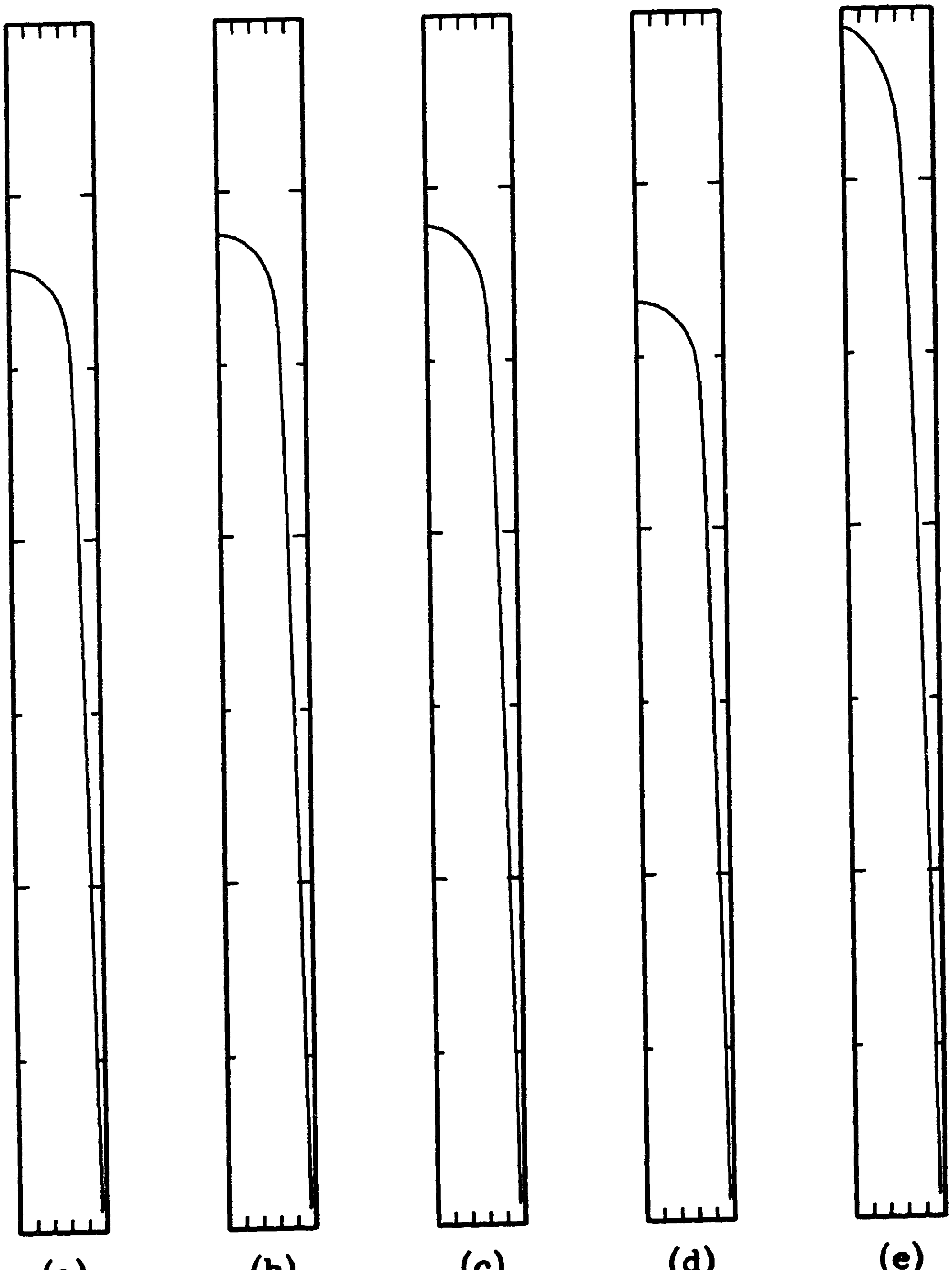

Figure 5.15: Sample interfaces showing the evolution of cell shape with P for non-zero ϵ_a. Letters correspond to points on Fig. 5.14.

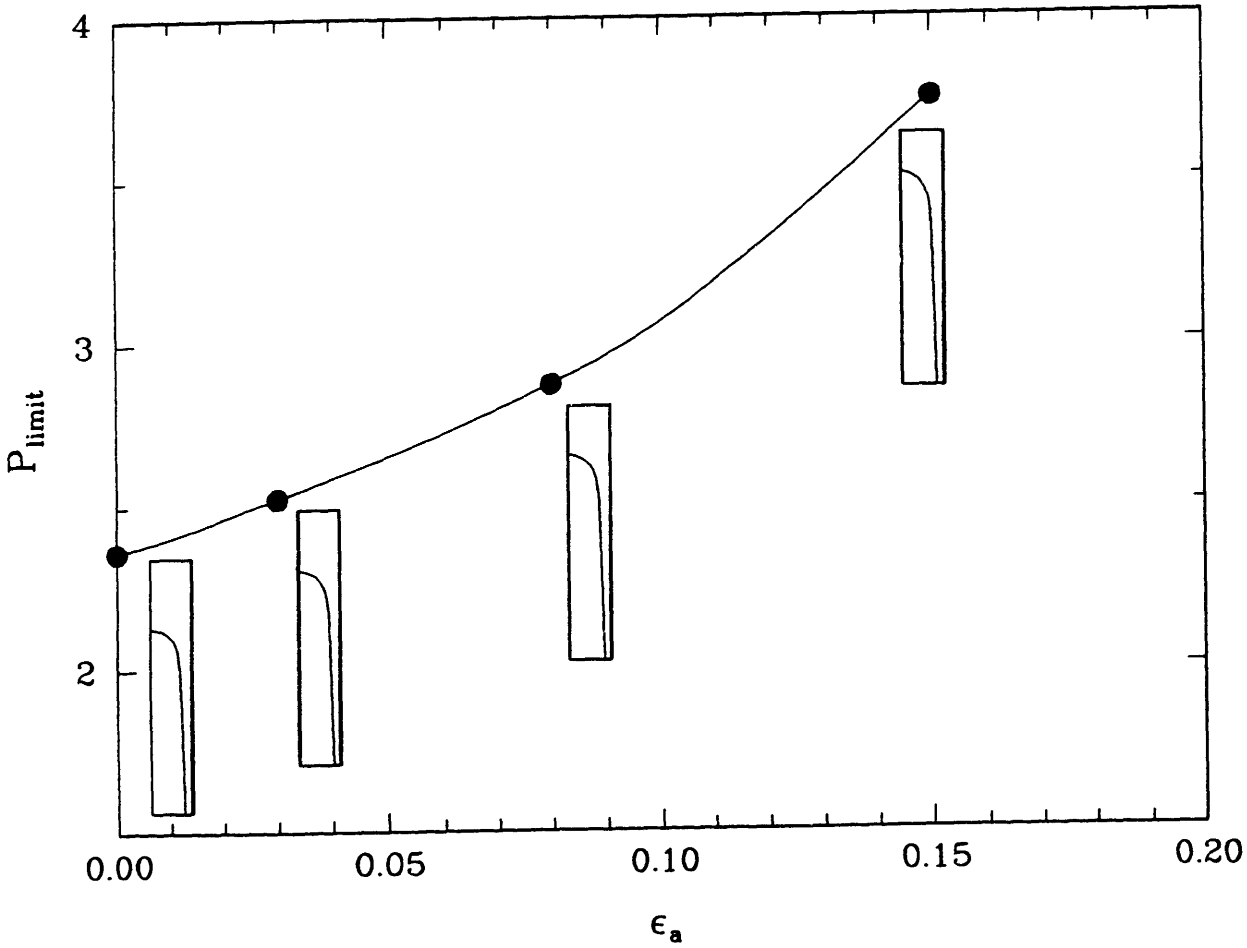

Figure 5.16: Maximum Peclet number of cells with $\lambda = 1/2$ as a function of ϵ_a for the solution families shown in Fig. 5.14.

for $\epsilon_a = 0.15$ and is shown in Fig. 5.14. The cell shapes along the lower portion of this family get increasingly flat as P is decreased as shown in Fig. 5.15 and undergo tip-splitting. This is the generic behavior of deep cellular families of a constant spatial wavelength as the growth rate is increased as described in Section 3.3. It is interesting to note that the lower portion of the family of solutions intersects the lower family of Fig. 5.10 when $P = 2.3615$ at point F. Thus there is a two-dimensional surface of solutions in ϵ_a–P–y_{tip} space with a fold which corresponds to the curve of limit points. Fig. 5.10 is thus a slice of this surface at $P = 2.3615$; the two families correspond to the upper and lower surfaces.

For $\epsilon_a = 0.5$, cells exist for Peclet numbers higher 10. No limit point was detected for the range of Peclet numbers used in the computations. While deep cells exist for higher value of growth rate, there is no indication of a transition to protodendritic interfaces. This is shown in Fig. 5.17 where the deep cell shape for $\epsilon_a = 0.5$ and $P = 9.0$ is plotted along with the parabola with the same radius at the tip as the deep cell. The deep cell is flatter than the parabola. This is to be expected as the flattening of the cell tip is a generic feature that is observed for cells before tip-splitting.

Fig. 5.18 shows the concentration contours around the cell tip for the deep cell in Fig. 5.17. The high value of P causes a bunching of the contours near the tip in a boundary layer but the assumption of a single isolated cell growing in an infinite medium is invalid as the symmetry condition at the lateral boundary $x = 1/2$ continues to influence the concentration field near the cell tip. Thus the concentration field also does not resemble the field expected around protodendritic forms as discussed in Section 1.5.

5.7 Discussion

An asymptotic analysis based on the slenderness of the sidewall has been developed. The parameter ϵ derived from an approximate estimate of the length of the cell is shown to be an accurate indicator of the degree of deviation from the planar state and is used as the perturbation parameter in the asymptotic analysis. In essence, deep cells are possible for small values of the temperature gradient and/or the segregation coefficient.

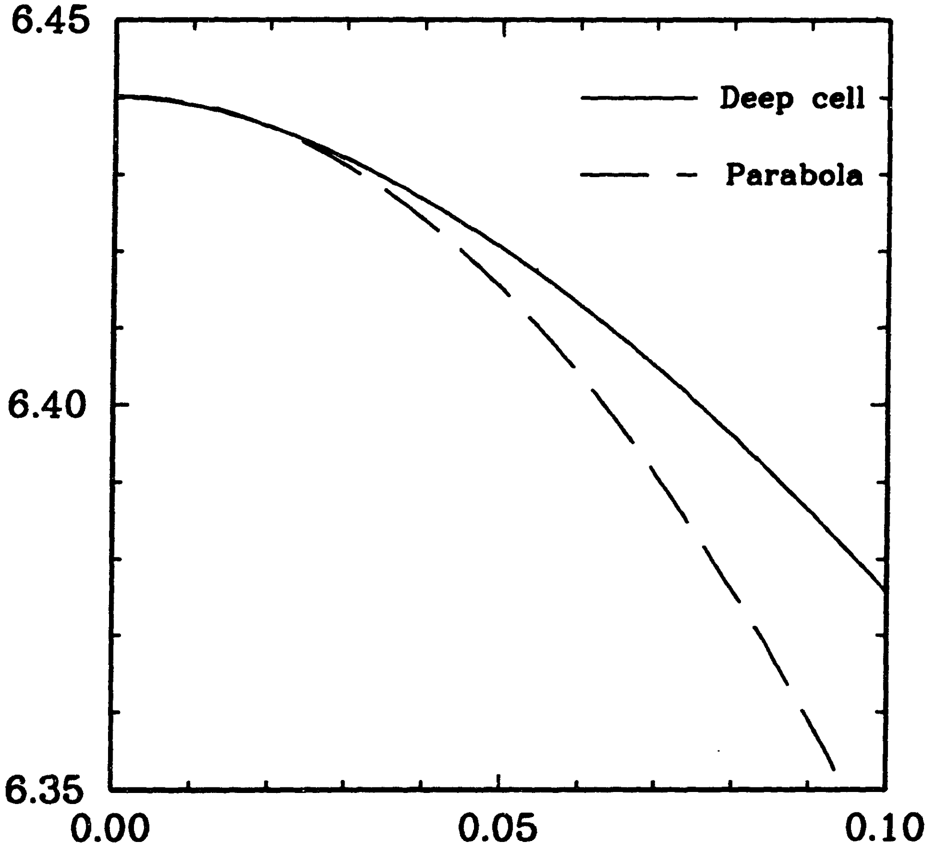

Figure 5.17: Comparison of the shape of the cell tip for $\epsilon_a = 0.5$ and $P = 9.0$ with a parabola with the same radius of curvature at the tip as the deep cell.

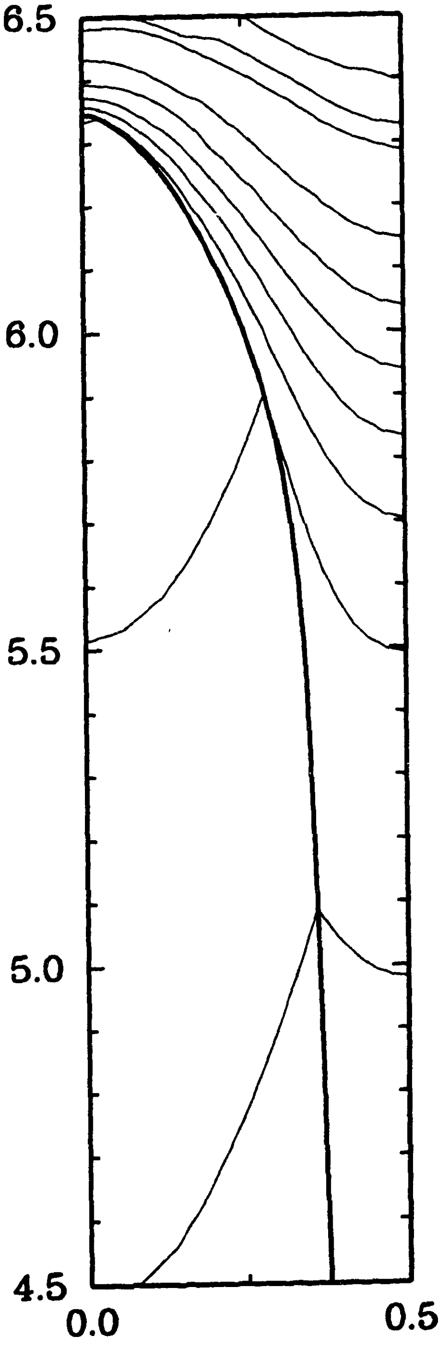

Figure 5.18: Concentration contours plotted near the cell tip for the deep cell in Fig. 5.17.

The sidewall region is assumed to be long and slender and of negligible curvature. The resulting solution predicts a linear sidewall to $\mathcal{O}(\epsilon^{1/2})$. The concentration field is linear to $\mathcal{O}(\epsilon^{1/2})$ and has a quadratic decay away from the interface at $\mathcal{O}(\epsilon)$. The interface shape and concentration field in this region are shown to agree with the finite element computations.

The most important result of the analysis of the sidewall is that this region can be completely determined; an overall solute balance at any cross section of the cell exactly locates the sidewall in the coordinate system so that no constants remain to be determined by matching of the sidewall to the cell tip or bottom regions. The cell tip and bottom regions are decoupled and can be separately analyzed. This also rules out the possibility of the existence of any small effect of the surface energy that propagate from the bottom towards the cell tip thus determining its shape; wavelength selection by microscopic solvability seems impossible.

The cell bottom and tip regions cannot be reduced by the perturbation analysis. The solid phase in the bottom region is an $\mathcal{O}(1)$ region where the full partial differential equations have to be solved. An averaged equation derived by performing an overall solute balance at an arbitrary cross-section is solved to predict qualitatively similar cell bottom shapes. The solution also predicts a reentrant transition region through which the cell bottom is attached to the sidewall; the sidewall is predicted accurately. The cell tip region is $\mathcal{O}(1)$ in both phases so that the partial differential equations have to solved fully for the analysis of this region.

To overcome the difficulty posed by the narrowing of the groove between cells as the cell grows deep, a modified numerical procedure is developed based on the results of the asymptotic analysis of the sidewall. The asymptotic interface shape and concentration field are specified as boundary conditions somewhere in the sidewall region and the equations are solved only for the remainder of the sidewall region and the cell tip region. Accurate solutions are obtained with less computational effort. The procedure also allows for computation of cells with a greater degree of nonlinearity that the original procedure outlined in Chapter 2.

Using this procedure, calculations were performed for cells of a constant wavelength with increasing anisotropy of the surface energy ϵ_a and at constant anisotropy with increasing growth rate. The calculations revealed a two-dimensional surface of solutions in ϵ_a–P–$y_{\rm tip}$ space. The surface has a fold that corresponds to curve of limit points that arise during calculations at a constant ϵ_a but increasing growth rate. The limit point $P_{\rm limit}$ is shown to move outward in P for increasing ϵ_a so that cells exist for a greater range of growth rates at higher anisotropy. However, these cells at higher value of P are not pointed and parabolic indicating that no transition to protodendrites is imminent. The cells get flatter at high P, eventually undergoing tip-splitting as the family of cells turns around at the limit point towards lower values of P; it is expected that these families join another family with half the spatial wavelength at a secondary bifurcation point. This behavior is similar to that for calculation at $\epsilon_a = 0$ that were described in Section 3.3.

Chapter 6

Conclusions

The work of this thesis confirms the general characteristics of the evolution of cellular interfaces that are seen in experiment and that have previously been simulated by other researchers. This study extends the general understanding of the morphology to large-amplitude interfaces. In addition this thesis is the first study to show conclusively that selection of the wavelength steadily growing cells is not seen in two-dimensional Thermal-Solutal models of directional solidification. Furthermore, this thesis is among the first works to attempt a comparative study of the existing experimental data with theoretical results obtained using a thermal-solutal model.

The results of the thesis are summarized in the following sections, and the major conclusions are enumerated. Finally, some possible directions for future research are suggested and discussed in Section 6.9.

6.1 Accuracy of the Numerical Method

The finite element methods used in the calculations presented in this thesis, based on the work of Ungar (1984), are effective for accurate solution of the steady-state problems arising from the Solutal and Thermal-Solutal Models of microstructure formation in binary alloy solidification and the time-dependent problem arising from the Solutal Model, as described in Sections 3.2 and 4.1. The combination of the Galerkin finite element discretization and the nonorthogonal mapping leads to accurate descriptions of deep cellular interfaces and the concentration and temperature field variables, as shown Fig. 3.6 and Fig. 4.1.

6.2 Tip-splitting and Wavelength Halving

The behavior of halving of the wavelength of steady-state cells has been previously established for shallow cells as a generic feature of their evolution from the planar state. Described generally, a family with initial wavelength λ terminates at a secondary bifurcation with the family of cellular solutions with the wavelength $\lambda/2$ as the bifurcation parameter is varied. This process occurs by the phenomenon of tip-splitting where the tip of the cell undergoes an indentation which becomes deeper as the bifurcation parameter is changed. Numerical simulations by Ungar & Brown (1984a, 1984b, 1985), Ungar *et al.* (1985), Bennett *et al.* (1987) and Bennett & Brown (1989) using the Mongé representation for shallow cellular interfaces show that wavelength halving occurs. In these studies with different sets of parameters, the growth rate or the temperature gradient was used as the bifurcation parameter; these results are reviewed by Bennett (1990).

The work of this thesis is the first to show that wavelength halving is not restricted to shallow cells; deep cells with reentrant interfaces also undergo tip-splitting and wavelength halving as shown in Sections 3.3 for a Pb-Sb alloy and in Section 3.6 for a CBr_4-Br_2 alloy. This is a significant result because of the observation that while the spacing between shallow cells changes quickly and often in experiments where the growth rate is increased, deep cells with narrow grooves and reentrant bottoms do not change their spacing dramatically; see Section 1.5.1. Indeed, the wavelength of cells reported at the onset of morphological instability in experiments is much lower than the critical wavelength predicted by linear theory. This phenomenon has been explained by Bennett (1990) as follows: the flatness of the marginal stability curve causes many spatially resonant modes to become unstable for a small increase in growth rate, resulting in repeated wavelength halving for growth rates that are just greater than the critical value. The decrease in wavelength at higher growth rates is less dramatic as shown in Fig. 1.27 for experiments with the CBr_4-Br_2 alloy by de Cheveigné *et al.* (1986). This is because any rearrangement of the concentration and temperature field in the narrow grooves and reentrant bottoms of deep cells is inherently more difficult. However, the results of this thesis clearly show that wavelength halving is yet possible in deep cells. The only difference between the results for shallow and deep cells is that the family of deep cells passes through a limit point and evolves towards lower values of the growth rate before tip-splitting starts, as described in Sections 3.3 and 3.6.

6.3 Wavelength Selection

The most important conclusion of this thesis is that no selection of the wavelength of steadily growing cellular interfaces is observed with the thermal-solutal models of directional solidification described here. At any growth rate, cells exist for a range of wavelengths bounded on the left by the left border of the neutral stability curve and on the right by a curve of limit points that corresponds to the set of turning points in calculations with a fixed wavelength and increasing growth rate described above. This conclusion has been supported by recent theoretical studies by Dombre & Hakim (1987) and numerical computations by Ben-Amar & Moussallam (1988) and Kessler & Levine (1989).

This study disproves the results of the analysis of Karma (1986) described in Section 1.5.2. The primary difference between the analyses is that smooth cell bottoms and finite-amplitude cells are predicted here for a range of velocities and wavelengths while Karma assumes an infinitely long slender region that ends in a cusp; the reflective symmetry at the cell bottom is forsaken. There are errors in Karma's analysis. Firstly, as Kessler & Levine (1988) note correctly, any finite diffusivity does not allow an infinite cusp. The numerical solution to the field equations shows that the concentration of solute increases linearly with distance from the tip. As the results of Chapter 3 show, the solute diffuses away into the solid phase and the cusp closes at a finite distance. In addition, the existence of an imposed temperature gradient sets the scale for the depth of the cell. In the solutal model, a sidewall of small, but finite slope is computed and the cell depth is hence bounded.

While theories for dendritic solidification have yielded selection mechanisms, the fundamental differences between cellular and dendritic solidification which probably cause these mechanisms to fail for cellular interfaces. The analysis in dendritic solidification is for an individual dendrite in isolation growing into an infinite melt ahead of it; the effects of the neighboring dendrites in a dendritic array on the temperature field are not considered. The effect of neighboring cells is an integral part of the formulation for cellular solidification; this effect is represented by the reflective symmetry boundary conditions along the center of the growing solid and the groove of the cell. In fact, even the selection mechanism for dendrites only selects the tip radius of an individual dendrite and there have been no satisfactory theoretical estimates yet of the primary spacing of dendrites. Warren & Langer (1990) argue that there is no reason to believe that there is any unique primary spacing at fixed growth conditions and that the selected state is probably dependent on the the sequence of events by which the system was set in motion. This is probably the case with cellular solidification as well as discussed below.

Dynamic calculations of shallow cells by Bennett (1990) indicate that the wavelength of the interface must be statistically described. The flatness of the neutral stability curve was shown to cause long transients between steady states. In addition, aperiodic dynamics were indicated in simulations with domains that allowed multiple cells. Thus the interface pattern at any instant is a function of the history of the system. It is therefore believed that any wavelength that is specified for the system has to be a statistical average over all system histories.

Owing to these dynamic phenomena, it is not clear whether truly steady-state morphologies have been reported by experimental researchers or whether the reported wavelengths only indicate instantaneous descriptions of the interface. The experimental system has additional factors that contribute to the need for a statistical description of the wavelength like spatial non-idealities in the thermal field, grain boundaries and noise. These variations often cause changes in wavelength over the length of the interface necessitating a spatial averaging to describe the primary spacing of the interface.

6.4 Comparison with Experimental Data

The results of the numerical procedure compare well with the experimental data of de Cheveigné *et al.* (1986) for the CBr_4-Br_2 system. Simulations using the solutal model in Section 3.6 show that the nonlinear transitions seen in the Pb-Sb system are qualitatively very similar to those for the CBr_4-Br_2 alloy. Wavelength reduction by repeated tip-splitting and absence of selection are confirmed. The range of predicted wavelengths at a given growth rate is shown to bracket the experimentally seen wavelengths as shown in Fig. 3.26. The computed and experimental cell shapes at a given growth rate and wavelength compare favorably as shown in Fig. 3.27

The comparison of cells for similar growth conditions seems extremely promising; however, other points of comparison clearly indicate the still considerable gaps in the understanding of the evolution of cellular microstructures. Although the evolution of the wavelength with increasing growth rate has the same functional form that describes the behavior of the limit point of the band of wavelengths, the insensitivity to the temperature gradient seen in the experiments. Some of the difficulties with accurate quantitative comparison of numerical and experimental results can be traced to some problems with the CBr_4-Br_2 system. Firstly, some of the thermophysical properties needed to describe the solutal model in the CBr_4-Br_2 are not accurately known. Bromine is generated *in situ* by spontaneous photo-decomposition of CBr_4 and the actual composition of the alloy can therefore not be determined with accuracy. In addition, the solid phase solute diffusivity is not known. However, the data on evolution of deep cellular interfaces and the selection of the spacing of these morphologies in the work of de Cheveigné *et al.* (1986) for CBr_4-Br_2 is the most extensive and was therefore selected in this comparative study. A more quantitative comparison will therefore be possible only when extensive data is available for a better characterized system.

6.5 Relative Advantages of TSM versus SM

While the thermal-solutal model can be used to specifically study the effect of latent heat release or thermal convection, the results of Chapters 3 and 4 show that steadily growing deep cells can be simulated quite effectively using the solutal model itself. The onset of cellular solidification and the transition to deep cells are simulated well by the solutal model and the model is adequate for qualitative comparison with experimental data as shown in Section 3.6.

While the results using both models are qualitatively similar, the solutal model has the advantage that the computational effort is approximately half that of the thermal-solutal model for the same accuracy in the concentration field and interface shape.

6.6 Asymptotic Analysis of Solutal Model

An asymptotic analysis based on the slenderness of the sidewall has been developed. The parameter

$$\epsilon = \frac{k}{P(1-k)}\frac{G}{m} \tag{6.1}$$

derived from an approximate estimate of the length of the cell is shown to be an accurate indicator of the degree of deviation from the planar state and is used as the perturbation parameter in the asymptotic analysis. In essence, deep cells are shown to be possible for small values of the temperature gradient and/or the segregation coefficient. The sidewall is predicted to be linear to $\mathcal{O}(\epsilon^{1/2})$. The concentration field is linear to $\mathcal{O}(\epsilon^{1/2})$ and has a quadratic decay away from the interface at $\mathcal{O}(\epsilon)$. The interface shape and concentration field in this region are shown to agree with the finite element computations.

The most important result of the asymptotic analysis of the sidewall in Section 5.2 is that this region can be completely determined without detailed analysis of the cell tip and bottom regions. An overall solute balance at any cross-section of the cell exactly locates the sidewall in the coordinate system so that no constants remain to be determined by matching of the sidewall to the cell tip and/or bottom regions. The cell tip and bottom regions are thus decoupled and can be separately analyzed. This result also rules out the possibility of the existence of any small effect of the surface energy that propagate from the bottom towards the cell tip thus determining its shape; wavelength selection by microscopic solvability is thus not possible.

An averaged equation derived by performing an overall solute balance at an arbitrary cross-section is solved to predict cell bottom with shapes that are qualitatively similar those that are computed using the finite element method as shown in Fig. 5.6.

The cell tip is $\mathcal{O}(1)$ in both phases so that no appropriate scalings could be determined; the partial differential equations have to solved fully for the analysis of this region.

Accurate representation of the domain in the melt region of narrow grooves requires a fine discretization and, thus, extra computational effort, as described in Section 3.3. The results of the asymptotic analysis of the sidewall are used to develop a modified numerical procedure to overcome this difficulty posed by the narrowing of the groove between deep cells. The asymptotic interface shape and concentration field are specified as boundary conditions somewhere in the sidewall region and the equations are solved only for the remainder of the sidewall region and the cell tip region. Accurate solutions are obtained with less computational effort as shown in Section 5.5. The procedure also allows for computation of cells with a greater degree of nonlinearity that the original procedure outlined in Chapter 2.

6.7 Effect of Anisotropy

Calculations using the modified procedure described in Section 5.5 were performed to investigate the effect of the anisotropy of the surface energy. The computations revealed a two-dimensional surface of solutions in ϵ_a–P–y_{tip} space. The surface has a fold that corresponds to curve of limit points that arise during calculations at a constant ϵ_a but increasing growth rate. The limit point P_{limit} is shown to move outward in P for increasing ϵ_a so that cells exist for a greater range of growth rates at higher anisotropy.

The cells get flatter at high P, eventually undergoing tip-splitting as the family of cells turns around at the limit point towards lower values of P; it is expected that these families join another family with half the spatial wavelength at a secondary bifurcation point. This behavior is similar to that for calculation at $\epsilon_a = 0$ that were described in Section 3.3. These deep cells at higher value of P are not pointed and parabolic indicating that no transition to protodendrites is imminent at higher anisotropy as discussed below.

6.8 Transition to Protodendrites

Another result of the calculations is that no transition to dendrites is seen. As discussed in Chapter 1 dendrites are believed to be dynamically changing three-dimensional structures but it is expected that before dendritic microstructures are formed, cells undergo a transition to two-dimensional steady-state protodendritic interfaces that have sharp parabolic tips; these interfaces have been reported in experiments as described in Section 1.3. The calculations reveal that the nonlinear transition to cells with a smaller spacing is a generic phenomenon seen for families of cells of all wavelengths so that no transition to protodendritic morphologies is predicted.

Dendrites have been simulated in theory only using purely thermal models in infinite media as described in Section 1.5.2. Solute segregation is neglected and a single isolated dendrite is assumed to grow into an infinite melt. These conditions are expected to be valid at high growth rates where the solute field in the is tightly wrapped around the cell tip so that the cell tip is shielded from the influence of the neighboring cell; hence, protodendritic interfaces were expected under such conditions. However, the calculation of interfaces at high growth rates using the results asymptotic analysis show that tip-splitting and wavelength halving is seen even in such families. While the concentration field wraps around the cell tip in a boundary layer, the lateral symmetry boundary condition imposed at the center of the cell groove is still ‘visible‘ to the cell tip and the cell tip is not isolated. This explains why protodendrites are not seen.

It is likely that protodendritic microstructures are also dynamically changing and time-dependent calculations are essential to simulate these structures. It is also possible that three-dimensional calculations are necessary to compute such structures.

6.9 Recommendations for Future Work

Develop a three-dimensional model. It is likely that quantitative agreement of simulations with experimental data requires a three-dimensional model. The thin-film experimental system is typically modeled as a two-dimensional system as the transverse direction is assumed to be thin and variations in the field variables and the interface in this direction are neglected. The three-dimensional model would account for the effect of contact angle between the alloy and the bounding plates in the transverse direction; this effect has been shown to be significant (Caroli *et al.* 1986, de Cheveigné *et al.* 1986). The model would also be able to account for any variations in the temperature field in this direction that are caused by heat loss across the boundaries.

McFadden *et al.* (1987) have performed numerical simulations using a three-dimensional one-sided solutal model. Unfortunately, the one-sided model is not appropriate for the computation of deep cells with reentrant grooves. In addition, an assumption of an infinite melt-solid interface was used; this assumption is not appropriate for alloy systems.

Perform time-dependent calculations with multiple cells. It is possible that wavelength selection can occur when one cell interacts dynamically with one or more cells. Bennett (1988) has done a series of time-consuming computations for collections of shallow cells which show a myriad of possibilities including periodic and chaotic solutions, but no pattern selection was indicated. Such calculations for deep cells have not been carried out. An added problem with the analysis for deep cells is the difficulty in finding a transformation which can be used to simulate an array of growing cells; the orthogonal curvilinear transformations of Tsiveriotis (1990) offer one solution. The number of equations to be solved to simulate a pool of even a few cells is large (in addition to the field variables of concentration and temperature and interface shape, the computations must simultaneously estimate the coordinate variables) and the sample size may have to be infinitely larger to simulate an "infinite" number of cells.

It is also possible that instabilities which give rise to dendritic growth and drop-shedding can be simulated with time-dependent calculations involving multiple cells.

Modify the physics in the narrow grooves between adjacent cells. It is possible that simple modifications of the Thermal-Solutal Model are necessary to accurately simulate the physics of deep cells in experimental systems; these modifications may provide a mechanism for wavelength selection. For example, it is possible that the small distance between the walls of the groove of deep cells results in surface effects of attraction or repulsion (Van der Waal's forces) that are not accounted for in the TSM. Fattinger *et al.* (1986) demonstrated that in dendritic growth, such forces affect the characteristics of the wetting of the interface with the wall in thin-film solidification and related the value of the critical spacing between the supporting plates for stable dendritic growth to the van der Waal's energy of the material.

References

Alexander, J. I. D, Wollkind, D. J., & Sekerka, R. F. 1986

The effect of latent heat on weakly nonlinear morphological stability. *J. Crystal Growth* **79**, 849-865.

Bechhoefer, J. & Libchaber, A. 1987

Testing shape selection in directional solidification. *Phys. Rev. B* **35**, 1393-1396.

Ben-Amar, M. & Moussallam, B. 1987

Numerical results on two-dimensional dendritic solidification. *Physica D* **25**, 155-164.

Ben-Amar, M. & Moussallam, B. 1988

Absence of selection in directional solidification. *Phys. Rev. Lett* **60**, 317-320.

Ben-Jacob, E., Goldenfeld, N., Langer, J. S. & Schön, G. 1983

Dynamics of interfacial pattern formation. *Phys. Rev. Lett.* **51**, 1930-1932.

Bennett, M. J. 1990

Morphology and Dynamics of Cellular Interfacial Microstructure During Directional Solidification. *Ph. D. Thesis.* Chemical Engineering, M. I. T.

Bensimon, D., Pelcé, P., & Shraiman, B. I. 1987

Dynamics of curved fronts and pattern selection. *J. Physique* **48**, 2081-2087.

Billia, B., Jamgotchian, H., & Capella, L. 1987a

Pattern selection during directional solidification. *J. Crystal Growth* **82**, 747-756.

Billia, B., Jamgotchian, H., & Trivedi, R. 1990

Cellular and dendritic regimes in directional solidification: microstructural stability diagram. *J. Crystal Growth* **106**, 410-420.

Boettinger, W. J. 1982

Growth kinetic limitations during rapid solidification. In *Rapidly Solidified Amorphous and Crystalline Alloys*, (ed. B. H. Kear, B. C. Giessen, and M. Cohen), pp. 15-31. North-Holland.

Boettinger, W. J., Coriell, S. R., & Sekerka, R. F. 1984

Mechanisms of microsegregation-free solidification. *Mat. Sci. Eng.* **65**, 27–36.

Brattkus, K. 1990

Capillary instabilities in deep cells during directional solidification. *J. Physique* Preprint.

Brice, J. C. 1965

The Growth of Crystals from the Melt. North-Holland.

Brice, J. C. 1986

Crystal Growth Processes. Blackie & Son Limited, distributed in the USA by Halsted Press, a division of John Wiley and Sons Inc.

Brower, R. C., Kessler, D. A., Koplik, J. & Levine, H. 1984

Geometric models of interface evolution. *Phys. Rev. B* **29**, 1335-1342.

Brown, R. A. 1979

Finite-element methods for the calculation of capillary surfaces. *J. Comp. Phys.* **33** 217–235.

Brown, R. A. 1988

Theory of transport processes in single crystal growth from the melt. *AIChE J.* **34**, 881-911.

Brown, R. A., Ramprasad, N., & Bennett, M. J. 1987

Numerical analysis of cellular solidification microstructures. In *Supercomputer Research in Chemistry and Chemical Engineering*, (ed. K. F. Jensen & D. G. Truhlar), pp. 295-333. American Chemical Society.

Burnett, D. S. 1987

Finite Element Analysis. Addison-Wesley.

Busse, F. H. 1982

Transition to turbulence in thermal convection. In *Convective Transport and Instability Phenomena* (ed. J. Zierep & H. Oertel Jr.), pp. 149-171. Braun.

Caroli, B., Caroli, C., Misbah, C., & Roulet, B. 1985a

Solutal convection and morphological instability in directional solidification of binary alloys. *J. Physique* **46**, 401-413.

Caroli, B., Caroli, C., Misbah, C., & Roulet, B. 1985b

Solutal convection and morphological instability in directional solidification of binary alloys. II. Effect of the density difference between the two phases. *J. Physique* **46**, 1657-1665.

Caroli, B., Caroli, C., & Roulet, B. 1982

On the emergence of one-dimensional front instabilities in directional solidification and fusion of binary mixtures. *J. Physique* **43**, 1767-1780.

Caroli, B., Caroli, C., & Roulet, B. 1986

The Mullins-Sekerka instability in directional solidification of thin samples. *J. Crystal Growth* **76**, 31-49.

Chalmers, B. 1964

Principles of Solidification. John Wiley & Sons, Inc.

Chang, C. J. & Brown, R. A. 1983

Radial segregation induced by natural convection and melt/solid interface shape in vertical Bridgman growth. *J. Crystal Growth* **63**, 343–364.

de Cheveigné , S., Guthmann, C., Kurowski, P., Vicente, E., & Biloni, H. 1988

Directional solidification of metallic alloys: The nature of the bifurcation from the planar to cellular interface. *J. Crystal Growth* **92**, 616-628.

de Cheveigné , S., Guthmann, C., & Lebrun, M.-M. 1985

Nature of the transition of the solidification front of a binary mixture from a planar to a cellular morphology. *J. Crystal Growth* **73**, 242-244.

de Cheveigné , S., Guthmann, C., & Lebrun, M. M. 1986

Cellular instabilities in directional solidification. *J. Physique* **47**, 2095-2103.

Coriell, S. R., Cordes, M. R., Boettinger, W. J., & Sekerka, R. F. 1980

Convective and interfacial instabilities during unidirectional solidification of a binary alloy. *J. Crystal Growth* **49**, 13-28.

Coriell, S. R. & McFadden, G. B. 1989

Buoyancy effects on morphological instability during directional solidification. *J. Crystal Growth* **94**, 513-521.

Coriell, S. R., McFadden, G. B., Boisvert, R. F., & Sekerka, R. F. 1984

Effect of a forced Couette flow on coupled convective and morphological instabilities during unidirectional solidification. *J. Crystal Growth* **69**, 15-22.

Coriell, S. R., McFadden, G. B., & Sekerka, R. F. 1985

Cellular growth during directional solidification. *Ann. Rev. Mater. Sci.* **15**, 119-145.

Coriell, S. R., McFadden, G. B., & Voorhees, P. W. 1987

Stability of a planar interface during solidification of a multicomponent system. *J. Crystal Growth* **82**, 295-302.

Coriell, S. R. & Sekerka, R. F. 1976

The effect of the anisotropy of surface tension and interface kinetics on morphological stability. *J. Crystal Growth* **34**, 157-163.

Coriell, S. R. & Sekerka, R. F. 1983

Oscillatory morphological instabilities due to non-equilibrium segregation. *J. Crystal*

Growth **61**, 499-508.

Dahlquist, G. & Björck, A. 1974

Numerical Methods, translated by N. Anderson. Prentice-Hall.

Dee, G. & Mathur, R. 1983

Cellular patterns produced by directional solidification of a binary-alloy. *Phys. Rev. B* **27**, 7073-7092.

Derby, J. J. 1986

Analysis of Heat Transfer, Stability, and Dynamics of Czochralski and Liquid Encapsulated Czochralski Growth of Semiconductor Material. *Ph. D. Thesis.* Chemical Engineering, M. I. T.

Dombre, T. & Hakim V. 1987

Saffman-Taylor fingers and directional solidification at low velocity. *Phys. Rev. A* **36**, 2811-2817.

Eshelman, M. A., Seetharaman, V., & Trivedi, R. 1988

Cellular spacings: I. Steady-state growth. *Acta Metall.* **36**, 1165-1174.

Eshelman, M. A. & Trivedi, R. 1987

The planar to cellular transition during the directional solidification of alloys. *Acta Metall.* **35**, 2443-2452.

Eshelman, M. A. & Trivedi, R. 1988

Wavelength selection of cellular patterns. *Scripta Metall.* **22**, 893-898.

Ettouney, H. M. & Brown, R. A. 1983

Finite element methods for steady solidification problems. *J. Comp. Phys.* **49**, 118-150.

Fattinger, Ch., Honegger, F., & Lukosz, W.

Dendritic solidification in narrow gaps and surface-pressure–induced wetting transition. *Phys. Rev. Lettrs* **57**, 2536-2539.

Finlayson, B. A. 1972

The Method of Weighted Residuals and Variational Principles. Academic Press.

Finlayson, B. A. 1980

Nonlinear Analysis in Chemical Engineering. McGraw-Hill.

Flemings, M. C. 1974

Solidification Processing. McGraw-Hill.

Glicksman, M. E. 1971

Direct Observation of Solidification. In *Solidification*, Papers presented at a seminar of the American Society for Metal, October 11 and 12. Chapter 6, pp. 155-200. American Society for Metals.

Glicksman, M. E., Schaefer, R. J. & Ayers, J. D. 1976

Dendritic growth - a test of theory. *Metall. Trans. A* **7**, 1747-1759.

Glicksman, M. E., Coriell, S. R., & McFadden, G. B. 1986

Interaction of flows with the crystal-melt interface. *Ann. Rev. Fluid Mech.* **18**, 307-335.

Gresho, P. M., Lee, R. L., & Sani, R. L. 1980

On the Time-Dependent Solution of the Incompressible Navier-Stokes Equations in Two and Three Dimensions. In *Recent Advances in Numerical Methods*, (ed. C. Taylor and K. Morgan), pp. 27–79. Pineridge Press Limited, Swansea, U. K.

Haug, P. 1987

Cellular solidification as a bifurcation problem. *Phys. Rev. A* **35**, 4364–4377.

Hele-Shaw, H. S. S. 1898

Investigation of the nature of surface resistance of water and of stream-line motion under certain experimental conditions. *Trans. Instn. Nav. Archit.*, London, **40**, 21.

Heslot, F. & Libchaber A. 1985

Unidirectional crystal growth and crystal anisotropy. *Physica Scripta* **T9**, 126–129.

Huang, S.-C. & Glicksman, M. E. 1981a

Fundamentals of Dendritic Solidification: I. Steady-State Tip Growth. *Acta. Metall.* **29**, 701–715.

Huang, S.-C. & Glicksman, M. E. 1981b

Fundamentals of Dendritic Solidification: II. Development of Sidebranch Structure. *Acta. Metall.* **29**, 717–734.

Horvay, G., & Cahn, J. W. 1961

Dendritic and spheroidal growth. *Acta Metall.* **9**, 695-705.

Hunt, J. D. 1979

Cellular and primary dendrite spacings. In *Solidification and Casting of Metals*, proceedings of an international conference on solidification, organized jointly by the Sheffield Metallurgical and Engineering Association and the University of Sheffield, in association with The Metals Society. The meeting was held at the University of Sheffield on 18-21 July 1977. Pp. 3-9. The Metals Society.

Hunt, J. D. & Jackson, K. A. 1966

Binary eutectic solidification. *Trans. Met. Soc. AIME* **236**, 843-852.

Hunt, J. D. & Jackson, K. A. 1967

The dendritic-eutectic transition. *Trans. Met. Soc. AIME* **239**, 864-867.

Hurle, D. T. 1983

The effect of Soret diffusion on the morphological stability of a binary alloy crystal. *J. Crystal Growth* **61**, 463-472.

Ivantsov, G. P. 1947

Dok. Akad. Nauk. SSSR **58**, 567.

Jackson, K. A. & Hunt, J.D. 1965

Transparent compounds that freeze like metals. *Acta Metall.* **13**, 1212-1215.

Jackson, K. A. & Hunt, J.D. 1966

Lamellar and rod eutectic growth. *Trans. Met. Soc. AIME* **236**, 1129-1142.

Jackson, K. A., Hunt, J.D., Uhlmann, D. R., & Seward, T. P. 1966

On the Origin of the Equiaxed Zone in Castings. *Trans. Met. Soc. AIME* **236**, 149-158.

Jackson, K. A., Uhlmann, D. R. & Hunt, J. D. 1967

On the nature of crystal growth from the melt. *J. Crystal Growth* **1**, 1-36.

Karma, A. 1986

Wavelength selection in directional solidification. *Phys. Rev. Lett.* **57**, 858-861.

Karma, A. 1987

Beyond steady-state lamellar eutectic growth. *Phys. Rev. Lett.* **59**, 71-74.

Karma, A. & Pelcé, P. 1988

Oscillatory instability of deep cells in directional solidfication. Preprint.

Kerszberg, M. 1983a

Pattern formation in directional solidification. *Phys. Rev.* **27** B, 6796-6810.

Kerszberg, M. 1983b

Pattern selection in directional solidification. *Phys. Rev.* **28** B, 247-254.

Kerszberg, M. 1984

Directional solidification fronts: structure and dynamics. *Physica D* **12**, 262-269.

Kessler, D. A., Koplik, J., & Levine, H. 1988

Pattern selection in fingered growth phenomena. *Advances in Physics* **37**, 255-339.

Kessler, D. A. & Levine, H. 1986a

Theory of the Saffman-Taylor "finger" pattern. I *Phys. Rev. A* **33**, 2621-2633.

Kessler, D. A. & Levine, H. 1986b

Theory of the Saffman-Taylor "finger" pattern. II *Phys. Rev. A* **33**, 2634-2639.

Kessler, D. A. & Levine, H. 1989a

Steady-state cellular growth during directional solidification. *Phys. Rev. A* **39**, 3041-3051.

Kessler, D. A. & Levine, H. 1989b

Cellular solutions for highly nonequilibrium directional solidification. *Phys. Rev. A* **39**, 3208-3210.

Kessler, D. A. & Levine, H. 1990

Linear stability of directional solidification cells. *Phys. Rev. A* **41**, 3197-3205.

Kruskal, M. & Segur, H. 1987

Physica D **28**, 228-240.

Kurowski, P., Guthmann, C., & de Cheveigné , S. 1990

Shapes, wavelength selection, and the cellular-dendritic "transition" in directional solidification. *Phys. Rev. A* **42**, 7368-7376.

Kurowski, P., de Cheveigné , S., Faivre, G., & Guthman, C. 1989

Cusp instability in cellular growth. To appear in *J. Physique.*

Kurz, W., & Fisher, D. J. 1986

Fundamentals of Solidification. Trans Tech Publications.

Langer, J. S. 1977

Studies in the theory of interfacial stability. II. Moving symmetric model. *Acta Metall.* **25**, 1121-1137.

Langer, J. S. 1980

Instabilities and pattern formation in crystal growth. *Rev. Mod. Phys.* **52**, 1-28.

Langer, J. S. 1984

Pattern selection in solidification. *Metall. Trans.* **15** A, 961-966.

Langer, J. S. 1986

Existence of needle crystals in local models of solidification. *Phys. Rev.* **33** A, 435-441.

Langer, J. S. & Müller-Krumbhaar, H. 1978

Theory of dendritic growth. I. Elements of a stability analysis. *Acta Metall.* **26**, 1681-1687.

Langer, J. S. & Turski, L. A. 1977

Studies in the theory of interfacial stability. I. Stationary symmetric model. *Acta Metall.* **25**, 1113-1119.

Lee, T. C. 1991

The Planar to Cellular Transition and the Long Time Scale Dynamics of Pattern Formation During Thin-film Directional Solidification. *Ph. D. Thesis* Chemical Engineering, M. I. T.

Mashaal, M., Ben Amar M., & Hakim V. 1990

Directional soldification cells at low velocities. *Phys. Rev. A* **41**, 4421-4432.

McCartney, D. G. & Hunt, J. D. 1981

Measurement of cell and primary dendrite arm spacings in directionally solidified aluminium alloys. *Acta Metall.* **29**, 1851-1863.

McCartney, D. G. & Hunt, J. D. 1984

A numerical finite difference model of steady state cellular and dendritic growth. *Metall. Trans.* **15** A, 983-994.

McFadden, G. B., Boisvert, R. F., & Coriell, S. R. 1987

Nonplanar interface morphologies during unidirectional solidification of a binary alloy: II. Three-dimensional computations. *J. Crystal Growth* **84**, 371-388.

McFadden, G. B. & Coriell, S. R. 1984

Nonplanar interface morphologies during unidirectional solidification of a binary alloy. *Physica D* **12**, 253-261.

McFadden, G. B., Coriell, S. R., & Boisvert, R. F. 1985 Double-diffusive convection with sidewalls. *Phys. Fluids* **28**, 2716-2722.

McFadden, G. B., Coriell, S. R., & Sekerka, R. F. 1988

Effect of surface tension anisotropy on cellular morphologies. *J. Crystal Growth* **91**, 180-198.

McFadden, G. B., Rehm, R. G., Coriell, S. R., Chuck, W., & Morrish, K. A. 1984

Thermosolutal convection during directional solidification. *Metall. Trans. A* **15**, 2125-2137.

McLean, M. 1983

Directionally solidified materials for high temperature service. The Metals Society.

McLean, J. W. & Saffman, P. G. 1983

The effect of surface tension on the shape of fingers in a Hele-Shaw cell. *J. Flui Mech.* **102**, 455-475.

Mehl, R. F., & Cahn, R. F. 1983

The Historical Development of Physical Metallurgy. In *Physical Metallurgy*, Third revised and enlarged edition, Part I, (ed. R. Cahn & P. Haasen), pp. 2–35. North-Holland Physics Publishing.

Merion, D. I. 1986

Selection of steady states in the two-dimensional symmetric model of dendritic growth. *Phys. Rev.* **33**, 2704–2715.

Mittelman H. D. 1977

On the approximation of capillary surfaces in a gravitational field. *J. Crystal Growth* **5**, 361–375.

Molho, P., Simon, A. J., & Libchaber, A. 1990

Peclet number and crystal growth in a channel. *Phys. Rev. A* **42**, 904-910.

Morris, L. R. & Winegard, W. C. 1969

The development of cells during the solidification of a dilute Pb-Sb alloy. *Computing* **18**, 141-148.

Mullins, W. W. 1962

J. Math. Phys. **3**, 754.

Mullins, W. W. & Sekerka, R. F. 1963

Morphological stability of a particle growing by diffusion of heat flow. *J. Appl. Phys.* **34**, 323-329.

Mullins, W. W. & Sekerka, R. F. 1964

Stability of a planar interface during solidification of a binary alloy. *J. Appl. Phys.* **35**, 444-451.

Nash, G. E. & Glicksman, M. E. 1971

A general method for determining solid-liquid interfacial free energies. *Philos. Mag.* **24**, 577-592.

Park, C. -W., & Homsy, G. M. 1984 hfill

Two-phase displacement in Hele Shaw cells: theory. *J. Fluid Mech.* **139**, 291-308.

Pelcé, P. & Pomeau, Y. 1986

Dendrites in the small undercooling limit. *Studies in Appl. Math.* **74**, 245-258.

Pelcé, P. & Pumir, A. 1985

Cell shape in directional solidification in the small peclet number limit. *J. Crystal Growth* **73**, 337-342.

Petzold, L. 1982

Differential/Algebraic Equations are not ODE's. *SIAM J. Sci. Stat. Comput.* **3**, 367–384.

Ramprasad, N., Lee, T. C., & Brown, R. A. 1991

Two-dimensional cellular structures in the solidification of CBr_4-Br_2: Comparison of calculations with experiment. Submitted to *Phys. Rev. Lett.*.

Rutter, J. W. & Chalmers, B. 1953

A prismatic substructure formed during solidification of metals. *Can. J. Phys.* **31**, 15–39.

Ryskin, G. & Leal, L. G. 1983

Orthogonal mapping. *J. Comp. Phys.* **50**, 71-100.

van Saarloos, W. & Weeks, J. D. 1985

Boundary-layer formulation of dendritic growth: existence of a family of steady-state needle solutions. *Phys. Rev. Lett.* **55**, 1685-1688.

Saffman, P.G. & Taylo, G. I. 1958

The pentration of a fluid into a porous medium or Hele-Shaw cell containing a more viscous liquid. *Proc. R. Soc. Lond. A* **245**, 312-329.

Saito, Y., Goldbeck-Wood, G., & Müller-Krumbhaar, H. 1987

Numerical simulation of crystal growth. *Phys. Rev. A* **38**, 2148-2157.

Seetharaman, V. & Trivedi, R. 1988

Eutectic growth: Selection of interlamellar spacings. *Metall. Trans. A* **19**, 2955-2964.

Seetharaman, V., Eshelman, M. A., & Trivedi, R. 1988

Cellular spacing: II. Dynamical studies. *Acta Metall.* **36**, 1175-1185.

Seydel, R. 1988

*From Equilibrium to Chaos: Practical Bifurcation and Stability Analysis.*Elsevier.

Somboonsuk, K., Mason, J. T. & Trivedi, R. 1984

Interdendritic spacing: part I experimental studies. *Metall. Trans.* **15** A, 967-975.

Sriranganathan, R., Wollkind, D. J. & Oulton, D. B. 1983

A theoretical development of interfacial cells during the solidification of a dilute binary alloy: comparison with the experiments of Morris and Winegard. *J. Crystal Growth* **62**, 256-283.

Strang, G. & Fix, G. J. 1973

An analysis of the Finite Element Method. Prentice-Hall.

Sullivan J.M. & Lynch, D. R. 1988

Nonlinear simulation of dendritic solidification of an undercooled melt. *Metall. Trans.* **25**, 415-444.

Tanveer S. 1987

Analytic theory for the selection of a symmetric Saffman-Taylor finger in a Hele-Shaw cell. *Phys. Fluids* **30**(6), 1589-1605

Thomas, P. D. & Brown, R. A. 1987

L U decomposistion of matrices with augmented dense constraints. *Int. J. Num. Meth. Eng.* **24**, 1451–1459.

Tiller, W. A. 1958

Production of dislocations during growth from the melt. *J. Appl. Phys.* **29**, 611-618.

Tiller, W. A. 1984

Quantitative solidification science. *Mat. Sci. Eng.* **65**, 3-5.

Tiller, W. A., Jackson, K. A., Rutter, J. W., & Chalmers, B. 1953

The redistribution of solute atoms during the solidification of metals. *Acta Metall.* **1**, 428-437.

Tiller, W. A. & Rutter, J. W. 1956

The effect of growth conditions upon the solidification of a binary alloy. *Can. J. Phys.* **34**, 96-121.

Trivedi, R. 1984

Interdendritic spacing: Part II. A comparison of theory and experiment. *Metall. Trans. A* **15**, 977-982.

Trivedi, R. & Somboonsuk, K. 1984a

Constrained dendritic growth and spacing. *Mat. Sci. Eng.* **65**, 65-74.

Trivedi, R. & Somboonsuk, K. 1984b

The effect of growth rate on interface morphology. In *Proceedings of the Flat-Plate Solar Array Project Research Forum on the High-Speed Growth and Characterization of Crystals for Solar Cells*, pp. 177-190. JPL Publication 84-23.

Trivedi, R. & Somboonsuk, K. 1985

Pattern formation during the directional solidification of binary systems. *Acta Metall.* **33**, 1061-1068.

Tsiveriotis, K. 1991

*Ph. D. Thesis*in preparation, Chemical Engineering, M. I. T.

Ungar, L. H. 1984

Directional Solidification from a Bifurcation Viewpoint. *Ph. D. Thesis*, Chemical Engineering, M. I. T.

Ungar, L. H., Bennett, M. J. & Brown, R. A. 1985

Cellular interface morphologies in directional solidification. III. The effects of heat transfer and solid diffusivity. *Phys. Rev. B* **31**, 5923-5929.

Ungar, L. H. & Brown, R. A. 1984a

Cellular interface morphologies in directional solidification. I. The one-sided model. *Phys. Rev. B* **29**, 1367-1380.

Ungar, L. H. & Brown, R. A. 1984b

Cellular interface morphologies in directional solidification. II. The effect of grain boundaries. *Phys. Rev. B* **30**, 3993-3999.

Ungar, L. H. & Brown, R. A. 1985

Cellular interface morphologies in directional solidification. IV. The formation of deep cells. *Phys. Rev. B* **31**, 5931-5940.

Ungar, L. H., Ramprasad, N., & Brown, R. A. 1988

Finite element methods for unsteady solidification problems arising in prediction of morphological structure. *J. Sci. Comp.* **3**, 77–108.

Venugopalan, D. & Kirkaldi, J. S. 1982

Prediction of configurational parameters in cellular solidification of succinonitrile-salol. *Scripta Metall.* **16**, 1183-1187.

Venugopalan, D. & Kirkaldi, J. S. 1984

Theory of cellular solidification of binary alloys with application to succinonitrile-salol. *Acta Metall.* **32**, 893-906.

Voorhees, P.W., Coriell, S.R., McFadden, G.B., & Sekerka, R.F. 1984

The effct of anisotropic crystal-melt surface tension on grain boundary groove morphology. *Acta Metall.* **32**, 893-906.

Warren, J. A. & Langer, J. S. 1990

Stability of dendritic arrays. *Phys. Rev. A* **42**, 3518-3525.

Weeks, J. D., & van Saarloos, W. 1988

Directional solidification cells with grooves for small partition coefficient. Preprint.

Weinberg, F. 1962

The thickness of the residual liquid layer on a decanted interface of tin. *Trans. Metall. Soc. AIME* **224**, 628–629.

Wesfreid, J. E. & Zaleski, S. 1984

Cellular Structures in Instabilities. Springer-Verlag.

Wheeler, A. A. 1986

A numerical scheme to model the evolution of the morphological instability of a freezing binary alloy. *Q. J. Mech. Appl. Math.* **39**, 381-401.

Winegard, W. C. 1964

An introduction to the solidification of metals. The Institute of Metals.

Wollkind, D. J., Oulton, D. B., & Sriranganathan, R. 1984

A nonlinear stability analysis of a model equation for alloy solidification. *J. Physique* **45**, 505-516.

Wollkind, D. J. & Segel, L. A. 1970

A nonlinear stability analysis of the freezing of a dilute binary alloy. *Phil. Trans. Roy. Soc. Lond.* **268**, 351-380.

Woodruff, D. D. 1973

The Solid-Liquid Interface. Cambridge University Press.

Yamaguchi, Y., Chang, C. J. & Brown, R. A. 1984

Multiple buoyancy-driven flows in a vertical cylinder heated from below. *Phil. Trans. R. Soc. Lond.* **312** A, 519–552.

Young, G. W., & Davis, S. H. 1986

Directional solidification with buoyancy in systems with small segregation coefficients. *Phys. Rev. B* **34**, 3388–3396.

Young, G. W., Davis, S. H., & Brattkus, K. 1987

Anisotropic interface kinetics and tilted cells in unidirectional solidification. *J. Crystal Growth* **83**, 560-571.

Appendix A

Asymptotic Analysis of Deep Cell

The asymptotic analysis of the slender region was briefly discussed in Chapter 5 where the results of the analysis were presented. The results are derived here in detail. The solutal model equations form the basis of the analysis and are reproduced here for convenience:

$$\nabla^2 c_m + P\frac{\partial c_m}{\partial y} = 0 \quad , \tag{A.1}$$

$$R_m \nabla^2 c_s + P\frac{\partial c_s}{\partial y} = 0 \quad , \tag{A.2}$$

$$\left[\hat{\mathbf{n}}\cdot\nabla c_m - R_m\,\hat{\mathbf{n}}\cdot\nabla c_s = (\hat{\mathbf{n}}\cdot\hat{y})(1-k)c_m\left(P+\frac{\partial h}{\partial t}\right)\right]_{\text{interface}} \quad , \tag{A.3}$$

$$[c_s = kc_m]_{\text{interface}} \quad , \tag{A.4}$$

$$\left[c_m = c_o + \frac{G}{m}y - \frac{\Gamma}{m}(2\mathcal{H})\right]_{\text{interface}} \quad , \tag{A.5}$$

$$\lim_{y\to\infty} c_m \to 1 \quad , \tag{A.6}$$

$$\lim_{y\to-\infty} c_s \to 1 \quad . \tag{A.7}$$

The boundary conditions far field into the melt and solid do not directly affect the asymptotic solution and will not be considered further.

A.1 Asymptotic Analysis of Sidewall Region

The scalings used in the sidewall region are as follows:

$$Y = yP\delta \quad , \tag{A.8}$$

$$X = \left(\frac{1}{2} - x\right) P \quad , \tag{A.9}$$

$$H = \left(\frac{1}{2} - h\right) P \quad , \tag{A.10}$$

$$\phi = \frac{k}{1-k} c_m \quad , \tag{A.11}$$

$$\psi = \frac{1}{1-k} c_s \quad , \tag{A.12}$$

where

$$\delta^2 = \epsilon = \frac{G}{m}\left(\frac{k}{1-k}\right)\frac{1}{P} \quad , \tag{A.13}$$

is the parameter used in the perturbation analysis as described in Chapter 5. Y is a compressed ordinate that is $\mathcal{O}(1)$ everywhere along the interface, and X and H are measured from the center of the groove as shown in Fig. 5.3. All lengths have been scaled by the diffusion length scale.

Using these scalings, the equation set (A.1)–(A.5) can be rewritten as

$$\phi_{XX} + \delta^2 \phi_{YY} + \delta \phi_Y = 0 \quad , \tag{A.14}$$

$$\psi_{XX} + \delta^2 \psi_{YY} + \frac{\delta}{R_m} \psi_Y = 0 \quad , \tag{A.15}$$

$$(\phi_X - \delta^2 H_Y \phi_Y) - (kR_m)(\psi_X - \delta^2 H_Y \psi_Y) = \delta(1-k)\phi H_Y \quad , \tag{A.16}$$

$$\left[\phi = \psi = \phi_r - \delta Y - \delta P\left(\frac{\Gamma}{m}\right)\left(\frac{k}{1-k}\right)\frac{H_{YY}}{\{1+(H_Y)^2\}^{3/2}}\right]_{X=H(Y)} \quad , \tag{A.17}$$

where

$$\phi_r = \frac{kC_o}{1-k} \quad , \tag{A.18}$$

is the reference concentration cast in terms of the scaled variables.

The parameter

$$\mathcal{G} = \frac{\Gamma}{m}\left(\frac{k}{1-k}\right) P\delta \tag{A.19}$$

represents the effect of surface and multiplies the highest order derivative in the interface shape. To view the parameter $\mathcal{G}$ in terms of the perturbation parameter δ, Eq. (A.19) is rewritten as

$$\mathcal{G} = \frac{\Gamma P^2}{G}\delta^3 \quad . \tag{A.20}$$

The value of the the fraction $(\Gamma P^2/G)$ is typically very small for organic crystals; for our calculations with the CBr$_4$ system the $(\Gamma P^2/G)$ is $\mathcal{O}(10^{-2})$. Hence, $\mathcal{G}$ can be safely assumed to be less than $\mathcal{O}(\delta^3)$ for the purposes of the asymptotic analysis.

Solution for $\delta = 0$

The melt concentration and solid concentrations and the interface shape can be looked upon as functions of the parameter δ. When $\delta = 0$ the domain of the free-boundary problem defined above has a simple shape. The equations set (A.14)–(A.17) are solved to obtain the concentration field and interface profile:

$$\phi_0 = \psi_0 = \phi_r \quad , \tag{A.21}$$

$$H_0 = D = \text{constant} \quad , \tag{A.22}$$

where the subcript '0' denotes the fact that these solutions can be viewed as the $\mathcal{O}(\delta^0)$ terms of a perturbation expansion in δ. Thus, in the absence of a temperature gradient an infinitely long cell of constant width is indicated. The solute concentration is uniform along the interface. The constant D, which can be viewed as the limit of the melt and solid domains for $\delta = 0$, can be determined by an overall mass balance; the solute entering the cross-section of the domain far field in the melt ($y \to \infty$) is matched with that leaving an arbitrary cross-section somewhere along the sidewall region, say $y = y_o$, as below:

$$P\frac{D}{P}c_o + Pk\left(\frac{1}{2} - \frac{D}{P}\right)c_o = \frac{P}{2} \quad , \tag{A.23}$$

where the first term represents solute leaving the melt region by convection at $y = y_o$ and the second term represents convection of solute in the solid at the same cross-section. The right hand side represents convection of solute at the bulk concentration far field ahead of the interface; the balance has been performed over a half-cell. The expression D/P arises from the substitution for interface shape at leading order, thus:

$$h|\,\delta = 0 = \frac{1}{2} - \frac{H}{P}\bigg|\,\delta = 0 = \frac{1}{2} - \frac{H}{P} \quad . \tag{A.24}$$

Note that, to leading order, no diffusive terms are included in accordance with the solution represented by Eq. (A.21). Simplifying Eq. (A.23) we obtain

$$D = P\frac{k}{2(1-k)}\left[\frac{1-kc_o}{kc_o}\right] \quad . \tag{A.25}$$

In the absence of an imposed temperature gradient a continuum of solutions to the sidewall region is indicated. The groove thickness depends on the value of the solute concentration at the interface c_o. Eq. (A.25) can also be drived using a perturbation analysis of the overall mass balance, as shown in Section A.2. Note that $D = 0$ for $C_o = 1/k$, and the solid is predicted to occupy the entire domain.

Domain Transformation

We now make the domain transformations

$$\text{melt} : \eta = \frac{XD}{H} \quad , \quad 0 \le \eta \le D \quad , \tag{A.26}$$

$$\text{solid} : \mu = \frac{(P/2 - X)E}{G} \quad , \quad 0 \le \mu \le E \quad , \tag{A.27}$$

$$\xi = Y \quad , \tag{A.28}$$

where $E = P/2 - D$ and $G = 1/2 - H$. After the transformation, the domain is no longer limited by a free-boundary.

Noting that

$$\eta_X = \frac{D}{H} \quad , \tag{A.29}$$

$$\eta_{XX} = 0 \quad , \tag{A.30}$$

$$\eta_Y = -\eta\frac{H_\xi}{H} \quad , \tag{A.31}$$

$$\eta_{YY} = \eta\left[\frac{2(H_\xi)^2}{H^2} - \frac{H_{\xi\xi}}{H}\right] \quad , \tag{A.32}$$

we can substite for ϕ_X, ϕ_{XX}, ϕ_Y, and ϕ_{YY} in Eq. (A.14) as follows:

$$\phi_X = \phi_\eta\frac{D}{H} \quad , \tag{A.33}$$

$$\phi_{XX} = \phi_{\eta\eta}\left(\frac{D}{H}\right)^2 \quad , \tag{A.34}$$

$$\phi_Y = -\eta\phi_\eta\left(\frac{H_\xi}{H}\right) + \phi_\xi \quad , \tag{A.35}$$

$$\phi_{YY} = \eta^2\phi_{\eta\eta}\left(\frac{H_\xi}{H}\right)^2 - 2\eta\phi_{\eta\xi}\left(\frac{H_\xi}{H}\right) + \phi_{\xi\xi} + \eta\phi_\eta\left[\left(\frac{2H_\xi}{H}\right)^2 - \frac{H_{\xi\xi}}{H}\right] \quad , \tag{A.36}$$

and Eqn(A.14) is rewritten as

$$\begin{aligned}&\left\{\frac{D^2}{H^2}\right\}\phi_{\eta\eta} - \delta\left[\left\{\frac{\eta H_\xi}{H}\right\}\phi_\eta + \phi_\xi\right] \\ &+\delta^2\left[\left\{\frac{\eta H_\xi{}^2}{H}\right\}\phi_{\eta\eta} + 2\left\{\frac{\eta H_\xi}{H}\right\}\phi_{\eta\xi} + \phi_{\xi\xi} + \eta\phi_\eta\left\{2\frac{H_\xi{}^2}{H} - \frac{H_{\xi\xi}}{H}\right\}\right] = 0 \quad .\end{aligned} \tag{A.37}$$

Similarly,

$$\mu_X = -\frac{E}{G} \quad , \tag{A.38}$$

$$\mu_{XX} = 0 \quad , \tag{A.39}$$

$$\mu_Y = -\mu\frac{G_\xi}{G} \quad , \tag{A.40}$$

$$\mu_{YY} = \mu\left[\frac{2(G_\xi)^2}{G^2} - \frac{G_{\xi\xi}}{G}\right] \quad . \tag{A.41}$$

Hence, we can substite for ψ_X, ψ_{XX}, ψ_Y, and ψ_{YY} in Eq. (A.17) as follows:

$$\psi_X = \psi_\mu\frac{E}{G} \quad , \tag{A.42}$$

$$\psi_{XX} = \psi_{\mu\mu}\left(\frac{E}{G}\right)^2 \quad , \tag{A.43}$$

$$\psi_Y = -\mu\psi_\mu\left(\frac{G_\xi}{G}\right) + \psi_\xi \quad , \tag{A.44}$$

$$\psi_{YY} = \mu^2\psi_{\mu\mu}\left(\frac{G_\xi}{G}\right)^2 - 2\mu\psi_{\mu\xi}\left(\frac{G_\xi}{G}\right) + \psi_{\xi\xi} + \mu\psi_\mu\left[\left(\frac{2G_\xi}{G}\right)^2 - \frac{G_{\xi\xi}}{G}\right] \quad , \tag{A.45}$$

and Eqn(A.17) is rewritten as

$$\begin{aligned}&\left\{\frac{E^2}{G^2}\right\}\psi_{\mu\mu} - \delta\left[\left\{\frac{\mu G_\xi}{R_m G}\right\}\psi_\mu + \frac{\psi_\xi}{R_m}\right] \\ &+\delta^2\left[\left\{\frac{\mu G_\xi{}^2}{G}\right\}\psi_{\mu\mu} - 2\left\{\frac{\mu G_\xi}{G}\right\}\psi_{\mu\xi} + \psi_{\xi\xi} + \mu\psi_\mu\left\{2\frac{G_\xi{}^2}{G} - \frac{G_{\xi\xi}}{G}\right\}\right] = 0 \quad .\end{aligned} \tag{A.46}$$

The interfacial boundary conditions Eqs. (A.16) and (A.17) now become

$$\begin{aligned}\phi_\eta\frac{D}{H} + kR_m\psi_\mu\frac{E}{G} + \delta^2\left[\left\{\eta\phi_\eta\left(\frac{H_\xi^2}{H}\right) - \phi_\xi H_\xi\right\} \right. &+ \left. kR_m\left\{\mu\psi_\mu\left(\frac{G_\xi^2}{G}\right) - \psi_\xi G_\xi\right\}\right] \\ &= \delta(1-k)\phi H_\xi\Big|_{\eta=D} \quad ,\end{aligned} \tag{A.47}$$

and

$$\phi = \psi = \phi_r - \delta\xi - \delta^3 \mathcal{G} \frac{H_{\xi\xi}}{\{1 + \delta^2 (H_\xi)^2\}^{3/2}} \bigg|_{\eta=D} \tag{A.48}$$

Perturbation Analysis

Equations (A.37) and (A.46), together with the boundary conditions (A.47) and (A.48) are solved using a regular perturbation analysis. The analysis assumes that the concentration in the melt and solid and interface shape can be represented as a power series in δ as follows:

$$\phi(\eta, \xi) = \phi_0(\eta, \xi) + \delta\phi_1(\eta, \xi) + \delta^2\phi_2(\eta, \xi) + \cdots \quad , \tag{A.49}$$

$$\psi(\mu, \xi) = \psi_0(\mu, \xi) + \delta\psi_1(\mu, \xi) + \delta^2\psi_2(\mu, \xi) + \cdots \quad , \tag{A.50}$$

$$H(\xi) = H_0(\xi) + \delta H_1(\xi) + \delta^2 H_2(\xi) + \cdots \quad , \tag{A.51}$$

The expansions for the independent variables given by Eqs. (A.49)–(A.51) are substituted in Eqs. (A.37), (A.46), (A.47), and (A.48) and solutions accurate to each order in δ are determined by including only terms that appear at that order, as shown below:

Order δ^0 :

Equations(A.37) and (A.46) are reduced to

$$\phi_{0_{\eta\eta}} = \psi_{0_{\mu\mu}} = 0 \quad . \tag{A.52}$$

Thus, the concentration field correct to $\mathcal{O}(\delta^0)$ are determined form Eq. (A.48) as

$$\phi_0 = \psi_0 = \phi_r \quad , \tag{A.53}$$

and the solute balance equation (A.47) is satisfied automatically.

Order δ^1 :

Equations(A.37) and (A.46) are reduced to

$$\phi_{1_{\eta\eta}} = \psi_{1_{\mu\mu}} = 0 \quad . \tag{A.54}$$

From Eq. (A.48) the concentration fields in the two phases are determined as

$$\phi_1 = \psi_1 = -\xi \quad . \tag{A.55}$$

These solutions are substituted in Eq. (A.47) to yield

$$D_\xi = 0 \tag{A.56}$$

which implies that D is a constant, as determined earlier; see Eq. (A.25).

Order δ^2 : Equations(A.37) can be rewritten, accurate to this order as

$$\phi_{2_{\eta\eta}} + \phi_{1_\xi} = 0 \quad . \tag{A.57}$$

Substituting for ϕ_1 from Eq. (A.55), Eq. (A.57) is rewritten as

$$\phi_{2_{\eta\eta}} = 1 \quad . \tag{A.58}$$

Thus,

$$\phi_2 = \frac{1}{2}\left(\eta^2 - D^2\right) \quad . \tag{A.59}$$

Similarly,

$$\psi_{2_{\mu\mu}} + \psi_{1_\xi} = 0 \tag{A.60}$$

Thus

$$\psi_{2_{\mu\mu}} = \frac{1}{R_m} \quad , \tag{A.61}$$

and

$$\psi_2 = \frac{1}{2R_m}\left(\mu^2 - E^2\right) \quad . \tag{A.62}$$

Equation (A.47) can be rewritten, correct to $\mathcal{O}(\delta^2)$ as

$$\phi_{2_\eta} + kR_m\psi_{2_\mu} = (1-k)(\phi_1 D_\xi + \phi_0 H_{1\xi})\Big| \eta = D \quad . \tag{A.63}$$

Substituting for ϕ_0, ϕ_1, ϕ_2, ψ_2, and D from Eqs. (A.53), (A.55), (A.59), (A.62) and (A.25), respectively Eq. (A.63) can be rewritten as

$$H_{1\xi} = \frac{D + kE}{(1-k)\phi_r} \quad . \tag{A.64}$$

Substituting for D and E from Eq. (A.25) and integrating, the interface shape, accurate to $\mathcal{O}(\delta^1)$ is determined as

$$H_1(\xi) = \left\{D + \frac{k/2}{1-k}\right\}\frac{1}{\phi_r}\xi + D_1 \quad , \tag{A.65}$$

where D_1 is the constant of integration that is also determined by an overall mass balance correct to $\mathcal{O}(\delta^1)$, as shown in the following section; $D_1 = 0$.

Using the scalings in Eqs. (A.8)–(A.12), and substituting for H_0 and H_1 in the perturbation expansion Eq. (A.51) the interface shape is rewritten in terms of the original variables x, y, and h as

$$h(y) = \frac{1}{2} - \frac{H}{P} = \frac{1}{2} - \frac{1}{P}\left[H_0 + \delta H_1 + \delta^2 H_2 + \ldots\right] \tag{A.66}$$

$$= \frac{1}{2} - \frac{k}{2(1-k)}\left(\frac{1-kc_o}{kc_o}\right) + \frac{G}{m}\frac{1}{2c_o^2(1-k)}y + \mathcal{O}(\delta^2) \quad . \tag{A.67}$$

The concentration field in the two phases is similarly determined as

$$c_m(y) = c_o - \frac{G}{m}y + \frac{P}{2}\left\{\left(\frac{1}{2} - x\right)^2 - \left(\frac{1}{2} - h\right)^2\right\} \quad , \tag{A.68}$$

$$c_s(y) = kc_o - k\frac{G}{m}y + k\frac{P}{2R_m}\left\{x^2 - h^2\right\} \quad . \tag{A.69}$$

In the special case of $c_o = 1/k$, the interface is given by

$$h = \frac{1}{2} - \frac{G}{m}\frac{k^2}{2(1-k)}y + \mathcal{O}(\delta^2) \quad . \tag{A.70}$$

A.2 Mass Balance

A mass balance is performed at an arbitrary cross-section, say at $y = y_o$; the solute entering the domain by convection far field in the melt ($y \to \infty$) is matched with the solute leaving at $y = y_o$ by diffusion and convection in the two phases. The balance is written as

$$\int_0^h \left(Pc_m + \frac{\partial c_m}{\partial y}\right)dx + \int_h^{1/2}\left(Pc_s + R_m\frac{\partial c_s}{\partial y}\right)dx = \frac{P}{2} \quad . \tag{A.71}$$

Equation (A.71) is rewritten in terms of the scaled variables as

$$\int_H^{P/2} (\phi + \delta\phi_Y)\,dx + k\int_0^H (\psi + \delta R_m \psi_Y)\,dx = P\frac{k}{2(1-k)} \quad . \tag{A.72}$$

The regular perturbation expansions for ϕ, ψ and H from Eqs. (A.49)–(A.51) are substituted into Eq. (A.72) and terms correct to each power in δ are matched, as shown below.

<u>Order δ^0</u>

$$\phi_0\left(\frac{P}{2} - H_0\right) + k\psi_0 H_0 = P\frac{k}{2(1-k)} \quad , \tag{A.73}$$

where the integrals are converted to products because ϕ_0 and ψ_0 are not functions of x. Substituting fot ϕ_0 and ψ_0 from Eq. (A.53) yields

$$H_0 = \frac{1}{2} - P\frac{k}{2(1-k)}\left\{\frac{1-\phi_r(1-k)}{\phi_r(1-k)}\right\} \quad . \tag{A.74}$$

Order δ^1

$$\phi_1\left(\frac{P}{2} - H_0\right) - \phi_0 H_1 + k\psi_1 H_0 + k\psi_0 H_1 = 0 \quad . \tag{A.75}$$

Substituting for ϕ_0 and ψ_0 from Eq. (A.53), ϕ_1 and ψ_1 from Eq. (A.55), and H_0 from Eq. (A.74) into Eq. (A.75) yields

$$H_1 = \frac{P}{\phi_r^2}\frac{k}{2(1-k)^2}Y \quad . \tag{A.76}$$

Similarly, higher order corrections to the interface shape can be determined.

Substituting H_0 and H_1 into the perturbation expansion Eq. (A.51), the interface shape is given as

$$h(y) = \frac{1}{2} - \frac{k}{2(1-k)}\left(\frac{1-kc_o}{kc_o}\right) + \frac{G}{m}\frac{1}{2c_o^2(1-k)}y + \mathcal{O}(\delta^2) \quad . \tag{A.77}$$

This result is exactly that obtained from the perturbation analysis of previous section. This is not unexpected since the effect of the curvature is not seen in either result; the influence of the surface energy can onlybe seen for higher orger solutions, greater than $\mathcal{O}(\delta^3)$ where the parameter $\mathcal{G}$ becomes part of the analysis. For the same reason, an asymptotic analysis with $\epsilon = \delta^2$ as the perturbation parameter yields similar results as the analysis of the previous section. The perturbation analysis with this news scaling is presented in the following section.

A.3 Perturbation analysis with $y \approx \epsilon^{-1}$

The scalings used here are

$$Y = yP\epsilon \quad , \tag{A.78}$$

$$X = \left(\frac{1}{2} - x\right)P \quad , \tag{A.79}$$

$$H = \left(\frac{1}{2} - h\right)P \quad , \tag{A.80}$$

$$\phi = \frac{k}{1-k}c_m \quad , \tag{A.81}$$

$$\psi = \frac{1}{1-k}c_s \quad , \tag{A.82}$$

The scaled equations are

$$\phi_{XX} + \epsilon^2\phi_{YY} + \epsilon\phi_Y = 0 \tag{A.83}$$

$$\psi_{XX} + \epsilon^2\psi_{YY} + \frac{\epsilon}{R_m}\psi_Y = 0 \tag{A.84}$$

$$(\phi_X - \epsilon^2 H_Y\phi_Y) - (kR_m)(\psi_X - \epsilon^2 H_Y\psi_Y) = \epsilon\phi(1-k)H_Y\Big| X = H(Y) \quad , \tag{A.85}$$

$$\phi = \psi = \phi_r - \epsilon Y - \epsilon^3\mathcal{G}\frac{H_{YY}}{(1+\epsilon^2 H_Y^2)^{3/2}}\Bigg| X = H(Y) \quad , \tag{A.86}$$

Equations (A.83)–(A.86) are solved in a similar manner to the procedure outlined in Section A.1. The perturbation expansions in this case are as follows

$$\phi(X,Y) = \phi_0(X,Y) + \epsilon\phi_1(X,Y) + \epsilon^2\phi_2(X,Y) + \cdots \quad , \tag{A.87}$$

$$\psi(X,Y) = \psi_0(X,Y) + \epsilon\psi_1(X,Y) + \epsilon^2\psi_2(X,Y) + \cdots \quad , \tag{A.88}$$

$$H(Y) = H_0(Y) + \epsilon H_1(Y) + \epsilon^2 H_2(Y) + \cdots \quad , \tag{A.89}$$

At order ϵ^0

$$\phi_{0XX} = \psi_{0X}X = 0 \quad , \tag{A.90}$$

so that

$$\phi_0 = \psi_0 = \phi_r - Y \tag{A.91}$$

$$\tag{A.92}$$

$H_0(y)$ can be determined at order ϵ^1

$$\phi_{1XX} = -\phi_{0Y} = 1 \quad , \tag{A.93}$$

so that

$$\phi_1 = \frac{1}{2}(X^2 - H^2) \quad . \tag{A.94}$$

Also,

$$\psi_{1XX} = -\frac{\psi_{0Y}}{R_m} = \frac{1}{R_m} \tag{A.95}$$

so that

$$\psi_1 = \frac{1}{2R_m}\left[(\frac{P}{2} - X)^2 - (\frac{P}{2} - H)^2)\right] \quad . \tag{A.96}$$

Equation (A.85) is reduced to

$$\phi_{1X} - (kR_m)\psi_{1X} = (1-k)\phi_0 H_{0Y} \quad . \tag{A.97}$$

Substituting for ϕ_1 and ψ_1 in Eq. (A.97) yields

$$H_0 + k\left(\frac{P}{2} - H_0\right) = (1-k)(\phi_r - y)H_{0Y} \quad . \tag{A.98}$$

Simplifying and integrating,

$$H_0 + \frac{Pk}{2(1-k)} = \frac{\alpha}{(\phi_r - y)} \quad , \tag{A.99}$$

where α is a constant of integration that can be determined from an overall mass balance as shown below.

Using the scalings given by Eqs. (A.78)-(A.82) and the perturbation expansions given by Eqs. (A.87)-(A.89), the mass balance Eq. (A.71) can be rewritten as

$$\begin{aligned}&\{(\phi_0 + \epsilon\phi_1) + \epsilon(\phi_{0Y} + \epsilon\phi_{1Y})\}\{H_0 + \epsilon H_1\} + k\{(\psi_0 + \epsilon\psi_1)\\ &+R_m\epsilon(\psi_{0Y} + \epsilon\psi_{1Y})\}\left\{\frac{P}{2} - (H_0 + \epsilon H_1)\right\} = (\phi_0 + \epsilon\phi_1)\frac{k}{2(1-k)} + \mathcal{O}(\epsilon^2)\end{aligned} \tag{A.100}$$

where the integrals in Eq. (A.71) have been converted to simple products because the expressions in the integrand are not functions of x up to $\mathcal{O}(\epsilon^2)$.

At order ϵ^0 we get

$$H_0 + \frac{Pk}{2(1-k)} = \frac{k}{2}\frac{P}{(1-k)^2(\phi_0 - Y)} \quad , \tag{A.101}$$

so that

$$\alpha = \frac{Pk}{2(1-k)^2} \quad . \tag{A.102}$$

Using $c_o = \frac{1}{k}$ and $\phi_0 = \frac{1}{1-k}$, the interface is determined in terms of the original variables.